Extreme Seismic Anomalies near Earth's Core Mantle Boundary

by

Shule Yu

A Dissertation Presented in Partial Fulfillment
of the Requirements for the Degree
Doctor of Philosophy

Approved December 2019 by the
Graduate Supervisory Committee:

Edward J. Garnero, Chair
Sang-Heon Shim
Mingming Li
James A. Tyburczy
Christy B. Till

ARIZONA STATE UNIVERSITY

May 2020

ABSTRACT

The interior of Earth is stratified due to gravity. Therefore, the lateral heterogeneities observed as seismic anomalies by seismologists are extremely interesting: they hold the key to understand the composition, thermal status and evolution of the Earth. This work investigates seismic anomalies inside Earth's lowermost mantle and focuses on patch-like ultra-low velocity zones (ULVZs) found on Earth's core-mantle boundary (CMB). Firstly, all previous ULVZ studies are compiled and ULVZ locations on the CMB are digitized. The result is a database, which is publicly available online. A key finding is that there is not a simple mapping between the locations of the observed ULVZs and the large low velocities provinces (LLVPs). Instead, ULVZs are more likely to occur near LLVP boundaries. This spatial correlation study supports a compositionally distinct origin for at least some ULVZs. Next, the seismic structure of the basal mantle beneath the Central America is investigated. This region hosts present and past subducted slabs, which could have brought compositionally distinct oceanic basalt all the way down to the CMB. The waveform distortions of a core-reflected seismic phase and a forward modeling method are used to constrain the causes of the CMB structures. In addition to ULVZ structures, isolated patches of thin zones with shear velocity increased by over 10% relative to background mantle are found for the first time. Ultra-high velocity zones (UHVZs) are interspersed with ULVZs and could be caused by subducted mid-ocean ridge basalt (MORB) that undergoes partial melting and melt segregation. Fe-rich partial melt of MORB can form ULVZs, and silica polymorphs (SiO_2) and calcium-perovskite (CaPv) rich solid residue can explain the UHVZs. Finally, large-scale heterogeneities in the lowermost mantle are investigated using S waveform broadening observations.

Several basal layer models are case-studied via synthetic calculations. S wave arrivals received at a distance larger than 80° in a global dataset from large earthquakes between the years 1994 and 2017 are examined and S waveform broadenings are documented. This approach exploits large distance data for the first time, and therefore is complementary to previous studies in terms of sampling locations. One possible explanation of S waveform broadening is velocity discontinuity inside the D″ layer due to the temperature controlled Bm-pPv phase transition.

DEDICATION

I dedicate this work to my parents, who always support me and help me develop my own interest. I would not achieve this without them.

ACKNOWLEDGMENTS

I owe greatest gratitude to my advisor, Edward Garnero. He led me to the seismology community, taught me how to process, analyze and interpret data, and inspired me how to manage work life balance with his own lifestyle. He also spent a lot of time help me present my work. He taught me how to write more clearly and accurately, how to make a fantastic figure and how to structure an efficient presentation. I also thank other members in my supervisory committee: Dan Shim, Jim Tyburczy, Mingming Li and Christy Till. I learned a lot in their lectures. Their comments on my work made it better, and their encouragements to me warmed my heart. I would also like to thank my previous committee member Allen McNamara. He is a wise guy and his humor always bring laughter to meetings and discussions.

I would like to thank my workmates. My academic brother, Hongyu Lai, who picked me up from the airport when I first came to the country. He is the one I discussed the most in coding, scheduling work and road trip plans. I also thank Mark Stevens, who maintains our clusters. A big hug to all my office mates for creating this integrated research environment: John West, Dan Frost, Divya Allu Peddiniti, Huawei Chen, Byeongkwan Ko, Hélèné Pièt, Taehyun Kim, Qian Yuan, Yongming Wang.

I would also like to thank all my basketball friends: Peiyuan (Boki) Wang, Chufeng Li, Jianlan Ye, Yonghao Wang, Yuzhen Xie, Chenyang Tao, Jing Hu and many others. I would also like to acknowledge Shuyao Hong. Hongyu and I spent a lot of great times in his house. Wish his PhD goes well.

My special thank goes to my soul mate Mengran Wang. Your love and companion supported me and helped me complete my PhD.

TABLE OF CONTENTS

Page

APPENDIX

LIST OF TABLES

Table Page

LIST OF FIGURES

Figure Page

Figure Page

CHAPTER 1

INTRODUCTION

In this chapter, I will first introduce the studies of the Earth, including their methods, main questions to answer and the links between them. Then I will introduce Earth's composition, structures and heterogeneities. Next I will review some heterogeneities seismically observed in Earth's lowermost mantle. Finally, a brief summary of each chapter is presented.

1.1 The Studies of Earth's Interior

Seismology is an important and efficient way to explore the Earth's interior. Earthquakes generate seismic waves, which travel through the interior of the Earth and are recorded by seismometers on Earth's surface. These seismic waves scan and examine the interior of the Earth in a similar way as X-rays from CT scanners in hospitals. By documenting the ray paths, finding the travel times and measuring the intensities of each arrival and echo, seismologists are able to reconstruct the material properties in Earth's interior at different locations. Based on seismic results, chemical compositions, mineral phases and degree of melting can be interpreted with help from petrologists and mineralogists (just like you need a doctor to interpret your CT scan results). Because we don't have direct access to materials in Earth's deep interior (the known deepest sample is a diamond inclusion, which was formed at Earth's transition zone [Pearson et al., 2015]), almost all observations of Earth's deep interior are results of seismology.

However, seismology has its limitations. First and foremost, the locations of earthquake and receivers are restricted. Most earthquakes happen along plate boundaries, and for now, seismic stations are mostly restricted to the lands. This geometry restriction results in under-sampling for certain regions, especially for the southern hemisphere. One solution is to deploy more and better ocean bottom seismometers. Another solution is exploiting new ray paths and new processing methods to manually compensate the insufficient samplings [Lai et al., 2019]. A second challenge is computer underpower when calculating synthetic seismograms for 3D models. Synthetic seismograms are crucial in seismology, especially for waveform analysis such as full waveform tomography. When high frequency content in synthetic seismograms is needed, computer speed is still a bottle neck. As a result, searching through numerous 3D models and justifying the uniqueness of one's result are not simple tasks.

Minerology is important because it links seismic observations to actual minerals. High pressure mineral physicists keep exploring and recording material properties from different samples under pressure-temperature conditions comparable to Earth's interior. The targeted material properties include density, crystal structure, elastic constants, viscosity, electric conductivity, solidus, diffusion rates etc. The different samples used broadly refers to different chemical compositions (starting materials), volatile contents, melting status etc. The mapping between pressure-temperature conditions, different samples and their material properties provides the fundamental interpretations for seismic observations as well as Earth's interior environments.

Geodynamic modeling plays significant roles in studying the evolution of Earth and other planets. Geodynamicists use laboratory experiments and computational methods, such as finite element and finite difference, to solve the time dependent partial differential governing equations. The three most important equations are conservations of mass, momentum and energy (heat flow). To test special cases, different boundary conditions or evolution rules can be imposed to the system. Geodynamic modeling keeps snapshots from each time step, recording the change in temperature field, compositions field, viscosity field and etc. Therefore, a movie of mantle material evolution can be made to cast lights on Earth's evolution histories (or the futures). In addition to that, statistic measurements (e.g. the averaged subduction stagnant depth; the averaged heterogeneity size) can also be estimated. Because reality is far more complicated than computers can handle, and also because some crucial parameters (such as viscosity) are not well constrained, geodynamic modeling results are usually compared to seismology or geochemistry observations to justify their assumptions. As the observation puzzle pieces come together, and as the computing power grow, geodynamic modeling will have higher resolution and become closer to reality.

Geochemistry is the most reliable way to study Earth interior's composition. Geochemists analyze rock samples for their composition to gain knowledge of Earth's interior. For example, the bulk composition of the Earth comes from studies of chondrites and studies of melting processes that happen at the mid-oceanic ridges. Another example would be the discovery of water in a ringwoodite inclusion in a diamond [Pearson et al., 2015], which added strength to the long-held speculation that the transition zone holds water comparable to several oceans. Rock formation processes then can be deduced from composition. For example, the Bowen melt and crystallization series provides a way to constrain the formation temperature when melt product compositions are provided. The limitations of geochemistry are (1) there are not many samples from the deep Earth, and therefore until new samples are discovered, we have to assume current samples are representative, and (2) because of geologic transportations, it's hard to decide where exactly the sample was formed.

The study of Earth's interior requires cooperation among multiple disciplinaries. For example, a recent geodynamic study provides explanation for previous geochemistry observations that tungsten isotope heterogeneity exists between large igneous provinces (LIPs) and oceanic island basalt (OIB) [Rizo et al., 2016; Mundl et al., 2017; Jones et al., 2019], linking the surface observations to interior processes. Minerology provides explanations to numerous seismic observations. Geodynamic modeling helps understanding what controls the morphologies of interpreted seismic structures, and therefore Geodynamics is crucial in learning how and where similar observations should happen (details of D″ discontinuity, large low shear wave velocity province (LLSVP) and ultra-low velocity zone (ULVZ) are introduced in section 1.3).

1.2 Composition, Mineral Phases and Heterogeneities of Earth's Mantle

Several compositional models of the Earth have been proposed. I will introduce the chondrite model and pyrolite model here [Ringwood 1962; Taylor, 1964; McDonough and Sun 1995]. The Chondrite model is based on compositions of CI carbonaceous chondrites. These chondrites, interestingly, don't have recognizable chondrules, and are thought to be the most primitive planet building blocks. The bulk composition of the Earth can be derived from their composition, after the volatiles (nebula compositions, including hydrogen, nitrogen, noble gas and etc.) are subtracted. In contrast, the pyrolite model is derived from peridotite melting experiments. This model was initially intended for the upper mantle composition. It was later suggested that the lower mantle may have the same composition based on sound velocity arguments [Hyung et al., 2016; Zhang et al., 2016] (though different options do exist [Ricolleau et al., 2009; Murakami et al., 2012]). The exact element concentrations of the pyrolite model are not fixed. In [Ringwood, 1962], its approximate composition was one part of basalt and four parts of dunite (ultramafic rock, 90% of which is olivine). The refractory lithophile element concentrations in pyrolite model match the chondrite model, after the core components are subtracted [McDonough and Sun, 1995]. But the transitional lithophile element (especially Mg and Si) concentrations don't match that of the chondrite model, which leads to a speculation that during Earth's differentiation, Si partitioned into Earth's outer core [Mao et al., 1990; O'Neill, 1991], or into a lower mantle primordial reservoir. The primordial reservoir could be formed by fractional crystallization of the magma ocean and persisted through Earth's history [Labrosse et al., 2007].

For pyrolitic composition, the major mineral phases in Earth's upper mantle are olivine, pyroxene and garnet. The fraction of olivine is around 60% [Xu et al., 2008; Stixrude and Lithgow-Bertelloni, 2012], and it undergoes phase transition to wadsleyite at around 13 GPa along a deduced geotherm [Ringwood, 1991]. Wadsleyite transforms to ringwoodite at around 18 GPa and finally ringwoodite disproportionates to bridgmanite and (Mg, Fe)O magnesiowüstite at around 23 GPa. The exact phase transition pressures depend on the temperature conditions (which are estimated to be around 1500˚C at the transition zone [Irifune, 1987]) and Fe content [Ringwood, 1991]. Pyroxene, however, is gradually replaced by garnet around depth of 460 km, and garnet will eventually transform to bridgmanite at around 700 km [Irifune, 1987]. At the same time, the calcium in garnet will separate and form Ca-perovskite as an independent phase in the lower mantle [Irifunea and Ringwood, 1987]. The calcium atom fraction in the lower mantle is around 5~10% [Stixrude and Lithgow-Bertelloni, 2012]. The major phase transition in the lower mantle is bridgmanite which transforms to post-perovskite at around 120 GPa, which is comparable to the condition in Earth's lowermost mantle [Murakami et al., 2004; Oganov and Ono, 2004; Tsuchiya et al., 2004; Shim et al., 2004; Shim 2008]. Post-perovskite could transform back to bridgmanite if the temperature gradient near the CMB is steep enough [Hernlund et al., 2015] to meet the adiabatically estimated outer core temperature [Anzellini et al., 2013].

Composition models and their subsequent phase transitions do not mean Earth's mantle is chemically homogeneous and mineral phases are evenly mixed. One of the most significant active sources of mantle chemical heterogeneities is the subducting oceanic crust. Because the chemical diffusion rate for oceanic crust to be destroyed is much slower than its production rate, it is estimated that the subducted oceanic crust could survive in the mantle for billions of years [Hofmann and Hart, 1978; Holzapfel et al., 2005]. Other sources of heterogeneities include residues from magma ocean crystallization [Labrosse et al., 2007; Lee et al., 2010], reactions between mantle and the core at the CMB [Knittle and Jeanloz, 1989; Buffet et al., 2000; Takafuji, 2005] and subducted continental crust [Loubet et al., 1988; Ye et al., 2000]. These mantle chemical heterogeneities are good explanations for lateral seismic velocity anomalies. It is noteworthy that chemical composition is only one factor affecting seismic velocity. Two other factors are temperature and mineral phases. Geodynamics of these chemical heterogeneities showing under what pressure temperature conditions they will form and where they should accumulate to be detectable by seismology are also needed to fully explain heterogeneity observations. In the next section, several lower mantle seismic heterogeneities related to my research topics are introduced. A comprehensive figure illustrating their locations, sizes and morphologies is plotted using previous seismic study results (Figure 1.1).

1.3 Seismic Structures in Earth's Mantle

1.3.1 1D Earth Models

Pressure and temperature have the most significant effects on material elastic properties, and these two parameters vary the most in Earth's radius direction. As a result, the lateral variations of seismic properties are much less than the vertically variations. Earth's seismic structure is well approximated by 1D models where seismic velocity, density, attenuation and anisotropy are depicted as a function of depth. Several 1D seismic models have been constructed using different datasets, different data types (e.g. seismic, gravitational), different inversion methods and different model parameterizations; To name a few: Preliminary Reference Earth Model (PREM [Dziewoński and Anderson, 1981]), International Association of Seismology and the Physics of the Earth's Interior (IASP91 [Kennett and Engdahl, 1991]) and AK135 [Kennett et al., 1995]). These models have different focuses because the datasets they used are different. For example, PREM used the most types of data and therefore is suitable for both body wave and long period surface wave studies. IASP91 used a large number (about six million) of body wave measurements and therefore is suitable for body wave and earthquake relocation studies. AK135 included PKP data (a body wave that propagates in the outer core) and therefore has better constrains on P velocity in the outer core. Both IASP91 and AK135 emphasize travel time fitting and as a result, have fewer implications relative to mineral phase changes, compared with PREM.

For projects in this thesis, PREM is used as the reference model to calculate synthetic seismograms. For the mantle part, PREM has four first-order discontinuities (jump of values) at depth 24.4 km, 220 km, 400 km, 670 km and four second-order discontinuities (change of slope) at depth 80 km, 600 km, 771 km, 2741 km. Five discontinuities in PREM are based on Earth's bulk properties from previous studies: 24.4 km is an area-weighted average (between continental and oceanic) crustal thickness; 80 km is roughly the thickness of lithosphere; 220 km hosts Lehmann discontinuity, which is regionally observed and somewhat controversial at the time; 400 km and 670 km are designed for the olivine phase changes (olivine transform to wadsleyite at around 13 GPa; ringwoodite transform to bridgmanite at around 23 GPa). On the other hand, some discontinuities are math solutions from inversions, trying to fit seismic travel time observations: the gradient change at 600 km and 771 km are proposed to fit travel times better; the gradient change at 2741 km is needed to explain arrival time trends for large distance data. My projects focus on mantle structures locates close to the core-mantle boundary (CMB), and therefore when we calculate synthetics, all the upper mantle discontinuities of PREM are smoothed out (see Appendix B for details) to avoid contaminating arrivals they generate.

1.3.2 Subducted Slabs

Cross-sections along subduction directions (perpendicular to trenches) from tomography models captured various slab morphologies [e.g. Li et al., 2008; Sigloch et al., 2008; Fukao et al., 2013; French and Romanowicz 2014]. Some slabs are stagnant at the uppermost region of the lower mantle, usually at 660 km or at 1000 km depth (e.g. subduction zone near Honshu, Izu-Bonin, Kurile, Java, Tonga-Kermadec and controversially, beneath south America). Others, however, descend to the lower mantle directly (e.g. Mariana, central America) [Fukao et al., 2013]. The seismic velocity in slabs are about 1~1.5% higher for P wave and around 3% higher for S wave than the surrounding mantle [Fuako et al., 2013; French and Romanowicz 2014]. It is often believed that the lower temperature in slabs cause their higher than average seismic velocity.

Oceanic lithospheres are made up of several kilometers thick oceanic crust on the top (consist of mid ocean ridge basalt (MORB) and gabbro) and tens of kilometers thick solid uppermost mantle (harzburgite and depleted pyrolite) beneath the crust. MORB has higher iron, calcium and aluminum content and less Magnesium comparing to the pyrolite model, while the harzburgite composition are close to pyrolite model but with less Ca, Al and more Mg [e.g. Schilling et al., 1983; Ringwood and Irifune, 1988; Workman and Hart, 2005; Xu et al., 2008]. The composition differences cause different mineral phase changes in slabs and the background mantle [Stixrude and Lithgow-Bertelloni, 2012], which have major effects on morphology and dynamics of slabs. The intrinsic density of MORB is higher than the background mantle throughout most of the mantle, however, its elevated aluminum content extends the stability field of garnet and delays its phase transition near 700 km depth. When the background mantle becomes bridgmanite, the garnet in MORB remaining relatively buoyant [Ringwood and Irifune, 1988]. This buoyancy deficit persists even after harzburgite and thermal effects are taken into account, and it is believed to be one contributor of the seismically observed slab stagnations [e.g. Fukao et al., 2009]. Except for the buoyancy deficit, other causes of slab stagnations are proposed: lower mantle viscosity jump, trench roll back, slab weakening etc. [e.g. Rubie, 1984; Gurnis and Hager, 1988; Christensen 1996]. However, most dynamical modeling shows slabs will eventually descend into the lowermost mantle.

The fate of oceanic crust in the lower mantle is under debate. It's a hot topic because the subducting oceanic crust is a major on-going chemical composition heterogeneity generator, and therefore it's a major candidate for many observed seismic anomalies. Minerology studies suggest MORB remains denser than the surrounding mantle, and therefore, it could reach the CMB area [e.g. Hirose et al., 2005; Ohta et al., 2008]. Two topics are extremely interesting: could MORB accumulate on the CMB; and what happens if MORB contacts and react with the hot core?

Geodynamic modeling shows that for oceanic crust to accumulate on the CMB, the separation between crust and lithosphere is crucial [Li and McNamara, 2013; McNamara, 2019]. The heating from the CMB and the Bm-pPv phase transition could make the lithosphere rheologically weaker, which will enhance the separation [Ammann et al., 2010]. The accumulation of oceanic crust on the CMB could explain the seismically observed large low shear velocity provinces (LLSVPs) [e.g. Mulyukova et al., 2015]. On the other hand, if the oceanic crust is entrained into the background mantle flow, it could get carried by mantle plumes, either all the way back to the surface and manifest in surface geochemical observations [Li et al., 2014], or exist in the mid mantle as seismic scatterers [Kaneshima, 2006].

The temperature at the CMB can't be well constrained because the exact chemical composition of lowermost mantle is unknown. An estimated value is between 3500 K to

4000 K from melting studies based on pyrolite composition, chondrite composition and iron alloy [Andrault et al., 2011; Anzellini et al., 2013; Nomura et al., 2014]. MORB melting studies show its solidus could be around 3800K to 4000K [Andrault et al., 2014; Pradhan et al., 2015]. Volatiles such as water in MORB could lower its solidus, but whether water could survive dehydration on its journey down is unknown. Therefore, it seems MORB is hard to melt under the CMB condition [Pradhan et al., 2015]. If, however, MORB melts at the CMB, its melting sequence would be bridgmanite, stishovite and finally calcium perovskite [Andrault et al., 2014; Pradhan et al., 2015]. The composition of the melt is not conclusive. Different scenarios based on the melt composition are proposed: the eventual destruction of MORB signatures; or a dense and stable Fe enriched partial melt (which is a possible origin of seismically observed ultra-low velocity zones); or locally SiO_2 concentrated regions [e.g. Andrault et al., 2014; Pradhan et al., 2015].

1.3.3 LLSVP

Two mountain-like, antipodal, large low shear-wave velocity provinces (LLSVPs) beneath the central Pacific and Africa are consistently observed sitting on (or rising from?) the core-mantle boundary (CMB) in tomography models [e.g. Dziewoński and Woodhouse 1987; Trampert et al., 2004; Ishii and Tromp, 2004; Grand, 2002; Ritsema et al., 2011]. Typical velocity reductions within LLSVPs range from 3% to 5% relative to reference 1D models. Normal mode studies [Woodhouse 1987; Trampert et al., 2004] suggest LLSVPs are denser than the surrounding mantle. However, this is not conclusive because normal mode observations are average of multiple depths [Koelemeijer et al., 2017]. There are numerous ways to define LLSVP locations on the CMB. Velocity reduction contours for each tomography model at CMB depth could be used as LLSVP boundaries, however, the contour values are chosen subjectively. In Garnero et al. [2016], the contour values for different tomography models are chosen such that the enclosed low velocity region takes up 30% of total CMB area. The contour values from this method range from 0.3% to 0.7% lower than PREM for different tomography models [Houser et al., 2008; Simmons et al., 2010; Ritsema et al., 2011; French and Romanowicz 2014]. Another way to find the boundary of LLSVPs is to calculate the lateral velocity reduction gradient and find locations with extreme gradient values [Thorne et al., 2004; Zhao et al., 2015]. Lekic et al. [2012] used cluster analysis on the vertical (from shallow to deep) velocity structure profiles at each geographic location for all tomography models. They defined LLSVP locations on the CMB as the agreement on where the classification with the lowest velocity locates across all models. LLSVP boundaries can also be characterized as seismically sharp contrasts. These observations are mostly regional, using forward modeling to explain wave broadenings, which happens when seismic waves experiences multipathing around sharp velocity contrasts [Bréger and Romanowicz, 1998; Ni and Helmberger, 2003abc; He and Wen, 2009; Zhao et al., 2015]. Due to earthquake and station geometry limitations, these regional results do not form enclosed regions as the velocity contour method does [e.g. Zhao et al., 2015]. For S waves, different definitions of LLSVP locations agree with each other to the first order. However, similar definitions for P waves result in large low P-wave velocity regions not as consistent to each other as the S-wave [Garnero et al., 2016, supplementary material]. Nonetheless, observations of sharp P velocity contrasts utilizing wave waveform broadening were also reported in the northeastern Pacific, matching the pacific LLSVP eastern boundary [e.g. Frost and Rost, 2014].

The spatial correlation between LLSVP edges and ancient and present hotspots on Earth's surface [Torsvik et al., 2014], as well as the fact LLSVPs are surrounded by subducted slabs, suggesting LLSVPs are important elements of lowermost mantle's dynamics: either controlling the mantle convection actively, or passively shaped by it. Several geodynamic models were proposed to explain LLSVPs (see reviews [Garnero et al., 2016; McNamara, 2019]). Lower than average seismic velocity suggests LLSVPs are hotter than background mantle and the matching geodynamic models are megaplume and plumes clusters [e.g. Thompson and Tackley, 1998; Schubert et al., 2004]. These models emphasize a purely thermal origin of LLSVPs. If, however, LLSVPs are required to be stable throughout Earth's history or, if LLSVPs are indeed denser than the surrounding mantle, an intrinsically denser material is needed. The models are further classified, depending on material's effective density (intrinsic density plus thermal effects), into superplume models [e.g. Jellinek and Manga, 2004; Davaille et al., 2005; Davies et al., 2012] and pile models [e.g. Tackely 1998; McNamara and Zhong 2005; Li et al., 2014]. The name "superplume" emphasizes that thermal effects are the main force for LLSVPs evolution, while the name "pile" emphasizes LLSVPs' overall negative buoyancy as a more controlling factor. In many cases, the intrinsically denser material is assumed to have distinct chemical composition, and thus the name "thermochemical superplumes" or "thermochemical piles". The distinct chemical compositions are introduced to explain LLSPVs properties in a complementary manner, for example, (1) LLSVPs have sharp edges, (2) LLSVPs have an anti-correlation or non-correlation between bulk sound velocity and shear wave velocity [Tan and Gurnis, 2005, 2007], (3) differences of trace element found in OIB and MORB [Hofmann, 1997; Graham, 2002; Tackely, 2007] (if LLSVPs link to surface processes).

The thermochemical models are particularly interesting because they present several lower mantle evolution scenarios. For instance, the chemically distinct material could be the result of fractional crystallization of the Earth's basal magma [Labrosse et al., 2007]; or be a dense primordial basal reservoir, generated during Earth's early differentiation or early subduction period [e.g. Tolstikhin and Hofmann, 2005; Lee et al., 2010; Nomura et al., 2011; Deschamps et al., 2012]; or is formed later by accumulation of subducted oceanic crust [e.g. Christensen and Hofmann, 1994; Tackley, 2011; Mulyukova et al., 2015]. It remains inconclusive which model represents the real Earth, or if the Earth is actually a system mixed from end members. Each model has its own assumptions and limitations. New LLSVP seismic observations [e.g. Roy et al., 2019; Sun et al., 2019] along with new minerology studies [Thomson et al., 2019] will slowly but surely contribute to future breakthroughs.

1.3.4 D″ Discontinuity

In the 1940s, Earth's mantle was categorized into three layers labeled as B, C and D [Bullen, 1940]. Layer D ranged from depth 984 km to 2900 km, which is comparable to today's lower mantle region. In [Bullen, 1949], layer D was further divided into D′ (984 km ~ 2700 km) and D″ (2700 km ~ 2900 km), based on Earth's interior compressibility gradient change. Nowadays, D″ layer becomes a term referring to Earth's lowermost mantle: the last several hundred kilometers above the core-mantle boundary (CMB). Since the 1980s, seismologists began to observe seismic velocity discontinuities within this depth range [e.g., Lay and Helmberger, 1983; Weber and Körnig, 1992; Hutko et al., 2006; Cobden and Thomas, 2013]. These discontinuities are therefore named as D″ discontinuities [Wysession et al., 1998; Cobden et al., 2015].

D″ discontinuities were mostly detected using an additional reflected phase (Scd), and their seismic velocity jump ranges from 1% to 3% [e.g. Davis and Weber, 1990; Lay et al., 2006]. However, decreased P-wave velocity is also occasionally reported [Kito et al., 2007, Hutko et al., 2008; Chaloner et al., 2009]. For some regions, shear wave speed anomalies and bulk sound speed anomalies are anti-correlated [Hutko et al., 2008]. The detection threshold of the velocity jump depends on data quality and method used. For 1D modeling, in [Weber, 1993], the minimal detectable velocity change is 1%; while [Hutko, et al., 2008] claim their velocity change error bar is 0.15%. S-wave and P-wave velocity change are not necessarily observed at the same location [Weber, 1993; Ding and Helmberger, 1997], and for some locations, no D″ discontinuity is observed [Young and Lay 1990; Neuberg and Wahr, 1991]. In recent studies, strong lateral variation in the strength and depth of D″ discontinuity is usual [Thomas et al., 2004a; Kito et al., 2007; Li et al., 2019]. Also, "yes-detections" are often found adjacent to "no-detections" [e.g., Garnero and Lay, 2003; Lay et al., 2004]. These lead to a widely accepted view that the D″ discontinuity is not a global feature. The height of D″ discontinuity (its distance from the CMB) varies a lot, ranging between 150 km to 400 km. A common trade-off exists between height and velocity, especially in the result of travel-time studies [e.g., Kendall and Shearer, 1994]. It is also suggested that modelled D″ discontinuity height could depend on the reference velocity model in use [Hutko et al., 2006]. Migration studies also found double reflectors for some D″ discontinuities and multiple stratifications in the D″

layer [Thomas et al., 2004a; Thomas et al., 2004b; Chambers and Woodhouse 2006b; van der Hilst et al., 2007; Kito et al., 2007, Chaloner et al., 2009]. For double reflectors, the deeper reflectors usually have an opposite velocity change compared to the shallower one. Anisotropies observed in the D″ layer sometimes are attributed to the nearby D″ discontinuities [e.g. Thomas and Kendall], but other times the link is only speculative [e.g. Rokosky et al., 2006]. Higher dimension modeling becomes more and more important nowadays. Because (1) higher dimension structures could produce waveforms too complex to be explained by 1D models, due to out of great circle plane reflections and scatterings, and (2) the laterally varying structures (either different topographies or rapid changes in velocity reduction strength) modelled from 1D methods could invalidate proxies such as waveform amplitude, travel time and detection threshold, resulting in inaccurate 1D modeling results [Thorne et al., 2007].

Several D″ discontinuity origins are proposed. A good candidate is the bridgmanite to post-perovskite (pPv) phase transformation [Murakami et al., 2004; Oganov and Ono, 2004; Tsuchiya et al., 2004; Shim et al., 2004; Shim 2008]. pPv is predicted to produce a 1~4% shear wave velocity increase, small or no change in P wave velocity and 1~2% density increase [Iitaka et al., 2004; Wookey et al., 2005; Murakami et al., 2007]. These minerology results match seismic observations. It can also explain the anti-correlation between increased shear wave velocity and decreased bulk sound velocity. The Bm-pPv transition pressure temperature condition varies for different Bridgmanite compositions and whether or not other mineral phases are present. Bridgmanite with high iron and aluminum concentration have a broad Bm-pPv transition [e.g. Tateno et al., 2007; Catalli et al., 2009; Andrault et al., 2010]. On the other hand, when harzburgite or MORB is present, because aluminum preferentially partitions into these rocks, the transition becomes sharp again [e.g. Kobayashi et al., 2005; Ohta et al., 2008; Grocholski et al., 2012]. Furthermore, the observed double reflectors in central America and Eurasian could be explained by pPv transforming back to Pv (a double-crossing through the phase boundary) when temperature gradient is steep enough [Hernlund et al., 2005]. However, Bm-pPv transition has difficulty explaining D″ discontinuities where P wave and S wave speed both experience an increase [e.g. Weber and Davis, 1990; Cobden and Thomas, 2013]. A possible explanation is Bridgmanite transitioned into anisotropic pPv [Thomas et al., 2011], and using the anisotropy of pPv to explain the velocity changes.

Another explanation for D″ discontinuities involves subduction [e.g. Ding et al., 1997; Wysession et al., 1998; Thomas et al., 2004b]. The cooler temperature of subducted slab is one potential origin for higher than average seismic velocities. It has been modelled that the temperature profile of accumulated cool slab matches a D″ discontinuity seismic velocity profile [Thomas et al., 2004b]. However, nowadays, subducted oceanic crust (MORB), cool harzburgite and Bm-pPv transition formed an integrated explanation and becomes more accepted [Cobden and Thomas, 2013; Whittaker et al., 2016]. Finally, distinct chemical compositions are possible origins. One candidate is silica (SiO_2) concentrated regions, which are expected to have higher than average seismic velocity. The speculated primordial reservoir in the lower mantle can host and the core-mantle reactions can give rise to high silica content [Ruff and Anderson, 1980; Knittle and Jeanloz, 1989; Goarant et al., 1992].

1.3.5 ULVZ

In the past two decades, seismic investigations of deep mantle heterogeneity have reported thin, patch-like mantle-side seismic anomalies adjacent to the core-mantle boundary (CMB) with strong velocity reductions. The reported ultra-low velocity zone (ULVZ) properties vary: thicknesses range from 3 to 100 km, but are most commonly 10's of km [e.g., Thorne and Garnero, 2004; He and Wen, 2009; Rost et al., 2010a], P-wave velocity reductions are up to 25% [e.g., Ross et al., 2004; Brown et al., 2015], S-wave velocity reductions are up to 50% [e.g., Rondenay and Fischer, 2003; Idehara, 2011], density increases are up to 20% [e.g., Koper and Pyle, 2004; Idehara, 2011], and lateral sizes range from tens of kilometers up to around 900 kilometers [e.g., Cottaar and Romanowicz, 2012; Jensen et al., 2013; Yuan and Romanowicz, 2017]. Occasionally, varying properties within ULVZs are proposed. These may include a diffusive top or a vertical velocity gradient [e.g., Rondenay and Fischer, 2003; Rost et al., 2006], or multi-layered structures [e.g., Ross et al., 2004; Idehara, 2011; Pachhai et al., 2015]. Using 2+D synthetic seismogram modeling, different ULVZ three dimensional shapes have been presented, including boxcar, dome, and Gaussian shapes [e.g., Wen and Helmberger, 1998b; To et al., 2011; Cottaar and Romanowicz, 2012; Thorne et al., 2013; Yuan and Romanowicz, 2017].

Many possible origins to ULVZs have been proposed, and essentially emphasize the role of very high temperature or chemically altered (and distinct) compositions. The modeled 3:1 ratio in S-wave to P-wave velocity reduction can be explained by 5 - 30% partial melting of the deepest mantle material [Williams and Garnero, 1996; Berryman, 2000], with the amount of melt depending on actual melt geometry [e.g., Williams and

Garnero, 1996]. Seismic wavefield scattering studies have also suggested a possible melt origin to small scale heterogeneities [Thomas et al., 2009]. ULVZs located beneath the surface locations of hotspots [e.g., Rost et al., 2005; Cottaar and Romanowicz, 2012; Yuan and Romanowicz, 2017] also point to a thermal origin (Figure 1.2a), though this does not preclude compositionally distinct material having been advected to plume root locations. The partial melt explanation faces difficulties in explaining ULVZs detected around the edge, or away from presumably hotter lowermost mantle regions (i.e., the large low velocity provinces, LLVPs) [Luo et al., 2001; Ni and Helmberger, 2001b; Rondenay and Fischer, 2003; Ross et al., 2004; Xu and Koper, 2009]. Also, we may expect to see more ULVZs in the center of LLVPs if their origin is related to the hottest mantle temperatures. Thermodynamical arguments advocate the necessity of compositional distinction to ULVZs [Hernlund and Tackley, 2007]. Nonetheless, their existence around the edge of LLVPs (Figure 1.2b) combined with a proposed density elevation [Havens and Revenaugh, 2001; Ross et al., 2004; Thorne and Garnero, 2004] appears compatible with a compositional difference between ULVZs and the surrounding mantle [McNamara et al., 2010; Li et al., 2017]. Various hypotheses have invoked iron-enrichment to account for the observed ULVZ density elevation [Dobson and Brodholt, 2005; Mao, 2006; Tsuchiya and Tsuchiya, 2006; Wicks et al., 2017]. The subduction of basaltic oceanic crust could bring chemically distinct materials to the lower mantle, which may explain the sporadic ULVZ distribution as well as compositional uniqueness [Andrault et al., 2014; Nomura et al., 2014; Hu et al., 2016; Liu et al., 2016]. Other possibilities exist, e.g., products from chemical reactions between the silicate mantle and core [Buffett et al., 2000], which could give rise to ULVZs far from LLVPs. These possibilities (and others) would result in ULVZ material which will then be swept towards upwelling regions (Figure 1.2c). It is noteworthy to mention that resolution issues may be at play that result in ULVZs erroneously going undetected (Figure 1.2d). That is, ULVZs may be missed if they are especially thin, e.g., < 3-5 km [Ross et al., 2004; Rost and Thomas, 2010], or if they have 3-dimensional structure that masks their detection. However, thin ULVZ possessing particularly anomalous properties have a better chance at being detected, especially with waves that depend upon velocities right at the CMB, like SPdKS. In summary, detecting ULVZ, analysis of their spatial locations as well as determining their seismic properties are important ways leading to comprehensive understanding of lower mantle large-scale dynamics and thermal chemical composition near the core-mantle boundary.

1.4 Summary

In this dissertation, we use forward waveform modeling to study lowermost mantle heterogeneities. In chapter 2, a digital ULVZ database is assembled including the ULVZ detection/non-detection locations from previous studies. Spatial analysis indicates ULVZs appear to be mostly correlated with low velocity region margins. In chapter 3, we focus on the CMB region beneath central America, utilizing an ScS-stripping method [Zhao et al., 2017]. A new kind of seismic anomaly, the ultra-high velocity zone (UHVZ), is discovered at this location alongside ULVZs. A possible origin of discovered UHVZs is the melt residue of MORB (high SiO_2 and CaPv concentration) when it reaches the CMB. In chapter 4, we first digitized previously detected D″ discontinuity locations. Then, we utilized a large global S-wave dataset to document the S waveform broadening phenomena in a global scale. The D″ discontinuity could be one possible cause for S waveform broadenings.

References

Ammann, M. W., J. P. Brodholt, J. Wookey, and D. P. Dobson (2010), First-principles constraints on diffusion in lower-mantle minerals and a weak D″ layer, Nature, 465(7297), 462–465, doi:10.1038/nature09052.

Andrault, D., G. Pesce, M. A. Bouhifd, N. Bolfan-Casanova, J. M. Henot, and M. Mezouar (2014), Melting of subducted basalt at the core-mantle boundary, Science, 344(6186), 892–895, doi:10.1126/science.1250466.

Andrault, D., M. Muñoz, N. Bolfan-Casanova, N. Guignot, J.-P. Perrillat, G. Aquilanti, and S. Pascarelli (2010), Experimental evidence for perovskite and post-perovskite coexistence throughout the whole D″ region, Earth and Planetary Science Letters, 293(1-2), 90–96, doi:10.1016/j.epsl.2010.02.026.

Andrault, D., N. Bolfan-Casanova, G. Lo Nigro, M. A. Bouhifd, G. Garbarino, and M. Mezouar (2011), Solidus and liquidus profiles of chondritic mantle: Implication for melting of the Earth across its history, Earth and Planetary Science Letters, 304(1-2), 251–259, doi:10.1016/j.epsl.2011.02.006.

Anzellini, S., A. Dewaele, M. Mezouar, P. Loubeyre, and G. Morard (2013), Melting of Iron at Earth's Inner Core Boundary Based on Fast X-ray Diffraction, Science, 340(6131), 464–466, doi:10.1126/science.1233514.

Berryman, J. G. (2000), Seismic velocity decrement ratios for regions of partial melt in the lower mantle, Geophysical Research Letters, 27(3), 421–424, doi:10.1029/1999GL008402.

Brown, S. P., M. S. Thorne, L. Miyagi, and S. Rost (2015), A compositional origin to ultralow-velocity zones, Geophysical Research Letters, 42(4), 1039–1045, doi:10.1002/2014GL062097.

Bréger, L., and B. Romanowicz (1998), Three-dimensional structure at the base of the mantle beneath the central Pacific, Science, 282(5389), 718–720, doi:10.1126/science.282.5389.718.

Buffett, B. A., E. J. Garnero, and R. Jeanloz (2000), Sediments at the Top of Earth's Core, Science, 290(5495), 1338–1342, doi:10.1126/science.290.5495.1338.

Bullen, K. E. (1940), The problem of the earth's density variation, Bulletin of the Seismological Society of America, 30(3), 235–250.

Bullen, K. E. (1949), Compressibility-pressure hypothesis and the Earth’s interior, Geophys J Int, 5, 335–368, doi:10.1111/j.1365-246X.1949.tb02952.x.

Catalli, K., S.-H. Shim, and V. Prakapenka (2009), Thickness and Clapeyron slope of the post-perovskite boundary, Nature, 462(7274), 782–785, doi:10.1038/nature08598.

Chaloner, J. W., C. Thomas, and A. Rietbrock (2009), P- and S-wave reflectors in D″ beneath southeast Asia, Geophys J Int, 179(2), 1080–1092, doi:10.1111/j.1365-246X.2009.04328.x.

Chambers, K., and J. H. Woodhouse (2006b), Investigating the lowermost mantle using migrations of long-period S - ScS data, Geophys J Int, 166(2), 667–678, doi:10.1111/j.1365-246X.2006.03002.x.

Christensen, U. R. (1996), The influence of trench migration on slab penetration into the lower mantle, Earth and Planetary Science Letters, 140(1-4), 27–39, doi:10.1016/0012-821X(96)00023-4.

Christensen, U. R., and A. W. Hofmann (1994), Segregation of subducted oceanic crust in the convecting mantle, Journal of Geophysical Research: Solid Earth (1978–2012), 99(B10), 19867–19884, doi: 10.1029/93JB03403.

Cobden, L., C. Thomas, and J. Trampert (2015), Seismic detection of post-perovskite inside the earth, in The Earth's Heterogeneous Mantle: A Geophysical, Geodynamical, and Geochemical Perspective, pp. 391–440, doi: 10.1007/978-3-319-15627-9_13.

Cobden, L., and C. Thomas (2013), The origin of D″ reflections: a systematic study of seismic array data sets, Geophys J Int, 194(2), 1091–1118, doi:10.1093/gji/ggt152.

Cottaar, S., and B. Romanowicz (2012), An unusually large ULVZ at the base of the mantle near Hawaii, Earth and Planetary Science Letters, 355-356, 213–222, doi:10.1016/j.epsl.2012.09.005.

Davaille, A., E. Stutzmann, G. Silveira, J. Besse, and V. Courtillot (2005), Convective patterns under the Indo-Atlantic « box », Earth and Planetary Science Letters, 239(3-4), 233–252, doi:10.1016/j.epsl.2005.07.024.

Davies, D. R., S. Goes, J. H. Davies, B. S. A. Schuberth, H. P. Bunge, and J. Ritsema (2012), Reconciling dynamic and seismic models of Earth's lower mantle: The dominant role of thermal heterogeneity, Earth and Planetary Science Letters, 353-354, 253–269, doi:10.1016/j.epsl.2012.08.016.

Davis, J. P., and M. Weber (1990), Lower Mantle Velocity Inhomogeneity Observed at GRF Array, Geophysical Research Letters, 17(2), 187–190, doi:10.1029/GL017i002p00187.

Deschamps, F., L. Cobden, and P. J. Tackley (2012), The primitive nature of large low shear-wave velocity provinces, Earth and Planetary Science Letters, 349-350(C), 198–208, doi:10.1016/j.epsl.2012.07.012.

Ding, X., and D. V. Helmberger (1997), Modelling D″ structure beneath Central America with broadband seismic data, Physics of the earth and planetary interiors, 101(3-4), 245–270, doi:10.1016/S0031-9201(97)00001-0.

Dobson, D. P., and J. P. Brodholt (2005), Subducted banded iron formations as a source of ultralow-velocity zones at the core–mantle boundary, Nature, 434(7031), 371–374, doi:10.1038/nature03430.

Dziewoński, A. M., and D. L. Anderson (1981), Preliminary reference Earth model, Physics of the earth and planetary interiors, 25(4), 297–356, doi:10.1016/0031-9201(81)90046-7.

Dziewoński, A. M., and J. H. Woodhouse (1987), Global Images of the Earth's Interior, Science, 236(4797), 37–48, doi:10.1126/science.236.4797.37.

French, S. W., and B. A. Romanowicz (2014), Whole-mantle radially anisotropic shear velocity structure from spectral-element waveform tomography, Geophys J Int, 199(3), 1303–1327, doi:10.1093/gji/ggu334.

Frost, D. A., and S. Rost (2014), The P-wave boundary of the Large-Low Shear Velocity Province beneath the Pacific, Earth and Planetary Science Letters, 403, 380–392, doi:10.1016/j.epsl.2014.06.046.

Fukao, Y., M. Obayashi, T. Nakakuki, the Deep Slab Project Group (2009), Stagnant Slab: A Review, Annu. Rev. Earth Planet. Sci., 37(1), 19–46, doi:10.1146/annurev.earth.36.031207.124224.

Fukao, Y., and M. Obayashi (2013), Subducted slabs stagnant above, penetrating through, and trapped below the 660 km discontinuity, J. Geophys. Res. Solid Earth, 118(11), 5920–5938, doi:10.1002/2013JB010466.

Garnero, E. J., and T. Lay (2003), D″ shear velocity heterogeneity, anisotropy and discontinuity structure beneath the Caribbean and Central America, Physics of the earth and planetary interiors, 140(1-3), 219–242, doi:10.1016/j.pepi.2003.07.014.

Garnero, E. J., A. K. McNamara, and S.-H Shim (2016), Continent-sized anomalous zones with low seismic velocity at the base of Earth's mantle, *Nature Geoscience*, *9*(7), 481–489, doi:10.1038/ngeo2733.

Goarant, F., F. Guyot, J. Peyronneau, and J. P. Poirier (1992), High-pressure and high-temperature reactions between silicates and liquid iron alloys in the diamond anvil cell, studied by analytical electron microscopy, Journal of Geophysical Research, 97(B4), 4477–4487, doi:10.1029/92JB00018.

Graham, D. W. (2002), Noble Gas Isotope Geochemistry of Mid-Ocean Ridge and Ocean Island Basalts: Characterization of Mantle Source Reservoirs, Reviews in Mineralogy and Geochemistry, 47(1), 247–317, doi:10.2138/rmg.2002.47.8.

Grand, S. P. (2002), Mantle shear-wave tomography and the fate of subducted slabs, edited by J. H. Davies, J. P. Brodholt, and B. J. Wood, Philosophical Transactions of the Royal Society of London Series a-Mathematical Physical and Engineering Sciences, 360(1800), 2475–2491, doi:10.1098/rsta.2002.1077.

Grocholski, B., K. Catalli, S.-H. Shim, and V. Prakapenka (2012), Mineralogical effects on the detectability of the postperovskite boundary, Proceedings of the National Academy of Sciences, 109(7), 2275–2279, doi:10.1073/pnas.1109204109/-/DCSupplemental/pnas.1109204109_SI.pdf.

Gurnis, M., and B. H. Hager (1988), Controls of the structure of subducted slabs, Nature, 335(6188), 317–321, doi:10.1038/335317a0.

Havens, E., and J. Revenaugh (2001), A broadband seismic study of the lowermost mantle beneath Mexico: Constraints on ultralow velocity zone elasticity and density, Journal of Geophysical Research: Solid Earth (1978–2012), 106(B12), 30809–30820, doi:10.1029/2000JB000072.

He, Y., and L. Wen (2009), Structural features and shear-velocity structure of the “Pacific Anomaly,” Journal of Geophysical Research, 114(B2), L07314, doi:10.1029/2008JB005814.

Hernlund, J. W., C. Thomas, and P. J. Tackley (2005), A doubling of the post-perovskite phase boundary and structure of the Earth's lowermost mantle, Nature, 434(7035), 882–886, doi: 10.1038/nature03472.

Hernlund, J. W., and P. J. Tackley (2007), Some dynamical consequences of partial melting in Earth’s deep mantle, Physics of the earth and planetary interiors, 162(1-2), 149–163, doi:10.1016/j.pepi.2007.04.005.

Hirose, K., N. Takafuji, N. Sata, and Y. Ohishi (2005), Phase transition and density of subducted MORB crust in the lower mantle, Earth and Planetary Science Letters, 237(1-2), 239–251, doi:10.1016/j.epsl.2005.06.035.

Hofmann, A. W. (1997), Mantle geochemistry: the message from oceanic volcanism, Nature, 385(6613), 219–229, doi: 10.1038/385219a0.

Hofmann, A. W., and S. R. Hart (1978), An assessment of local and regional isotopic equilibrium in the mantle, Earth and Planetary Science Letters, 38(1), 44–62, doi:10.1016/0012-821X(78)90125-5.

Holzapfel, C., D. C. Rubie, D. J. Frost, and F. L. Science (2005), Fe-Mg interdiffusion in (Mg, Fe) SiO3 perovskite and lower mantle re-equilibration, Science, 309(5741), 1707–1710, doi:10.1126/science.1111895.

Houser, C., G. Masters, P. Shearer, and G. Laske (2008), Shear and compressional velocity models of the mantle from cluster analysis of long-period waveforms, Geophys J Int, 174(1), 195–212, doi:10.1111/j.1365-246X.2008.03763.x.

Hu, Q., D. Y. Kim, W. Yang, L. Yang, Y. Meng, L. Zhang, and H.-K. Mao (2016), FeO2 and FeOOH under deep lower-mantle conditions and Earth's oxygen-hydrogen cycles, Nature, 534(7606), 241–244, doi:10.1038/nature18018.

Hutko, A. R., T. Lay, E. J. Garnero, and J. Revenaugh (2006), Seismic detection of folded, subducted lithosphere at the core–mantle boundary, Nature, 441(7091), 333–336, doi:10.1038/nature04757.

Hutko, A. R., T. Lay, J. Revenaugh, and E. J. Garnero (2008), Anticorrelated seismic velocity anomalies from post-perovskite in the lowermost mantle, Science, 320(5879), 1070–1074, doi:10.1126/science.1155822.

Hyung, E., S. Huang, M. I. Petaev, and S. B. Jacobsen (2016), Is the mantle chemically stratified? Insights from sound velocity modeling and isotope evolution of an early magma ocean, Earth and Planetary Science Letters, 440(C), 158–168, doi:10.1016/j.epsl.2016.02.001.

Idehara, K., A. Yamada, and D. Zhao (2007), Seismological constraints on the ultralow velocity zones in the lowermost mantle from core-reflected waves, Physics of the earth and planetary interiors, 165(1-2), 25–46, doi:10.1016/j.pepi.2007.07.005.

Iitaka, T., K. Hirose, K. Kawamura, and M. Murakami (2004), The elasticity of the MgSiO3 post-perovskite phase in the Earth's lowermost mantle, Nature, 430(6998), 442–445, doi:10.1038/nature02702.

Irifune, T. (1987), An experimental investigation of the pyroxene-garnet transformation in a pyrolite composition and its bearing on the constitution of the mantle, Physics of the earth and planetary interiors, 45(4), 324–336, doi:10.1016/0031-9201(87)90040-9.

Irifune, T. and Ringwood, A. E. (1987). Phase transformations in primitive MORB and pyrolite compositions to 25 GPa and some geophysical implications. In High-pressure research in mineral physics: a volume in honor of Syun-iti Akimoto, pp 231-242. doi:10.1029/GM039p0231.

Ishii, M., and J. Tromp (2004), Constraining large-scale mantle heterogeneity using mantle and inner-core sensitive normal modes, Physics of the earth and planetary interiors, 146(1-2), 113–124, doi:10.1016/j.pepi.2003.06.012.

Jellinek, A. M., and M. Manga (2004), Links between long-lived hot spots, mantle plumes, D″, and plate tectonics, Rev. Geophys., 42(3), doi:10.1029/2003RG000144.

Jensen, K. J., M. S. Thorne, and S. Rost (2013), SPdKS analysis of ultralow-velocity zones beneath the western Pacific, Geophysical Research Letters, 40(17), 4574–4578, doi:10.1002/grl.50877.

Jones, T. D., D. R. Davies, and P. A. Sossi (2019), Tungsten isotopes in mantle plumes: Heads it's positive, tails it's negative, Earth and Planetary Science Letters, 506, 255–267, doi:10.1016/j.epsl.2018.11.008.

Kaneshima, S. (2016), Seismic scatterers in the mid-lower mantle, Physics of the earth and planetary interiors, 257, 105–114, doi:10.1016/j.pepi.2016.05.004.

Kendall, J. M., and P. M. Shearer (1994), Lateral variations in D″ thickness from long-period shear wave data, Journal of Geophysical Research, 99(B6), 11575–11590, doi:10.1029/94JB00236.

Kennett, B. L. N., E. R. Engdahl, and R. Buland (1995), Constraints on seismic velocities in the Earth from traveltimes, Geophys J Int, 122(1), 108–124, doi:10.1111/j.1365-246X.1995.tb03540.x.

Kennett, B., and E. R. Engdahl (1991), Traveltimes for global earthquake location and phase identification, Geophysical Journal International, 105(2), 429–465, doi:10.1111/j.1365-246X.1991.tb06724.x.

Kito, T., S. Rost, C. Thomas, and E. J. Garnero (2007), New insights into the P- and S-wave velocity structure of the D″ discontinuity beneath the Cocos plate, Geophys J Int, 169(2), 631–645, doi:10.1111/j.1365-246X.2007.03350.x.

Knittle, E., and R. Jeanloz (1989), Simulating the core-mantle boundary: An experimental study of high-pressure reactions between silicates and liquid iron, Geophysical Research Letters, 16(7), 609–612, doi:10.1029/GL016i007p00609.

Kobayashi, Y., T. Kondo, E. Ohtani, N. Hirao, N. Miyajima, T. Yagi, T. Nagase, and T. Kikegawa (2005), Fe-Mg partitioning between (Mg, Fe)SiO3 post-perovskite, perovskite, and magnesiowüstite in the Earth's lower mantle, Geophysical Research Letters, 32(19), n/a–n/a, doi:10.1029/2005GL023257.

Koelemeijer, P., A. Deuss, and J. Ritsema (2017), Density structure of Earth's lowermost mantle from Stoneley mode splitting observations, Nature Communications, 8(1), 15241, doi:10.1038/ncomms15241.

Koper, K. D., and M. L. Pyle (2004), Observations of PKiKP/PcP amplitude ratios and implications for Earth structure at the boundaries of the liquid core, Journal of Geophysical Research: Solid Earth (1978–2012), 109(B3), 1227, doi:10.1029/2003JB002750.

Labrosse, S., J. W. Hernlund, and N. Coltice (2007), A crystallizing dense magma ocean at the base of the Earth’s mantle, Nature, 450(7171), 866–869, doi:10.1038/nature06355.

Lai, H., E. J. Garnero, S. P. Grand, R. W. Porritt, and T. W. Becker (2019), Global travel time data set from adaptive empirical wavelet construction, Geochem. Geophys. Geosyst., 22(2), 231–24, doi:10.1029/2018GC007905.

Lay, T., E. J. Garnero, and S. A. Russell (2004), Lateral variation of the D″ discontinuity beneath the Cocos Plate, Geophysical Research Letters, 31(15), L15612, doi:10.1029/2004GL020300.

Lay, T., J. Hernlund, E. J. Garnero, and M. S. Thorne (2006), A Post-Perovskite Lens and D″ Heat Flux Beneath the Central Pacific, Science, 314(5), 1272–1276, doi:10.1126/science.1133280.

Lay, T., and D. V. Helmberger (1983), A lower mantle S-wave triplication and the shear velocity structure of D″, Geophysical Journal of the Royal Astronomical Society, 75(3), 799–837, doi:10.1111/j.1365-246X.1983.tb05010.x.

Lee, C.-T. A., P. Luffi, T. Höink, J. Li, R. Dasgupta, and J. Hernlund (2011), Upside-down differentiation and generation of a “primordial” lower mantle, Nature, 463(7283), 930–933, doi:10.1038/nature08824.

Lekic, V., S. Cottaar, A. Dziewoński, and B. Romanowicz (2012), Cluster analysis of global lower mantle tomography: A new class of structure and implications for chemical heterogeneity, Earth and Planetary Science Letters, 357-358(C), 68–77, doi:10.1016/j.epsl.2012.09.014.

Li, C., R. D. van der Hilst, E. R. Engdahl, and S. Burdick (2008), A new global model for P-wave speed variations in Earth's mantle, Geochem. Geophys. Geosyst., 9(5), n/a–n/a, doi:10.1029/2007GC001806.

Li, M., A. K. McNamara, E. J. Garnero, and S. Yu (2017), Compositionally-distinct ultra-low velocity zones on Earth’s core-mantle boundary, Nature Communications, 8(1), 977, doi:10.1038/s41467-017-00219-x.

Li, M., A. K. McNamara, E. J. Garnero (2014), Chemical complexity of hotspots caused by cycling oceanic crust through mantle reservoirs, Nature Geoscience, 7(5), 366–370, doi:10.1038/ngeo2120.

Li, M., and A. K. McNamara (2013), The difficulty for subducted oceanic crust to accumulate at the Earth's core-mantle boundary, J. Geophys. Res. Solid Earth, 118(4), 1807–1816, doi:10.1002/jgrb.50156.

Li, Y., M. S. Miller, and D. Sun (2019), Seismic imaging the D″ region beneath the Central Atlantic, Physics of the earth and planetary interiors, 292, 76–86, doi:10.1016/j.pepi.2019.05.005.

Liu, J., J. Li, R. Hrubiak, and J. S. Smith (2016), Origins of ultralow velocity zones through slab-derived metallic melt, Proc. Natl. Acad. Sci. U.S.A., 113(20), 5547–5551, doi:10.1073/pnas.1519540113.

Loubet, M., R. Sassi, and G. Di Donato (1988), Mantle heterogeneities: a combined isotope and trace element approach and evidence for recycled continental crust materials in some OIB sources, Earth and Planetary Science Letters, 89(3-4), 299–315, doi:10.1016/0012-821X(88)90118-5.

Luo, S. N., S. Ni, and D. V. Helmberger (2001), Evidence for a sharp lateral variation of velocity at the core–mantle boundary from multipathed PKPab, Earth and Planetary Science Letters, 189(3-4), 155–164, doi:10.1016/S0012-821X(01)00364-8.

Mao, H. K., Y. Wu, L. C. Chen, J. F. Shu, and A. P. Jephcoat (1990), Static compression of iron to 300 GPa and Fe0.8Ni0.2 alloy to 260 GPa: implications for composition of the core, Journal of Geophysical Research, 95(B13), doi: 10.1029/JB095iB13p21737.

Mao, W. L. (2006), Iron-Rich Post-Perovskite and the Origin of Ultralow-Velocity Zones, Science, 312(5773), 564–565, doi:10.1126/science.1123442.

McDonough, W. F., and S. S. Sun (1995), The Composition of the Earth, Chemical Geology, 120(3-4), 223–253, doi:10.1016/0009-2541(94)00140-4.

McNamara, A. K. (2019), A review of large low shear velocity provinces and ultra-low velocity zones, Tectonophysics, 760, 199–220, doi:10.1016/j.tecto.2018.04.015.

McNamara, A. K., E. J. Garnero, and S. Rost (2010), Tracking deep mantle reservoirs with ultra-low velocity zones, Earth and Planetary Science Letters, 299(1-2), 1–9, doi:10.1016/j.epsl.2010.07.042.

McNamara, A. K., and S. Zhong (2005), Thermochemical structures beneath Africa and the Pacific Ocean, Nature, 437(7062), 1136–1139, doi:10.1038/nature04066.

Mulyukova, E., B. Steinberger, M. Dabrowski, and S. V. Sobolev (2015), Survival of LLSVPs for billions of years in a vigorously convecting mantle: Replenishment and destruction of chemical anomaly, J. Geophys. Res. Solid Earth, 120(5), 3824–3847, doi:10.1002/2014JB011688.

Mundl, A., M. Touboul, M. G. Jackson, J. M. D. Day, M. D. Kurz, V. Lekic, R. T. Helz, and R. J. Walker (2017), Tungsten-182 heterogeneity in modern ocean island basalts, Science, 356(6333), 66–69, doi:10.1126/science.aal4179.

Murakami, M., K. Hirose, K. Kawamura, N. Sata, and Y. Ohishi (2004), Post-Perovskite Phase Transition in MgSiO3, Science, 304(5672), 855-858, doi:10.1126/science.1095932.

Murakami, M., S. V. Sinogeikin, J. D. Bass, N. Sata, Y. Ohishi, and K. Hirose (2007), Sound velocity of MgSiO3 post-perovskite phase: A constraint on the D″ discontinuity, Earth and Planetary Science Letters, 259(1-2), 18–23, doi:10.1016/j.epsl.2007.04.015.

Murakami, M., Y. Ohishi, N. Hirao, and K. Hirose (2012), A perovskitic lower mantle inferred from high-pressure, high-temperature sound velocity data, Nature, 485(7396), 90–94, doi:10.1038/nature11004.

Neuberg, J., and J. Wahr (1991), Detailed Investigation of a Spot on the Core Mantle Boundary Using Digital Pcp Data, Physics of the earth and planetary interiors, 68(1-2), 132–143, doi:10.1016/0031-9201(91)90013-8.

Ni, S., and D. V. Helmberger (2001b), Probing an ultra-low velocity zone at the core mantle boundary with P and S waves, Geophysical Research Letters, 28(12), 2345–2348, doi:10.1029/2000GL012766.

Ni, S., and D. V. Helmberger (2003a), Further constraints on the African superplume structure, Physics of the earth and planetary interiors, 140(1-3), 243–251, doi:10.1016/j.pepi.2003.07.011.

Ni, S., and D. V. Helmberger (2003b), Ridge-like lower mantle structure beneath South Africa, Journal of Geophysical Research, 108(B2), 3433–14, doi:10.1029/2001JB001545.

Ni, S., and D. V. Helmberger (2003c), Seismological constraints on the South African superplume: Could be the oldest distinct structure on earth, Earth and Planetary Science Letters, 206(1-2), 119–131, doi:10.1016/S0012-821X(02)01072-5.

Nomura, R., H. Ozawa, S. Tateno, K. Hirose, J. Hernlund, S. Muto, H. Ishii, and N. Hiraoka (2011), Spin crossover and iron-rich silicate melt in the Earth's deep mantle, Nature, 473(7346), 199–202, doi:10.1038/nature09940.

Nomura, R., K. Hirose, K. Uesugi, Y. Ohishi, A. Tsuchiyama, A. Miyake, and Y. Ueno (2014), Low Core-Mantle Boundary Temperature Inferred from the Solidus of Pyrolite, Science, 343(6170), 522–525, doi:10.1126/science.1248186.

O'Neill, H. S. C. (1991), The origin of the moon and the early history of the earth-A chemical model. Part 2: The earth, Geochimica et Cosmochimica Acta, 55(4), 1159–1172, doi:10.1016/0016-7037(91)90169-6.

Oganov, A. R., and S. Ono (2004), Theoretical and experimental evidence for a post-perovskite phase of MgSiO3 in Earth's D″ layer, Nature, 430(6998), 445–448, doi:10.1038/nature02701.

Ohta, K., K. Hirose, T. Lay, N. Sata, and Y. Ohishi (2008), Phase transitions in pyrolite and MORB at lowermost mantle conditions: Implications for a MORB-rich pile above the core–mantle boundary, Earth and Planetary Science Letters, 267(1-2), 107–117, doi:10.1016/j.epsl.2007.11.037.

Pachhai, S., J. Dettmer, and H. Tkalčić (2015), Ultra-low velocity zones beneath the Philippine and Tasman Seas revealed by a trans-dimensional Bayesian waveform inversion, Geophys J Int, 203(2), 1302–1318, doi:10.1093/gji/ggv368.

Pearson, D. G. et al. (2015), Hydrous mantle transition zone indicated by ringwoodite included within diamond, Nature, 507(7491), 221–224, doi:10.1038/nature13080.

Pradhan, G. K., G. Fiquet, J. Siebert, A.-L. Auzende, G. Morard, D. Antonangeli, and G. Garbarino (2015), Earth and Planetary Science Letters, Earth and Planetary Science Letters, 431(C), 247–255, doi:10.1016/j.epsl.2015.09.034.

Ricolleau, A. et al. (2009), Density profile of pyrolite under the lower mantle conditions, Geophysical Research Letters, 36(6), 789–5, doi:10.1029/2008GL036759.

Ringwood, A. E. (1962), A model for the upper mantle, Journal of Geophysical Research: Solid Earth (1978–2012), 67(2), 857–867, doi.org/10.1029/JZ067i002p00857

Ringwood, A. E. (1991), Phase transformations and their bearing on the constitution and dynamics of the mantle, Geochimica et Cosmochimica Acta, 55(8), 2083–2110, doi:10.1016/0016-7037(91)90090-R.

Ringwood, A. E., and T. Irifune (1988), Nature of the 650-km seismic discontinuity: Implications for mantle dynamics and differentiation, Nature, 331(6152), 131–136, doi:10.1038/331131a0.

Ritsema, J., A. Deuss, H. J. Van Heijst, and J. H. Woodhouse (2011), S40RTS: a degree-40 shear-velocity model for the mantle from new Rayleigh wave dispersion, teleseismic traveltime and normal-mode splitting function measurements, Geophys J Int, 184(3), 1223–1236, doi: 10.1111/j.1365-246X.2010.04884.x.

Rizo, H., R. J. Walker, R. W. Carlson, M. F. Horan, S. Mukhopadhyay, V. Manthos, D. Francis, and M. G. Jackson (2016), Preservation of Earth-forming events in the tungsten isotopic composition of modern flood basalts, Science, 352(6287), 809-812, doi: 10.1126/science.aad8563.

Rokosky, J. M., T. Lay, and E. J. Garnero (2006), Small-scale lateral variations in azimuthally anisotropic D″ structure beneath the Cocos Plate, Earth and Planetary Science Letters, 248(1-2), 411–425, doi:10.1016/j.epsl.2006.06.005.

Rondenay, S., and K. M. Fischer (2003), Constraints on localized core-mantle boundary structure from multichannel, broadband SKS coda analysis, Journal of Geophysical Research, 108(B), 2537, doi:10.1029/2003JB002518.

Ross, A. R., H. Thybo, and L. N. Solidilov (2004), Reflection seismic profiles of the core-mantle boundary, Journal of Geophysical Research, 109(B8), 1335, doi:10.1029/2003JB002515.

Rost, S., E. J. Garnero, Q. Williams, and M. Manga (2005), Seismological constraints on a possible plume root at the core–mantle boundary, Nature, 435(7042), 666–669, doi:10.1038/nature03620.

Rost, S., E. J. Garnero, and Q. Williams (2006), Fine-scale ultralow-velocity zone structure from high-frequency seismic array data, Journal of Geophysical Research, 111(B9), 1169, doi:10.1029/2005JB004088.

Rost, S., E. J. Garnero, and W. Stefan (2010a), Thin and intermittent ultralow-velocity zones, Journal of Geophysical Research: Solid Earth (1978–2012), 115(B6), 443, doi:10.1029/2009JB006981.

Rost, S., and C. Thomas (2010), High resolution CMB imaging from migration of short-period core reflected phases, Physics of the earth and planetary interiors, 183(1), 143–150, doi:10.1016/j.pepi.2010.04.005.

Roy, S. K., N. Takeuchi, D. Srinagesh, M. Ravi Kumar, and H. Kawakatsu (2019), Topography of the western Pacific LLSVP constrained by S-wave multipathing, Geophys J Int, 218(1), 190–199, doi:10.1093/gji/ggz149.

Rubie, D. C. (1984), The olivine → spinel transformation and the rheology of subducting lithosphere, Nature, 308(5959), 505–508, doi:10.1038/308505a0.

Ruff, L., and D. L. Anderson (1980), Core formation, evolution, and convection: a geophysical model, Physics of the earth and planetary interiors, 21(2-3), 181–201, doi:10.1016/0031-9201(80)90069-2.

Schilling, J. G., M. Zajac, R. Evans, T. Johnston, W. White, J. D. Devine, and R. Kingsley (1983), Petrologic and geochemical variations along the Mid-Atlantic Ridge from 29 degrees N to 73 degrees N, Am J Sci, 283(6), 510–586, doi:10.2475/ajs.283.6.510.

Schubert, G., G. Masters, P. Olson, and P. Tackley (2004), Superplumes or plume clusters? Physics of the earth and planetary interiors, 146(1-2), 147–162, doi:10.1016/j.pepi.2003.09.025.

Shim, S. H., T. S. Duffy, R. Jeanloz, and G. Shen (2004), Stability and crystal structure of MgSiO3 perovskite to the core-mantle boundary, Geophysical Research Letters, 31(10), doi:10.1029/2004GL019639.

Shim, S.-H. (2008), The Postperovskite Transition, Annual Review of Earth and Planetary Sciences, 36(1), 569-599, doi:10.1146/annurev.earth.36.031207.124309.

Sigloch, K., N. McQuarrie, and G. Nolet (2008), Two-stage subduction history under North America inferred from multiple-frequency tomography, Nature Geoscience, 1(7), 458–462, doi:10.1038/ngeo231.

Simmons, N. A., A. M. Forte, L. Boschi, and S. P. Grand (2010), GyPSuM: A joint tomographic model of mantle density and seismic wave speeds, Journal of Geophysical Research, 115(B12), B12310, doi:10.1029/2010JB007631.

Stixrude, L., and C. Lithgow-Bertelloni (2012), Geophysics of Chemical Heterogeneity in the Mantle, Annu. Rev. Earth Planet. Sci., 40(1), 569–595, doi:10.1146/annurev.earth.36.031207.124244.

Sun, D., D. Helmberger, V. H. Lai, M. Gurnis, J. M. Jackson, and H. Y. Yang (2019), Slab Control on the Northeastern Edge of the Mid-Pacific LLSVP Near Hawaii, Geophysical Research Letters, 46(6), 3142–3152, doi:10.1029/2018GL081130.

Tackley, P. J. (2007), Mantle Geochemical Geodynamics, in Treatise on Geophysics, vol. 7, pp. 437–505, Elsevier, doi:10.1016/B978-044452748-6.00124-3.

Tackley, P. J. (2011), Living dead slabs in 3-D: The dynamics of compositionally-stratified slabs entering a “slab graveyard” above the core-mantle boundary, Physics of the earth and planetary interiors, 188(3-4), 150–162, doi:10.1016/j.pepi.2011.04.013.

Tackley, P.J., 1998. Three-dimensional simulations of mantle convection with a thermochemical basal boundary layer: D″? In: Gurnis, M., Wysession, M.E., Knittle, E., Buffett, B.A. (Eds.), The Core-Mantle Boundary Region. American Geophysical Union (p. 334).

Takafuji, N. (2005), Solubilities of O and Si in liquid iron in equilibrium with (Mg,Fe)SiO 3perovskite and the light elements in the core, Geophysical Research Letters, 32(6), 49–4, doi:10.1029/2005GL022773.

Tan, E., and M. Gurnis (2005), Metastable superplumes and mantle compressibility, Geophysical Research Letters, 32(20), 1–4, doi:10.1029/2005GL024190.

Tan, E., and M. Gurnis (2007), Compressible thermochemical convection and application to lower mantle structures, J. Geophys. Res. Solid Earth, 112(6), doi:10.1029/2006JB004505.

Tateno, S., K. Hirose, N. Sata, and Y. Ohishi (2007), Solubility of FeO in (Mg,Fe)SiO3 perovskite and the post-perovskite phase transition, Physics of the earth and planetary interiors, 160(3-4), 319–325, doi:10.1016/j.pepi.2006.11.010.

Taylor, S. R. (1964), Chondritic earth model, Nature, 202(4929), 281–282, doi:10.1038/202281a0.

Thomas, C., E. J. Garnero, and T. Lay (2004a), High-resolution imaging of lowermost mantle structure under the Cocos plate, Journal of Geophysical Research, 109(B8), 2016–11, doi:10.1029/2004JB003013.

Thomas, C., J. Wookey, J. Brodholt, and T. Fieseler (2011), Anisotropy as cause for polarity reversals of D″ reflections, Earth and Planetary Science Letters, 307(3-4), 369–376, doi:10.1016/j.epsl.2011.05.011.

Thomas, C., J.-M. Kendall, and G. Helffrich (2009), Probing two low-velocity regions with PKPb-caustic amplitudes and scattering, Geophys J Int, 178(1), 503–512, doi:10.1111/j.1365-246X.2009.04189.x.

Thomas, C., J.-M. Kendall, and J. Lowman (2004b), Lower-mantle seismic discontinuities and the thermal morphology of subducted slabs, Earth and Planetary Science Letters, 225(1-2), 105–113, doi:10.1016/j.epsl.2004.05.038.

Thomas, C., and J. M. Kendall (2002), The lowermost mantle beneath northern Asia - II. Evidence for lower-mantle anisotropy, Geophys J Int, 151(1), 296–308, doi:10.1046/j.1365-246X.2002.01760.x.

Thompson, P. F., and P. J. Tackley (1998), Generation of mega-plumes from the core-mantle boundary in a compressible mantle with temperature-dependent viscosity, Geophysical Research Letters, 25(11), 1999–2002, doi:10.1029/98GL01228.

Thomson, A. R., W. A. Crichton, J. P. Brodholt, I. G. Wood, N. C. Siersch, J. M. R. Muir, D. P. Dobson, and S. A. Hunt (2019), Seismic velocities of CaSiO3 perovskite can explain LLSVPs in Earth's lower mantle, Nature, 572(7771), 643–647, doi:10.1038/s41586-019-1483-x.

Thorne, M. S., E. J. Garnero, G. Jahnke, H. Igel, and A. K. McNamara (2013), Mega ultra-low velocity zone and mantle flow, Earth and Planetary Science Letters, 364, 59–67, doi:10.1016/j.epsl.2012.12.034.

Thorne, M. S., E. J. Garnero, and S. P. Grand (2004), Geographic correlation between hot spots and deep mantle lateral shear-wave velocity gradients, Physics of the earth and planetary interiors, 146(1-2), 47–63, doi:10.1016/j.pepi.2003.09.026.

Thorne, M. S., and E. J. Garnero (2004), Inferences on ultralow-velocity zone structure from a global analysis of SPdKS waves, Journal of Geophysical Research, 109(B8), 421, doi:10.1029/2004JB003010.

To, A., Y. Fukao, and S. Tsuboi (2011), Evidence for a thick and localized ultra-low shear velocity zone at the base of the mantle beneath the central Pacific, Physics of the earth and planetary interiors, 184(3-4), 119–133, doi:10.1016/j.pepi.2010.10.015.

Tolstikhin, I., and A. W. Hofmann (2005), Early crust on top of the Earth's core, Physics of the earth and planetary interiors, 148(2-4), 109–130, doi:10.1016/j.pepi.2004.05.011.

Torsvik, T. H., R. van der Voo, P. V. Doubrovine, K. Burke, B. Steinberger, L. D. Ashwal, R. G. Tronnes, S. J. Webb, and A. L. Bull (2014), Deep mantle structure as a reference frame for movements in and on the Earth, Proceedings of the National Academy of Sciences, 111(24), 8735–8740, doi:10.1073/pnas.1318135111.

Trampert, J. (2004), Probabilistic Tomography Maps Chemical Heterogeneities Throughout the Lower Mantle, Science, 306(5697), 853–856, doi:10.1126/science.1101996.

Tsuchiya, T., J. Tsuchiya, K. Umemoto, and R. M. Wentzcovitch (2004), Phase transition in MgSiO3 perovskite in the earth's lower mantle, Earth and Planetary Science Letters, 224(3-4), 241–248, doi:10.1016/j.epsl.2004.05.017.

Tsuchiya, T., and J. Tsuchiya (2006), Effect of impurity on the elasticity of perovskite and postperovskite: Velocity contrast across the postperovskite transition in (Mg,Fe,Al)(Si,Al)O3, Geophysical Research Letters, 33(12), 383, doi:10.1029/2006GL025706.

van der Hilst, R. D., M. V. De Hoop, P. Wang, S. H. Shim, P. Ma, and L. Tenorio (2007), Seismostratigraphy and thermal structure of earth's core-mantle boundary region, Science, 315(5820), 1813–1817, doi:10.1126/science.1137867.

Weber, M. (1993), P-Wave and S-Wave Reflections from Anomalies in the Lowermost Mantle, Geophys J Int, 115(1), 183–210, doi:10.1111/j.1365-246X.1993.tb05598.x.

Weber, M., and J. P. Davis (1990), Evidence of a laterally variable lower mantle structure from P- and S-waves, Geophys J Int, 102(1), 231–255, doi:10.1111/j.1365-246X.1990.tb00544.x.

Weber, M., and M. Körnig (1992), A search for anomalies in the lowermost mantle using seismic bulletins, Physics of the earth and planetary interiors, 73(1-2), 1–28, doi:10.1016/0031-9201(92)90104-4.

Wen, L., and D. V. Helmberger (1998b), A two-dimensional P-SV hybrid method and its application to modeling localized structures near the core-mantle boundary, Journal of Geophysical Research, 103(B8), 17901–17918, doi:10.1029/98JB01276.

Whittaker, S., M. S. Thorne, N. C. Schmerr, and L. Miyagi (2016), Seismic array constraints on the D″ discontinuity beneath Central America, J. Geophys. Res. Solid Earth, 121(1), 152–169, doi:10.1002/2015JB012392.

Wicks, J. K., J. M. Jackson, W. Sturhahn, and D. Zhang (2017), Sound velocity and density of magnesiowüstites: Implications for ultralow-velocity zone topography, Geophysical Research Letters, 44(5), 2148–2158, doi:10.1002/2016GL071225.

Williams, Q., and E. J. Garnero (1996), Seismic Evidence for Partial Melt at the Base of Earth's Mantle, Science, 273(5), 1528–1530, doi:10.1126/science.273.5281.1528.

Wookey, J., S. Stackhouse, J.-M. Kendall, J. Brodholt, and G. D. Price (2005), Efficacy of the post-perovskite phase as an explanation for lowermost-mantle seismic properties, Nature, 438(7070), 1004–1007, doi:10.1038/nature04345.

Workman, R. K., and S. R. Hart (2005), Major and trace element composition of the depleted MORB mantle (DMM), Earth and Planetary Science Letters, 231(1-2), 53–72, doi:10.1016/j.epsl.2004.12.005.

Wysession, M. E., T. Lay, J. Revenaugh, Q. Williams, E. J. Garnero, R. Jeanloz, and L. H. Kellogg (1998), The D″ discontinuity and its implications, The core-mantle boundary region, 28, 273–297, doi: 10.1029/GD028p0273.

Xu, W., C. Lithgow-Bertelloni, L. Stixrude, and J. Ritsema (2008), The effect of bulk composition and temperature on mantle seismic structure, Earth and Planetary Science Letters, 275(1-2), 70–79, doi:10.1016/j.epsl.2008.08.012.

Xu, Y., and K. D. Koper (2009), Detection of a ULVZ at the base of the mantle beneath the northwest Pacific, Geophysical Research Letters, 36(17), L14612, doi:10.1029/2009GL039387.

Ye, K., B. Cong, and D. Ye (2000), The possible subduction of continental material to depths greater than 200 km, Nature, 407(6805), 734–736, doi:10.1038/35037566.

Young, C. J., and T. Lay (1990), Multiple phase analysis of the shear velocity structure in the D″ region beneath Alaska, J. Geophys. Res. Solid Earth, 95(B), 17–, doi:10.1029/JB095iB11p17385.

Yuan, K., and B. Romanowicz (2017), Seismic evidence for partial melting at the root of major hot spot plumes, Science, 357(6349), 393–397, doi:10.1126/science.aan0760.

Zhang, S., S. Cottaar, T. Liu, S. Stackhouse, and B. Militzer (2016), High-pressure, temperature elasticity of Fe- and Al-bearing $MgSiO_3$: Implications for the Earth's lower mantle, Earth and Planetary Science Letters, 434, 264–273, doi:10.1016/j.epsl.2015.11.030.

Zhao, C., E. J. Garnero, A. K. McNamara, N. Schmerr, and R. W. Carlson (2015), Seismic evidence for a chemically distinct thermochemical reservoir in Earth's deep mantle beneath Hawaii, Earth and Planetary Science Letters, 426, 143–153, doi:10.1016/j.epsl.2015.06.012.

Zhao, C., E. J. Garnero, M. Li, A. McNamara, and S. Yu (2017), Intermittent and lateral varying ULVZ structure at the northeastern margin of the Pacific LLSVP, J. Geophys. Res. Solid Earth, 122(2), 1198–1220, doi:10.1002/2016JB013449.

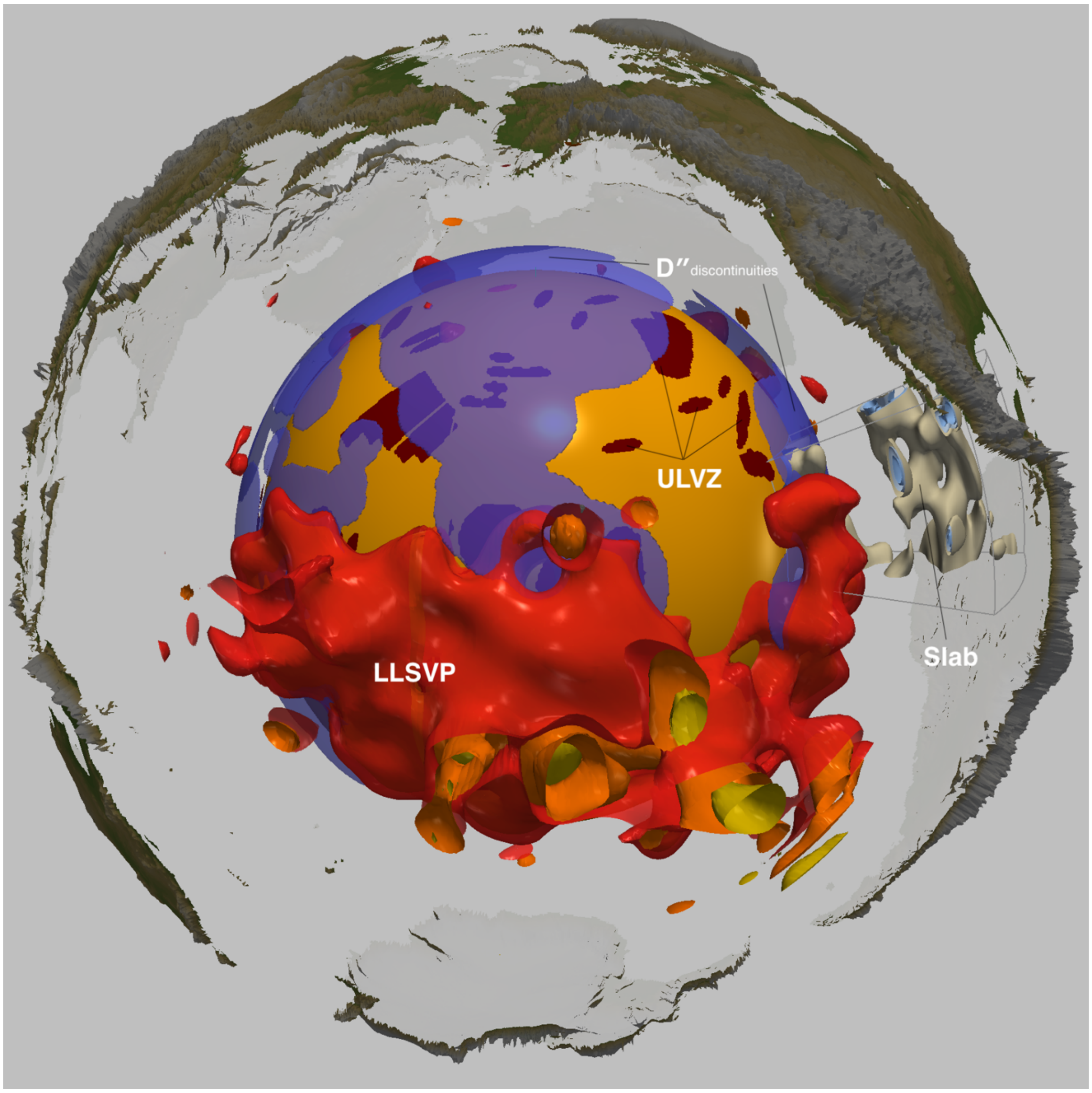

Figure 1.1. Seismic heterogeneities of Earth's lower mantle. Viewpoint is centered on the Pacific region. The core-mantle boundary (CMB) is plotted as a yellow sphere. Pacific large-low shear wave velocity provinces (LLSVPs) is plotted as S-wave velocity anomaly contours (model used is SEMUCB-WM1 [French and Romanowicz, 2014]). The contour values are -1.5% (yellow), -1% (orange) and -0.75% (red). Slab beneath the Central America is represented as high S-wave velocity anomaly contours (model used is S40RTS [Ritsema et al., 2011]). Their contour values are 0.7%, 0.8% and 0.9%. Locations of reported D″ discontinuities are plotted in transparent light blue, for references, see Chapter 4. D″ discontinuities distance from the CMB is set to 300 km for plotting purpose. Locations of detected ULVZs are plotted on the CMB in dark red, for references, see Chapter 2.

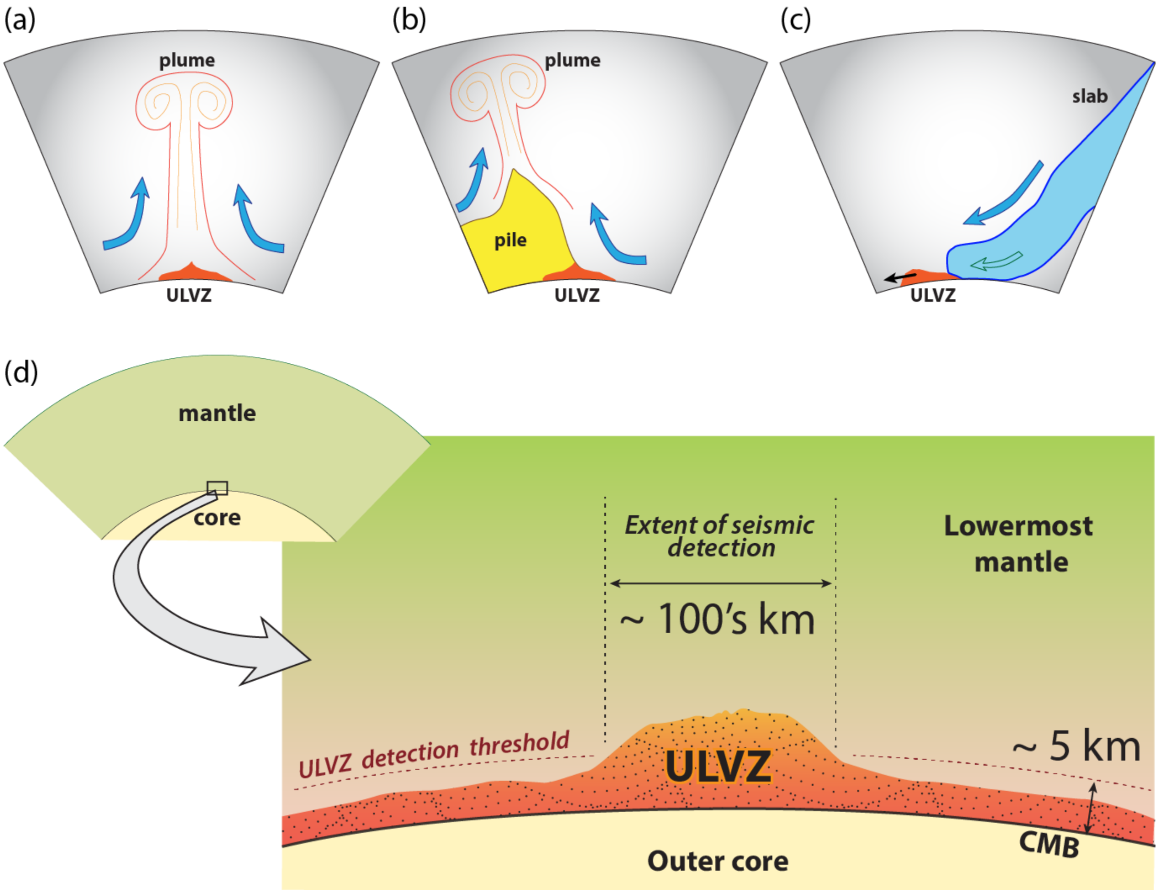

Figure 1.2. Cartoons showing ULVZ detection locations and other phenomena. (a) ULVZs have been reported to exist beneath surface hotspots, associated with mantle plumes. Arrows indicate large-scale mantle flow. These basal zones may be the hottest deep mantle locations and relate to the origin of partial melt in ULVZs. (b) Compositionally distinct ULVZs will advect to the margins of thermochemical piles, which have been advocated as the origin of LLVPs. (c) ULVZs in relatively cold regions might be due to deeply subducted oceanic crust, or possible accumulated products of chemical reactions between the core and mantle. Subduction-related flow can advect these ULVZs towards LLVP regions. (d) The possibility of widespread thin ULVZs. They are seismically imaged only when the accumulated thickness of ULVZ material extends off the CMB above the seismic resolution limitations (roughly 5 km vertically, depending on the seismic phase and ULVZ properties). This cartoon depicts a detectable ULVZ with lateral dimension of 100's of km.

CHAPTER 2

ULTRA-LOW VELOCITY ZONE LOCATIONS: A GLOBAL ASSESSMENT

The work presented in this chapter was published as *Yu, Shule & Garnero, Edward. (2018). "Ultra-Low Velocity Zone Locations: A Global Assessment." Geochemistry, Geophysics, Geosystems. 19. 10.1002/2017gc007281.*

2.1 Abstract

We have compiled all previous ultra-low velocity zone (ULVZ) studies and digitized their core-mantle boundary (CMB) sampling locations. For studies that presented sampling locations based on infinite frequency ray theory, we approximated Fresnel zones onto a 0.5˚x 0.5˚ grid. Results for these studies were separated according to wave type: (1) core-reflected phases, which have a single location of ULVZ sampling (ScS, ScP, PcP), (2) core waves that can sample ULVZs at the core entrance and exit locations of the wave (e.g., SP_dKS, PKKP and PKP), and (3) waves which have uncertainties of ULVZ location due to long CMB sampling paths, e.g., diffracted energy sampling over a broad region (P_{diff}, S_{diff}). For studies that presented specific modeled ULVZ geographical shapes or PKP scatter probability maps, we digitized the regions. We present summary maps of the ULVZ coverage, as well as published locations arguing against ULVZ presence. A key finding is that there is not a simple mapping between lowermost mantle reduced tomographic velocities and observed ULVZ locations,

especially given the presence of ULVZs outside of lowermost mantle large low velocity provinces (LLVPs). Significant location uncertainty exists for some of the ULVZ imaging wave types. Nonetheless, this compilation supports a compositionally distinct origin for at least some ULVZs. ULVZs are more likely to be found near LLVP boundaries, however, their relationship to overlying surface locations of hotspots are less obvious. The new digital ULVZ database is freely available for download.

2.2 Introduction

The focus of this work is a comprehensive assessment of ULVZ distribution and properties. A summary of seismic phases used in previous ULVZ studies is presented in Figure 2.1. These phases share a common feature in that they interact with the CMB, and thus hold opportunity to detect and image ULVZ structure. In this study, we group results from previous investigations according to the type of seismic wave: namely, (1) a CMB reflection, (2) a core wave with different core entry and exit locations, (3) CMB diffraction, and (4) scattering at the CMB. A reflected wave¬ (including ScS, ScP and PcP) samples the CMB once, at the reflection point (Figure 2.1a). If the ULVZ has an abrupt discontinuity at the top (and is locally flat to first order), a reflection off the top of the ULVZ will result in a precursory (early) arrival relative to the main phase. Internal reflections or P-to-S or S-to-P conversions within the ULVZ layer can result in additional delayed arrivals (post-cursors) relative to the main phase (Figure 2.1b-d). Therefore, analyses of CMB reflected waves for investigating ULVZ structure commonly utilize the timing and amplitudes of pre- and post-cursors [e.g., Rost et al., 2005; Avants et al., 2006; Hutko et al., 2009]. Diffracted phases encounter the CMB either once (e.g., Pdiff and Sdiff) or twice (e.g., SPdKS and PKKPab_diff, Figures 2.2e and 2.2h). Reduced seismic wave speeds at the very base of the mantle can cause delays and waveform distortions of the diffracted arrivals. However, since the diffraction paths can be relatively long (e.g., Pdiff and Sdiff), or occur at two separate CMB crossing locations (e.g., SPdKS and PKKPab_diff) there is uncertainty in uniquely identifying the exact ULVZ location. To resolve the ambiguities of a source-side versus receiver-side location for ULVZ structure (or both), either knowledge from crossing path sampling [e.g., Rondenay and Fischer, 2003] or incorporation of previously published models [e.g., Thorne et al., 2013] is typically required. Detailed waveform modeling utilizing 2- and 3-D models helps in the imaging process, but a larger model space means more trade-offs [e.g., To et al., 2011; Cottaar and Romanowicz, 2012; Thorne et al., 2013]. PKP used in waveform studies also encounter the CMB twice, and thus can involve source- vs. receiver-side ULVZ location ambiguity [e.g., Wen and Helmberger 1998; Thomas et al., 2009]. In contrast, scattered PKP observed at pre-critical distance and identified by azimuth-slowness analyses (Figures 2.2j and 2.2k) circumvent the source-receiver side uncertainty by pointing to specific scattering heterogeneities.

The study of [McNamara et al., 2010] summarized over 40 ULVZ studies and produced a ULVZ distribution map, suggesting that ULVZs are preferably grouped around LLVP regions. However, as they also noted, many ULVZs were not within or near LLVPs. The ULVZ regions presented in that study were graphically redrawn from previous studies; that is, they were not digitally reproduced. In this study, we digitize these regions (including ULVZ regions from more recent studies). This enables a more quantitative comparison of ULVZ locations to other lower mantle related phenomena, such as LLVPs and hotspots. In addition to geographical comparisons, the database presented here is available to public [Yu and Garnero, 2017].

2.3 Digitizing ULVZ Regions

2.3.1 ULVZ Information Collection

We have surveyed all seismologically determined ULVZ regions from studies self-identifying their observations as ULVZs. We applied no filter regarding ULVZ properties such as the degree of velocity drop or ULVZ height. Some ULVZ models do not have a particularly “ultra” velocity drop, but the velocity anomaly exceeds typical maximum levels in lowermost mantle tomography models. This, combined with evidence in many cases for an abrupt change to the reduced velocities, suggests the structure is consistent with the ULVZ concept. However, we do not set a filter since our database of past studies separately lists every study. Thus, future work using the database can define ULVZs based on any criteria. A list of previous studies is presented in Table 2.1. Studies are grouped according to the type of seismic probe, then further grouped by sampling region (the region names in Table 2.1 are presented in Figure 2.2). Authors of all studies were emailed with requests for digital ULVZ locations. For studies in which we did not receive digital locations, we proceeded with digitizing ULVZs from figures and tables in their papers. Our database includes three types of raw information for ULVZ locations: (1) CMB reflection point locations for reflected waves, (2) CMB ray path lines where diffraction occurs at the CMB for waves with diffraction, and (3) CMB areas, namely, for (a) PKP wave scattering probability maps, and also for (b) past studies that presented specific ULVZ geographical shapes. Each information entry is either a positive detection with ULVZ properties, a non-detection, or an uncertain detection. The uncertain detections are for complex waveforms which could not be unambiguously modeled or were described as uncertain in original studies. In our online database, each CMB sampling zone is a single file described by an individual entry in the online database table.

2.3.2 Digitizing ULVZs

We used the freeware software package GraphClick for Cartesian and Mercator map projections. For other map projections, we utilized the Generic Mapping Tools (GMT) freeware plotting software package [Wessel et al., 2013] and reproduced the map projection in published figures by trial and error (using coastlines and political boundaries for guidance). Once the geographic projection was identified, we digitized ULVZ geographic information from the published figures. For studies of core-reflected waves, the CMB sampling point locations were digitized (these came from twenty-three studies, corresponding to the following study numbers in Table 2.1: 2, 4, 9, 12, 13, 15, 16, 18, 22, 24, 27, 28, 29, 30, 33, 34, 37, 38, 40, 41, 42, 50, and 51). If the study binned the sampling points together, the centers of these bins were digitized (this corresponded to three studies: numbers 3, 43, and 53 in Table 2.1). For studies involving diffraction along the CMB, the end points of each diffraction path were digitized (from four studies: numbers 19, 23, 25, and 31 in Table 2.1). The ray theoretical diffraction path can be re-constructed by the end points. For studies that reported a specific preferred ULVZ model region, the boundary of the ULVZ region was digitized as a series of points (this came from five studies: numbers 45, 46, 47, 52, and 54 in Table 2.1). The same process was assumed for studies presenting general ULVZ detection areas, which includes two sub-categories: computed Fresnel zone ULVZ areas (four studies: numbers 1, 21, 26, and 49 in Table 2.1), and PKP scattering high probability regions (four studies: numbers 10, 14, 20, and 48 in Table 2.1). Additionally, three PKP studies (numbers 6, 32, and 36 in Table 2.1) and one SKKS study (number 39 in Table 2.1) designated approximate regions. We note that other studies compared SKKS to SKS for low velocity inference but did not advocate any particular region for the ULVZ [Zhang et al., 2009] (though this may overlap with other ULVZ study regions) or the structure was not a ULVZ [Silver and Bina, 1993]. If a study reported a 2D cross-section model, we placed the cross-section at its geographical position along the great circle path of the reported data, and digitized the two ULVZ edge locations along the cross-section (this was done for seven studies: numbers 5, 7, 8, 11, 17, 35, and 44 in Table 2.1). Regions from study numbers 35 and 44 are further extended azimuthally from the great circle plane to accommodate areas sampled by data (Sdiff and Pdiff) presented in those studies. This digital collection of ULVZ locations constitutes what we refer to as the “raw” ULVZ distribution information.

2.3.3 Approximating Fresnel zones

As noted, many studies presented CMB sampling location information using infinite frequency ray paths (e.g., reflection points and diffraction lines). Here we use the raw ray path information to approximate Fresnel zones, in order to more realistically consider the spatial distribution of ULVZs. For CMB reflected phases, we conduct a grid search on the CMB around the ray theoretical bounce point location to find all grid points rendering source-to-CMB-to-receiver travel times within a quarter of the dominant period (Figure 2.3a). The dominant periods were either discerned from data shown in the original papers, or assumed, using the published corner frequencies in filters used on the seismic data. The path geometry (i.e., great circle distance and azimuths for different studies) was either calculated from event-station location information or measured on maps (see online database table for the values of dominant periods, azimuths and distances of each study). In practice, we found the resulting Fresnel zones could be well approximated by ellipses. Thus, using the period and path geometry information, we found the elliptical estimate of the Fresnel zone for each reflected wave. For diffracted wave studies, we similarly constructed ellipses to approximate Fresnel zones for the diffracted segment of the wave path (again, assuming quarter wavelength for the time of the diffraction sampling the elliptical zone, Figure 2.3b). This technique was also applied to studies whose raw information involved ULVZ edge locations from published 2D cross-section models. We emphasize this method is approximate, but adequate given (a) the diverse and sometimes incomplete nature of the information provided from the past studies; (b) the CMB is not well sampled by ULVZ probing studies due to limitations in source-receiver geometries, thus the conclusions based on our derived sampling zones will not be compromised; (c) ULVZ structure can vary over sub-Fresnel zone scales, thus overemphasizing a computed Fresnel zone for any one study may not be warranted; (d) a majority of past ULVZ studies employed 1-D modeling approaches, thus ULVZ locations and shapes may be offset from solution models (and thus, that which is estimated here), e.g., see [Brown et al., 2015] supplementary information; and (e) a ULVZ non-detection does not preclude ULVZ presence with a thickness smaller than 5 km or so. These interesting but complicating factors are discussed further later in this paper.

2.4 Results

We present the raw digitized ULVZ distribution information in Figure 2.4a (Figure 2.4b presents the same map with numbers corresponding to studies in Table 2.1). Both detections and non-detections are shown. The sampling area size differs among studies: ULVZs mapped with diffracted waves, including Sdiff, Pdiff and SPdKS, account for a large portion of the sampled area, while studies based on reflected waves amount to much smaller areas. Some regions are characterized as both having and lacking a ULVZ. These disagreements may be due to the ULVZ location detection ambiguity mentioned in Section 1.2. Alternatively, fine-scale variations in ULVZ structure may be at play, since different probes are sensitive to structure at different lateral scales (thus may be visible to one probe, but not another).

Most studies have their sampling locations in and around the Pacific Ocean, due to the dominance of source-receiver geometries sampling there. Large low shear velocity provinces (LLSVPs) are shaded pink and appear to be near most of the positive detections. However, the pattern has some complexities. For example, many ULVZs are detected outside of LLSVPs, suggesting an origin that is independent from LLSVPs for those zones. Also, many non-ULVZ zones are within LLSVPs.

Figure 2.5 displays the Fresnel zone approximated ULVZ locations, along with mapped ULVZ model locations, resulting in a larger CMB sampling (compare to Figure 2.4a). The ULVZs outside of LLSVPs are more apparent (Figure 2.5a), which has a strong contribution from the globally distributed SPdKS diffraction paths. While many non-detections occur within LLSVPs, a majority of them occur outside of LLSVPs (Figure 2.5b). Data that are deemed complex (which thus yield uncertainties in ULVZ presence) are presented in Figure 2.5c, but not interpreted here. The total percentage of CMB area sampled by past ULVZ studies as presented in Figure 2.5 is 17.1%.

The level of detail about the ULVZ model properties presented in past studies is variable. Some studies present only the P-wave velocity reduction (δVP), others, only the S-wave reduction (δVS). Some present both, and some additionally report a density increase. Most (but not all) studies provide an estimate of ULVZ thickness. Trade-offs between these parameters have been explored in many studies [e.g., Garnero and Helmberger, 1998; Vidale and Hedlin, 1998; Rost et al., 2005; Idehara et al., 2007; Thorne et al., 2013]. We summarize published ULVZ model properties in Figure 2.6. Plotted properties include S- and P-wave velocity reduction, density elevation, and ULVZ thickness. While many studies present a range of models that could fit their data reasonably well, only the properties of stated best-fitting models are included in this summary figure. A large number of studies advocate a density increase. ULVZ model thicknesses are up to more than 50 km, and as thin as 2.5 km. A majority of the studies that present both P and S wave reductions conclude the S velocity drop is 2-3 times (or more) of the P velocity drop, plotting with a δVS:δVP ratio of 3:1 or 2:1. We note that in many studies, δVS:δVP values are a priori fixed at integer levels and not necessarily well constrained.

2.5 Comparison with Other Phenomena

2.5.1 ULVZs and Lowermost Mantle S-wave Heterogeneity

Here, we explore the possibility of a spatial relationship between ULVZs and larger scale deep mantle heterogeneity, by measuring distances between ULVZs and lowermost mantle S-wave velocity contours in δVS tomography models. This is motivated in part because geodynamic studies argue ULVZ material, if chemically dense, will be swept towards thermochemical pile margins [e.g., McNamara et al., 2010; Hernlund and McNamara, 2015; Li et al., 2017], and thermochemical piles are an interpretation for LLVPs [e.g., McNamara and Zhong, 2005; Torsvik et al., 2014; Garnero et al., 2016]. On the other hand, if ULVZs are solely due to partial melt of some major lower mantle component (though, argued unlikely [Hernlund and Tackley, 2007]), then they would be expected in the hottest regions of the deep mantle, which should be within LLVPs [Li et al., 2017].

We approximate the boundaries of LLSVPs as in Garnero et al. [2016], by choosing a δVS contour value which encloses 30% of the area of the CMB that contains the lowest velocities in the model. A similar thing is done for the highest δVS values, which can be speculated to correspond to the coldest lower mantle regions beneath subduction related downwellings. For example, in S40RTS [Ritsema et al., 2011] at 2800 km depth, the contour values for the lowest and highest velocity regions amounting to 30% area each are -0.27% and 0.44%, respectively (Figure 2.7a). Due to ULVZ detection location ambiguities mentioned in Section 1.2, only ULVZs identified from reflected wave phases are selected for a calculation of proximity to these velocity regions (Figure 2.7b). We first decimate ULVZ models and Fresnel zones onto a 0.5˚ by 0.5˚ grid at the CMB, then for each ULVZ grid cell, calculate the area and CMB distance to the nearest high and low velocity 30% area δVS contour. We summarize this information in histograms of fractional accumulated ULVZ area versus distance (Figure 2.7c). Distances are plotted relative to the low and high δVS contours. The upper panel of Figure 2.7c is for the low velocity contour (and thus the proxy for LLSVP boundaries). To put the distance scale into perspective, the average distance between the Pacific and African LLSVP boundaries is 4250 km for model S40RTS (thus ~2100 km is the average midpoint between the two LLSVPs). The upper panel of Figure 2.7c shows that ULVZs (mapped with reflected seismic waves) tend to be located near LLSVP boundaries, with comparable amounts locating within (~49%) and outside (~51%) of the LLSVPs. On the other hand, the lower panel of Figure 2.7c shows the same ULVZs tend to group away from (outside of) the high δVS (plausibly downwelling) regions. Nonetheless, there is still ~11% of ULVZ areas located within (and near) high δVS regions.

We explore the stability of this conclusion using two types of tests. In Test I, we randomly populate the CMB with circular shaped ULVZs that add up to the ULVZ area modeled by reflected phases. In reality, due to events and stations having limited spatial distribution, data from reflected phases sample limited CMB regions. Therefore, the location of observed ULVZs could be biased by limited path coverage possibilities. To account for this issue, we restrict the locations of randomly populated ULVZs to the CMB regions where CMB sampling is possible (see Figures 2.9a and 2.9b for details). The radius of these circular ULVZs are randomly chosen from 1° up to 6.5°, which spans the range of modeled ULVZ sizes (Figure 2.8c). Then we calculate the distance-area pattern for this synthetic random ULVZ location scenario in the same way as before. In Test II, 3 random angles are generated, then the contours are rotated around the three perpendicular axes with origin at the center of the earth using these three angles (thus, a Eulerian rotation, Figure 2.8d). After the random rotation, we calculate the distance-area pattern as before. Tests I and II were each repeated 1000 times before averages and standard deviations were computed for each distance bin. Results are shown as orange

(Test I) and dark green (Test II) filled circles in Figure 2.7c. The two randomized tests give similar patterns. Both random tests result in the peak ULVZ accumulations shifted to outside LLSVPs compared to observed locations (Figure 2.7c, upper panel). This shift appears robust: the observed ULVZ accumulations lie outside of the standard deviations of both random tests for the distance bins in the range between -1600 and -800 km. This supports the idea that ULVZs show a likelihood of being spatially correlated with LLSVP boundaries. For the high δVS regions (Figure 2.7c, lower panel), the location of the peaks in the random tests are close to the boundaries, which may relate to the tendency of the high δVS regions being more linear and less concentrated compared to the particularly concentrated low δVS regions. We also explore this spatial relationship in the same procedure for another five tomography models: S362ANI+M [Kustowski et al., 2008], HMSL-S06 [Houser et al., 2008], GyPsum [Simmons et al., 2010], SEMUCB-WM1 [French and Romanowicz, 2014], and SP12RTS [Koelemeijer et al., 2015]. Results are shown in Figure 2.9b-f. The same general patterns are observed for these models. The observations as well as the random test results for model SP12RTS have a broader character to the histogram peaks (Figure 2.9c, upper panel). This is partially due to SP12RTS possessing less short wavelength structure. In contrast, model SEMUCB-WM1 (Figure 2.9e, upper panel) has increased short scale structures outside of the two main LLSVPs – this results in shorter distances to the nearest LLSVP, and hence results in a more concentrated histogram peak.

We also explore the pattern of ULVZ proximity to high and low velocity zone boundaries for ULVZs of all 54 studies (Figure 2.5a), which are presented in Figure 2.9g-l for the six tomography models shown in Figure 2.9a-f. Similar to Test I, we computed random populated ULVZ statistics but without sampling-region restriction, mainly because the ULVZ location ambiguity for non-reflection phases used in ULVZ studies. Since the ULVZs are more widely distributed than those of solely the reflected wave studies, the histograms are somewhat more spread out than those of Figure 2.9a-f. More rigorous tests are possible; however, they would be warranted with a more geographically comprehensive ULVZ catalog.

2.5.2 ULVZs and Hotspots

Hotspots have long been considered linked to whole mantle plumes [Morgan, 1971] . While not every hotspot may signify a surface to CMB connection [Courtillot et al., 2003], a connection to ULVZs has been made in several studies [e.g., Helmberger et al., 1998; Williams et al., 1998; Wen, 2000; Cottaar and Romanowicz, 2012; Yuan and Romanowicz, 2017]. Also, a link between hotspots and LLSVP margins [Thorne et al., 2004; Torsvik et al., 2014], combined with the ULVZs appearing to group near LLSVP margins (Figure 2.7a), motivates a plot of minimum distance between ULVZs and hotspots (similar to that in Figure 2.7c). We use a compilation of 61 hotspots locations from Morgan and Morgan [2007]. Of those hotspots, 7 possible deep-sourced ones are identified in Courtillot et al. [2003]. For the surface location of each hotspot, we find the distance along the CMB to the nearest ULVZ. Figure 2.10 displays the results (similar to that done in Figure 2.7). We conduct random ULVZ location and random hotspot rotation tests (similar to that with LLSVPs in Figure 2.7c). Figures 2.11a and 2.11b only consider ULVZs reported from reflected wave studies. There is no clear association for ULVZs to be associated with hotspot locations, however, the CMB sampling coverage is low for reflected wave analyses. The presumed deep plume hotspots (thick crosses in Figure

2.10b) are similarly uncorrelated in distance. The random tests mimic the observed trend: ULVZs do not show distance preference to hotspot locations (orange-filled circles); the random rotations of the hotspot reference frame (green-filled circles), similarly does not demonstrate any trend with distance.

The story changes when all the ULVZ locations (from Figure 2.5a) are considered. Figures 2.11c and 2.11d show the result, which indicates that significantly more hotspots are close to ULVZ locations than far away from them. Some recent ULVZ studies beneath deep plume hotspot volcanoes have found the largest volume ULVZs to date, namely, Hawaii [Cottaar and Romanowicz, 2012], Samoa [Thorne et al., 2013] and Iceland [Yuan and Romanowicz, 2017]. Here we find that the deep plume hotspots are no more than 1000 km away from any mapped ULVZ, and that more than 90% of the 61 hotspots (from [Morgan and Morgan, 2007]) are within 1000 km of a ULVZ, and 38% of them are within 200 km away. Our random tests, however, suggest that these correlations do not hold statistical significance. Both Test I (for the globally randomized ULVZ locations) and Test II (random rotation of hotspots) produce a similar pattern to that which is observed. It could very well be that hotspots are well correlated to ULVZs, but that some of the ULVZs placed on source or receiver sides of path (e.g., from some SPdKS analyses) are erroneous, thus yielding an artificially higher small-distance hotspot count in our observation. Also, many ULVZs, especially if compositionally distinct, may be initially far from plumes but advecting towards plume zones [Yuan and Romanowicz, 2017] or thermochemical piles [Garnero et al., 2016; Li et al., 2017].

2.6 Discussion

2.6.1 Current CMB Coverage

Our Fresnel zone representations of ULVZs combined with defined ULVZ zones from published models cover roughly 17.1% of the CMB, by area. Positive ULVZ detection amounts to over 10.3% of the total CMB, and 6.5% of the CMB's area lacks ULVZ evidence. The complex data regions account for 3.8% of the CMB's area (we note that some regions have multiple ULVZ classifications, i.e., presence, absence, and complex). Other CMB areas may have been sampled, but normal and complex data regions may have been left unreported.

A typical ULVZ detection threshold for reflected waves phase is around 5 km in thickness (though some array methodologies using high frequency data can detect thinner ULVZs, e.g., Rost et al. [2010a]). The minimum thickness detection threshold will be larger for longer period waves, such as diffracted waves. It will also be larger if the ULVZ properties are less extreme, owing to the classic trade-off between ULVZ thickness and velocity reduction [e.g, Garnero and Helmberger, 1998; Rost et al., 2006]. Therefore, it is possible that ULVZs may exist in sampled areas that have been designated as lacking ULVZs, if the structure is thin and/or the properties are not particularly anomalous. This raises the possibility of a global ULVZ layer that is too thin to detect, but only appears where the mantle is hot, upwelling, or convection has generated accumulations of distinct ULVZ material.

2.6.2 Conflicting Results

We observed regions where ULVZ detection overlapped with ULVZ non-detection (Figure 2.5e). While our Fresnel zones are reasonable approximations to the

CMB area that contributes to waveform distortions caused by ULVZs, it is always possible to have sub-Fresnel zone variations in structure. Such a dual classification is not particularly common in the studies presented here: only 1.7% of the CMB area has models advocating both ULVZ presence and absence (i.e., about 10% of the surveyed CMB area). Consideration of finite frequency effects for the sensitivity of different probes to structure at the CMB will be an important next step in future studies.

2.7 Conclusion

We digitized the locations and models of ULVZs in 54 past studies. Locations of ULVZ presence and absence were digitized, as well as regions which authors depicted as unsure or uncertain, due to data complexities. This database contains five types of information: (1) the digitized bouncing locations for the core-reflected phases PcP, ScP and ScS; (2) the digitized ray path segments for diffraction at the CMB associated with the phases SPdKS, PKKPab_diff, Pdiff, and Sdiff; (3) the digitized high likelihood ULVZ zones for PKP scatterers; (4) the digitized area associated with ULVZ model regions presented in some studies; and (5) estimation of Fresnel zones (digitized) for the information in (1) and (2). This database can be freely accessed [Yu and Garnero, 2017]. ULVZs appear to be mostly correlated with low velocity regions in the lowermost mantle, and in particular, are commonly found near LLSVP margins. While not statistically significant with the distribution of ULVZs studied, there is a preference for ULVZs to be found beneath or near many hotspots.

References

Avants, M., T. Lay, and E. J. Garnero (2006), A new probe of ULVZ S-wave velocity structure: Array stacking of ScS waveforms, *Geophysical Research Letters*, *33*(7), 297, doi:10.1029/2005GL024989.

Brown, S. P., M. S. Thorne, L. Miyagi, and S. Rost (2015), A compositional origin to ultralow-velocity zones, *Geophysical Research Letters*, *42*(4), 1039–1045, doi:10.1002/2014GL062097.

Castle, J. C., and R. D. Van Der Hilst (2000), The core–mantle boundary under the Gulf of Alaska: no ULVZ for shear waves, *Earth and Planetary Science Letters*, *176*(3-4), 311–321, doi:10.1016/S0012-821X(00)00027-3.

Cottaar, S., and B. Romanowicz (2012), An unusually large ULVZ at the base of the mantle near Hawaii, *Earth and Planetary Science Letters*, *355-356*, 213–222, doi:10.1016/j.epsl.2012.09.005.

Courtier, A. M., B. Bagley, and J. Revenaugh (2007), Whole mantle discontinuity structure beneath Hawaii, *Geophysical Research Letters*, *34*(17), 51, doi:10.1029/2007GL031006.

Courtillot, V., A. Davaille, J. Besse, and J. Stock (2003), Three distinct types of hotspots in the Earth's mantle, *Earth and Planetary Science Letters*, *205*(3), 295–308, doi:10.1016/S0012-821X(02)01048-8.

Dziewonski, A. M., and D. L. Anderson (1981), Preliminary reference Earth model, *Physics of the earth and planetary interiors*, *25*(4), 297-356, doi:10.1016/0031-9201(81)90046-7.

French, S. W., and B. A. Romanowicz (2014), Whole-mantle radially anisotropic shear velocity structure from spectral-element waveform tomography, *Geophys J Int*, *199*(3), 1303–1327, doi:10.1093/gji/ggu334.

Garnero, E. J., A. K. McNamara, and S.-H Shim (2016), Continent-sized anomalous zones with low seismic velocity at the base of Earth's mantle, *Nature Geoscience*, *9*(7), 481–489, doi:10.1038/ngeo2733.

Garnero, E. J., and D. V. Helmberger (1998), Further structural constraints and uncertainties of a thin laterally varying ultralow-velocity layer at the base of the mantle, *J. Geophys. Res. Solid Earth*, *103*(6), 12495–12509, doi:10.1029/98JB00700.

Garnero, E. J., and J. E. Vidale (1999), ScP; A probe of ultralow velocity zones at the base of the mantle, *Geophysical Research Letters*, *26*(3), 377–380, doi:10.1029/1998GL900319.

Gassner, A., C. Thomas, F. Krüger, and M. Weber (2015), Probing the core-mantle boundary beneath Europe and Western Eurasia: A detailed study using PcP, *Physics of the earth and planetary interiors*, *246*, 9–24, doi:10.1016/j.pepi.2015.06.007.

Havens, E., and J. Revenaugh (2001), A broadband seismic study of the lowermost mantle beneath Mexico: Constraints on ultralow velocity zone elasticity and density, *Journal of Geophysical Research: Solid Earth (1978–2012)*, *106*(B12), 30809–30820, doi:10.1029/2000JB000072.

He, Y., and L. Wen (2009), Structural features and shear-velocity structure of the "Pacific Anomaly," *Journal of Geophysical Research*, *114*(B2), L07314, doi:10.1029/2008JB005814.

Helmberger, D. V., L. Wen, and X. Ding (1998), Seismic evidence that the source of the Iceland hotspot lies at the core-mantle boundary, *Nature*, *396*(6708), 251–255, doi:10.1038/24357.

Helmberger, D., S. Ni, L. Wen, and J. Ritsema (2000), Seismic evidence for ultralow-velocity zones beneath Africa and eastern Atlantic, *Journal of Geophysical Research*, *105*(B10), 23865–23878, doi:10.1029/2000JB900143.

Hernlund, J. W., and A. K. McNamara (2015), The Core-Mantle Boundary Region, in *Treatise on Geophysics*, pp. 461–519, Elsevier.

Hernlund, J. W., and P. J. Tackley (2007), Some dynamical consequences of partial melting in Earth's deep mantle, *Physics of the earth and planetary interiors*, *162*(1-2), 149–163, doi:10.1016/j.pepi.2007.04.005.

Houser, C., G. Masters, P. Shearer, and G. Laske (2008), Shear and compressional velocity models of the mantle from cluster analysis of long-period waveforms, *Geophys J Int*, *174*(1), 195–212, doi:10.1111/j.1365-246X.2008.03763.x.

Hutko, A. R., T. Lay, and J. Revenaugh (2009), Localized double-array stacking analysis of PcP: D″ and ULVZ structure beneath the Cocos plate, Mexico, central Pacific, and north Pacific, *Physics of the earth and planetary interiors*, *173*(1-2), 60–74, doi:10.1016/j.pepi.2008.11.003.

Idehara, K. (2011), Structural heterogeneity of an ultra-low-velocity zone beneath the Philippine Islands: Implications for core–mantle chemical interactions induced by massive partial melting at the bottom of the mantle, *Physics of the earth and planetary interiors*, *184*(1), 80–90, doi:10.1016/j.pepi.2010.10.014.

Idehara, K., A. Yamada, and D. Zhao (2007), Seismological constraints on the ultralow velocity zones in the lowermost mantle from core-reflected waves, *Physics of the earth and planetary interiors*, *165*(1-2), 25–46, doi:10.1016/j.pepi.2007.07.005.

Jensen, K. J., M. S. Thorne, and S. Rost (2013), SPdKS analysis of ultralow-velocity zones beneath the western Pacific, *Geophysical Research Letters*, *40*(17), 4574–4578, doi:10.1002/grl.50877.

Koelemeijer, P., J. Ritsema, A. Deuss, and H. J. Van Heijst (2015), SP12RTS: a degree-12 model of shear- and compressional-wave velocity for Earth's mantle, *Geophys J Int*, *204*(2), 1024–1039, doi:10.1093/gji/ggv481.

Kohler, M. D., J. E. Vidale, and P. M. Davis (1997), Complex scattering within D″ observed on the very dense Los Angeles Region Seismic Experiment Passive Array, *Geophysical Research Letters*, *24*(15), 1855–1858, doi:10.1029/97GL01823.

Koper, K. D., and M. L. Pyle (2004), Observations of PKiKP/PcP amplitude ratios and implications for Earth structure at the boundaries of the liquid core, *Journal of Geophysical Research: Solid Earth (1978–2012)*, *109*(B3), 1227, doi:10.1029/2003JB002750.

Kustowski, B., G. Ekström, and A. M. Dziewoński (2008), Anisotropic shear-wave velocity structure of the Earth's mantle: A global model, *Journal of Geophysical Research*, *113*(B6), B06306, doi:10.1029/2007JB005169.

Li, M., A. K. McNamara, E. J. Garnero, and S. Yu (2017), Compositionally-distinct ultra-low velocity zones on Earth's core-mantle boundary, *Nature Communications*, *8*(1), 977, doi:10.1038/s41467-017-00219-x.

Luo, S. N., S. Ni, and D. V. Helmberger (2001), Evidence for a sharp lateral variation of velocity at the core–mantle boundary from multipathed PKPab, *Earth and Planetary Science Letters*, *189*(3-4), 155–164, doi:10.1016/S0012-821X(01)00364-8.

McNamara, A. K., and S. Zhong (2005), Thermochemical structures beneath Africa and the Pacific Ocean, *Nature*, *437*(7062), 1136–1139, doi:10.1038/nature04066.

McNamara, A. K., E. J. Garnero, and S. Rost (2010), Tracking deep mantle reservoirs with ultra-low velocity zones, *Earth and Planetary Science Letters*, *299*(1-2), 1–9, doi:10.1016/j.epsl.2010.07.042.

Morgan, W. J. (1971), Convection Plumes in the Lower Mantle, *Nature*, *230*(5288), 42–43, doi:10.1038/230042a0.

Morgan, W. J., and J. P. Morgan (2007), Plate velocities in the hotspot reference frame, *Geological Society of America Special Papers*, *430*, 65–78, doi:10.1130/2007.2430(04).

Mori, J., and D. V. Helmberger (1995), Localized boundary layer below the mid-Pacific velocity anomaly identified from a PcP precursor, *Journal of Geophysical Research: Solid Earth (1978–2012)*, *100*(B10), 20359–20365, doi:10.1029/95JB02243.

Ni, S., and D. V. Helmberger (2001a), Horizontal transition from fast to slow structures at the core–mantle boundary; South Atlantic, *Earth and Planetary Science Letters*, *187*(3-4), 301–310, doi:10.1016/S0012-821X(01)00273-4.

Ni, S., and D. V. Helmberger (2001b), Probing an ultra-low velocity zone at the core mantle boundary with P and S waves, *Geophysical Research Letters*, *28*(12), 2345–2348, doi:10.1029/2000GL012766.

Niu, F., and L. Wen (2001), Strong seismic scatterers near the core-mantle boundary west of Mexico, *Geophysical Research Letters*, *28*(18), 3557–3560, doi:10.1029/2001GL013270.

Pachhai, S., J. Dettmer, and H. Tkalčić (2015), Ultra-low velocity zones beneath the Philippine and Tasman Seas revealed by a trans-dimensional Bayesian waveform inversion, *Geophys J Int*, *203*(2), 1302–1318, doi:10.1093/gji/ggv368.

Persh, S. E., J. E. Vidale, and P. S. Earle (2001), Absence of Short-Period ULVZ Precursors to PcP and ScP from two Regions of the CMB, *Geophysical Research Letters*, *28*(2), 387–390, doi:10.1029/2000GL011607.

Reasoner, C., and J. Revenaugh (2000), ScP constraints on ultralow-velocity zone density and gradient thickness beneath the Pacific, *Journal of Geophysical Research: Solid Earth (1978–2012)*, *105*(B12), 28173–28182, doi:10.1029/2000JB900331.

Revenaugh, J., and R. Meyer (1997), Seismic Evidence of Partial Melt Within a Possibly Ubiquitous Low-Velocity Layer at the Base of the Mantle, *Science*, *277*(5326), 670–673, doi:10.1126/science.277.5326.670.

Ritsema, J., A. Deuss, H. J. Van Heijst, and J. H. Woodhouse (2011), S40RTS: a degree-40 shear-velocity model for the mantle from new Rayleigh wave dispersion, teleseismic traveltime and normal-mode splitting function measurements, Geophys J Int, 184(3), 1223–1236, doi: 10.1111/j.1365-246X.2010.04884.x.

Rondenay, S., and K. M. Fischer (2003), Constraints on localized core-mantle boundary structure from multichannel, broadband SKS coda analysis, *Journal of Geophysical Research*, *108*(B), 2537, doi:10.1029/2003JB002518.

Ross, A. R., H. Thybo, and L. N. Solidilov (2004), Reflection seismic profiles of the core-mantle boundary, *Journal of Geophysical Research*, *109*(B8), 1335, doi:10.1029/2003JB002515.

Rost, S., and C. Thomas (2010), High resolution CMB imaging from migration of short-period core reflected phases, *Physics of the earth and planetary interiors*, *183*(1), 143–150, doi:10.1016/j.pepi.2010.04.005.

Rost, S., and E. J. Garnero (2006), Detection of an ultralow velocity zone at the core-mantle boundary using diffracted PKKPab waves, *Journal of Geophysical Research: Solid Earth (1978–2012)*, *111*(B7), 151, doi:10.1029/2005JB003850.

Rost, S., and J. Revenaugh (2001), Seismic detection of rigid zones at the top of the core, *Science*, *294*(5548), 1911–1914, doi:10.1126/science.1065617.

Rost, S., and J. Revenaugh (2003), Small-scale ultralow-velocity zone structure imaged by ScP, *Journal of Geophysical Research: Solid Earth (1978–2012)*, *108*(B1), 421, doi:10.1029/2001JB001627.

Rost, S., E. J. Garnero, and Q. Williams (2006), Fine-scale ultralow-velocity zone structure from high-frequency seismic array data, *Journal of Geophysical Research*, *111*(B9), 1169, doi:10.1029/2005JB004088.

Rost, S., E. J. Garnero, and W. Stefan (2010a), Thin and intermittent ultralow-velocity zones, *Journal of Geophysical Research: Solid Earth (1978–2012)*, *115*(B6), 443, doi:10.1029/2009JB006981.

Rost, S., E. J. Garnero, M. S. Thorne, and A. R. Hutko (2010b), On the absence of an ultralow-velocity zone in the North Pacific, *Journal of Geophysical Research*, *115*(B4), L14612, doi:10.1029/2009JB006420.

Rost, S., E. J. Garnero, Q. Williams, and M. Manga (2005), Seismological constraints on a possible plume root at the core–mantle boundary, *Nature*, *435*(7042), 666–669, doi:10.1038/nature03620.

Silver, P. G., and C. Bina (1993), An anomaly in the amplitude ratio of SKKS/SKS in the range 100–108° from portable teleseismic data, *Geophysical Research Letters*, *20*(12), 1135–1138, doi:10.1029/92GL02464.

Simmons, N. A., A. M. Forte, L. Boschi, and S. P. Grand (2010), GyPSuM: A joint tomographic model of mantle density and seismic wave speeds, *Journal of Geophysical Research*, *115*(B12), B12310, doi:10.1029/2010JB007631.

Simmons, N. A., and S. P. Grand (2002), Partial melting in the deepest mantle, *Geophysical Research Letters*, *29*(11), 161, doi:10.1029/2001GL013716.

Sun, D., D. Helmberger, S. Ni, and D. Bower (2009), Direct measures of lateral velocity variation in the deep Earth, *Journal of Geophysical Research*, *114*(B5), 97, doi:10.1029/2008JB005873.

Thomas, C., J.-M. Kendall, and G. Helffrich (2009), Probing two low-velocity regions with PKPb-caustic amplitudes and scattering, *Geophys J Int*, *178*(1), 503–512, doi:10.1111/j.1365-246X.2009.04189.x.

Thomas, C., M. Weber, C. W. Wicks, and F. Scherbaum (1999), Small scatterers in the lower mantle observed at German broadband arrays, *Journal of Geophysical Research: Solid Earth (1978–2012)*, *104*(B7), 15073–15088, doi:10.1029/1999JB900128.

Thorne, M. S., and E. J. Garnero (2004), Inferences on ultralow-velocity zone structure from a global analysis of SPdKS waves, *Journal of Geophysical Research*, *109*(B8), 421, doi:10.1029/2004JB003010.

Thorne, M. S., E. J. Garnero, and S. P. Grand (2004), Geographic correlation between hot spots and deep mantle lateral shear-wave velocity gradients, *Physics of the earth and planetary interiors*, *146*(1-2), 47–63, doi:10.1016/j.pepi.2003.09.026.

Thorne, M. S., E. J. Garnero, G. Jahnke, H. Igel, and A. K. McNamara (2013), Mega ultra-low velocity zone and mantle flow, *Earth and Planetary Science Letters*, *364*, 59–67, doi:10.1016/j.epsl.2012.12.034.

To, A., Y. Fukao, and S. Tsuboi (2011), Evidence for a thick and localized ultra-low shear velocity zone at the base of the mantle beneath the central Pacific, *Physics of the earth and planetary interiors*, *184*(3-4), 119–133, doi:10.1016/j.pepi.2010.10.015.

Torsvik, T. H., R. van der Voo, P. V. Doubrovine, K. Burke, B. Steinberger, L. D. Ashwal, R. G. Tronnes, S. J. Webb, and A. L. Bull (2014), Deep mantle structure as a reference frame for movements in and on the Earth, *Proceedings of the National Academy of Sciences*, *111*(24), 8735–8740, doi:10.1073/pnas.1318135111.

Vanacore, E. A., S. Rost, and M. S. Thorne (2016), Ultralow-velocity zone geometries resolved by multidimensional waveform modelling, *Geophys J Int*, *206*(1), 659–674, doi:10.1093/gji/ggw114.

Vidale, J. E., and H. M. Benz (1992), A sharp and flat section of the core-mantle boundary, *Nature*, *359*(6396), 627–629, doi:10.1038/359627a0.

Vidale, J. E., and M. A. H. Hedlin (1998), Evidence for partial melt at the core-mantle boundary north of Tonga from the strong scattering of seismic waves, *Nature*, *391*(6668), 682–685, doi:10.1038/35601.

Wen, L. (2000), Intense seismic scattering near the Earth's core-mantle boundary beneath the Comoros hotspot, *Geophysical Research Letters*, *27*(22), 3627–3630, doi:10.1029/2000GL011831.

Wen, L., and D. V. Helmberger (1998a), Ultra-Low Velocity Zones Near the Core-Mantle Boundary from Broadband PKP Precursors, *Science*, *279*(5357), 1701–1703, doi:10.1126/science.279.5357.1701.

Wen, L., and D. V. Helmberger (1998b), A two-dimensional P-SV hybrid method and its application to modeling localized structures near the core-mantle boundary, *Journal of Geophysical Research*, *103*(B8), 17901–17918, doi:10.1029/98JB01276.

Wessel, P., W. H. F. Smith, R. Scharroo, J. Luis, and F. Wobbe (2013), Generic Mapping Tools: Improved Version Released, *Eos Trans. AGU*, *94*(45), 409–410, doi:10.1002/2013EO450001.

Williams, Q., J. Revenaugh, and E. J. Garnero (1998), A Correlation Between Ultra-Low Basal Velocities in the Mantle and Hot Spots, *Science*, *281*(5376), 546–549, doi:10.1126/science.281.5376.546.

Xu, Y., and K. D. Koper (2009), Detection of a ULVZ at the base of the mantle beneath the northwest Pacific, *Geophysical Research Letters*, *36*(17), L14612, doi:10.1029/2009GL039387.

Yao, J., and L. Wen (2014), Seismic structure and ultra-low velocity zones at the base of the Earth's mantle beneath Southeast Asia, *Physics of the earth and planetary interiors*, *233*, 103–111, doi:10.1016/j.pepi.2014.05.009.

Yu, S., and E. J. Garnero (2017), ULVZ Distribution Database from 54 studies [Data set]. Zenodo. http://doi.org/10.5281/zenodo.1000998

Yuan, K., and B. Romanowicz (2017), Seismic evidence for partial melting at the root of major hot spot plumes, *Science*, *357*(6349), 393–397, doi:10.1126/science.aan0760.

Zhang, Y., J. Ritsema, and M. S. Thorne (2009), Modeling the ratios of SKKS and SKS amplitudes with ultra-low velocity zones at the core-mantle boundary, *36*(19), B05305–5, doi:10.1029/2009GL040030.

Zhao, C., E. J. Garnero, M. Li, A. McNamara, and S. Yu (2017), Intermittent and lateral varying ULVZ structure at the northeastern margin of the Pacific LLSVP, *J. Geophys. Res. Solid Earth*, *122*(2), 1198–1220, doi:10.1002/2016JB013449.

Zou, Z., F. Leyton, and K. D. Koper (2007), Partial melt in the lowermost mantle near the base of a plume, *Geophys J Int*, *168*(2), 809–817, doi:10.1111/j.1365-246X.2006.03266.x.

Table 2.1 A summary of all past ULVZ studies surveyed in this Chapter. They are grouped according to seismic wave used.

No.	Reference	Phase & Method [i]	Region & Detection [ii]
54	Yuan and Romanowicz [2017]	S_{diff} (t,w)	Iceland (y)
45	Cottaar and Romanowicz [2012]	S_{diff} (a,t,w)	Central Pacific (y)
44	To et al. [2011]	S_{diff} (t,w)	Central Pacific (y,c)
35	Xu and Koper [2009]	P_{diff} (a,t)	Northwest Pacific (y)
31	Rost and Garnero [2006]	$PKKP_{ab\_diff}$ (a,t)	North Atlantic (y)
46	Thorne et al. [2013]	SKS (w)	Southwest Pacific (y)
7	Wen and Helmberger [1998]	SKS (w)	Southwest Pacific (y)
47	Jensen et al. [2013]	SKS (w)	Coral Sea (y), Philippine Sea (n), South China Sea (y), Celebes Sea (y)
25	Thorne and Garnero [2004]	SKS (w)	Global (y,n,c)
23	Rondenay and Fischer [2003]	SKS (w)	North America (y,n), Northwest Pacific (n)
19	Ni and Helmberger [2001]	SKS (w)	Central Africa (y,n)
11	Helmberger et al. [2000]	SKS (w)	Central Africa (y), North Atlantic (y)
5	Helmberger et al. [1998]	SKS (w)	Iceland (y)
52	Vanacore et al. [2016]	SKS (w)	South Atlantic (y), West Pacific (c), South America (c)
36	Thomas et al. [2009]	PKP (a,w)	Coral Sea (y), West Pacific (c), Tasman Sea (n)
32	Zou et al. [2007]	PKP (a,s)	Amazon (y)
48	Yao and Wen [2014]	PKP (t,s)	South China Sea (y), Celebes Sea (y)
20	Niu and Wen [2001]	PKP (s)	Central America (y)
14	Wen [2000]	PKP (s)	North Madagascar (y)
17	Luo et al. [2001]	PKP (t,w)	Central Pacific (y,n,c)
10	Thomas et al. [1999]	PKP (s)	Southwest Pacific (y), Europe (y)
6	Vidale and Hedlin [1998]	PKP (s)	Southwest Pacific (y)
8	Wen and Helmberger [1998]	PKP (w)	Southwest Pacific (y)
39	Sun et al. [2009]	SKKS (t)	South Africa (c)
26	Ross et al. [2004]	PcP (w)	North Siberia (y), West Siberia (n,c)
41	Rost et al. [2010]	PcP (w)	Northeast Pacific (n)
40	Rost and Thomas [2010]	PcP (m)	Alaska (n)

(Continue on next page)

Table 2.1 (*continued*)

No.	Reference	Phase & Method [i]	Region & Detection [ii]
1	Vidale and Benz [1992]	ScP (w)	Alaska (n)
3	Revenaugh and Meyer [1997]	PcP (t,m)	Alaska (y), Central America (c) Central Pacific (y)
37	Hutko et al. [2009]	PcP (w)	Alaska (c), Central America (n) Central Pacific (y)
21	Persh et al. [2001]	SdP/ScP(r), PdP/PcP (r)	Alaska (n), Central America (n)
12	Castle and Hilst [2000]	ScP/P (r)	Alaska (n), Central America (n)
4	Kohler et al. [1997]	PcP (w)	Alaska (n), Central Pacific (y)
16	Havens and Revenaugh [2001]	PcP (m)	Central America (y,n,c)
29	Avants et al. [2006]	ScS (m)	Central America (n), Central Pacific (y)
2	Mori and Helmberger [1995]	PcP (w)	Central America (n), Central Pacific (y)
33	Courtier et al. [2007]	ScS (m)	Central Pacific (c)
53	Zhao et al. [2017]	ScS (w)	Central Pacific (y)
49	Gassner et al. [2015]	PcP (w)	Europe (y,n)
43	Idehara [2011]	ScP (w)	Philippine Sea (y,n,c)
34	Idehara et al. [2007]	ScP (w)	Celebes Sea (y,n), Philippine Sea (y,n), Coral Sea (y,n), Banda Sea (n)
50	Pachhai et al. [2015]	ScP (w)	Philippine Sea (y), Tasman Sea (y)
28	Rost et al. [2005]	ScP (w)	Coral Sea (y,n,c)
30	Rost et al. [2006]	ScP (w)	Coral Sea (y,n,c)
42	Rost et al. [2010]	ScP (w)	Coral Sea (y,n)
51	Brown et al. [2015]	ScP (w)	Coral Sea (y)
24	Rost and Revenaugh [2003]	ScP (w)	Coral Sea (y,n)
15	Rost and Revenaugh [2001]	ScP (w)	Coral Sea (y)
27	Koper and Pyle [2004]	PKiKP/PcP (r)	Coral Sea (y)
38	He and Wen [2009]	ScS (t,w)	West Pacific (y)
13	Reasoner and Revenaugh [2000]	ScP (w)	Southwest Pacific (y,n,c), West Pacific (c)
9	Garnero and Vidale [1999]	ScP (w)	Southwest Pacific (y,n,c), West Pacific (n)
18	Ni and Helmberger [2001]	ScS (t,w)	South Atlantic (y,c)
22	Simmons and Grand [2002]	ScS, PcP (t)	South Atlantic (y)

i. Methods used: (a)rray-analysis, 1D (m)igration, (s)catters, (t)ravel-time, (w)aveform modeling, amplitude (r)atio.

ii. Detection classification: (y)es detection, (n)o detection, (c)omplex or uncertain observations.

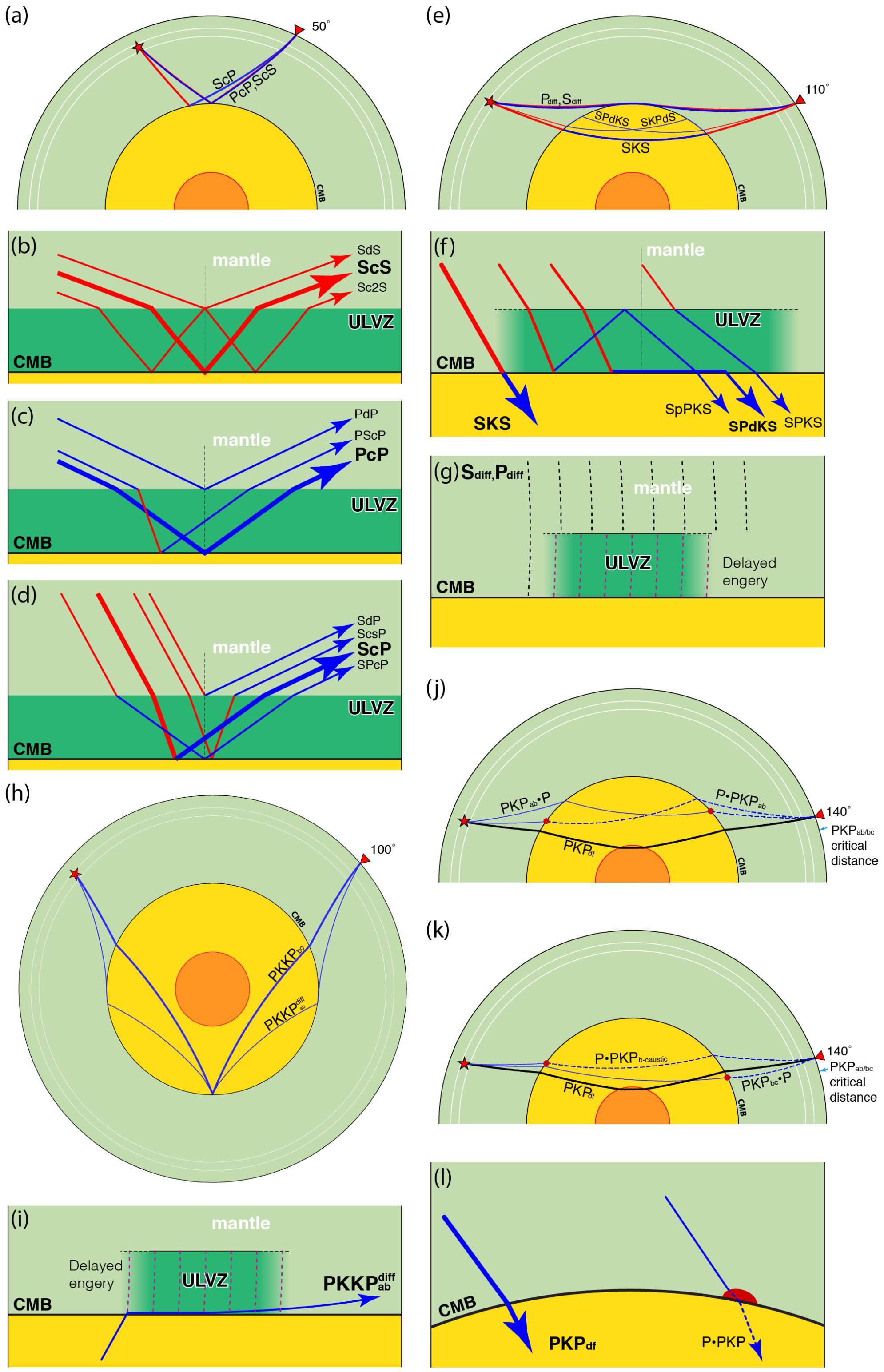

Figure 2.1. Ray paths of seismic phases used in past ULVZ studies. Sources (red stars) are at 500 km. Receivers are red reversed triangles. Red ray paths represent S-waves,

blue ray paths are P-waves. Bold ray paths represent reference phases. Gradient ULVZ color represents the uncertainties of its lateral size or top-side shape. (a) ScS, ScP, PcP at 50˚. ScS and PcP are nearly identical. Multiple reflections and conversions arise due to a ULVZ layer are shown for a flat top ULVZ for ScS in (b), PcP in (c), and ScP in (d). (e) SKS, SP_dKS, SKP_dS and S_{diff}, P_{diff} are shown at 110˚. (f) A zoom in on the source-side of SKS and SP_dKS in the present of ULVZ. (g) Horizontally propagating S_{diff} and P_{diff} interact with the ULVZ at the CMB. Dashed lines represent diffracted wave fronts which can be delayed enough to affect the overall waveform. (h) $PKKP_{bc}$ and $PKKP_{ab\_diff}$ at 260˚. (i) A zoom in at the receiver side of $PKKP_{ab\_diff}$ depicting its interaction with a ULVZ. (j, k) Examples of scattered PKP ray paths received before the PKP-caustic critical distance are depicted. (l) A zoomed in look at source side of PKP_{df} showing scattered P energy.

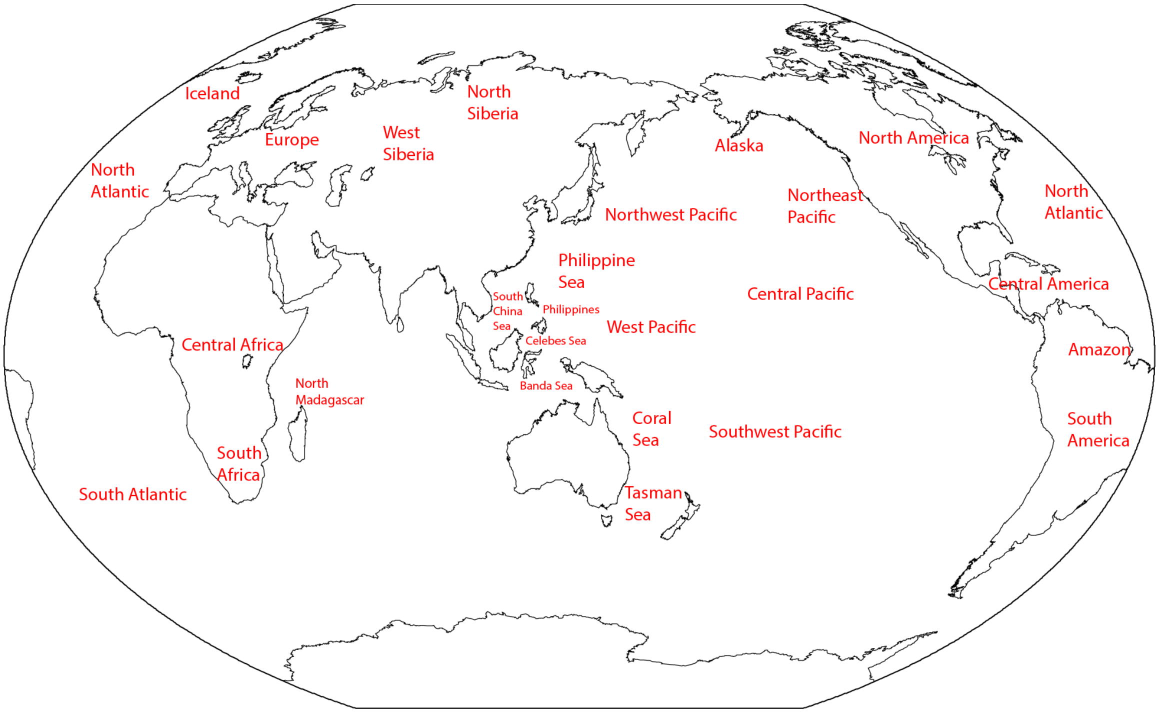

Figure 2.2. Map showing location region naming convention used in Table 2.1.

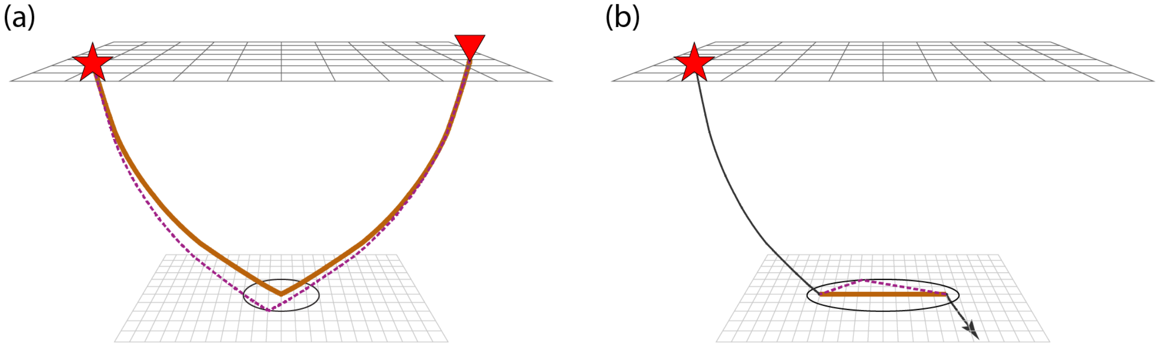

Figure 2.3. Schematic plot depicting addition of Fresnel zone approximations. Stars represent events and reversed triangle represents the seismic station at Earth's surface. The lower grid represents the CMB. (a) Fresnel zone approximation ellipse around sampling points of PcP, ScP and ScS. An ellipse on the CMB is found such that for each point on it, the travel time difference between original ray path (brown) and an alternative ray path (dashed purple) is equal to one quarter dominant period of the data. (b) Fresnel zone approximation ellipse around a CMB diffraction segment; this segment could be the P-diffraction part of SPdKS (shown), as well as SKPdS and PKKPab_diff.

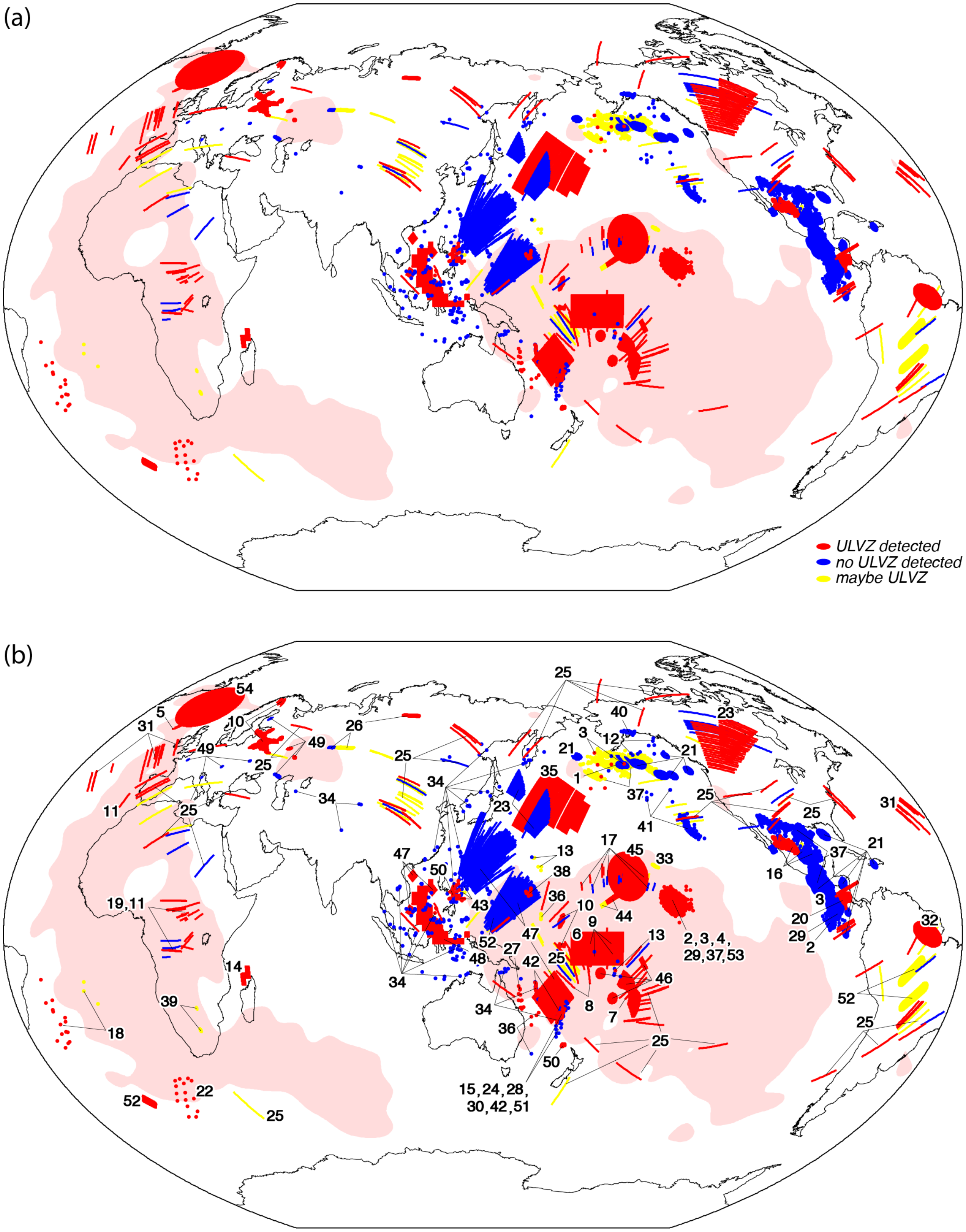

Figure 2.4. (a) Summary map of ULVZ distribution information from the 54 digitized ULVZ studies in Table 2.1. Three kinds of ULVZ geographic information are shown here: small circles represent core-reflection locations; lines correspond to CMB diffraction locations as well as regions of 2-D cross-section ULVZ models; and filled

areas represent ULVZ models presented in some studies. Colors indicate the presence (red) or absence (blue) of ULVZs; yellow corresponds to complex or uncertain observations. The larger pink regions in the background denote large low shear wave provinces (LLSVPs) from model S40RTS [Ritsema et al., 2011] at depth of 2800 km. These LLSVPs occupy 30% of the CMB surface area; this corresponds to regions with $\delta VS \leqslant -0.27\%$. For plotting clarity, smaller sampling areas are plotted on top of larger ULVZ zones. (b) as in (a), with the addition of study numbers for each CMB sampling zone, which correspond to first column of Table 2.1.

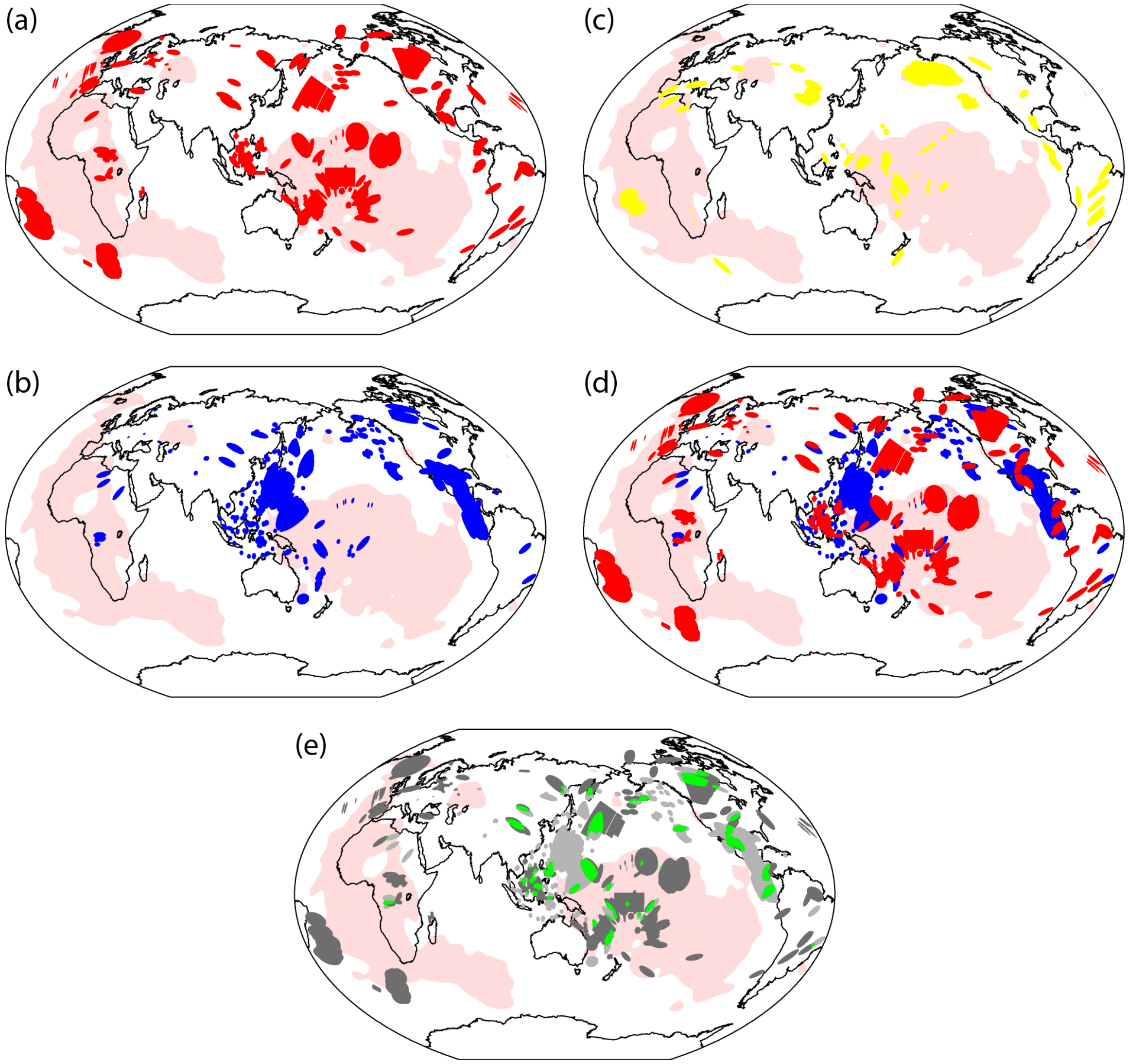

Figure 2.5. ULVZ distribution information (color scheme as in Figure 2.4), with the ULVZ point and line information converted to Fresnel zones, for (a) regions with detected ULVZs, (b) regions where ULVZs were not detected, (c) regions with complex waveforms, and (d) the combined information from panels (a) and (b) showing regions possessing and lacking evidence for ULVZs. (e) shows the same regions as in (d), but the ULVZ and non-ULVZ zones are dark and light gray, respectively, with green regions representing areas showing evidence for both a ULVZ (from panel (a)) and lacking ULVZ (from panel (b)). The pink regions are the LLSVPs as in Figure 2.4.

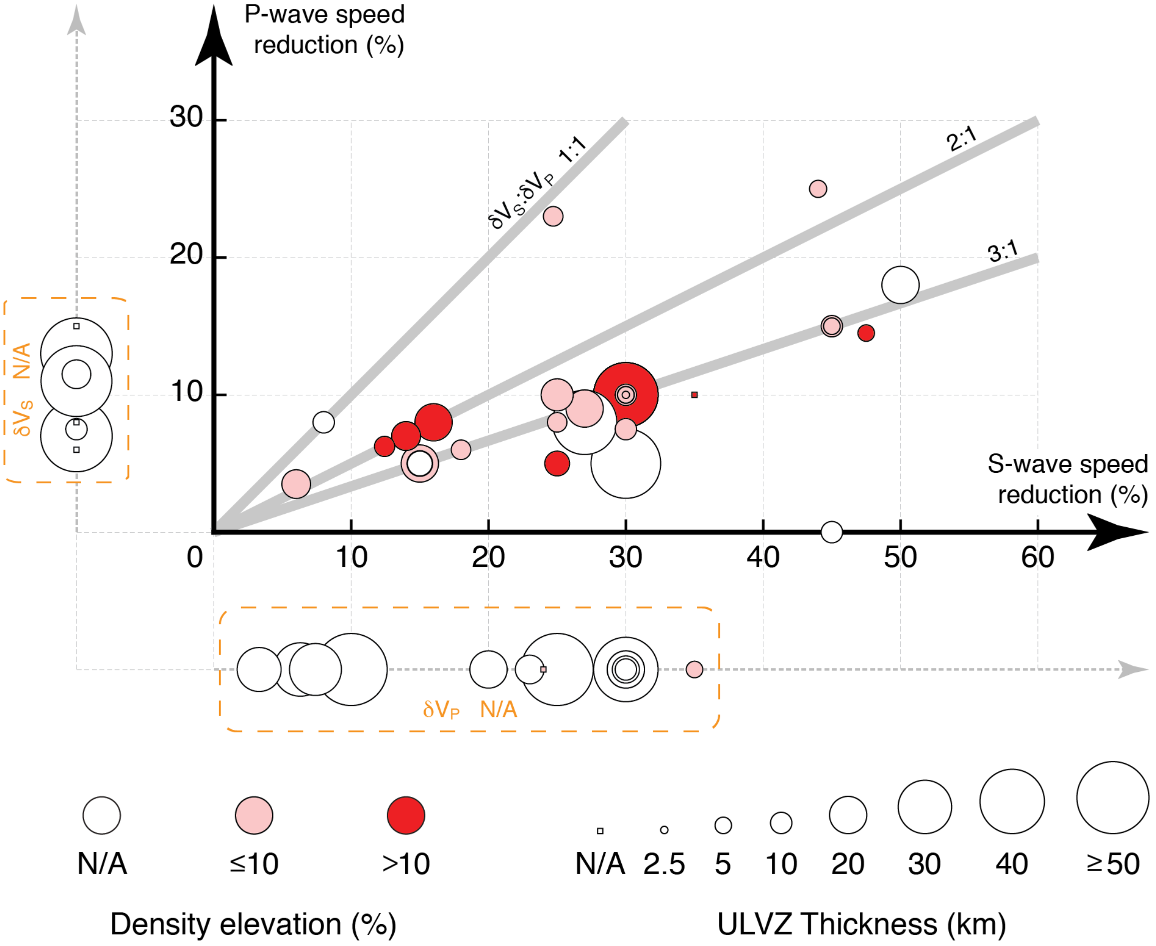

Figure 2.6. Summary of reported ULVZ properties including P- and S-wave velocity reduction, density elevation, and ULVZ thickness. Each symbol represents the preferred model from each distinct result in surveyed studies. For studies that only report a P-wave velocity reduction but no S-wave information, symbols are plotted along the gray dashed line to the left of the plot domain y-axis, Similarly, studies only reporting an S-wave velocity reduction are plotted on the gray dashed line below the plot domain x-axis. Studies reporting a density elevation are plotted in pink/red symbols, otherwise the symbol color is white. Studies that report a ULVZ thickness are plotted in circles, and sized according to thickness, otherwise they are plotted as small squares. Bold gray lines in the background represent a $\delta V_S:\delta V_P$ ratio of 1:1, 2:1 and 3:1.

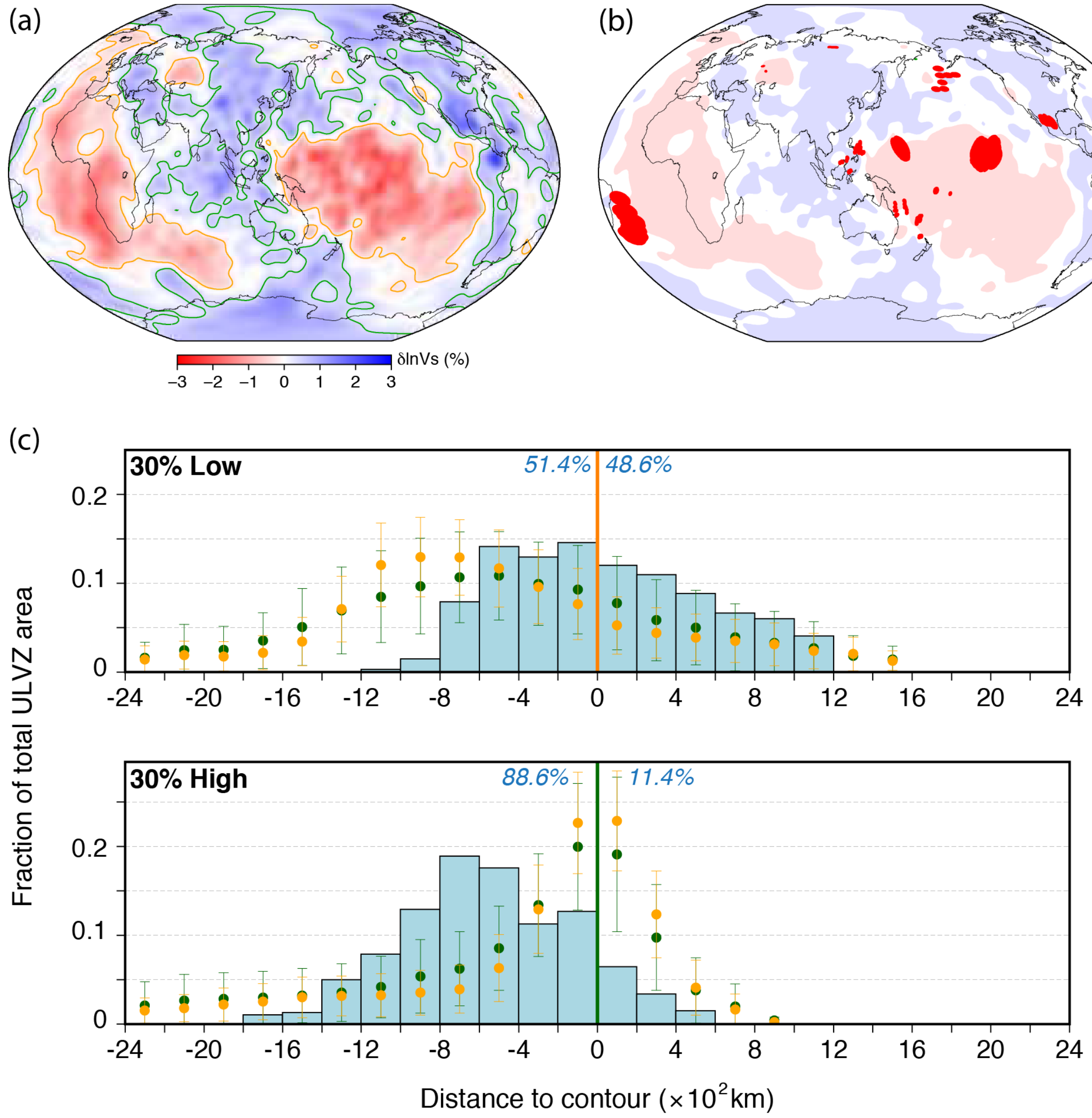

Figure 2.7. Spatial relation between lowermost mantle structure and ULVZs. Only studies using reflected phases are included (i.e. ScS, ScP, PcP, see text for details). (a) S40RTS [Ritsema et al., 2011] S-wave anomalies at 2800 km. Orange lines are S-wave velocity contours enclosing 30% of the CMB's area containing the lowest wave speeds at 2800 km depth. Green lines similarly surround 30% of the CMB's area with the highest velocities. The orange contour has value δVS = -0.27%, the green contour corresponds to δVS = 0.44%. (b) The contour enclosed areas in (a) are colored in pink (low velocity) and light blue (high velocity). ULVZs from reflection studies are plotted on top as red regions. (c) Minimum distance of ULVZ areas to the low (top panel) and high (bottom panel) velocity contours. Negative distance means ULVZ areas are located outside of contour enclosed regions, positive means inside. The cumulative ULVZ area outside and inside the contoured regions is shown in the italicized light blue numbers for this model (left is outside contoured regions, right is inside). Orange and dark-green circles represent

results from an identical distance measurement calculation, but on random ULVZ distributions: orange corresponds to a random distribution of circular shaped ULVZs; dark-green corresponds to the actual ULVZ data set and distances to random rotations of the tomographic velocity contours (which correspond to Tests I and II in the text). Error bars correspond to the standard deviation of the average of fractional ULVZ area estimated after 1000 random tests (for each of Test I and II).

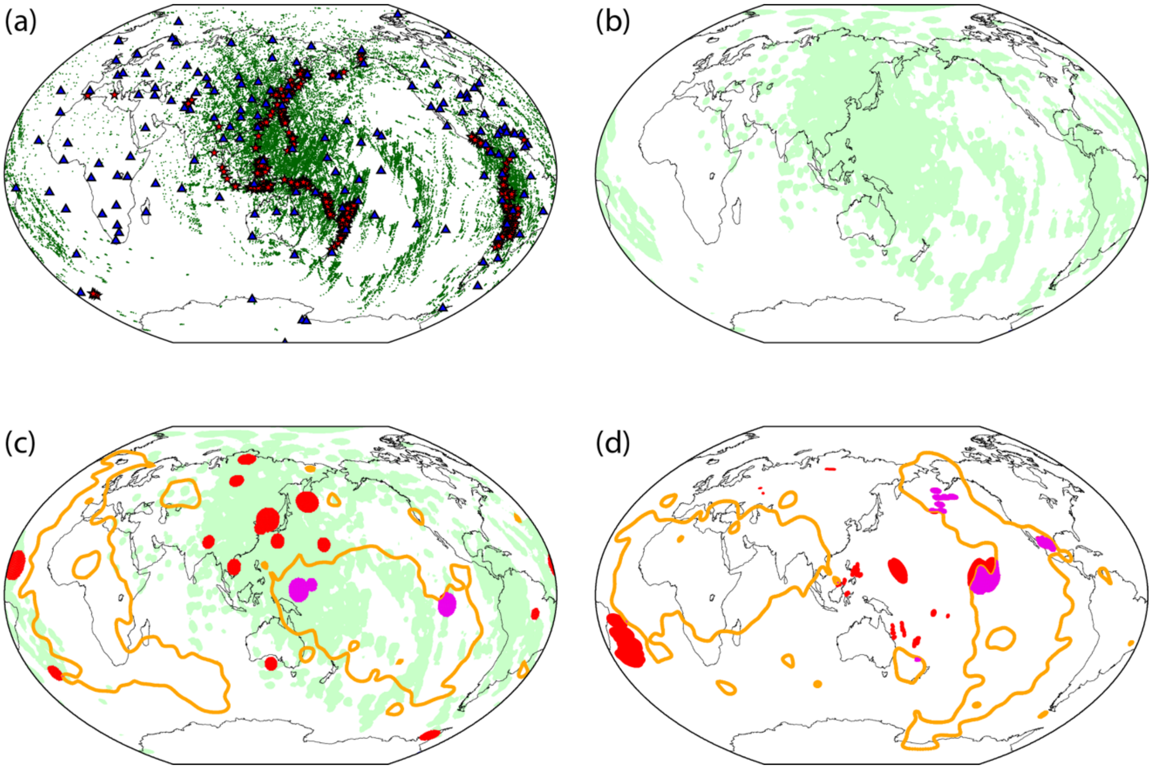

Figure 2.8. (a) Reflected phases sampling. Red stars: events are from 2005 to 2015 with magnitude greater than 5.7 and source depth greater than 100 km. Blue triangles: 150 stations from the Global Seismic Network (GSN). Green points: calculated theoretical CMB reflection locations from event-station pairs with distance greater than 30˚ using 1D model PREM [*Dziewonski and Anderson*, 1981], for ScS, ScP and PcP phases. (b) Light green shows the Test I restricted CMB sampling regions, which include locations have at least 20 reflection points within any 2˚ radius neighborhood. (c) An example from Test I: randomly populated ULVZs within the restricted CMB regions. (d) An example random contour rotation from Test II. In (c) and (d), the orange lines represent the S40RTS low velocity contours corresponding to LLSVPs with an enclosing area 30% of the CMB. Red regions show ULVZs outside the LLSVPs, and magenta regions are ULVZs inside the LLSVPs. Each of these tests is repeated 1000 times (see text for more details).

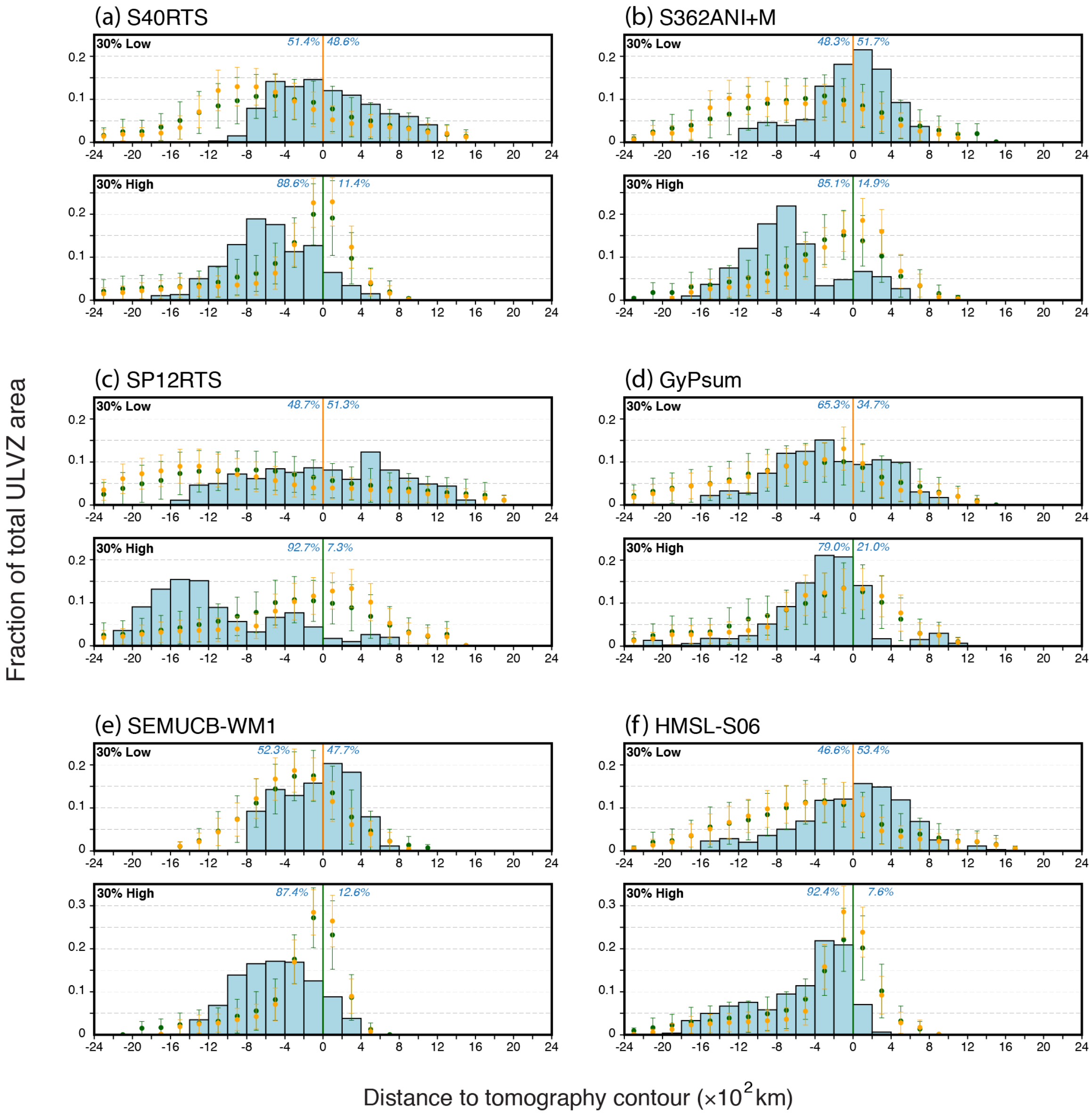

(*continue on next page*)

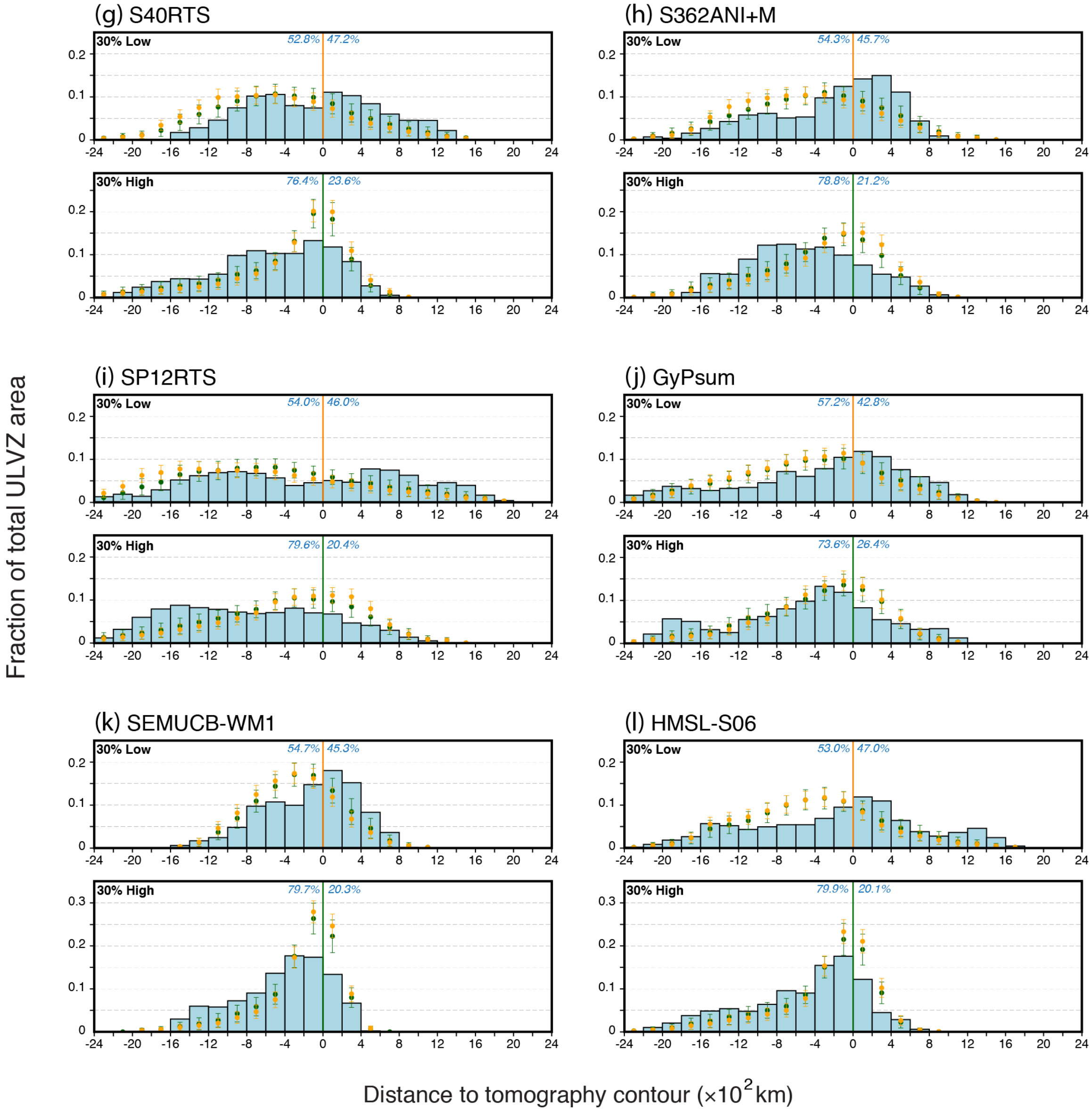

Figure 2.9. Fractional area of observed ULVZs from reflected phases (panels a-f), and all phases from all 54 studies (panels g-l) with respect to distance to high or low velocity contours in tomographic models (as in Figure 2.7c), for tomography models (a, g) S40RTS [Ritsema et al., 2011], (b, h) S362ANI+M [Kustowski et al., 2008], (c, i) SP12RTS [Koelemeijer et al., 2015], (d, j) GyPsum [Simmons et al., 2010], (e, k) SEMUCB-WM1 [French and Romanowicz, 2014] and (f, l) HMSL-S06 [Houser et al., 2008].

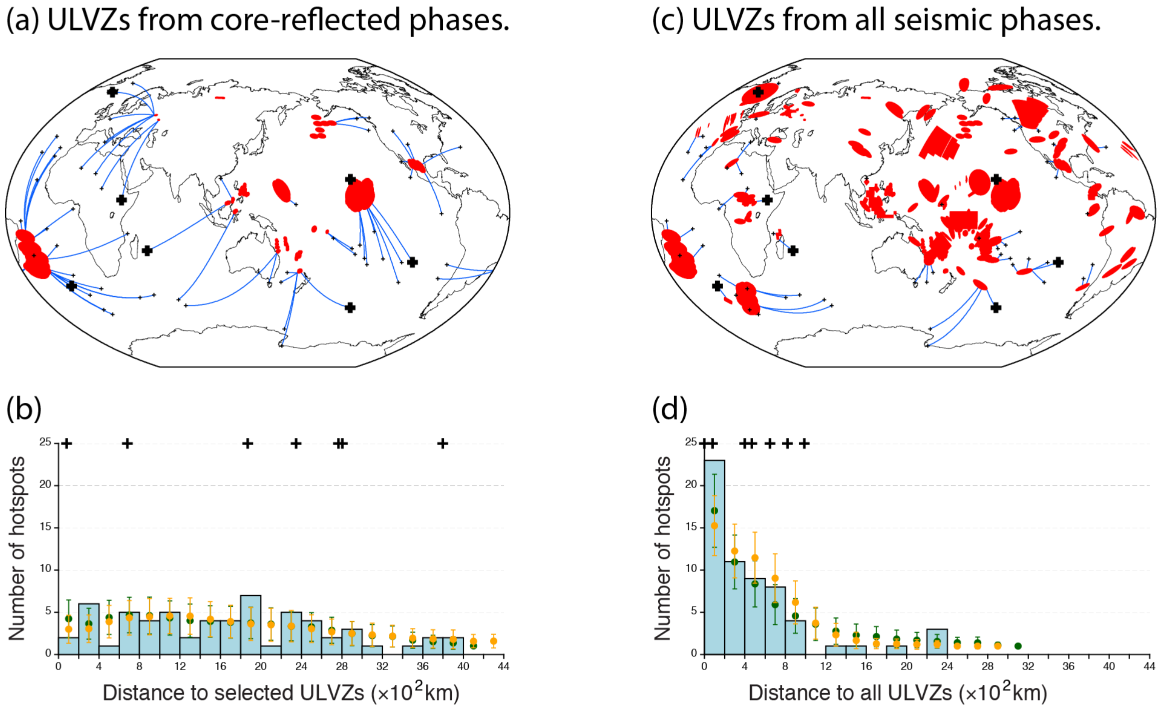

Figure 2.10. Spatial relation between surface hotspots and ULVZs. (a) and (b) are for ULVZ zones mapped using core-reflected phases (ScS, ScP and PcP). In (a), ULVZs are shown as red regions and hotspot locations are black crosses; the larger and bold crosses are the 7 hotspots noted for having possible deep plume sources [Courtillot et al., 2003]. The blue lines depict the shortest path between each hotspot and the nearest ULVZ. In (b) the number of hotspots for different distance to ULVZ bins are shown (blue histogram bars), along with the same measurements for the random ULVZ distributions of Test I (orange-filled circles, for sampling region-restricted randomly located circular shaped ULVZs) and Test II (dark green-filled circles, for random rotations of the hotspots). The distance for the 7 deep-sourced hotspots are denoted at the top as black crosses. Panels (c) and (d) are identical to (a) and (b), except computations are done using ULVZs imaged with any seismic phase, also, with the geographic domain of ULVZs in Test I is global. In this case, hotspots show a relationship to ULVZ locations, but statistical significance is not established.

CHAPTER 3

EXTREME SEISMIC VELOCITY HETEROGENEITIES AT THE CORE-MANTLE BOUNDARY BENEATH CENTRAL AMERICA

3.1 Abstract

Using seismic shear waves reflected from the CMB, we show evidence for ultra-low velocity zones (ULVZs) beneath a location of long-lived subduction (Central America and the Caribbean). In addition, a previously unreported kind of thin basal mantle structure is detected in this region, whose seismic shear wave velocities are increased by ~10% over reference values. We named these newly discovered seismic anomalies ultra-high velocity zones (UHVZs). The UHVZs and ULVZs alternate in an elongated geometry in a direction consistent with the implied convective flow direction from subduction. These observations may correspond to partial melt of subducted oceanic crust to cause the ULVZs, and some remnant of subducted crust (e.g., solid calcium perovskite residue) to give rise to the UHVZs. Geodynamic simulations show two compositionally distinct components can spatially segregate along the CMB in a manner that matches the seismic observations. These results highlight large-scale present-day chemical cycles within the planet, which may have been operating over much of Earth's history.

3.2 Introduction

Seismological studies have identified isolated zones with anomalous seismic wave speed reductions at Earth's core-mantle boundary (CMB), called ultra-low velocity zones (ULVZs). The ULVZs are often explained by either partial melting or a distinct composition, or both. In particular, ULVZs in relatively cold regions beneath subduction may require a compositionally distinct origin. However, the origin of compositional heterogeneities and their links with seismic anomalies in the lowermost mantle remain unclear. If subducted oceanic crust reaches the core-mantle boundary (CMB) and has different seismic properties from the surrounding mantle, it should be seismically detectable. For a more detailed introduction of ULVZs, see section 1.3.5.

We investigate the seismic structure of the deepest mantle beneath Central America and the surrounding region. This region is unique for several reasons: (1) it is a place on Earth with clear seismic evidence for subduction of former oceanic lithosphere to reach the lower mantle [Grand et al., 1997; Li et al., 2008]; (2) it is expected to be relatively cool because of the descending cold lithosphere, thus, if ULVZs are found there, it supports them being compositionally distinct from the background mantle; (3) the abundance of strong and deep South American earthquakes recorded at dense North American seismic networks afford excellent sampling of the CMB in this study area using core-reflected S waves; and (4) some ULVZ evidence has been found near this study region using different seismic wave types and event-station geometries [Revenaugh and Meyer, 1997; Niu and Wen, 2001; Thorne and Garnero, 2004]. On the other hand, non-detections are also reported [Mori and Helmberger, 1995; Castle and Van Der Hilst, 2000; Persh et al., 2001; Avants et al., 2006; Hutko et al., 2009]. Therefore, corroborating this with core-reflected waves is important.

Using an ScS stripping method [Zhao et al., 2017], we show seismic evidence for ULVZs beneath Central America. In addition, a previously unreported kind of thin basal mantle structure is also detected. Because their S-wave velocities are increased by over 10% (relative to PREM), therefore they are named as ultra-high velocity zones (UHVZs). The two structures are spatially adjacent to each other. Higher dimension synthetics are designed to benchmark the validity of our modeling method and the seismic structure spatial pattern in our result. The nature of this region indicates a subduction-related origin for both seismic structures co-existing in the neighborhood of each other.

3.3 Method

A forward modeling scheme is adopted in this study. For different mantle basal layer structures, synthetic seismograms are calculated. The synthetic waveforms are then processed in the same way as data. The seismic structure of the study region is constrained by comparing the data waveforms to synthetic waveforms. This section introduces the method we process the ScS waveform before the comparison.

3.3.1 Waveform Distortion for a 1D Heterogenous Layer

We use the reflectivity method [Fuchs and Müller, 1971; Müller, 1985] to calculate synthetic waveforms (calculation details are provided in Appendix A). 1D basal layers with velocity and density perturbations were added to the mantle side of the reference model Preliminary Reference Earth Model (PREM, [Dziewoński and Anderson, 1981]) to simulate 1D seismic anomalies. Two additional seismic arrivals adjacent to ScS were observed (Figure 3.1 and 3.2): a pre-cursor (SdS) reflects off the layer top side, and a post-cursor (ScscS) originates from internal multi-reflections within the layer. For a ULVZ model (Figure 3.1), due to the S-wave velocity drop at the top of the layer, the pre-cursor (SdS) has an opposite polarity compared to ScS, while the post-cursor (ScscS) has the same polarity as ScS. In addition, the ScS ray path has two more segments within the 1D layer compared to SdS, and similarly, the ScscS ray path has two more segments within the 1D layer compared to ScS. This similarity of ray path length difference causes ScscS to arrive after ScS almost the same amount as SdS arrives ahead of ScS. The opposite polarity and equally spaced arrival form an antisymmetric pattern for SdS and ScscS around the main arrival ScS, which inspired a new data processing procedure called the Flip-Reverse-Sum (FRS, [Zhao et al., 2017]).

For a UHVZ model (Figure 3.2), this anti-symmetric pattern holds for small receiver distances. For large receiver distances, the high velocity layer will cause ScS to undergo total reflection. If the receiver is at 55˚ (Figure 3.2a), the pre-cursor (SdS) and post-cursor (ScscS) behaves similarly to the ULVZ case (with polarity flipped). When receiver is positioned at 65˚, the top-side reflection is close to a total reflection, and its travel time is similar to that of ScS (Figure 3.2b). The post-cursor is delayed relative to ScS only by 1.5 second and becomes unobservable. Therefore, as the distance increases, the anti-symmetric pattern will disappear. When receiver is at 75˚ (Figure 3.2c), the ScS distortion mainly comes from a phase-shift introduced at the top-side reflection. However, as we will discuss in the next section, the FRS procedure still produces a distinguishable FRS trace from ULVZ or PREM.

3.3.2 FRS Operation

To utilize the anti-symmetric pattern of ScS distortion brought by a 1D anomalous layer, a new data processing method is proposed in [Zhao et al., 2017] called the Flip-Reverse-Sum (FRS, Figure 3.3). The waveform is cut in half at the peak of ScS, and the left portion (containing pre-cursor SdS) is polarity-flipped and time-reversed, then it is summed to the right portion (containing post-cursor ScscS). The result is a simple pulse combining the amplitudes of both additional arrivals, which is named FRS trace. For a ULVZ, the FRS trace has positive polarity (bottom trace in Figure 3.3a), and for a UHVZ, the FRS trace has negative polarity (bottom trace in Figure 3.3b), compared to PREM, where the FRS trace is a flat line (cyan traces in Figure3.3a-b).

The major advantage of FRS operation is enhancing the anomalous signal generated by a 1D anomalous layer (the additional arrivals of ScS). The additional arrivals usually have much smaller amplitude compared to ScS, and they usually are too close to ScS to be observed. After FRS operation, however, the ScS is stripped away from the waveform, all that remains is anomalous signal. Moreover, the anomalous signal amplitude is doubled by combining the pre-cursor and post-cursor. In terms of signal to noise ratio, the FRS operation is important for observing subtle structural features at the CMB. Because of the boosted signal in the FRS trace, we use them in modeling, instead of the original distorted ScS waveform.

One prerequisite for FRS operation is that the ScS arrival must to be symmetric. An asymmetric ScS arrival undergoing FRS treatment will be partially stripped from the waveform, and whatever remains will be falsely interpreted as signal generated by CMB structure. For real data, the event source time function is the major contributor to ScS asymmetry. We addressed this issue by equalizing the event source time functions using deconvolution, which will be discussed in the Data section.

3.3.2.1 FRS Trace Variation Case Study

The amplitude and timing of the FRS traces are indicative of the 1D layer properties at the CMB. Here we use synthetics to show how ScS distortions and FRS traces vary through different layer properties. From seismic ray theory, the amplitudes of the reflection or refraction energy depend on material impedance contrast and ray path incident angle. For ULVZs, generally speaking, larger property contrasts and larger receiver distances give larger FRS amplitudes (Figure 3.4a, c and d). The travel times of the additional phases are sensitive to ray path length as well as S-wave velocity. In other words, the ULVZ thickness and the S-wave speed anomaly controls the FRS pulse timing (Figure 3.4a, b). P-wave speed has no effects on ScS distortions (Figure 3.4f), therefore P-wave speed is not constraint in this study. Finally, we explored how a gradient velocity layer affect FRS traces (Figure 3.4f). The main difference between a gradient model and a velocity contrast model is the timing of the FRS peak. However, when the velocity gradient within the layer is mild enough (<0.5% per km), FRS amplitude is also lowered (comparing black and gray traces in Figure 3.4f).

For UHVZ models, ScS distortions and FRS traces for different cases are shown in Figure 3.5. To the first order, the FRS traces from UHVZ models differ from ULVZ FRS traces in polarity. For a given UHVZ model, as the receiver distance increases, the FRS amplitude increases before the receiver distance reaches the critical distance (which is about 60° for the example in Figure 3.5d). As the receiver distance approaches the critical distance, the FRS amplitude quickly diminishes, and then gradually recovers (Figure 3.5d). The mechanism for ScS distortion switches from multipathing to phase shift when receiver distance crosses over the critical distance. Due to this mechanism switch, the FRS amplitude and timing variations with respect to velocity contrast are not as obvious as for ULVZ counterpart (Figure 3.5a). The changes in UHVZ thickness slightly modify FRS pulse timing, but with a more severe effect on its amplitude (Figure 3.5b). Effects of density increase are opposite to the ULVZ counterpart: a denser layer lowers FRS pulse amplitude (Figure 3.5c). Similar to ULVZ, P-wave velocity doesn't affect ScS distortion (Figure 3.5e), and a gradient velocity layer affects FRS amplitude (Figure 3.5f).

3.3.2.2 FRS Amplitude-Distance Trend

As mentioned above, for a given 1D layering model, receivers at larger distance have larger FRS amplitudes (Figure 3.5d). Real data are recorded at different distances. Therefore, to recover the earth's structure, the receiver distance effect on FRS amplitude must be removed, such that the FRS pulse depends solely on structure properties. We observe that the timings of FRS pulses don't change much for different distances (Figure. 3.4d and Figure 3.5d). Therefore, we believe properly re-scaling the FRS traces (both data and synthetics) in amplitude will be a correct way to remove this trend.

To study the FRS amplitude distance trend, FRS amplitudes of synthetics at different distances are measured. Measurements for some ULVZ models are shown in Figure 3.6 as green dots. A moving average window (width 3˚) is applied to the trend to smooth out measurement errors.

As illustrated in Figure 3.6, the FRS amplitude-distance trend varies through different models. Therefore, we designed a model-based modeling procedure: when comparing data against a given model, the trend for this model is first obtained, then data and synthetics FRS traces are both re-scaled to a reference distance. The average receiver distance of data is used as this reference distance.

3.4 Data Processing

3.4.1 Data Collection and Selection

We collected transverse component seismic records via SOD [Owens et al., 2004] from IRIS data service for south America large (m>=5.7) and deep events (>=100 km) between 2006 and 2016. Deep events have less interference from the depth phases and large events have higher signal to noise ratio. The receivers were in North America with epicenter distances between 45° and 85° (Figure 3.7a-b). 61,480 displacement records of 91 events from IRIS DMC and CNDC data center are received. We keep events have simple source time functions as well as sufficient records with clear S and ScS arrivals. In total, 11,117 records from 58 events were used in this study (Figure 3.7a and Table 1). We then pre-processed the records with instrument response removal and a 2-pass Butterworth filter with corner frequency between 0.0333 Hz and 0.3 Hz. Data profiles for several events are shown in Figure 3.8.

3.4.2 Receiver Distance Correction

Because synthetic waveforms are calculated for a source depth of 500 km, a corrected great circle distance for each event-station pair is calculated by virtually moving event source depths to 500 km along predicted ScS ray paths (Figure 3.9). The great circle distance after the correction is used for FRS amplitude re-scaling. For event sources shallower than 500 km, the corrected distances are less than the original distances and vice versa.

3.4.3 Constructing Empirical Source Wavelet

As mentioned in FRS procedure section, one prerequisite for FRS operation is ScS needs to be symmetric (i.e. without source time function). The records are pre-processed to meet this prerequisite by deconvolving with empirical source time function.

Empirical source wavelets (ESW) for each event are constructed by adaptively stacking the corresponding records of these phases (S and ScS) [e.g. Helmberger and Wiggins, 1971; Rawlinson and Kennett, 2004]. Records are first aligned along PREM predicted arrivals and stacked. An arrival time anchor is hand-picked on the stack and then each record is cross correlated with the stack and its arrival are updated. This procedure is repeated several times, each time starts with the updated arrival alignment. The final stacks (Figure 3.10, black and green traces) become empirical wavelets, as descriptions of the general waveforms of S and ScS phases of each event. The weighting scheme for the stacking is as follows. A cross-correlation coefficient (CCC) between record and stack is calculated within the -5 ~ 15 second window centered on their own arrivals. A signal-to-noise ratio (SNR) is measured on the enveloped trace (calculated by Hilbert transform). The noise window is 2-minutes long and 1-minute ahead of S arrival, and the signal window is 10-seconds long and centered on S or ScS peak. The stack weight is the multiple of CCC and the result of a ramp function on SNR.

The waveform within a -30 ~ 30 second time window around the S-wave ESW peak are cut out and further stretched/shrunk to generate the empirical source time function for deconvolution (dashed red lines in Figure 3.10). A properly stretched/shrunk S-wave ESW is a good approximation of the event source time function and will also stabilized the deconvolution. The proper stretch or shrink is found by a grid search through the horizontal stretching/shrinking factor (with step size 0.01). In each grid step, the waveforms above a quarter peak amplitude from modified S-wave ESW and ScS-wave ESW are compared (Figure 3.10), and the minimum waveform difference indicates the modification needed.

3.4.4 Deconvolution

All ScS waveforms are cut between the time window 100 seconds ahead and after ScS peaks. 30-second and 10-second Hanning tapers are applied to ScS waveforms and the S empirical source time function. Then all signals are padded with zeros, evenly at both ends, to 400 seconds (Figure 3.11a). The padding has two purposes: (a) eliminate the deconvolution wrapping around phenomenon and (b) validating frequency domain division.

Water-level deconvolution [Clayton and Wiggins, 1976] is used to equalize different sources from event to event. We use $\mathcal{F}$ and $\mathcal{F}^{-1}$ to represent Fourier transform and inverse Fourier transform in Eq. (3.1-3.5). This procedure is as follows. First, ScS waveforms ($w(t)$ term in Eq. 3.1) and the S empirical source time function ($s(t)$ term in Eq. 3.1) of a given event are taken to frequency domain ($W(\omega)$ and $S(\omega)$ terms in Eq. 3.1; their amplitudes are plotted in black and red lines in Figure 3.11d). For the S empirical source time function spectrum, frequencies with low amplitudes are filled to a certain water-level (blue lines in Figure 3.11d, shorten as wl in Eq. 3.2), and their phases are kept unchanged (Eq. 3.2). The water-level for each event is 0.1 times the maximum amplitudes of its S empirical source time function spectrum (Eq. 3.3). Finally, the spectrums of every ScS waveforms are divided by the water-filled S empirical source time function spectrum (Eq. 3.4, the amplitudes of the division results are plotted in black lines in Figure 3.11e), and an inverse Fourier transform is carried out for the results to take signals back to time domain (Eq. 3.5, Figure 3.11b).

$$\begin{gathered} W(\omega) = \mathcal{F}(w(t)) \\ S(\omega) = \mathcal{F}(\mathrm{s}(t)) \end{gathered} \tag{3.1}$$

$$S'(\omega) = \begin{cases} \mathrm{wl} & \text{if } |S(\omega)| = 0 \\ \mathrm{wl} * e^{\arg(S(\omega))} & \text{if } |S(\omega)| < \mathrm{wl} \\ S(\omega) & \text{if } |S(\omega)| \geq \mathrm{wl} \end{cases} \tag{3.2}$$

$$\mathrm{wl} = 0.1 * \max_{\omega} |S(\omega)| \tag{3.3}$$

$$D(\omega) = \frac{W(\omega)}{S'(\omega)} \tag{3.4}$$

$$d(t) = \mathcal{F}^{-1}(D(\omega)) \tag{3.5}$$

A frequent issue in frequency domain division is that the amplitudes at both ends of the spectrum are usually enhanced. The usual way to dealt with this issue is adding a post-processing to the result of frequency domain division, which can be a band-pass filter, or what we adopted here, a high pass-filter with a gaussian smooth (Figure 3.12). The high pass filter is cornered at 0.03 Hz and the Gaussian smoothing has σ=1.274, at which its half-height width is three seconds.

In summary, three parameters control the deconvolution: the water-level, the gaussian smoothing width and the high-pass filter corner frequency in the post-processing. Our choice is empirical: water-level parameter equals 0.1, gaussian smoothing half-height width equals 3 sec and high-pass filter is cornered at 0.03 Hz. The effects of varying each one of the parameters are shown in Figure 3.13. Our choice (as a reference case) is colored in red.

3.4.5 Bin Stacking

To enhance coherent signals, FRS traces are geographically bin stacked according to their ScS bouncing locations on the CMB. Bins have radius of 1.5° and bin centers are separated by 2° (Figure 3.14a). For each bin, an averaged location of its bouncing points is calculated (green crosses in Figure 3.14b) as a shifted bin center. After modeling, the best fit model for a given bin will be assigned to its averaged location.

Two weights are combined as the bin stacking weight. The first weight (*w*) is a gaussian cap based on distance between record's bouncing point and the bin's shifted bin center. The gaussian function is chosen such that when the sampling point is 1.5° (1 bin radius) away from the shifted bin center, the weight (*w*) is 0.5 (Figure 3.15c). This weight is fixed for each record when stacking for a certain bin.

The second weight (*v*) is decided by data noise level and additional arrival amplitudes on synthetic waveforms. Figure 3.15 shows the weight calculation for a record (event #33, station 336A) stacking within bin 132, which is modeling against a ULVZ model with properties: H=30 km, dVs=-15%. Firstly, the data noise level is measured as the ratio between ScS peak amplitude and data maximum amplitude within a noise window (Figure 3.15a). The noise window starts at three minutes ahead S arrival and has a window length of two minutes. This ratio is then mapped to a weight (*v*) using a ramp function (Figure 3.15b, lower panel). The upper bound of the ramp function is decided by the FRS amplitude, at the data great circle distance, of current comparing model (Figure 3.15b, upper panel). Therefore, this weight is dynamic when each record is modeling against different models. The multiplication of the two weights (*w*v*) is the bin stacking weight for this record, when this certain bin is modeled against a certain model.

3.4.6 FRS Re-scaling

As discussed in section 3.3.2.2, before stacking the FRS from a certain bin and modeling against a certain model, the FRS traces need to be amplitude re-scaled to correct the FRS amplitude-distance trend of that model. We introduce a scaling factor *f* for each record as the ratio between FRS amplitude at the reference distance and at the record distance. Figure 3.16 shows an example of calculating *f* when stacking a 70.04° record in bin 100 and modeling against a ULVZ model (H=15 km, dVs=-10%). One thing to notice is that when data FRS traces are amplitude re-scaled, the noise they carried is also re-scaled. The stacking scheme can be written in equations for clarity. Let subscript i, j and *k* represent a certain record, a certain bin and a certain model. Let S_i be the FRS trace of the given record, $S'_{i,k}$ be the synthetic FRS trace at the same distance as the given record from the given model. Let the data stack of the given bin when modeling against the given mode be $X_{j,k}$ and synthetics stack be $Y_{j,k}$. Then they can be represented as Eq. (3.7) and Eq. (3.8). The matching quality between $X_{j,k}$ and $Y_{j,k}$ indicates how well model *k* fits bin *j*'s location.

$$X_{j,k} = \frac{\sum_{i\in\, Bin\ j} w_{i,j} v_{i,k} f_{i,j,k} S_i}{\sum_{i\in\, Bin\ j} \frac{w_{i,j} v_{i,k}}{f_{i,j,k}}} \tag{3.7}$$

$$Y_{j,k} = \frac{\sum_{i\in\, Bin\ j} w_{i,j} v_{i,k} f_{i,j,k} S'_{i,k}}{\sum_{i\in\, Bin\ j} \frac{w_{i,j} v_{i,k}}{f_{i,j,k}}} \tag{3.8}$$

3.4.7 Comparison Quality and Modeling Confidence

Once the data FRS stack ($X_{j,k}$ in Eq. 3.7) and the synthetics stack ($Y_{j,k}$ in Eq. 3.8) are constructed, a comparison quality is calculated to indicate how well these two traces are similar to each other, and therefore, a measurement how well the given bin (indexed by subscript j) and the given model (indexed by subscript k) fit each other. The comparison quality is defined as the multiple of amplitude-corrected correlation coefficient and the norm-2 difference between data stack and synthetics stack (Eq. 3.9-3.12, its value range is fixed to [0,1] with 1 means a perfect fit). We further defined the confidence of the modeling result of a given bin using the comparison quality difference between its best fit model and PREM. If the best fit model renders a comparison quality larger than that of PREM by 0.3, the bin is considered significantly different from PREM and is well-constrained.

$$E_{data} = \sqrt{\int X_{j,k}^{2}(t)dt} \quad , \quad E_{syn} = \sqrt{\int Y_{j,k}^{2}(t)dt}$$

$$E_{diff} = \sqrt{\int [X_{j,k}(t) - Y_{j,k}(t)]^{2} dt} \tag{3.9}$$

$$CC = \frac{\sqrt{\int [X_{j,k}(t) Y_{j,k}(t)] dt}}{E_{data} * E_{syn}} * \frac{\min{(E_{data}, E_{syn})}}{\max{(E_{data}, E_{syn})}}$$

$$\mathrm{N2} = \frac{E_{diff}}{E_{data}} \tag{3.10}$$

$$\mathrm{CQ} = \frac{1 + CC}{2} * \frac{1}{1 + N2} \tag{3.11}$$

3.5 Results

3.5.1 Structure beneath Central America

For the 7620 considered 1D models, the best-fitting models for each bin are presented in Figure 3.17 (see Appendix A for model space details). A large number of bins do not have a single model that well explains the observed FRS stacks markedly different from the PREM model. These bins are colored grey-green in Figure 3.17a.

These are commonly low amplitude FRS stacks. Bins explained by UHVZ models are more common than those fit with ULVZ models (Figure 3.17b), and they are regionally grouped. ULVZ bins are similarly clustered. The UHVZ region and ULVZ forming an alternating pattern. The properties of best-fit UHVZ and ULVZ models are widely ranging (Figure. 3.17c), with ULVZ properties similar to those presented in past studies. Trade-offs between layer thickness and velocity perturbation are presented in Figure 3.18. Each enclosed region represents the properties range of the top five best fitting models of each bin. Generally speaking, a larger velocity perturbation model with a thinner layer thickness fits the data equally well. The confidently modeled UHVZ bins have thickness around 25 to 30 km with increased S-wave velocity perturbation around several percent.

3.5.2 1D Synthetics Pseudo Dataset Benchmark

To demonstrate the correctness and find out the detection limitation of our data-processing method and modeling procedure, a record by record replica of the dataset (a pseudo dataset) is generated using 1D synthetic seismograms calculated by reflectivity method. We picked three input seismic structures: PREM (no seismically anomalous layer), a ULVZ layer (20 km, -20% dVs) and a UHVZ layer (20 km, $+10\%$ dVs). The synthetics are calculated by putting the source depth at each event depth. We then hand-picked the correct receiver distances from the synthetics to assemble the pseudo dataset event by event. Finally, the pseudo dataset is processed and modeled in the exact same way as the real data. The modeling results for these three models are shown in Figure 3.19. For the ULVZ input model, all bins identified it as ULVZ (Figure 3.19a); the best fit models for each bin forms a curved line around 20 km, -20% dVs (Figure 3.19b).

This curved line represents the trade-offs between layer thickness and velocity reduction in our modeling procedure. For the UHVZ input model, all bins also identified it as UHVZ (Figure 3.19c); the best fit models clustered around 20 km, $+10\%$ dVs (Figure 3.19d). However, the trade-off between layer thickness and velocity increase is not as clear as that of ULVZs. The PREM input model, compared to ULVZ and UHVZ input models, is not well recovered (Figure 3.19e-f). The data stack amplitude is very small when the input model is PREM, but the comparison coefficient is still significantly large. A possible reason is the stack process creates some random waveform shapes which happens to look like a ULVZ or UHVZ signal. The maximum FRS amplitude for the PREM result is 0.025 from Bin 32. We adopted this value as additional stack amplitude threshold (as a detection limitation). Bins with maximum data stack amplitude less than 0.025 will be regarded as non-significant.

3.5.3 High Dimension Synthetics Pseudo Dataset Benchmark

The grouping and locations of UHVZ and ULVZ zones in our study area (dashed regions in Figure 3.17a) implicate CMB anomalies more complex than a 1D layer, but with a clear trend of UHVZ structures interspersed with ULVZs. We designed a 2.5 D synthetics benchmark using package SHAXI [Jahnke et al., 2008] (see Appendix B for synthetics calculation details). Our method is inspired by an 1D CMB layer anomaly multipathing patterns. Therefore, the purpose of this benchmark is to see if a 3D structure in a similar geometry can be correctly resolved using this method. SHAXI is a finite difference seismic wave propagation simulation program. User input is a 2D velocity structure on a great circle plane (Figure 3.20a), then the program will rotate the input structure and solve wave equations in the resulting axisymmetric 3D model (Figure 3.20b), hence the name 2.5D.

The pseudo dataset is replicated by the synthetics in a record by record manner, similar to the 1D benchmark. For each event in the dataset, the according synthetic run has the same source depth. Receivers are put at the same distances as each record. This same event-receiver geometry can generate similar phase arrival times as the data, which can minimize traffic phase effects. After the synthetics are calculated for each receiver, we process this pseudo dataset the same way as the real data. One slight change in this benchmark is we mask the sS phase in each seismogram. Due to surface boundary condition and source mechanism in SHAXI, the traffic phase sS has high amplitude in synthetic seismograms and can't be suppressed during the calculation. Therefore, before making empirical source time function of ScS, the S wave empirical wavelet is cross correlated with waveform around predicted sS arrival time, and then subtracted from it at the best fitting position to mask sS phase.

For the input structure, we combine the nature of 2.5D of SHAXI and the spatial distribution of detected ULVZ/UHVZ regions. Our benchmark input structure is based on structures along a southeast to northwest cross-section (AA' in Figure 3.21a and b). Several choices including the structure thickness (30 km), S-wave velocity perturbation ($\pm 10\%$) and structure width (4.5° and 8° on the CMB) roughly represent the modeling results on this cross-section. In real data, the distances between each event and the Central America region varies. Therefore, for each run, the 2D input structure are shifted in distance by a certain amount so that the input structures roughly represent the velocity anomaly at the same geographic spot. An averaged S-wave perturbation map is calculated after axis rotation (Figure 3.21c). This equivalent 3D structure looks alike the ULVZ and UHVZ spatial distribution in the detections result (Figure 3.17) and will be the structure our method intended to recover in the benchmark.

The resolved structures are shown in Figure 3.22, which is colored similarly to Figure 3.17. As shown in Figure 3.22a, the UHVZ region in the center is successfully recovered. If the low amplitude stacks from bin 8 and 14 are deemed as insignificant (Figure 3.22b), then the recovered UHVZ bin locations are roughly consistent with the 8°-wide UHVZ in the input structures. The southeast UHVZ region is roughly recovered by bins 45 and 46. In contrast, the ULVZ region are not well recovered. Only the eastern-most two bins (bin 27 and 28) are identified as ULVZ structure. Two bins in the most northwest suggest ULVZ (bins 2 and 6), where there was no structure in the input model. However, their bin stacks have low amplitudes, and their best fit models have properties close to PREM (see Figure 3.22 b and c). Therefore, this part of the structure is believed to be reasonably recovered.

In summary, the 2.5D benchmark result suggest our 1D method works generally well on the input structure. The failed recovery of main ULVZ regions could be due to the event azimuth differences relative to the 3D structure. When different events have different azimuths relative to the structure, the direction of the rotation axis in SHAXI differs. The averaged input structure, however, can't show this spatial smoothing effect. To conduct a full 3D benchmark, a feasible (fast) synthetics calculation package is needed. Nevertheless, the waveform distortion observation is robust. Due to the imperfect recovery results, we will emphasize our results on the discovery of the UHVZs, rather than modelled structure morphologies or properties.

3.6 Discussion

3.6.1 Density Effects and Trade-Offs

As stated in section 3.3.2.1 and shown in Figure 3.4 and 3.5, when the density of the anomalous layer is increased, the amplitude of FRS traces for ULVZs will also increase, while amplitudes of FRS traces for UHVZs will decrease. This adds a new dimension to the existing thickness-dVs trade-off. From Figure 3.17c, ULVZs are predominantly to be fit with models whose density are increased. This is consistent with previous ULVZ detections. However, due to a suspected more dominant effects from 3D structures, density (and other properties) are deemed not well constrained.

3.6.2 Possible Origins of Observations

To explain the larger than 10% S wave velocity increase in detected UHVZs, chemical heterogeneities are needed. Using Burnman package [Cottaar et al., 2014] and SLB2011 dataset [Stixrude and Lithgow-Bertelloni, 2011], seismic properties of several mineral phases are calculated under pressure temperature conditions of base mantle (135 GPa and 4500 K, Figure 3.23). The high velocities and density of calcium perovskite (CaPv, blue color in Figure 3.23) makes it a candidate for UHVZs. Recent MORB melting experiments suggest CaPv could be the last remaining solid phase [Andrault et al., 2014; Pradhan et al., 2015]. Combined with the subduction history of this particular region, a possible scenario for the coexistence of ULVZs and UHVZs is partial melting of subducted oceanic crust, with possible Fe-enriched partial melt explaining ULVZs and solid melt residues explaining UHVZs (Figure 3.24a). A recent CaPv high pressure study, however, suggest titanium enriched CaPv is predicted to have low seismic velocity [Thomson et al., 2019]. An alternative candidate for UHVZ is free silica (SiO_2, seifertite, brown color in Figure 3.23), whose predicted velocity increase is not as large as CaPv, but its predicted increased density fits our modeling results. More importantly, the existence of free silica will consume low seismic velocity phases such as ferropericlase, and therefore SiO_2 enriched regions have the potential to be high velocity. The origin of free silica could be oceanic sediments brought down to the CMB by subductions or core exsolution process [Helffrich et al., 2018] (Figure 3.24b).

3.7 Conclusion

In this study, we show seismic evidence for extreme velocity heterogeneities exist near the core-mantle boundary beneath the Central America. Ultra-high velocity zones (UHVZs) are discovered coexisting with nearby ultra-low velocity zones (ULVZs). Full 3D waveform modeling is required if structure properties and morphologies are to be constrained, but the detections are robust. Combined with the subduction history in this region, a possible explanation for observed seismic structures distribution is that partial melt of subducted oceanic crust causes the ULVZs, and solid melt residue gives rise to the UHVZs.

Acknowledgement

We thank Incorporated Research Institutions for Seismology (IRIS) Data Management Center for making the seismic data available. We thank NSF’s EarthScope program that hosts and maintain the Transportable Array project, which provides the high quality, high density seismic data we used in this research. This study is funded by National Science Foundation (NSF) NSF-1161038, NSF-1853911.

References

Andrault, D., G. Pesce, M. A. Bouhifd, N. Bolfan-Casanova, J. M. Henot, and M. Mezouar (2014), Melting of subducted basalt at the core-mantle boundary, Science, 344(6186), 892–895, doi:10.1126/science.1250466.

Avants, M., T. Lay, and E. J. Garnero (2006), A new probe of ULVZ S-wave velocity structure: Array stacking of ScS waveforms, Geophysical Research Letters, 33(7), 297, doi:10.1029/2005GL024989.

Castle, J. C., and R. D. Van Der Hilst (2000), The core–mantle boundary under the Gulf of Alaska: no ULVZ for shear waves, Earth and Planetary Science Letters, 176(3-4), 311–321, doi:10.1016/S0012-821X(00)00027-3.

Clayton, R. W., and R. A. Wiggins (1976), Source shape estimation and deconvolution of teleseismic body waves, Geophysical Journal of the Royal Astronomical Society, 47(1), 151–177, doi:10.1111/j.1365-246X.1976.tb01267.x.

Cottaar, S., T. Heister, I. Rose, and C. Unterborn (2014), BurnMan: A lower mantle mineral physics toolkit, Geochem. Geophys. Geosyst., 15(4), 1164–1179, doi:10.1002/2013gc005122.

Dziewoński, A. M., and D. L. Anderson (1981), Preliminary reference Earth model, Physics of the earth and planetary interiors, 25(4), 297–356, doi: 10.1016/0031-9201(81)90046-7.

Fuchs, K., and G. Muller (1971), Computation of Synthetic Seismograms with the Reflectivity Method and Comparison with Observations, Geophysical Journal of the Royal Astronomical Society, 23(4), 417–433, doi:10.1111/j.1365-246X.1971.tb01834.x.

Grand, S. P., R. D. Van Der Hilst, and S. Widiyantoro (1997), Global seismic tomography: A snapshot of convection in the earth, GSA Today, 7(4).

Helffrich, G., M. D. Ballmer, and K. Hirose (2018), Core-Exsolved SiO 2Dispersal in the Earth's Mantle, J. Geophys. Res. Solid Earth, 123(1), 176–188, doi:10.1002/2017JB014865.

Helmberger, D., and R. A. Wiggins (1971), Upper mantle structure of midwestern United States, Journal of Geophysical Research: Solid Earth (1978–2012), 76(14), 3229–3245, doi:10.1029/JB076i014p03229.

Hutko, A. R., T. Lay, and J. Revenaugh (2009), Localized double-array stacking analysis of PcP: D″ and ULVZ structure beneath the Cocos plate, Mexico, central Pacific, and north Pacific, Physics of the earth and planetary interiors, 173(1-2), 60 – 74, doi:10.1016/j.pepi.2008.11.003.

Jahnke, G., M. S. Thorne, A. Cochard, and H. Igel (2008), Global SH-wave propagation using a parallel axisymmetric spherical finite-difference scheme: application to whole mantle scattering, Geophys J Int, 173(3), 815–826, doi:10.1111/j.1365-246X.2008.03744.x.

Li, C., R. D. van der Hilst, E. R. Engdahl, and S. Burdick (2008), A new global model for P-wave speed variations in Earth's mantle, Geochem. Geophys. Geosyst., 9(5), n/a–n/a, doi:10.1029/2007GC001806.

Mori, J., and D. V. Helmberger (1995), Localized boundary layer below the mid ‐ Pacific velocity anomaly identified from a PcP precursor, Journal of Geophysical Research: Solid Earth (1978 ‐ 2012), 100(B10), 20359 ‐ 20365, doi:10.1029/95JB02243.

Müller, G. (1985), The reflectivity method: a tutorial, Journal of Geophysics, 58(1-3), 153–174.

Niu, F., and L. Wen (2001), Strong seismic scatterers near the core ‐ mantle boundary west of Mexico, Geophysical Research Letters, 28(18), 3557 ‐ 3560, doi:10.1029/2001GL013270.

Owens, T. J., H. P. Crotwell, C. Groves, and P. Oliver-Paul (2004), SOD: STANDING ORDER FOR DATA, Seismological Research Letters, 75(4), 515–520, doi:10.1785/gssrl.75.4.515-a.

Persh, S. E., J. E. Vidale, and P. S. Earle (2001), Absence of Short ‐ Period ULVZ Precursors to PcP and ScP from two Regions of the CMB, Geophysical Research Letters, 28(2), 387 ‐ 390, doi:10.1029/2000GL011607.

Pradhan, G. K., G. Fiquet, J. Siebert, A.-L. Auzende, G. Morard, D. Antonangeli, and G. Garbarino (2015), Earth and Planetary Science Letters, Earth and Planetary Science Letters, 431(C), 247–255, doi:10.1016/j.epsl.2015.09.034.

Rawlinson, N., and B. L. N. Kennett (2004), Rapid estimation of relative and absolute delay times across a network by adaptive stacking, Geophys J Int, 157(1), 332–340, doi:10.1111/j.1365-246X.2004.02188.x.

Revenaugh, J., and R. Meyer (1997), Seismic Evidence of Partial Melt Within a Possibly Ubiquitous Low-Velocity Layer at the Base of the Mantle, Science, 277(5326), 670–673, doi:10.1126/science.277.5326.670.

Stixrude, L., and C. Lithgow-Bertelloni (2011), Thermodynamics of mantle minerals - II. Phase equilibria, Geophys J Int, 184(3), 1180–1213, doi:10.1111/j.1365-246X.2010.04890.x.

Thomson, A. R., W. A. Crichton, J. P. Brodholt, I. G. Wood, N. C. Siersch, J. M. R. Muir, D. P. Dobson, and S. A. Hunt (2019), Seismic velocities of CaSiO3 perovskite can explain LLSVPs in Earth's lower mantle, Nature, 572(7771), 643–647, doi:10.1038/s41586-019-1483-x.

Thorne, M. S., and E. J. Garnero (2004), Inferences on ultralow-velocity zone structure from a global analysis of SPdKS waves, Journal of Geophysical Research, 109(B8), 421, doi:10.1029/2004JB003010.

Wiggins, R. W. C. A. R. A. (1976), Source shape estimation and deconvolution of teleseismic body waves, Geophysical Journal of the Royal Astronomical Society, 47(1), 151–177, doi:10.1111/j.1365-246X.1976.tb01267.x.

Zhao, C., E. J. Garnero, M. Li, A. McNamara, and S. Yu (2017), Intermittent and lateral varying ULVZ structure at the northeastern margin of the Pacific LLSVP, J. Geophys. Res. Solid Earth, 122(2), 1198–1220, doi:10.1002/2016JB013449.

Table 3.1 Events used in this study.

Event Num.	Date	Latitude (˚)	Longitude (˚)	Depth (km)	Magnitude (Mw)	Number of Records (after selection)
1	25 Aug. 2006	-24.4	-67.03	184	6.6	118
2	22 Sep. 2006	-26.87	-63.15	598	6	32
3	23 Oct. 2006	-21.86	-65.59	262	5.8	30
4	13 Nov. 2006	-26.05	-63.28	572	6.8	81
5	25 May. 2007	-24.22	-67.03	180	5.9	134
6	12 Jul. 2007	-7.93	-74.38	152	6.1	147
7	21 Jul. 2007	-8.13	-71.27	645	6.1	405
8	21 Jul. 2007	-22.15	-65.78	290	6.4	210
9	16 Nov. 2007	-2.31	-77.84	123	6.8	553
10	18 Nov. 2007	-22.64	-66.32	246	6	199
11	16 Feb. 2008	-21.35	-68.39	130	6.1	33
12	24 Mar. 2008	-20.04	-68.96	120	6.2	45
13	08 Jul. 2008	-15.99	-71.75	123	6.2	103
14	26 Aug. 2008	-7.64	-74.38	154	6.4	182
15	03 Sep. 2008	-26.74	-63.23	570	6.3	188
16	12 Oct. 2008	-20.12	-64.97	353	6.2	417
17	12 Jul. 2009	-15.04	-70.44	199	6.1	290
18	14 Jul. 2009	-21.82	-67.09	176	5.7	58
19	05 Sep. 2009	-15.12	-70.25	210	5.8	255
20	13 Nov. 2009	-17.92	-64.09	608	5.8	178
21	14 Nov. 2009	-22.96	-66.64	220	6.2	233
22	25 Jan. 2010	-8.5	-74.47	147	5.9	89
23	28 Jan. 2010	-23.36	-66.71	208	5.9	48
24	04 Mar. 2010	-22.23	-68.33	114	6.3	131
25	24 May. 2010	-8.09	-71.56	581	6.5	237
26	12 Jul. 2010	-22.15	-68.22	115	6.3	50
27	12 Aug. 2010	-1.27	-77.31	207	7.1	243
28	13 Sep. 2010	-14.61	-70.78	180	5.9	210
29	22 Oct. 2010	-20.88	-68.37	132	5.8	90
30	01 Jan. 2011	-26.8	-63.14	577	7	282
31	06 Mar. 2011	-18.02	-69.36	118	6.3	214
32	02 Apr. 2011	-19.54	-69.01	110	5.9	76

(Continue on next page)

Table 3.1 (continued)

Event Num.	Date	Latitude (˚)	Longitude (˚)	Depth (km)	Magnitude (Mw)	Number of Records (after selection)
33	17 Apr. 2011	-27.6	-63.2	557	5.7	157
34	08 Jun. 2011	-17.08	-69.52	146	5.9	149
35	20 Jun. 2011	-21.7	-68.23	128	6.4	211
36	15 Aug. 2011	-1.81	-76.91	177	5.7	230
37	24 Aug. 2011	-7.64	-74.53	147	7	26
38	02 Sep. 2011	-28.4	-63.03	579	6.7	102
39	22 Nov. 2011	-15.36	-65.09	550	6.6	651
40	14 May. 2012	-17.68	-69.59	106	6.2	320
41	28 May. 2012	-28.04	-63.09	587	6.7	290
42	02 Jun. 2012	-22.06	-63.55	527	5.9	280
43	07 Jun. 2012	-15.88	-72.41	110	6.1	284
44	02 Aug. 2012	-8.41	-74.26	145	6.1	383
45	08 Oct. 2012	-21.73	-68.17	122	5.7	86
46	10 Nov. 2012	-8.87	-75.07	129	6	29
47	22 Nov. 2012	-22.74	-63.57	517	5.9	385
48	22 Feb. 2013	-27.93	-63.1	575	6.1	209
49	23 Aug. 2013	-22.27	-68.59	111	5.8	198
50	24 Sep. 2014	-23.8	-66.63	224	6.2	58
51	26 Oct. 2014	-10.56	-74.08	125	5.7	91
52	11 Feb. 2015	-23.11	-66.69	223	6.7	189
53	23 Mar. 2015	-18.35	-69.17	130	6.4	272
54	10 Jun. 2015	-22.4	-68.43	124	6	57
55	28 Sep. 2015	-23.8	-66.61	219	5.9	147
56	24 Nov. 2015	-10.06	-71.02	621	7.6	96
57	26 Nov. 2015	-9.18	-71.26	603	6.7	454
58	14 Jan. 2016	-19.76	-63.33	583	6.1	202

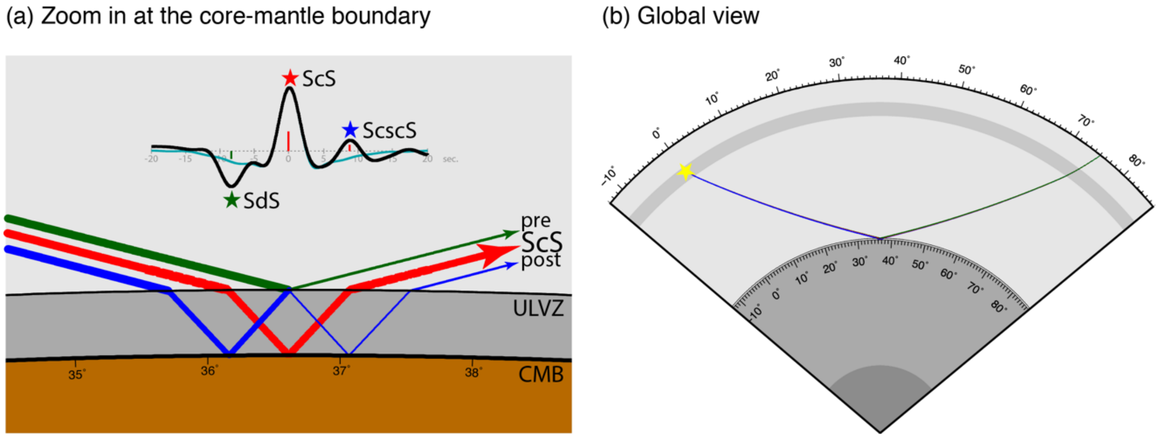

(a) Zoom in at the core-mantle boundary

(b) Global view

Figure 3.1 (a) Synthetic waveform and infinite frequency ray paths for ScS (500 km, 75˚) and its additional arrivals. The 1D ULVZ layer has property: dVs = −30%, dρ = 0%, H = 30 km. Ray paths are colored for different arrivals: ScS in red, pre-cursor (SdS) in green and post-cursor(ScscS) in blue. Pen thickness is proportional to arrival amplitudes. Ticks on the CMB denote the great circle distance from the source. Synthetic waveform of the reference model (PREM, no 1D layer) is plotted in cyan for comparison (amplitude re-scaled to ScS). Arrivals are marked by stars in the same color scheme as ray paths. The antisymmetric pattern of the two additional arrivals can be clearly observed. (b) ScS (500 km, 75˚) ray path global view. (a) is a zoom-in of (b) near the CMB.

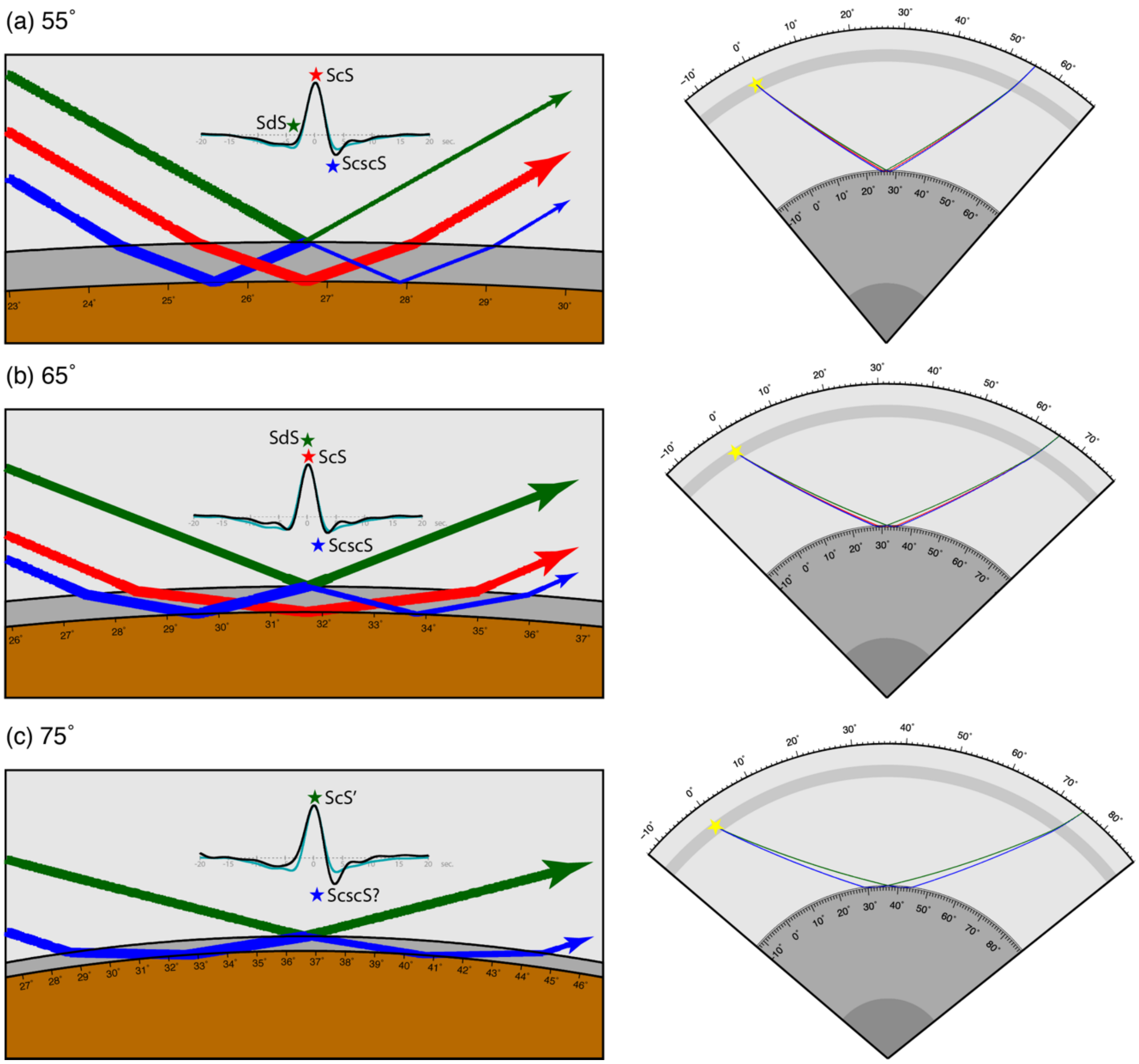
(a) 55°

(b) 65°

(c) 75°

Figure 3.2 Synthetic waveform and infinite frequency ray paths for ScS (500 km, distance varies through a-c) and its additional arrivals. The 1D UHVZ layer has property: dVs=10%, dρ=0%, H=30 km. Ray paths are colored in the same way as Figure 3.1. (a) receiver is at 55˚. The pattern is similar to that of ULVZ with observable pre-cursor (SdS) and post-cursor (ScscS). Notice the polarity of the additional arrivals are flipped, compared to ULVZ. (b) receiver is at 65˚. Ray path difference is large enough for the anti-symmetric pattern to disappear. (c) receiver is at 75˚. Due to a large incident angle, top-side reflection becomes a total reflection. ScS undergo a phase shift and post-cursor arrival becomes too close to ScS to be observed. Panels on the right-hand side show ray paths in a global view.

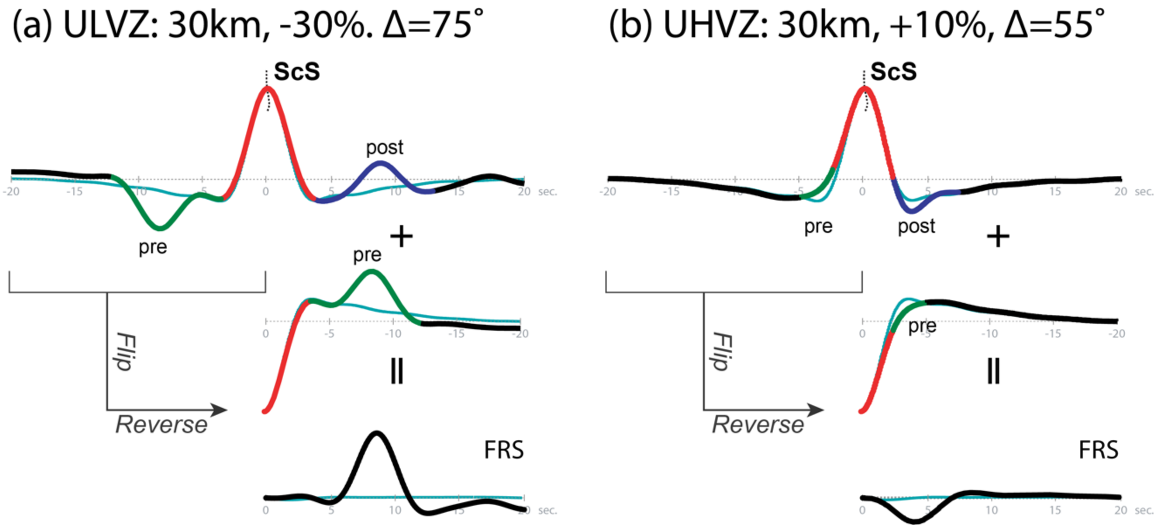

Figure 3.3 Illustration of the FRS procedure. (a). Waveform is ScS received at 75˚ from a ULVZ with H=30 km, dVs=−30%, dρ=0%. The waveform is first cut at ScS peak. Then the pre-cursor (SdS) part is flipped in polarity and reversed in time. Finally, it is summed with post-cursor (ScscS) part. (b). Similar with (a), this example comes from a UHVZ model with H=30 km, dVs=+20%, dρ=0%. The FRS-trace for a ULVZ model is a positive signal (compared to FRS-trace of PREM, cyan), the FRS-trace for a UHVZ model is a negative signal.

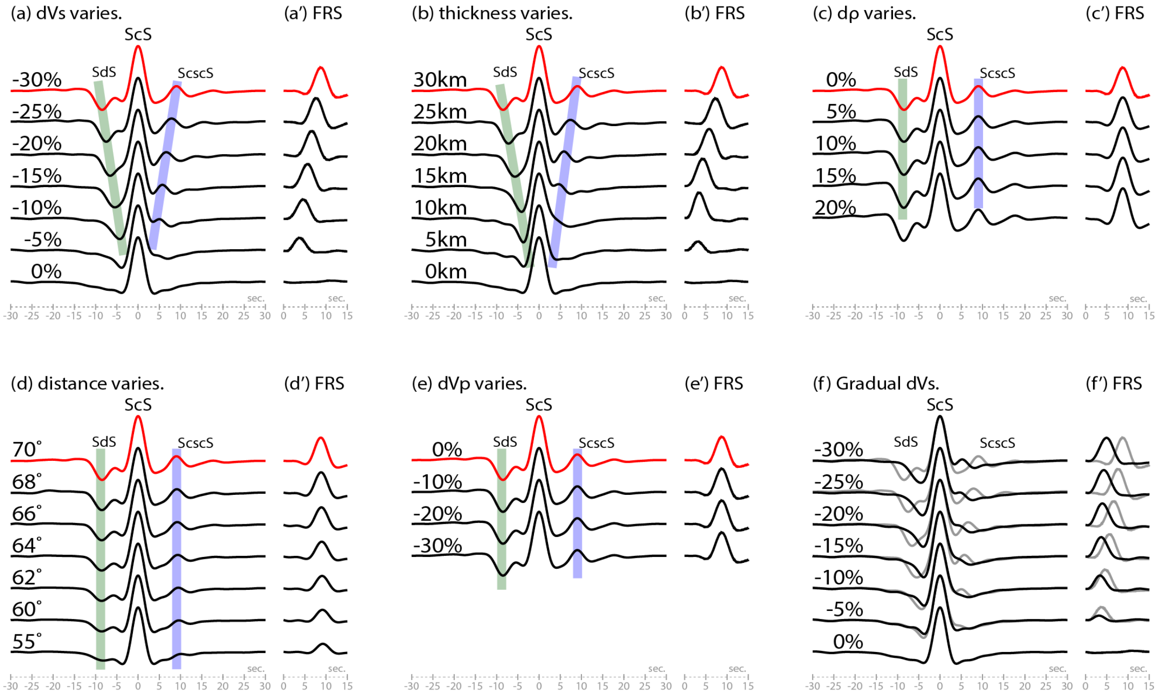

Figure 3.4 Synthetic ScS distortions (a-f) and their FRS traces (a'-f') for different ULVZ cases. Pre-cursor (SdS) is marked in green thick line and post-cursor (ScscS) in blue. One property is varying within each panel. The reference waveform (in red) is ScS received at 70˚ from a ULVZ model: H=30 km, dVs=−30%, dVp=0% and dρ=0%. (a) Varying S-wave speed reduction in the layer. Smaller S-wave velocity contrast results in lower amplitude and closer additional arrivals. (b) Varying layer thickness. Thin layer has closer additional arrivals. A 5 km layer will also decrease their amplitudes. (c) Varying density. Higher density slightly increases the additional arrivals' amplitudes. (d) Varying receiver distance. Larger receiver distance gives larger amplitudes. (e) P-wave speed has no effects on ScS distortion. (f) Models have S-wave velocity gradient within the layer are explored. These models have PREM S-wave velocity at layer top side, and S-wave velocity linearly decreased to the designated value at the CMB. Gray traces come from panel (a) for comparison.

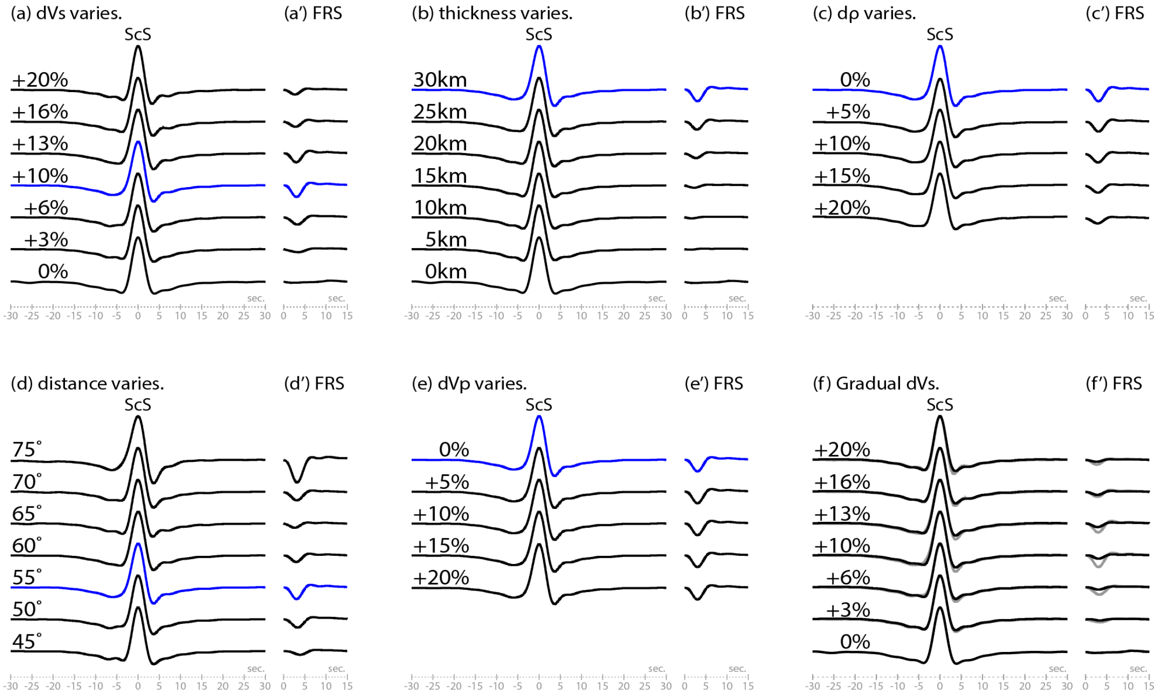

Figure 3.5 Synthetic ScS distortions (a-f) and their FRS traces (a'-f') for different UHVZ cases. One property is varying within each panel. The reference waveform (in blue) is ScS received at 55° from a UHVZ model: H=30 km, dVs=+10%, dVp=0% and dρ=0%. Because UHVZs has total reflection effect, the amplitude pattern is not as clear as ULVZs. Moreover, the timing doesn't change as much as ULVZ cases. (a) Varying S-wave speed reduction in the layer. (b) Varying layer thickness. Decreasing layer thickness results in a slightly timing decrease, which can be observed on the FRS traces. (c) Varying density. (d) Varying receiver distance. The total reflection for this model happens around 65°. (e) P-wave speed has no effects on ScS distortion. (f) Gradient S-wave velocity within the layer. These models have PREM S-wave velocity at layer top side, and S-wave velocity linearly increased to the designated value at the CMB. Gray traces come from panel (a) for comparison.

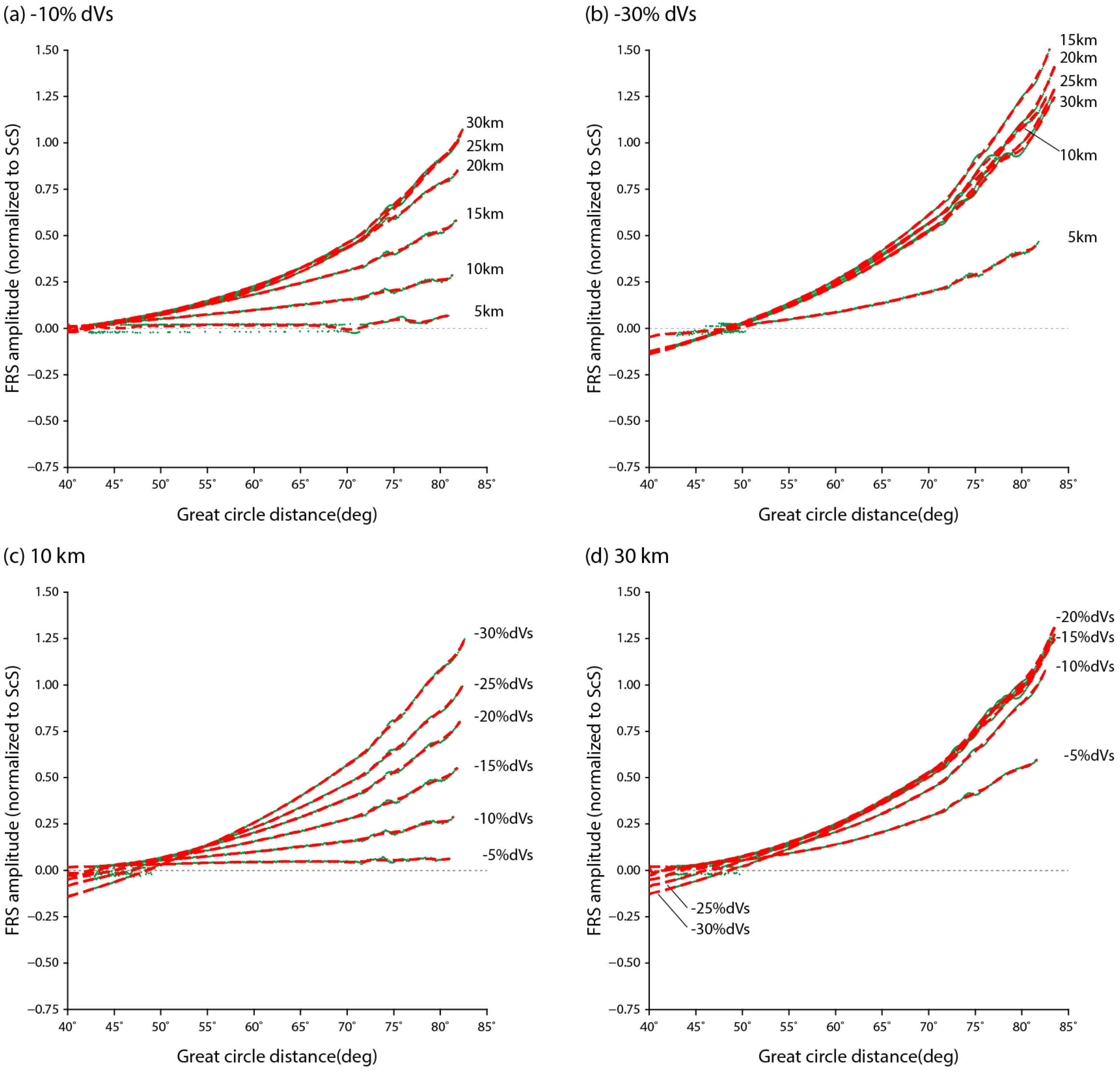

Figure 3.6 FRS amplitude-distance trends examples. Green dots are FRS amplitude measurements on individual synthetic FRS traces. Red dashed lines are obtained by applying a moving average (3˚ window width) through measurements, which smooths out traffic phases and near-zero values. The red dashed lines are the trends used to re-scale FRS traces. (a-b) fixed velocity reduction, varying layer thickness. (c-d) fixed layer thickness, varying velocity reduction.

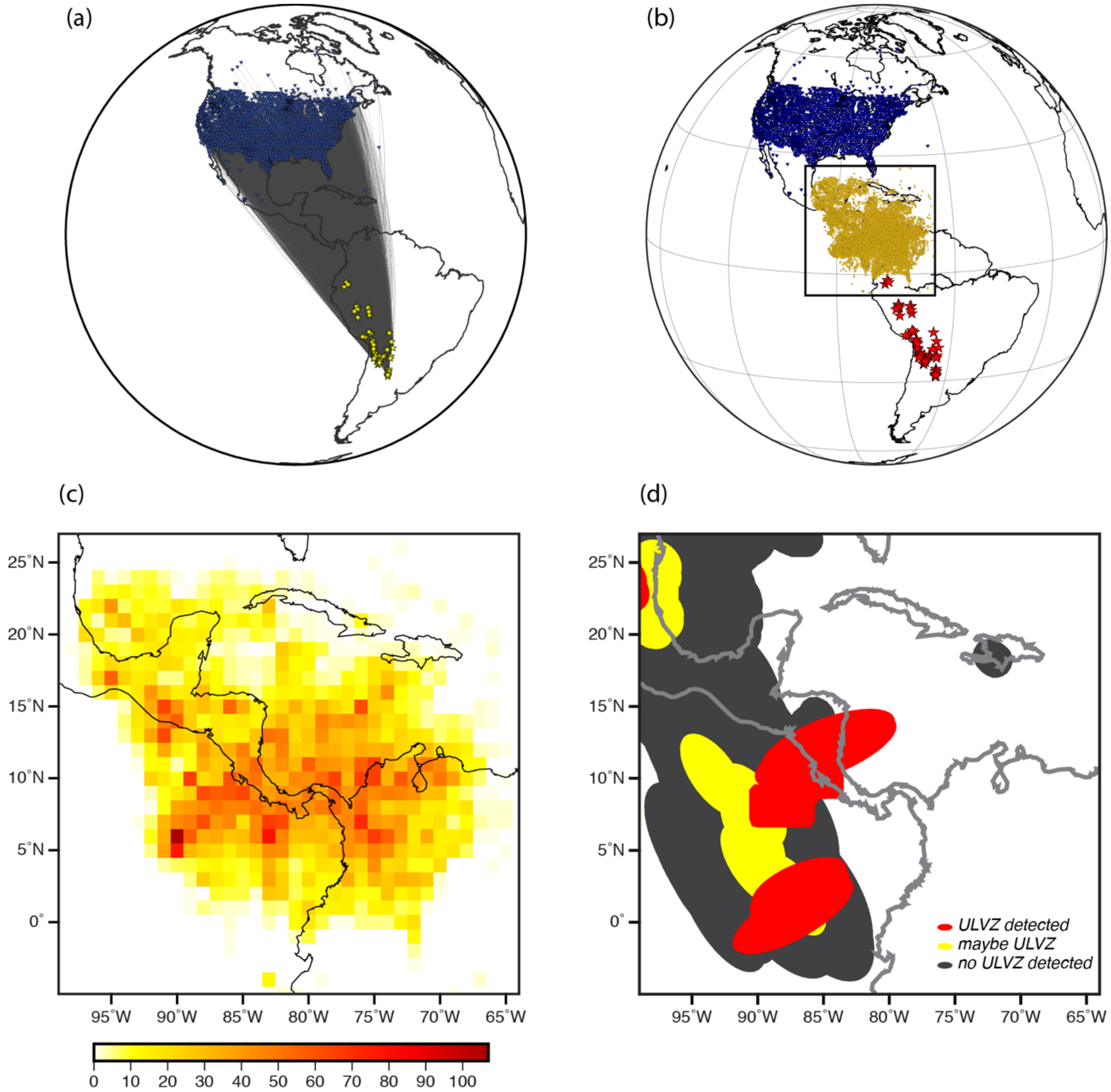

Figure 3.7 (a) Event-station geometries. 58 events are shown in yellow stars, 2,603 stations in blue inverted triangles, ray paths in gray lines. (b) ScS CMB bouncing points. 58 events are shown in red stars, 2,603 stations are shown in blue inverted triangles. 11,117 ScS CMB bouncing points predicted by PREM are shown in yellow dots. The region within the square is blown up in (c) and (d). (c) ScS bounce point hit map. This region is gridded into 1˚ by 1˚ bins. The numbers of ScS bouncing point inside each bin are plotted according to the scale bar. (d) Previous ULVZ study results for this region. Dark area represents ULVZ non-detections [Mori and Helmberger, 1995; Castle and Van Der Hilst, 2000; Persh et al., 2001; Avants et al., 2006; Hutko et al., 2009]; yellow for complex detections (not PREM but can't be well-modelled by ULVZ models) [Revenaugh and Meyer, 1997]; red for positive ULVZ detections [Niu and Wen, 2001; Thorne and Garnero, 2004].

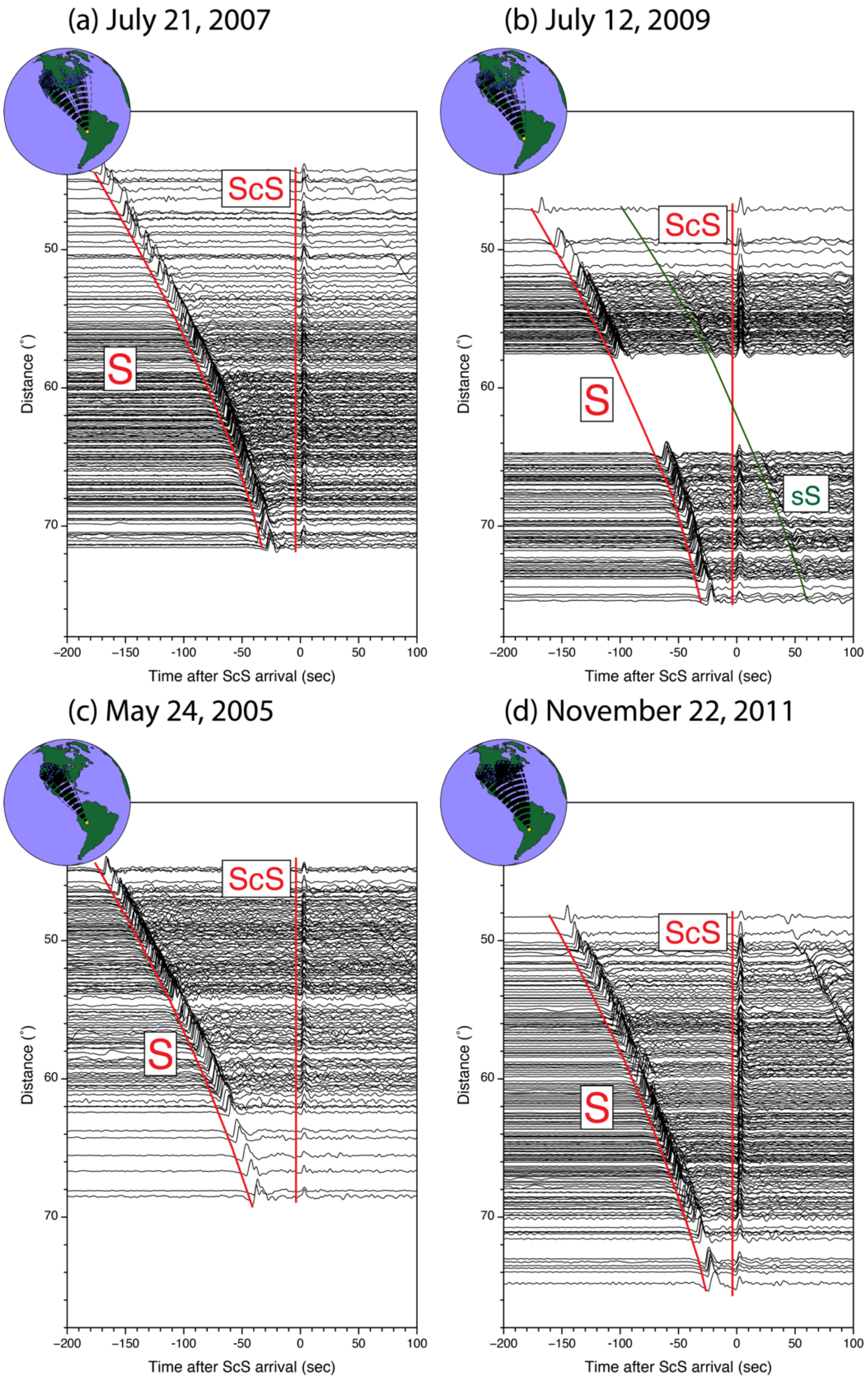

Figure 3.8 ScS data profile. (a) Event #7, July 21, 2007. (b) Event #17, July 12, 2009. (c) Event #25, May 24, 2005. (d) Event #39, November 22, 2011. Waveforms are cross correlated with empirical wavelet and aligned on ScS. These waveforms are randomly chosen for each event, to avoid plot cluttering. Notice in (b), records around 59° to 62° are not used because the traffic phase sS.

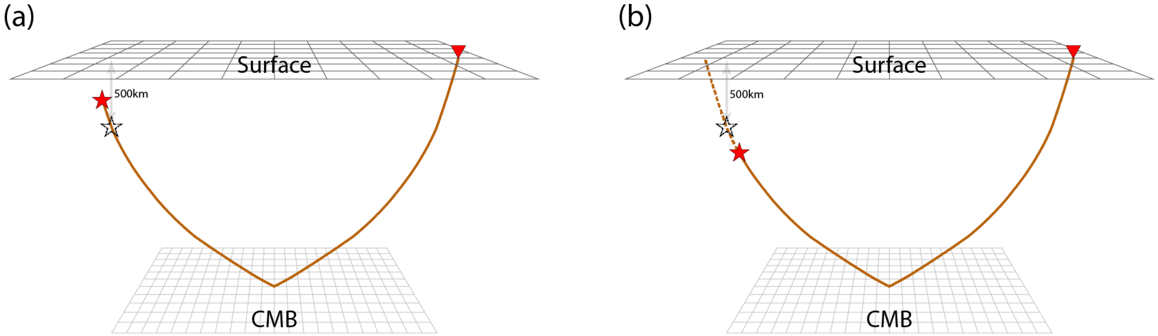

Figure 3.9 Cartoon illustrating the receiver distance correction. We move the source according to predicted ScS ray path for an actual event depth (a) less than 500 km and (b) greater than 500 km. Red star is the actual event location, and dashed star is the virtual source. Red invert triangle is the location of the receiver. Brown solid lines are the ScS ray paths. The corrected distance is the great circle distance between the virtual source and the receiver.

(a) shrink

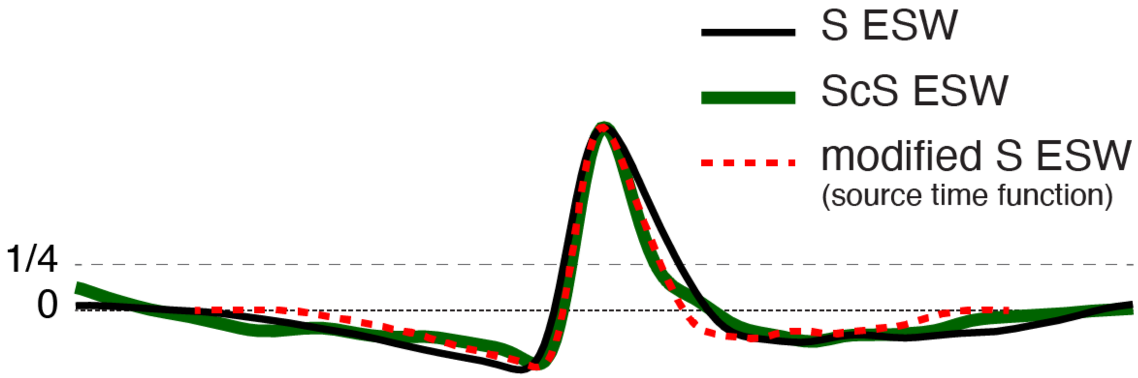

(b) stretch

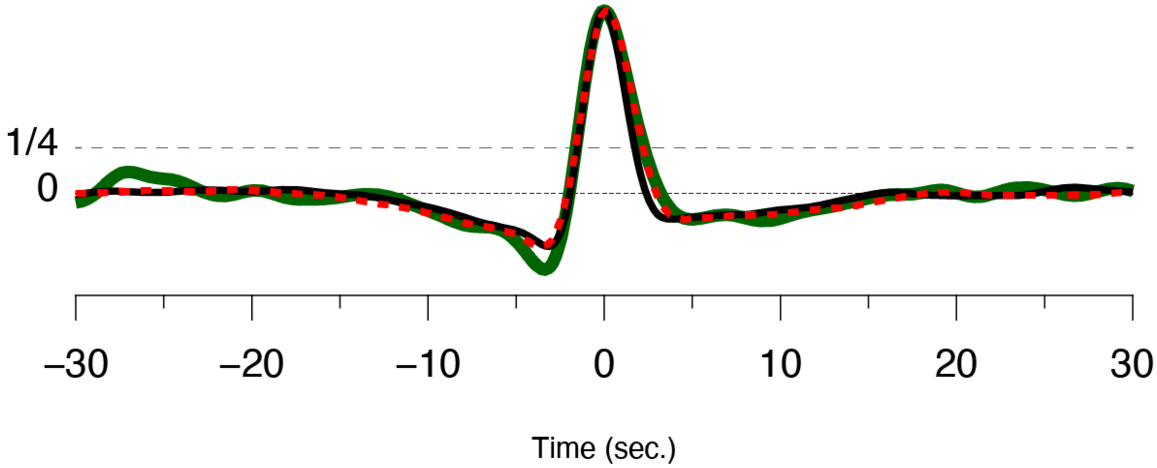

Figure 3.10 Empirical source wavelets and its modification. The horizontal gray dashed line marks the compare level (a quarter of the peak amplitude). (a) Event #16, whose S empirical wavelet (black) is broader than ScS empirical wavelet (green). For this event, the S-wave ESW is shrunk to 77% of its original width (red dashed line). (b) similar as (a) for Event #20, whose S empirical wavelet is narrower. For this event, S-wave ESW is expanded to 117% of its original width. The modified S empirical wavelets are then used as the event source time function for deconvolution.

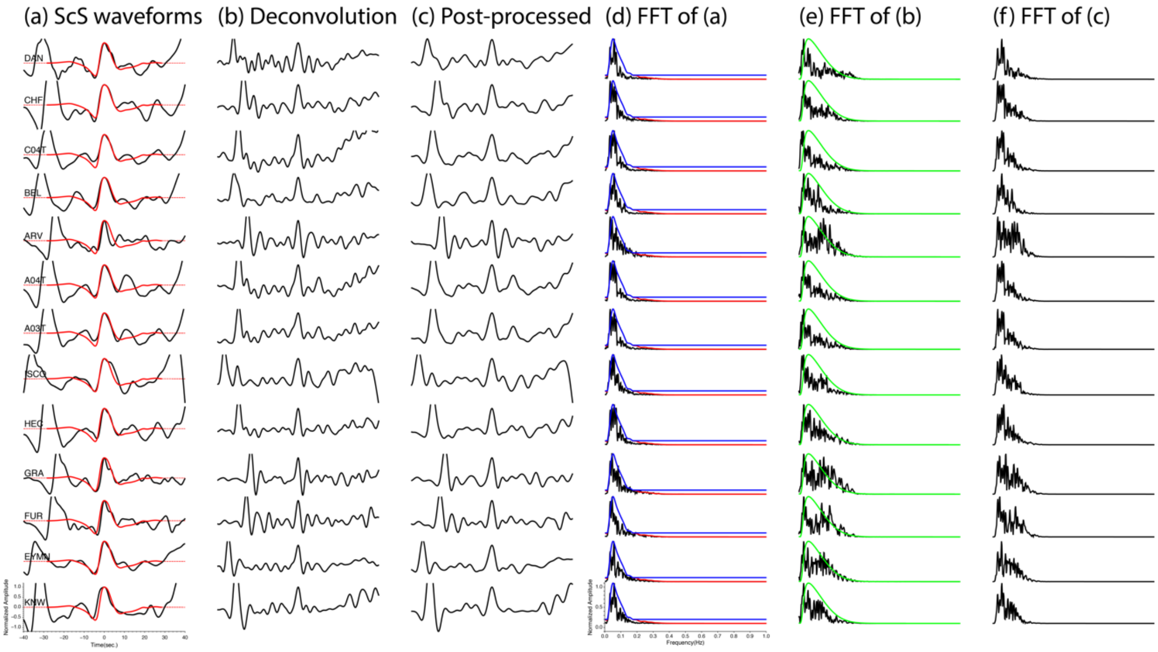

Figure 3.11 Deconvolution examples from event #1. (a) ScS waveforms are plotted in black lines; S empirical source time functions are plotted in red lines. Dashed red lines shows the zero-padding. (b) The deconvolution result before any post-processing. (c) The deconvolution result after post-processing. FRS operation is carried out on these traces. (d) the amplitude contents of each ScS waveform are plotted in black lines; the amplitude contents of the S empirical source time function are plotted in red lines. The water-filled amplitude contents are plotted in blue lines. (e) the amplitude contents of the spectrum division are plotted in black lines; the amplitude contents of the post-processing signal are plotted in green. (f) Amplitude contents of final deconvolution results.

(a) Time doamin

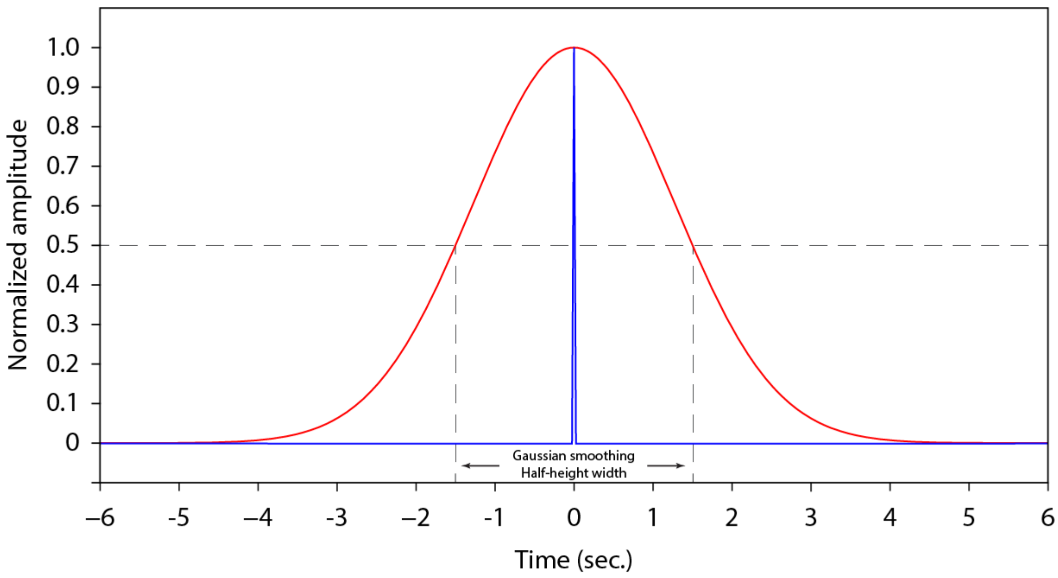

(b) Frequency doamin

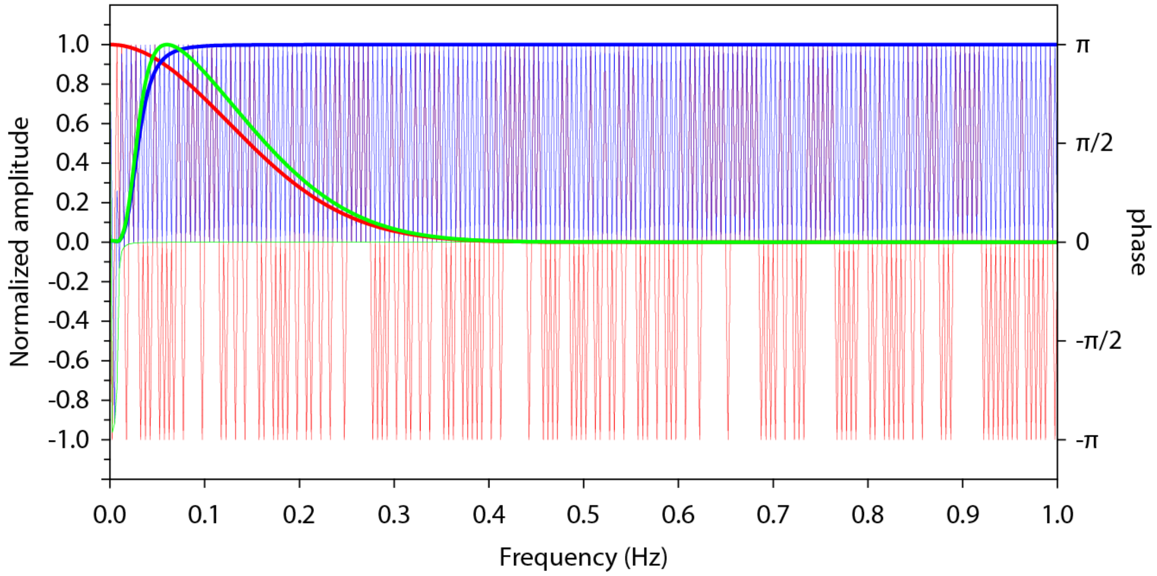

Figure 3.12 (a) Impulse responds of the high pass Butterworth filter (blue line) and the gaussian blur (red line) we used in post-processing. (b) Frequency contents of the Butterworth filter and the Gaussian blur (colored in the same way). The solid lines are the amplitudes and the thin lines are phases. Both the gaussian and the filter are close to zero-phase shifting. The green lines represent the combined effects of the gaussian blur and the high pass filter on the frequency contents, which is also plotted in Figure 3.11e.

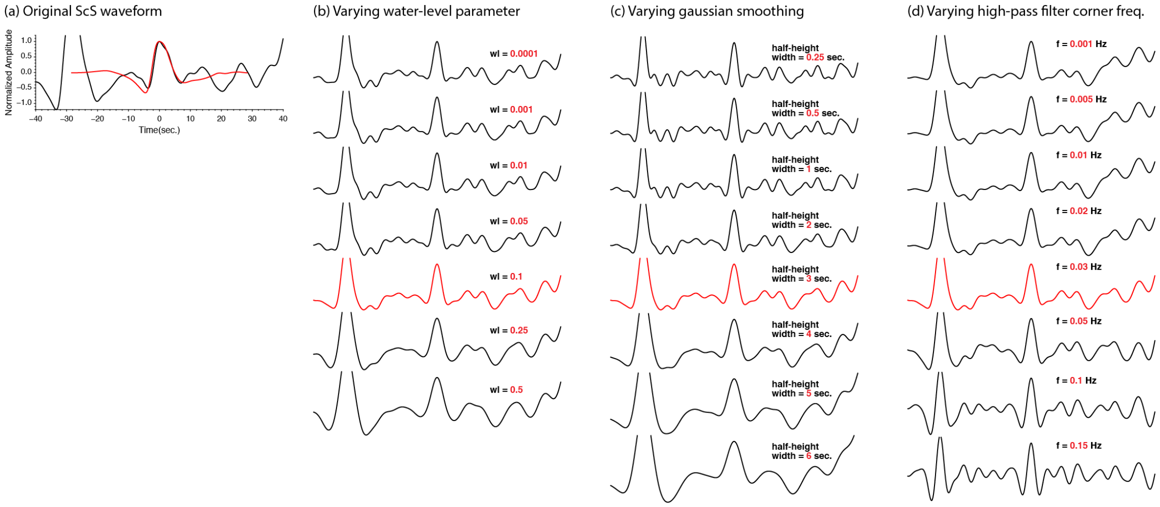

Figure. 3.13 (a) The original ScS waveform at station HEC for event #1. The red line is the empirical source time function for this event. (b-d) deconvolution results for different deconvolution parameters. The red waveform is the result for chosen parameters. (b) only varying the water-level. (c) only varying the gaussian function in the post-processing. (d) only varying the high-pass filter corner frequency in the post-processing.

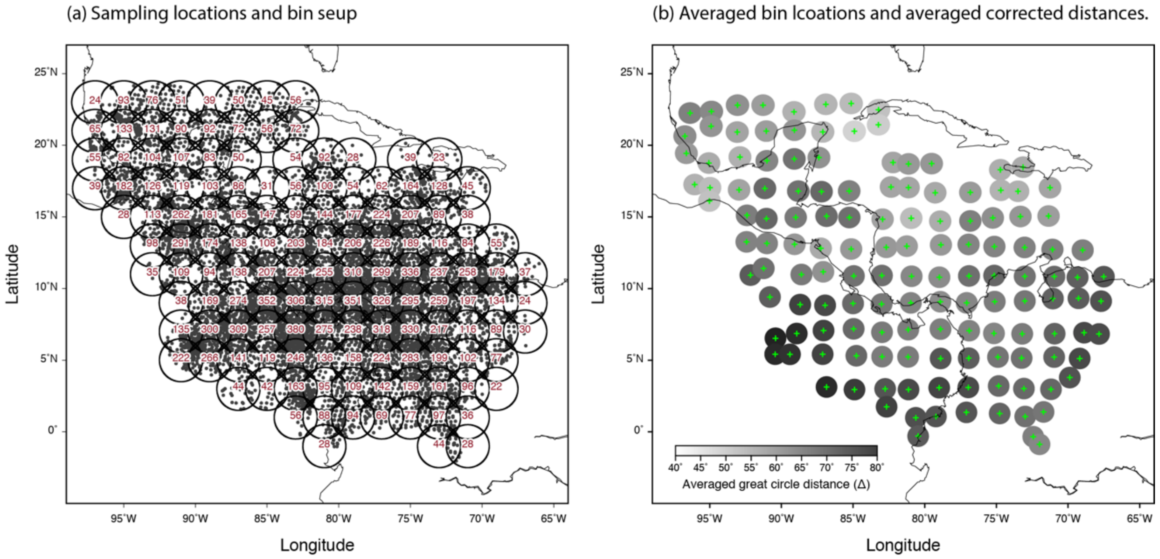
(a) Sampling locations and bin seup

(b) Averaged bin lcoations and averaged corrected distances.

Figure 3.14 (a) Gray dots are individual data ScS bouncing points. Black circles are geographic bins. Bin radius is 1.5˚. Originally, bin centers were located on a 2˚x2˚ grid. The numbers at bin centers are number of records in each bin. (b) Bins were relocated to the averaged position of the ScS bouncing locations within that bin (green plus signs). Small circles were shaded according to the averaged event-receiver distances in each bin. The averaged distances were used as reference distances in FRS amplitude re-scaling (see section 3.3.2.2).

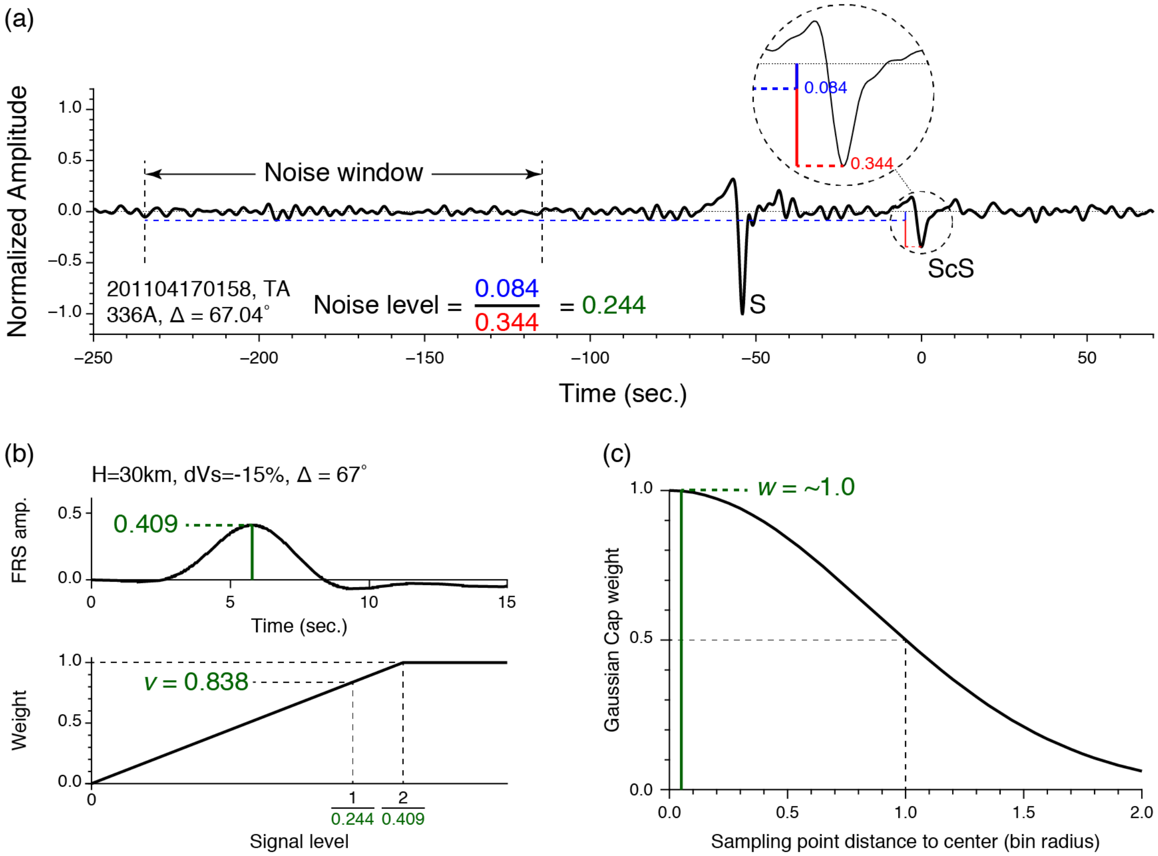

Figure 3.15 Example of bin stacking weight of event #33, station 336A when modeling against H=30 km, dVs=−15%. (a) The noise level is 0.244. (b) The FRS amplitude on synthetic waveform is 0.409, which is used as signal level upper bound of the ramp function. The second weight (*v*) for this record is 0.838. (c) The Gaussian cap weight calculation. Because this record is close to the bin center, its first weight (*w*) is close to 1.

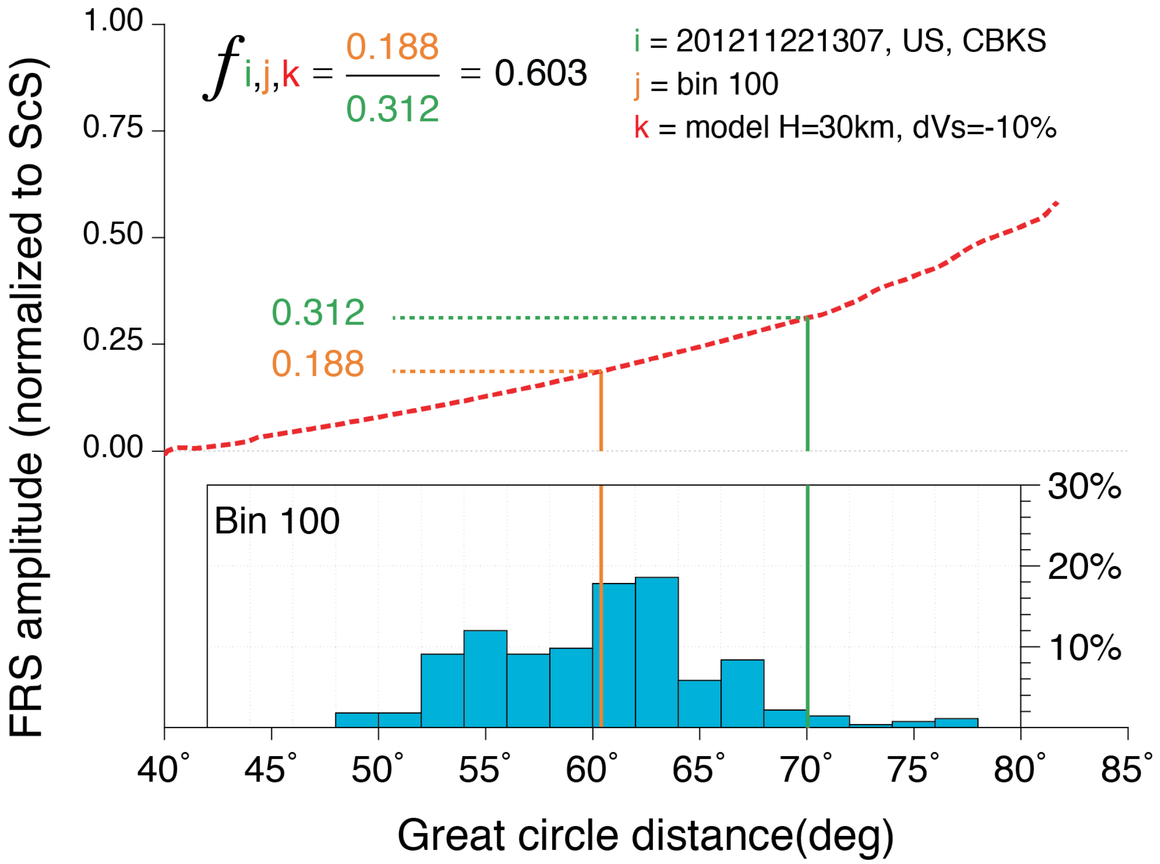

Figure 3.16 Example of scaling factor ($f_{i,j,k}$) in Eq. (3.7) and Eq. (3.8) for record 201211221307, US, CBKS when it is bin stacked within bin 100 and modeling against a H=15 km, dVs=−10% ULVZ. Inset histogram shows the record distance distribution for bin 100. The bin has an averaged distance 60.4˚ (orange-colored lines and numbers). The example record has a distance 70.04˚ (green-colored lines and numbers). The FRS amplitude-distance trend of the given model is shown in the red line. The scaling factor is calculated as the ratio between model FRS amplitude at the reference distance and at the record distance (f = 0.603).

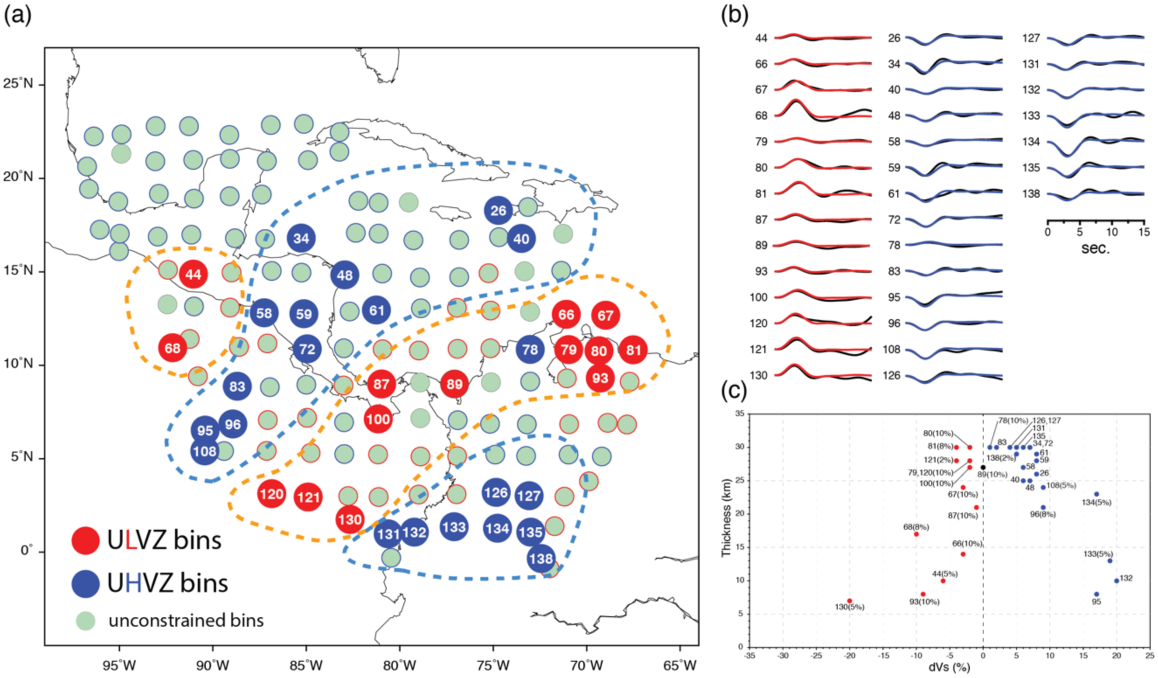

Figure 3.17 Modeling results. (a) Map view of best fitting models for each bin. The unconstrained bins are plotted as grey-green dots (see section 3.4.8 for details on modeling confidence). Constrained bins with best fitting ULVZ model are plotted as red dots, and with best fitting UHVZ models, bins are plotted in blue dots. Four major regions are circled out by hand in orange and blue dashed lines. Constrained bin numbers are marked at bin centers in white texts. (b) Data FRS stacks (black traces) and synthetic FRS stacks (colored traces) for constrained bins. Synthetic stacks come from the best fit model of each bin. If the best fit model is a ULVZ model, the synthetic stack is colored in red. Similarly, UHVZ synthetic stacks are colored in blue. (c) The properties of best fit models for each bin. Bin numbers are marked in text. If the best fit model has a density anomaly, the density anomaly is appended in parenthesis after the bin number.

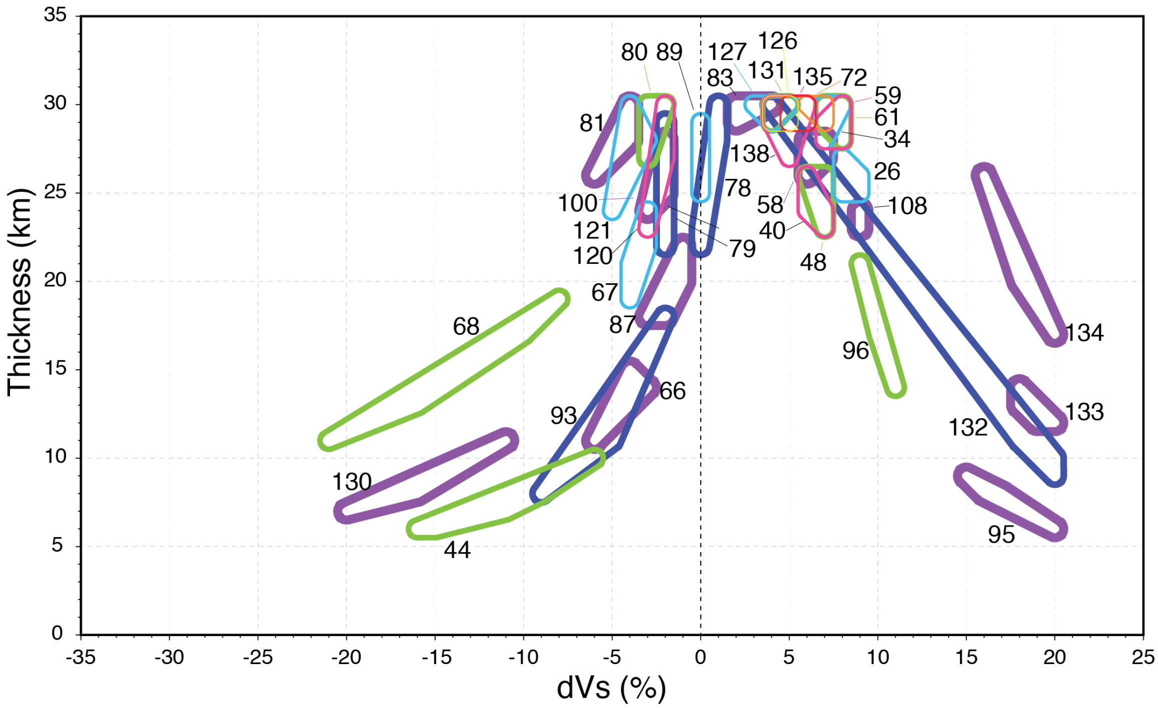

Figure 3.18 Range of the top five best fitting models for each bin. Bin numbers are marked near each region. Different colors and line thickness are just for plotting clarity. Notice that trade-offs in density dimension is not shown.

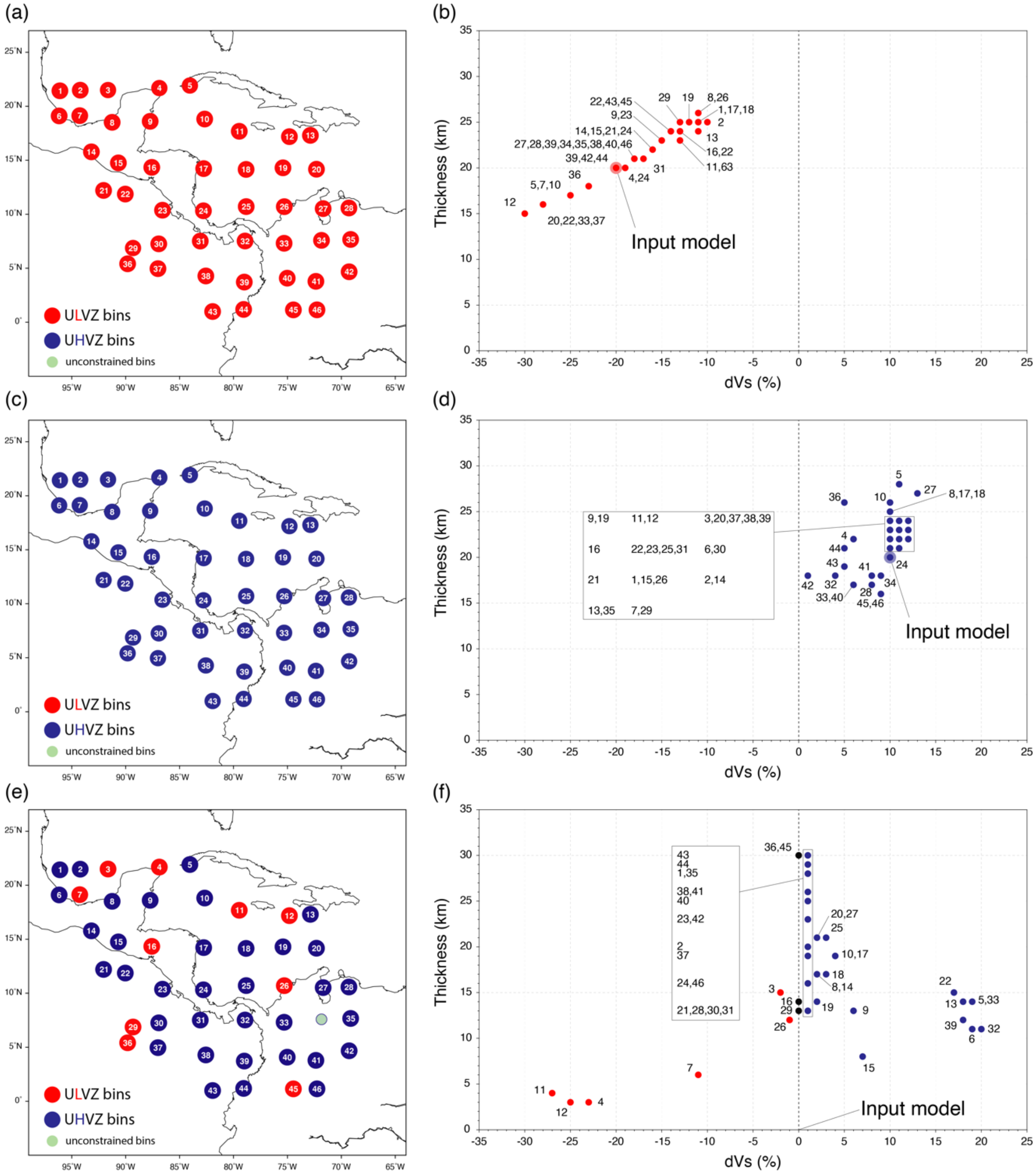

Figure 3.19 1D pseudo dataset benchmark modeling result. Color code see Figure 3.17. (a-b) Input model is a ULVZ 1D layer (20 km, −20% dVs). (c-d) Input model is a UHVZ 1D layer (20 km, +10% dVs). (e-f) Input is PREM.

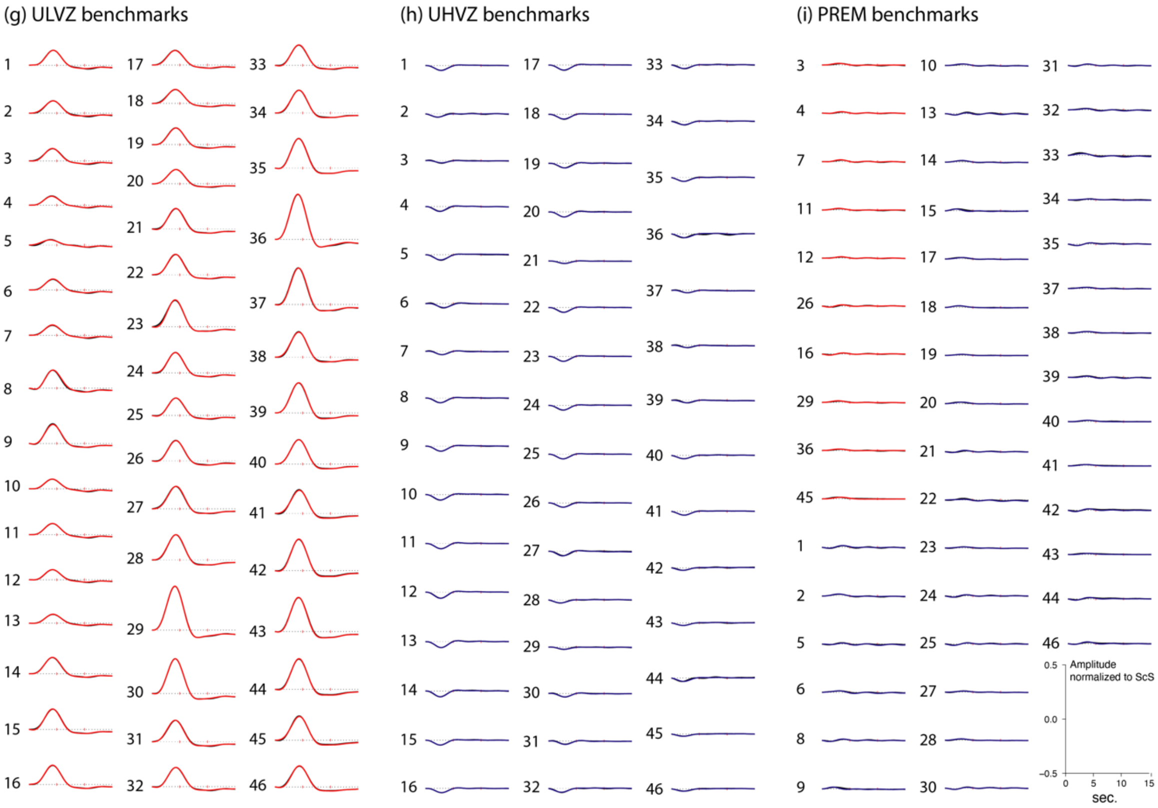
(g) ULVZ benchmarks

(h) UHVZ benchmarks

(i) PREM benchmarks

Figure 3.19 (continued) Benchmark waveforms for each bin. Bin number is marked. Model stacks are colored according to the best fit model type: red for ULVZ-like bins, blue for UHVZ-like bins. Pseudo-data stacks are in black. (g) Best fit model and pseudo-data bin stacks for a 1D ULVZ input. (h) Best fit model and pseudo-data bin stacks for a 1D UHVZ input. (i) Best fit model and pseudo-data bin stacks for PREM input.

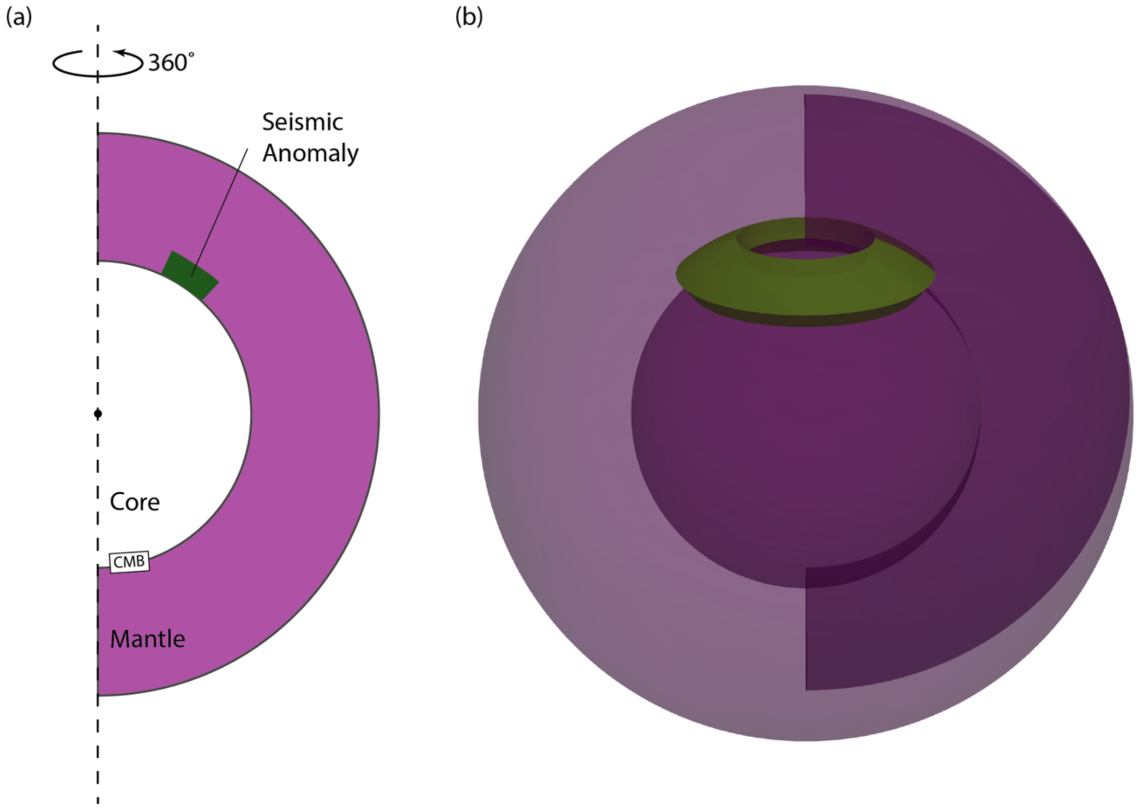

Figure 3.20 Cartoon illustrating SHAXI model set up. (a) a 2D user input structure. The thickness of the anomaly in this cartoon is extremely exaggerated. (b) the structure equivalent for SHAXI calculations, which is the 2D input structure rotated 360˚ along its z-axis.

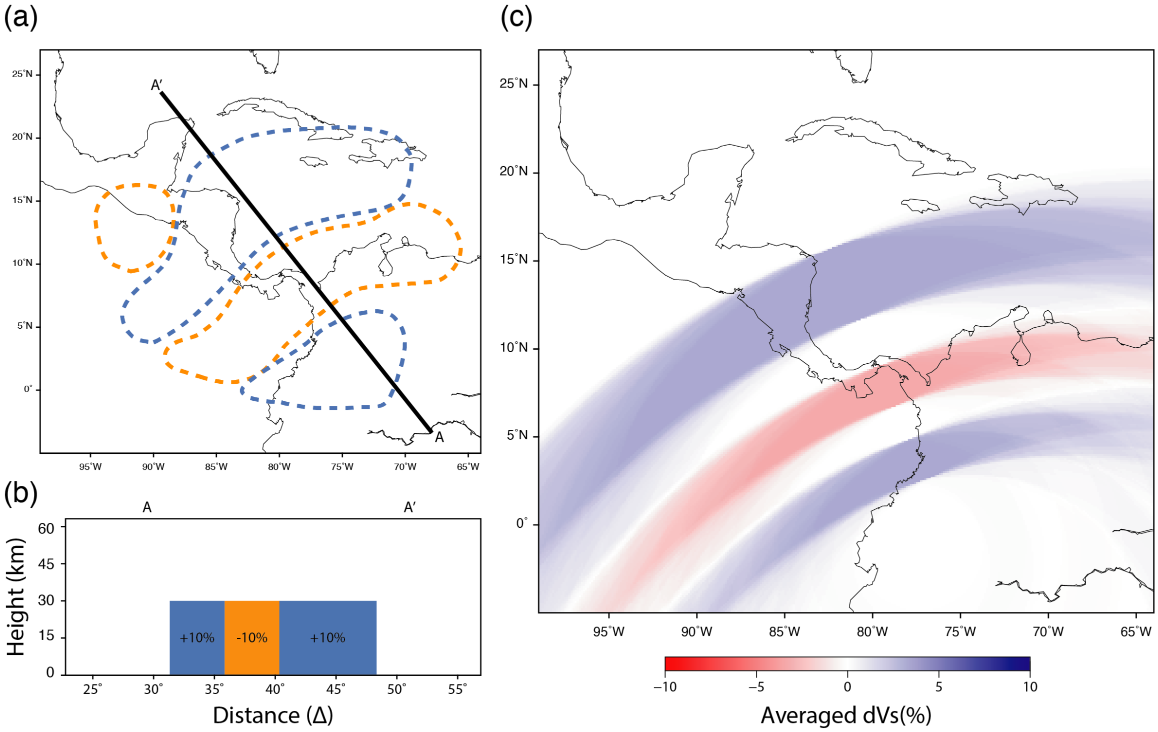

Figure 3.21 2.5D benchmark input model set up. (a) derivation of the input model from detection result. AA' is the selected cross-section. Three structures alternate on this cross-section (b) The approximate 2D box-car model for SHAXI input. (c) An azimuthal average velocity perturbation for all 58 runs after the axis rotation. This model is the one we try to recover using our method, which was based on 1D layer velocity anomaly.

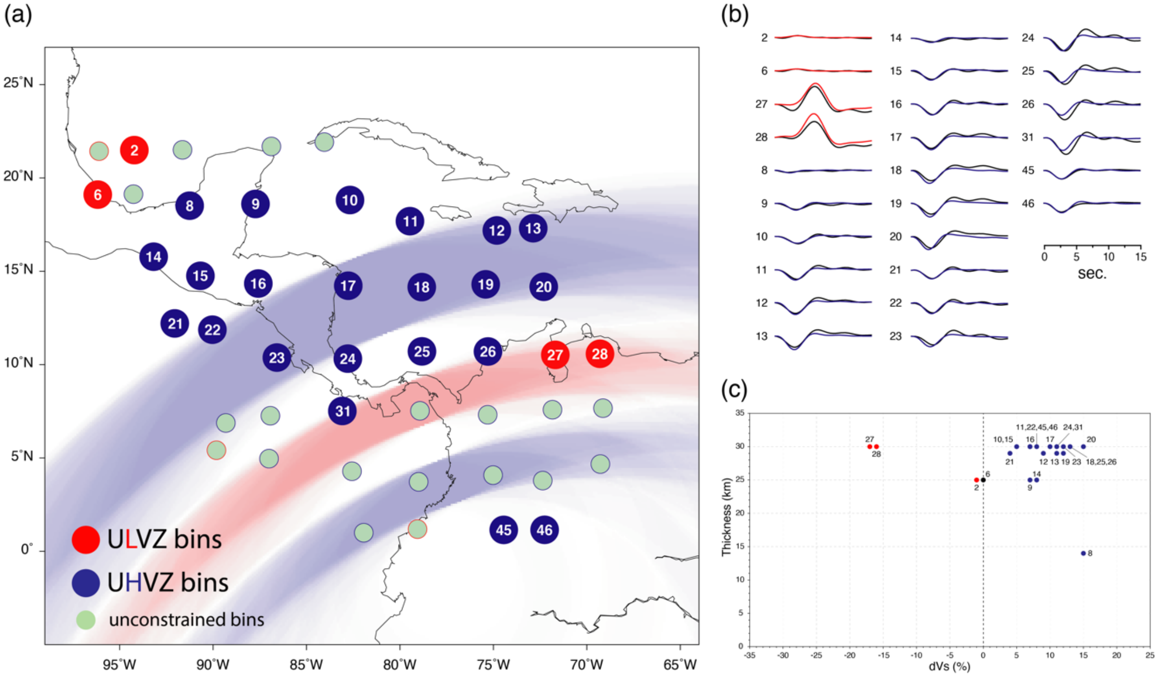

Figure 3.22 2.5D benchmark modeling result. (a) Map view of best fitting models for each bin. See Figure 3.17 for color code. The background shading indicates the input model (Figure 3.20c) (b) Pseudo data FRS stacks (black traces) and synthetic FRS stacks (colored traces) for constrained bins. Synthetic stacks come from the best fit model of each bin. (c) The properties of best fit models for each bin. Bin number are marked in texts.

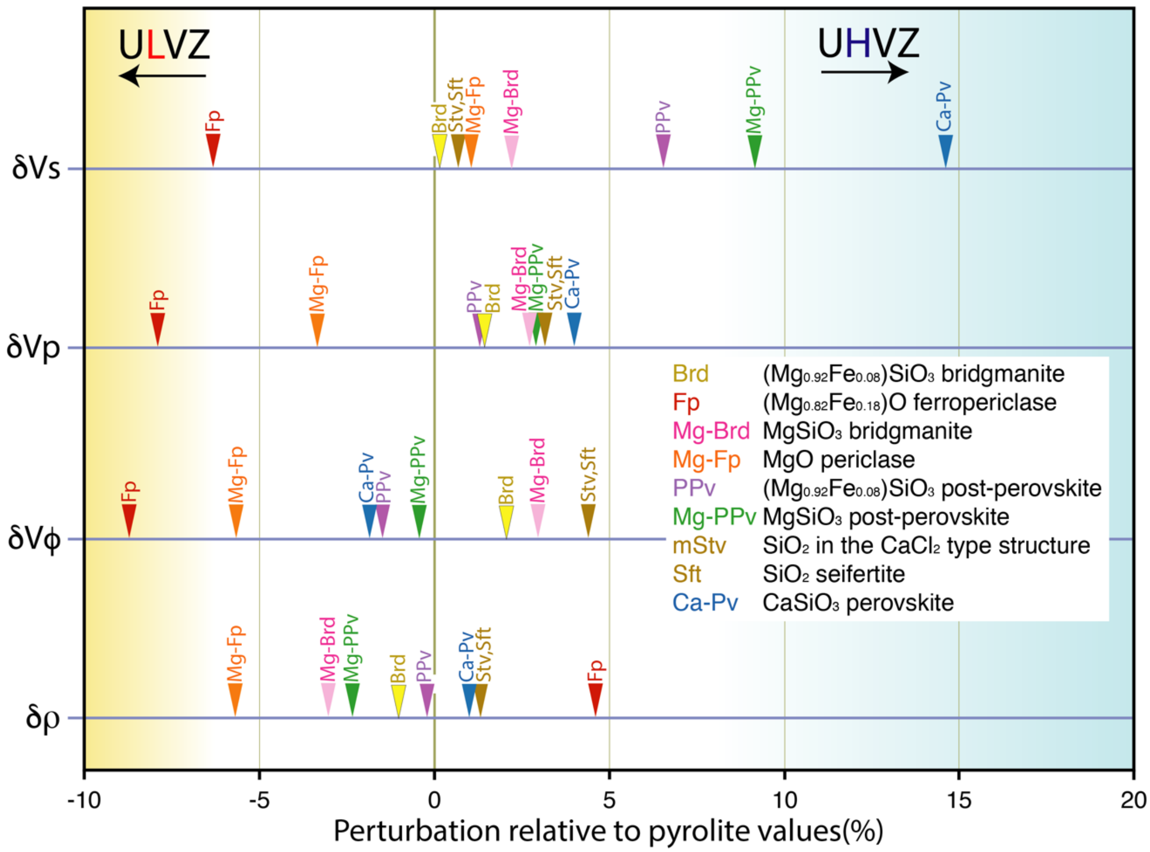

Figure 3.23 Expected changes in seismic velocities and density (ρ) by mineralogy. Calculations were conducted for the base of the mantle (135 GPa and 4500 K) and referenced to predictions for pyrolite using Burnman package and SLB2011 dataset [Stixrude and Lithgow-Bertelloni, 2012; Cottaar et al., 2014]. From top to bottom: S, P, bulk sound speed and density. The high velocities and density of CaPv and silica present viable explanations for UHVZs.

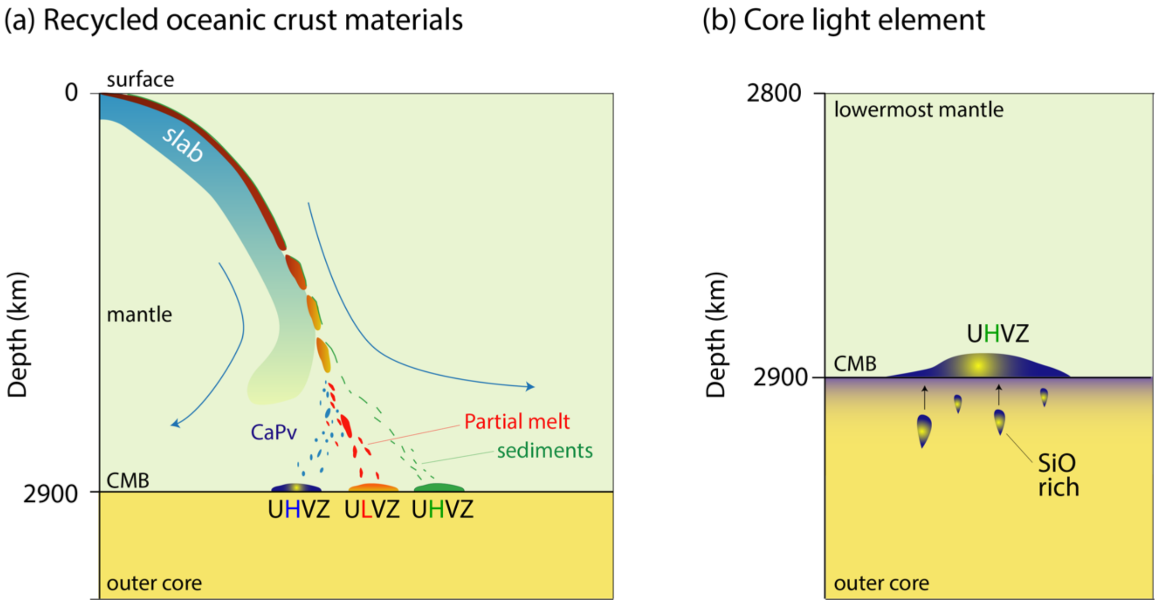

Figure 3.24 Cartoons showing potential processes for our observations. (a) Subducted oceanic crust separated from lithosphere and undergo partial melts. The (Fe enriched) partial melts may explain the observed ULVZs. The melt residue, CaPv, may explain the UHVZs. Alternatively, silica-rich region could have high seismic velocity. The silica-rich sediments in oceanic crust could be one source. (b) The exsolution of Si from the outer core could be another silica source [Helffrich et al., 2018].

CHAPTER 4

GLOBAL S-WAVE BROADENING OBSERVATIONS AND IMPLICATIONS FOR D″ DISCONTINUITIES

4.1 Abstract

We assembled and digitized detection locations of previous studies on D″ discontinuities. Most previous studies utilized a top side reflection phase and most of their results are in the northern hemisphere due to phase geometry restriction. Here we utilized phases generated by multipathing, which can cause a broadened S waveform and manifest beyond the usual data distances. Several synthetic models are studied, and their S broadening characters are analyzed. A global dataset from 1994 to 2017 is collected and their S waveform broadenings are investigated. In additional to previous studies, we find new sampling positions showing potential for D″ discontinuities, especially in the southern hemisphere.

4.2 Introduction

D″ is a historical name for the lowermost several hundred kilometers of Earth's mantle, right above the core-mantle boundary (CMB) [Bullen, 1949]. Seismologists have found seismic discontinuities within this depth range since the 1980s (see section 1.3.4 for more information). Most of the studies phases utilized (called Pcd and Scd) are generated by a down-going wave reflected at the top side of a different seismic velocity layer at the bottom of the mantle (a basal velocity layer, hereafter). We collected and digitized previous D″ discontinuity studies. Studies details are listed in Table 4.1 and detection locations for P- and S-waves are plotted separately in Figure 4.1. Most of the digitized sampling points are theoretical PcP or ScS bouncing point locations, approximating the reflection locations for Pcd and Scd. Occasionally the turning points of direct S-wave or P-wave ray paths are used instead. It can be seen from Figure 4.1 that some ambiguities or even conflicts between studies exist in detection locations: In some regions the non-detection and yes-detections overlapped; and in other locations there exists a sharp lateral change of detections. These lead to a widely accepted view that the D″ discontinuity is not a global feature.

We further explore the spatial relation between detected D″ discontinuities and the most seismically anomalous lower mantle regions: two large low shear wave velocity provinces (LLSVPs) and their opposites, the general high velocity regions. Fresnel zones are approximated by adding circular regions around the theoretical bouncing or turning points. This approximation is crude because it's not taking the exact ray direction into account. But it is sufficient for the crisscrossing paths and approximating the frequency contents. For S waves, the circle radius is chosen to be 10˚ and for P waves, the radius is 5˚ (P waveforms usually have higher frequency contents than S waveforms, which makes their Fresnel zone smaller). After this Fresnel zone approximation, the sampled regions are categorized into those located inside the LLSVPs, inside the general high velocity regions or inside the normal regions (Figure 4.1e and f). The boundaries of the regions are defined in the same way as in [Garnero et al., 2016], using the velocity contour enclosing the highest and lowest 30% CMB area (Figure 4.1). For this analysis, tomography model S40RTS is used [Ritsema et al., 2011]. The area of each category is summed and compared for P- and S-waves separately. 6.7% of the P-wave D″

discontinuity area locates in the general low velocity regions (red areas in Figure 4.1e); 55.3% locates in the high velocity regions (blue areas in Figure 4.1e). For S-waves, 12.24% of its D″ discontinuity area locates in the general low velocity regions (red areas in Figure 4.1f); 51.76% locates in the high velocity regions (blue areas in Figure 4.1f). This result agrees with previous suggestions that D″ discontinuities are preferably detected in the high velocity regions of the lowermost mantle [e.g. Lay and Garnero, 2011].

The phases used (Scd and Pcd) are usually recorded at great circle distances between 60˚ to 80˚, where the reflection coefficients of these phases are high. Beyond this distance range, either their arrival amplitudes are too low, or they are mixed with the direct P- or S- wave, which make their waveforms difficult to model. Therefore, certain regions, especially the southern hemisphere (Figure 4.1 a and b), are under-sampled due to the geometry restrictions of these phases. In this study, we investigated S wave arrivals larger than 80˚ from events during 1994 and 2017 and documented S waveform broadening observations. Using reflectivity synthetics, several basal layer models are analyzed for their waveform broadening characteristics. The larger distance records in our dataset show implications of existence of D″ discontinuities. Some locations are consistent with previous studies, while other locations are fresh, filling in the unsampled areas such as the southern hemisphere.

4.3 Synthetics Analysis

4.3.1 S-wave Multipathing Ray Paths

When a basal layer exists, the seismic waves reaching this depth would undergo multipathing. Here we categorize these newly generated waves into two kinds, distinguished by their different patterns on the ray path section within the basal velocity layer: waves whose ray paths turn before hitting the core-mantle boundary (CMB, Figure 4.2a), due to an increasing seismic velocity with increasing depth; and waves whose ray paths reflect at the CMB (Figure 4.2b), due to their small takeoff angle (steep enough), which let the waves reach the CMB before turning could happen. For clarity and simplicity, we renamed and label these waves in a new convention. Names start with a capital R is reserved for waves whose ray paths turn before reaching the CMB; and a capital G for waves whose takeoff angle is small enough to reflect at the CMB (Figure 4.2). The number after each capital R and G means the number of refractions or reflections ray path section within the basal velocity layer. Notice that as the ray takeoff angle decreases, the turning waves (R waves) will transition to an according reflection waves (G waves). For example, R0 (S arrivals) will transition to G0 (Scd arrivals).

4.3.2 1D Model Case Studies

When the basal velocity layer is thick enough, the multipathing will manifest as independent, additional arrivals on seismograms. These additional arrivals complicate the travel time curves, resulting in triplication for a high velocity basal layer, or a shadow zone for a low velocity basal layer. In Figure 4.3, travel time curves for three selected representative basal layer models are presented. The high velocity basal layer is 300 km thick, dVs = 3%, dρ = 0%. For the low velocity case, we fixed thickness and dρ, then tuned dVs down to −3%. The sources are at 500 km depth. A reference case where no basal layer (PREM) is included (Figure 4.3a). PREM has two travel time curves: R0 (previous S) and G0 (previous ScS).

On the travel time curve, the transition between R arrivals and G arrivals manifests as red curves meet the same numbered green curves at large distance. For example, in Figure 4.3b, R0 (previous S) transits to G0 (previous Scd), and their travel time curves meet at around 87˚; similarly, R1 transits to G1 at around 96˚. The amplitudes of these additional arrivals depend on the velocity contrast of the basal layer, as well as the incident angles at the layer boundary (different receiver distances). In a real case, R2, R3 and G2, G3 (and up) have really low amplitudes which make them hard to observe. The main arrivals in the discussion hereafter will be the arrivals sampling the anomalous layer at most once (R0, G0, R1 and G1). To better illustrate the S wave multipathing on travel time curves, the low amplitude arrivals are omitted in the zoom-in figures (right column of Figure 4.3).

At distances where the multipathing arrivals come closer to each other, the original S waveform will be broadened. We quantify this broadening using a measurement called half-height width difference. It is defined as the difference, in percentage, between each individual S waveform and a reference wave shape. The reference wave shape is a stack of close distance S waves (received at less than 80˚), which don't sample the basal layer and therefore their averaged waveform is representative of the source time function. For real data, this baseline set up is important when the structure is constrained from various earthquakes with different source time functions. First, the peak of each S waveform is found as the largest amplitude within in a time window decided by cross-correlation between the reference wave shape and the S waveform. After the peak is found, the waveform is normalized to the peak, and the half-height width on each record is calculated (see schematic Figure 4.4). The cross-correlation also provide an arrival time of the S waveform, which here is measured as a relative time to the predicted S and Sdiff arrival time for PREM.

Synthetics waveform profiles for the chosen three representative models are shown in Figure 4.5 to 4.7, along with their half-height width difference and arrival time measurements. In this study, S waveforms between 40˚ and 75˚ are stacked to form the reference shape. As observed in Figure 4.5b, S waveform is steadily broadened as distance increase (from 40˚ to around 80˚). This is due to attenuation in the PREM model which makes waveforms loose high frequency content as propagate distance increase (R0 is broadened by attenuation). Because we use the averaged shape from 40˚ to 75˚ as the comparison reference, waveforms between 40˚ and 60˚ are narrower, while waveforms between 60˚ and 75˚ are wider. The slightly decrease of half-height width difference values between 80˚ and around 86˚ is due to the closing of negative filter sidelobes of G0, which pull the second half of R0 waveform downwards and narrow its waveform. The half-height width differences increase and eventually reach a peak around 91˚. This is due to the closing in G0 arrival (see the waveform near the green travel time curve in Figure 4.5a). As the distance continue to increase, the core-diffraction wave becomes dominant (after around 101˚) and controls the waveform broadening, again, due to attenuation. Two things to notice at this distance range. The slope of broadening measurement (the half-height width difference) is different from the slope at closer distance (between 40˚ and 75˚). This could due to a different attenuation scheme for diffraction waves propagating on the CMB versus body waves, which can be used to diagnose diffraction waves. Another thing to notice is that the arrival time picked using the cross-correlation method is delayed, relative to Sdiff PREM prediction (see Figure 4.5c, beyond 100˚). This delay is because the best window found by cross-correlation is biased towards the center of waveform, rather than the onset of a waveform (Figure 4.5a).

The synthetic waveform profile for a high velocity basal layer and its travel time curves are presented in Figure 4.6a. The multipathing gives rise to well separated multiple arrivals (R0, R1, G0 and G1). The meaning of "S wave" becomes vague, here we will use the cross-correlation result to define the "S wave" as the first onset on the seismogram. Through observation, it is R0 from 40˚ to around 80˚, a combination of R0, R1, G0 and G1 from 80˚ to 87˚, R1 from 87˚ to 97˚ and finally S diffraction along the CMB beyond 97˚. G0 (previous Scd) is the signature of D″ discontinuities and is often utilized in previous studies (see Table 4.1). G0's amplitude increases and becomes visible from 55˚, and it joins R0 then disappears at around 85˚, therefore most studies only use data from 60˚ to 80˚. However, at the same distance where G0 disappears, R1 is born and manifest itself ahead of R0 ("shouldering" of R0). R1 causes a detectable waveform broadening at and beyond 80˚, which means more data can be used to constrain lowermost mantle structure and potentially new regions are sampled. The diffraction along CMB (beyond 97˚) can be verified using the travel time move out in Figure 4.6c. The slope of broadening measurement in this distance range is also similar to the CMB diffraction part in the PREM model (103˚ to 110˚ in Figure 4.5b). The significant difference in waveform broadening measurements compared to PREM is its two larger peaks around 80˚ and 87˚ (Figure 4.6b). Cause of the peak at 80˚ is G0 comes closer, similar to the 91˚ peak in PREM. Because the amplitude of G0 in this model is increased with distance, this peak becomes larger than PREM. The cause of peak at 87˚ is the birth of R1, starts at around 84˚. The gradual increase and the sudden drop of the broadening measurement from 85˚ to 90˚ is due to the separation of two arrivals (R0 and R1). A speculated diffraction along the top side of the basal layer is marked out in gray in Figure 4.6a between 89˚ and 96˚.

Figure 4.7 shows the result from a low velocity basal layer. Different from the high velocity case, the multipathing has travel time curves more separated from each other, which creates a shadow zone rather than a triplication. The shadow zone (Figure 4.7a, marked in gray between 89˚ and 99˚) is filled with amplitude-decreasing waves diffracting along the top side of the low velocity layer. This diffraction behavior can be confirmed by the move out in the picked arrival time (Figure 4.7c, between 90˚ and 95˚). This diffraction causes a wide, large waveform broadening measurement (Figure 4.7b, between 89˚ and 99˚). Comparing to a high velocity layer case, the waveform broadening in this case has different signatures. There exists one fatter half-height width difference measurement peak, while for high velocity basal layer, there exist two skinny peaks, at a relatively closer distance range (Figure 4.6b, between 77˚ and 87˚). This different signature could distinguish whether the observed S waveform broadening comes from a high velocity layer (for example, a high S wave velocity D″ discontinuity) or a low velocity layer (for example, the top side of LLSVP, [Zhao et al., 2015]). Another different signature is the birth of R1 from R0 and replace it as the first arrival. This behavior can cause the so called “shouldering” or “double-peak” observations.

Next we vary the properties of the basal layer slightly away from the chosen cases to illustrate how each property affects the broadening and arrival measurements. The results are presented in Figure 4.8 and 4.9. In addition to the variations shown, density of the layer is increased and tested. The waveforms from density increased models show little differences and therefore results from density variations are not presented.

In Figure 4.8 and 4.9, the general characters of S waveform broadening for each category of model is consistent: All high velocity models show two narrower peaks, while low velocity models show one fatter peak. Decreasing the basal layer thickness delay the broadening to a larger distance. The broadening peak amplitudes are generally the same (Figure 4.8a and 4.9a). Changing the velocity contrast of the layer mainly affect the broadening peak amplitudes: the larger velocity contrast, the higher half-height width difference values. The distances of the broadening peaks are slightly affected, which implicate a potential trade-off between layer thickness and velocity contrast (Figure 4.8b and 4.9b). Placing the source depth at shallower depth doesn’t affect the broadening measurement peak shape, and the peaks are only slightly shifted to a larger distance (Figure 4.8c and 4.9c).

4.4 Data Processing and Results

4.4.1 Data Collection

We collected transverse component seismic records for large (m>=6) events between 1994 and 2017 from several data centers: SOD [Owens et al., 2004] was used to access data from IRIS data service; BREQ_FAST request was used to download data from Observatories & Research Facilities for European Seismology (ORFEUS) data center; website service was used to collect Japan F-net data from National Research Institute for Earth Science and Disaster Resilience (NIED); AutoDRM service (now deprecated) was used for Canadian National Data Centre (CNDC). In total, 123,946 displacement records from 360 events are received and selected after instrument responses are removed.

4.4.2 Source Time Function and R1 Observation

For each event in our dataset, its source time function is constructed by stacking its close distance S waveforms, using a similar procedure to that described in section 3.4.3. The records are pre-processed with one-pass Butterworth filter with corner frequency 0.01 Hz and 0.0625 Hz (16 second to 100 second). This frequency band preserves more low frequency contents and is suitable for S waveform studies at relatively large distance. The dataset is plotted out and inspected record by record for obvious “shouldering” or “double peak” on the front half of the first arrival, around the predicted S wave arrival from PREM. For each record, the source time function of its event is firstly shrunk or stretched (see details in section 3.4.3) to best fit its waveform and then overlapped and plotted, at the location found by cross-correlation. These source time functions help humans to recognize the “shouldering” phenomenon. Several examples of selected records are presented in Figure 4.10. The selection criteria are subjective but strict: only low noise level records with simple source time functions qualify. In total, 1205 traces are selected. Their sampling locations (PREM predicted S wave turning points) are presented in Figure 4.11b. In Figure 4.11 a and c, locations of previously detected S-wave D″ discontinuity are presented. The background tomography is the same as Figure 4.1d. As shown in Figure 4.11c, the locations of some picked records are consistent with the previous detections, and others provide information for new regions, especially in the southern hemisphere. To better illustrate this, the globe is divided into 10˚ by 10˚ cells. Cells with only the new samplings are shown in Figure 4.11d with large purple points.

4.5 Discussion and Future Works

As shown in Figure 4.11b, some of the selected records sample the low velocity regions of the lowermost mantle. However, as mentioned before, the “shouldering” phenomenon should only happen when a high velocity basal layer exists. One possible explanation is that potential anomalous seismic structures beneath stations are causing the similar observations. Therefore, S waves recorded at the same station, from different events should be compared to rule out a receiver structure effect. Nonetheless, our global observation of “shouldering” on large distance S-wave arrivals suggests that D″ discontinuity is most likely global, and therefore temperature-controlled Bm-pPv phase transition is the most possible cause.

The characteristics of waveform broadening and arrival times versus receiver distance (those details discussed in synthetic case studies) have the potential to constrain lowermost mantle structure by modeling against the same measurements from data. However, two major difficulties exist. Firstly, the average shape (comparison baseline) in synthetic analysis was chosen to be a stack of close distance records, which then work as an approximation of the event’s source time function. For real data, the source time function of one earthquake could be azimuthally dependent. Therefore, the stack of close distance records must be within a certain azimuthal corridor to be the proper comparison baseline of the records within the same azimuthal corridor. Secondly, the real Earth could have much more complicated 3D seismic structures, as indicated by the laterally sharp changes of previous detected D″ discontinuity properties. These high dimension structures could generate their own unique multipathing and S waveform broadening patterns, which are not included in our 1D synthetic waveform analyses. High dimension synthetics should be calculated and analyzed to justify the modeling results.

4.6 Conclusion

By investigating individual waveforms from a global dataset, records with unique S wave broadening are documented. These records hold potential for new D″ discontinuity samplings. The cause of the S wave broadening is the birth of one additional phase generated by multipathing and manifests itself ahead of the original S arrival at distance beyond 80˚. The exact cause of this observation at each individual station should be furtherly studied to rule out receiver structure possibility. Nevertheless, comparing to previous studies, this method provides new sampling locations, especially in the southern hemisphere.

References

Avants, M., T. Lay, S. A. Russell, and E. J. Garnero (2006), Shear velocity variation within the D″ region beneath the central Pacific, Journal of Geophysical Research, 111(B5), doi:10.1029/2004JB003270.

Bullen, K. E. (1949), Compressibility-pressure hypothesis and the Earth's interior, Geophys J Int, 5, 335–368, doi:10.1111/j.1365-246X.1949.tb02952.x.

Chaloner, J. W., C. Thomas, and A. Rietbrock (2009), P- and S-wave reflectors in D″ beneath southeast Asia, Geophys J Int, 179(2), 1080 – 1092, doi:10.1111/j.1365-246X.2009.04328.x.

Chambers, K., and J. H. Woodhouse (2006a), Transient D″ discontinuity revealed by seismic migration, Geophysical Research Letters, 33(17), L17312, doi:10.1029/2006GL027043.

Chambers, K., and J. H. Woodhouse (2006b), Investigating the lowermost mantle using migrations of long-period S - ScS data, Geophys J Int, 166(2), 667–678, doi:10.1111/j.1365-246X.2006.03002.x.

Cobden, L., and C. Thomas (2013), The origin of D″ reflections: a systematic study of seismic array data sets, Geophys J Int, 194(2), 1091 – 1118, doi:10.1093/gji/ggt152.

Davis, J. P., and M. Weber (1990), Lower Mantle Velocity Inhomogeneity Observed at GRF Array, Geophysical Research Letters, 17(2), 187–190, doi:10.1029/GL017i002p00187.

Ding, X., and D. V. Helmberger (1997), Modelling D″ structure beneath Central America with broadband seismic data, Physics of the earth and planetary interiors, 101(3-4), 245 – 270, doi:10.1016/S0031-9201(97)00001-0.

Gaherty, J. B., and T. Lay (1992), Investigation of laterally heterogeneous shear velocity structure in D″ beneath Eurasia, Journal of Geophysical Research, 97(B1), 417 – 435, doi:10.1029/91JB02347.

Garnero, E. J., A. K. McNamara, S. Shim (2016), Continent-sized anomalous zones with low seismic velocity at the base of Earth's mantle, Nature Geoscience, 9(7), 481 – 489, https://dx.doi.org/10.1038/ngeo2733

Garnero, E. J., D. V. Helmberger, and S. Grand (1993), Preliminary evidence for a lower mantle shear wave velocity discontinuity beneath the central Pacific, Physics of the earth and planetary interiors, 79(3-4), 335–347, doi:10.1016/0031-9201(93)90113-N.

Garnero, E. J., and T. Lay (2003), D″ shear velocity heterogeneity, anisotropy and discontinuity structure beneath the Caribbean and Central America, Physics of the earth and planetary interiors, 140(1-3), 219 – 242, doi:10.1016/j.pepi.2003.07.014.

Houar, S., and H. C. Nataf (1993), Laterally Varying Reflector at the Top of D″ Beneath Northern Siberia, Geophys J Int, 115(1), 168 – 182, doi:10.1111/j.1365-246X.1993.tb05597.x.

Hutko, A. R., T. Lay, E. J. Garnero, and J. Revenaugh (2006), Seismic detection of folded, subducted lithosphere at the core–mantle boundary, Nature, 441(7091), 333–336, doi:10.1038/nature04757.

Hutko, A. R., T. Lay, J. Revenaugh, and E. J. Garnero (2008), Anticorrelated seismic velocity anomalies from post-perovskite in the lowermost mantle, Science, 320(5879), 1070–1074, doi:10.1126/science.1155822.

Kendall, J. M., and C. Nangini (1996), Lateral variations in D″ below the Caribbean, Geophysical Research Letters, 23(4), 399 – 402, doi:10.1029/95GL02659.

Kendall, J. M., and P. M. Shearer (1994), Lateral variations in D″ thickness from long-period shear wave data, Journal of Geophysical Research, 99(B6), 11575 – 11590, doi:10.1029/94JB00236.

Kito, T., S. Rost, C. Thomas, and E. J. Garnero (2007), New insights into the P- and S-wave velocity structure of the D″ discontinuity beneath the Cocos plate, Geophys J Int, 169(2), 631 – 645, doi:10.1111/j.1365-246X.2007.03350.x.

Lay, T., E. J. Garnero, and S. A. Russell (2004), Lateral variation of the D″ discontinuity beneath the Cocos Plate, Geophysical Research Letters, 31(15), L15612, doi:10.1029/2004GL020300.

Lay, T., J. Hernlund, E. J. Garnero, and M. S. Thorne (2006), A Post-Perovskite Lens and D″ Heat Flux Beneath the Central Pacific, Science, 314(5), 1272 – 1276, doi:10.1126/science.1133280.

Lay, T., and C. J. Young (1991), Analysis of seismic SV waves in the core's penumbra, Geophysical Research Letters, 18(8), 1373–1376, doi:10.1029/91GL01691.

Lay, T., and D. V. Helmberger (1983), A lower mantle S – wave triplication and the shear velocity structure of D″, Geophysical Journal of the Royal Astronomical Society, 75(3), 799 – 837, doi:10.1111/j.1365-246X.1983.tb05010.x.

Lay, T., and E. J. Garnero (2011), Deep Mantle Seismic Modeling and Imaging, Annual Review of Earth and Planetary Sciences, 39(1), 91–123, doi:10.1146/annurev-earth-040610-133354.

Neuberg, J., and J. Wahr (1991), Detailed Investigation of a Spot on the Core Mantle Boundary Using Digital Pcp Data, Physics of the earth and planetary interiors, 68(1-2), 132–143, doi:10.1016/0031-9201(91)90013-8.

Owens, T. J., H. P. Crotwell, C. Groves, and P. Oliver-Paul (2004), SOD: STANDING ORDER FOR DATA, Seismological Research Letters, 75(4), 515–520, doi:10.1785/gssrl.75.4.515-a.

Reasoner, C., and J. Revenaugh (1999), Short-period P wave constraints on D″ reflectivity, J. Geophys. Res. Solid Earth, 104(B), 955 – 961, doi:10.1029/1998JB900053.

Ritsema, J., A. Deuss, H. J. Van Heijst, and J. H. Woodhouse (2011), S40RTS: a degree-40 shear-velocity model for the mantle from new Rayleigh wave dispersion, teleseismic traveltime and normal-mode splitting function measurements, Geophys J Int, 184(3), 1223–1236.

Russell, S. A., C. Reasoner, T. Lay, and J. Revenaugh (2001), Coexisting shear- and compressional-wave seismic velocity discontinuities beneath the central Pacific, Geophysical Research Letters, 28(11), 2281–2284, doi:10.1029/2000GL012553.

Thomas, C., E. J. Garnero, and T. Lay (2004a), High-resolution imaging of lowermost mantle structure under the Cocos plate, Journal of Geophysical Research, 109(B8), 2016–11, doi:10.1029/2004JB003013.

Thomas, C., J. M. Kendall, and M. Weber (2002), The lowermost mantle beneath northern Asia - I. Multi-azimuth studies of a D″ heterogeneity, Geophys J Int, 151(1), 279 – 295, doi:10.1046/j.1365-246X.2002.01759.x.

Thomas, C., J.-M. Kendall, and J. Lowman (2004b), Lower-mantle seismic discontinuities and the thermal morphology of subducted slabs, Earth and Planetary Science Letters, 225(1-2), 105–113, doi:10.1016/j.epsl.2004.05.038.

Thorne, M. S., T. Lay, E. J. Garnero, G. Jahnke, and H. Igel (2007), Seismic imaging of the laterally varying D″ region beneath the Cocos Plate, Geophys J Int, 170(2), 635 – 648, doi:10.1111/j.1365-246X.2006.03279.x.

van der Hilst, R. D., M. V. De Hoop, P. Wang, S. H. Shim, P. Ma, and L. Tenorio (2007), Seismostratigraphy and thermal structure of earth's core-mantle boundary region, Science, 315(5820), 1813–1817, doi:10.1126/science.1137867.

Wallace, M., and C. Thomas (2005), Investigating D″ structure beneath the North Atlantic, Physics of the earth and planetary interiors, 151(1-2), 115 – 127, doi:10.1016/j.pepi.2005.02.001.

Weber, M. (1993), P-Wave and S-Wave Reflections from Anomalies in the Lowermost Mantle, Geophys J Int, 115(1), 183–210, doi:10.1111/j.1365-246X.1993.tb05598.x.

Weber, M., and J. P. Davis (1990), Evidence of a laterally variable lower mantle structure from P ‐ and S ‐ waves, Geophys J Int, 102(1), 231 ‐ 255, doi:10.1111/j.1365-246X.1990.tb00544.x.

Weber, M., and M. Körnig (1992), A search for anomalies in the lowermost mantle using seismic bulletins, Physics of the earth and planetary interiors, 73(1-2), 1–28, doi:10.1016/0031-9201(92)90104-4.

Young, C. J., and T. Lay (1990), Multiple phase analysis of the shear velocity structure in the D″ region beneath Alaska, J. Geophys. Res. Solid Earth, 95(B), 17 ‐ , doi:10.1029/JB095iB11p17385.

Zhang, J., and T. Lay (1984), Investigation of a lower mantle shear wave triplication using a broadband array, Geophysical Research Letters, 11(6), 620–623, doi:10.1029/GL011i006p00620.

Zhao, C., E. J. Garnero, A. K. McNamara, N. Schmerr, and R. W. Carlson (2015), Seismic evidence for a chemically distinct thermochemical reservoir in Earth's deep mantle beneath Hawaii, Earth and Planetary Science Letters, 426, 143–153, doi:10.1016/j.epsl.2015.06.012.

Table 4.1 Summary of previous D″ discontinuity studies.

Reference	Phase [i]	Region [ii]	Property [iii]
Cobden and Thomas [2013]	PdP, SdS (a)	Siberia (y)	1~3(P), 2~3(S)
		Bering Sea (y)	1~1.5(P), 1~2(S)
Thomas et al. [2004a]	SdS (m)	Caribbean (y)	2~3(S),
Thomas et al. [2004b]	SdS (m)	Siberia (y)	1~3(S), 206~316(H)
Kito et al. [2007]	PdP (a,m), SdS (a)	Caribbean (y)	−2~−3(P), 2~3(S), 290(H)
Chaloner et al. [2009]	SdS, PdP (a,m)	Southeast Asia(y)	−1~−2(P), 1~3(S), 200~340(H)
Garnero and Lay [2003]	SdS (o)	Central America(y,c,n)	n/a
Hutko et al. [2008]	PdP, SdS (m)	Cocos plate (y)	−0.07(P), 1.5(S), −1.0(ϕ), 320(H)
Hutko et al. [2006]	SdS (m)	Cocos plate (y)	160~290(H)
Avants et al. [2006]	SdS (a)	Central Pacific(y)	0.5~2.3(S), 156~400(H)
Lay et al. [2006]	SdS (a)	Central Pacific (y)	0.6,0.7,1.1(S), 236,156,345(H)
Chambers and Woodhouse [2006a]	S, ScS (m,s)	Siberia (y)	3.0~3.5(S), 350(H)
Chambers and Woodhouse [2006b]	S, ScS (m,s)	Alaska and west Canada	+(S), 250~340(H)
		Aleutians(y)	+(S), 50~100(H)
Neuberg and Wahr [1991]	PcP,P (r)	North Australia (c,n)	n/a
Wallace and Thomas [2005]	SdS (w)	North Atlantic Ocean Nova Scotia (y)	1~3(S), 86~286(H)
Thomas et al. [2002]	PdP (a,t)	Siberia (y)	3(S), 210, 310(H)
Davis and Weber [1990]	PdP (a)	Siberia (y,n,c)	3(P), 290(H)
Gaherty and Lay [1992]	SdS (t,w)	Eurasia (y)	2.75(S), 290(H)
Garnero et al. [1993]	SdS (t,w)	Central Pacific (y,c)	180, 280(H)
Houard and Nataf [1992, 1993]	PdP (t,r)	Siberia (y)	2~3(P), 300(H)
Kendall and Nangini [1996]	SdS (t,w)	Northeast Caribbean (n)	n/a
		Southeast Caribbean (y)	2.75(S), 250(H)
		Northwest Caribbean (y)	2.45(S), 290(H)
Kendall and Shearer [1994]	SdS (t,w)	Central Asia (y)	140~370(H)
		Central America (y)	~340(H)
		Alaska (y)	160~375(H)

(Continue on next page)

Table 4.1 (*continued*)

Reference	Phase [i]	Region [ii]	Property [iii]
		Australasia (y)	245~300(H)
		Arctic (y)	~268(H)
Lay et al. [2004]	SdS (a)	Central America (y,n)	0.9~2.6(S), 264(H)
Russell et al. [2001]	PdP, SdS (a)	Central Pacific (y)	0.75(P), 1.7(S), 230(H)
Weber [1993]	PdP, SdS (a,t,w,r)	North Siberia (y,n,c)	1.5~3.0(P), ~230(H)
		North Siberia (y,n,c)	2.3(S), ~280(H)
Weber and Körnig [1992]	PdP (-)	N. Atlantic Ridge (y)	2~3(P), 250(H)
		N. Central America (y)	2~3(P), 230(H)
		Japan (y)	2~3(P), 180(H)
		Central MAR (y)	2~3(P), 260,310(H)
		Ecuador (y)	2~3(P), 340(H)
		Central America(n),	n/a
		Eastern Pacific(n),	n/a
		Northern Atlantic (n)	n/a
Weber and Davis [1990]	PdP (a,t,w,r)	Northern Siberia (y,n,c)	~3(P), ~2(S), 290(H)
Young and Lay [1990]	S, ScS, sS, sScS, etc (w,t)	Alaska (y,n)	~2.75(S), 243(H)
Ding and Helmberger [1997]	SdS (w)	Central America (y)	~3.0(S), 200(H)
	PdP (w)	Central America (n)	< 1.0(P)
van der Hilst et al. [2007]	ScS (i)	Central America (y)	150~300(H)
Lay and Helmberger [1983]	SdS (w,r)	Alaska (y,n)	2.75(S), 280(H)
Zhang and Lay [1984]	SdS (w)	Central America (y)	2.75(S), 250(H)
Lay and Young [1991]	S (w)	Alaska (y)	2.1(S), 175(H)
Reasoner and Revenaugh [1999]	PdP (a)	Central America(y) Central Pacific (y)	2~3(S), 0.5~0.6(P), 190(H)

i. Methods used: (a)rray-analysis, 1D (m)igration, (s)catters, (t)ravel-time, (w)aveform modeling, amplitude (r)atio modeling, (o)bservation documentation, waveform (i)nversion.

ii. Detection classification: (y)es detection, (n)o detection, (c)omplex or uncertain observations.

iii. Anomaly type: (P)-wave velocity, (S)-wave velocity, (ϕ) bulk sound velocity, these have unit percentage. (H) D″ discontinuity thickness, it has unit kilometer.

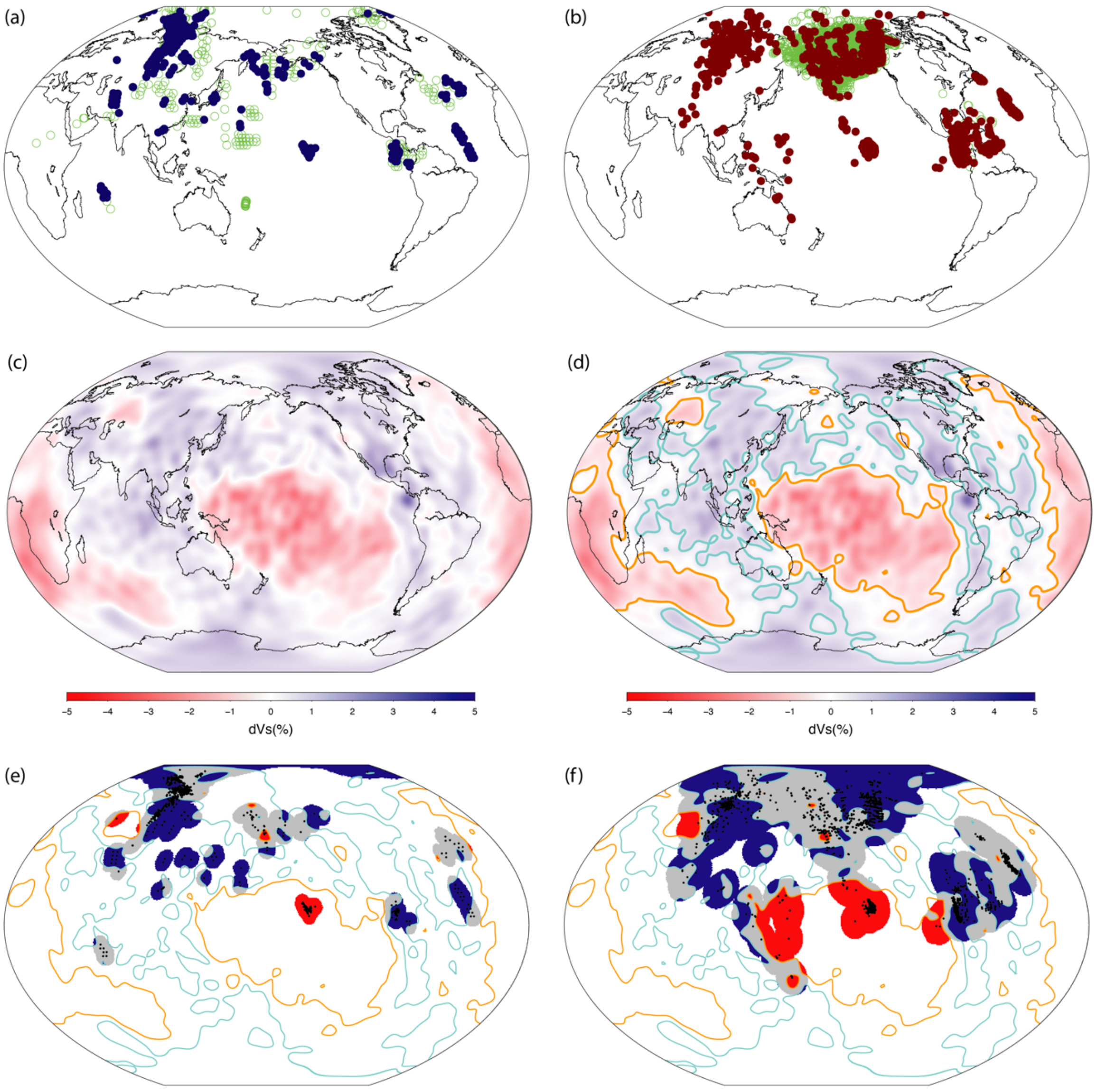

Figure 4.1. Previous D″ discontinuity detection locations. (a) Blue dots: D″ discontinuity locations from previous studies using P waves; open green circle: non-detection of P-wave speed D″ discontinuity. (b) similar as (a), but from S wave studies. Red dots: yes-detections. (c) S-wave tomography model S40RTS at the lowermost mantle (2800 km) [Ritsema et al., 2011]. (d) Velocity contour enclosing the highest 30% CMB area (dark blue line, dVs= 0.442%) and velocity contour enclosing the lowest 30% CMB area (orange line, dVs= −0.269%). (e, f) Fresnel zone approximated D″ discontinuity regions relative to high/low S-velocity contour. In (e), 6.7% of the total D″ discontinuity area lies in low velocity regions; 55.3% lies in high velocity regions. Fresnel zone size has radius of 5˚. In (f), 12.24% of the total D″ discontinuity area lies in low velocity regions; 51.76% lies in high velocity regions.

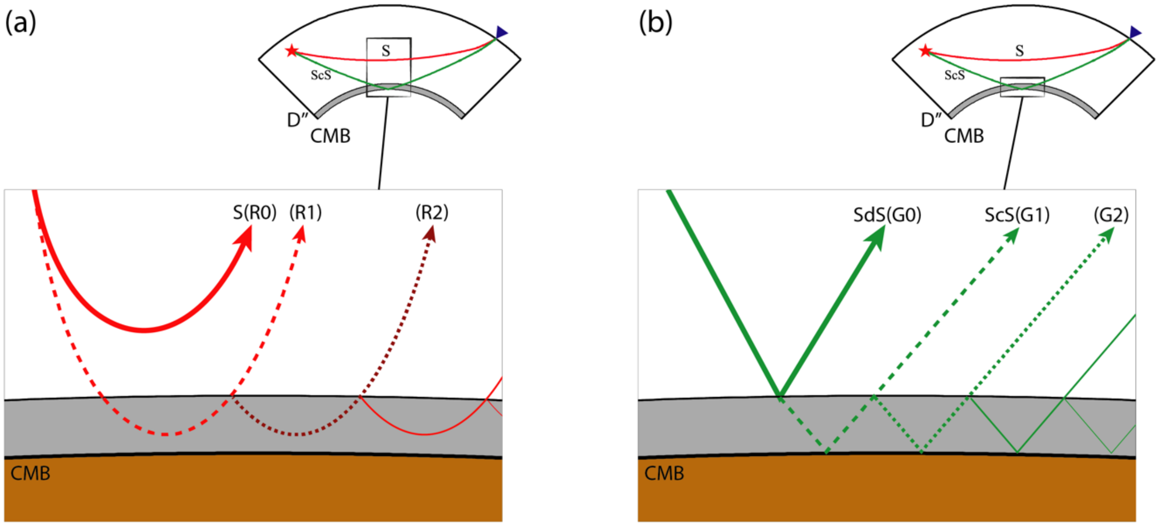

Figure 4.2 S wave multi-pathing possibilities. Cartoons illustrating two kinds of waves: waves turn before reaching the CMB; and waves with a steep takeoff angle and reflect at the CMB. (a) The cartoon ray paths of turning waves. Their names start with a capital R, and they are colored in red. (b) The cartoon ray paths of reflecting waves, whose names start with G. They are colored in green. The number after each R or G means the number of refractions or reflections within the basal velocity layer. For example, R0 doesn't propagate through the basal layer, and R1 samples the basal layer once.

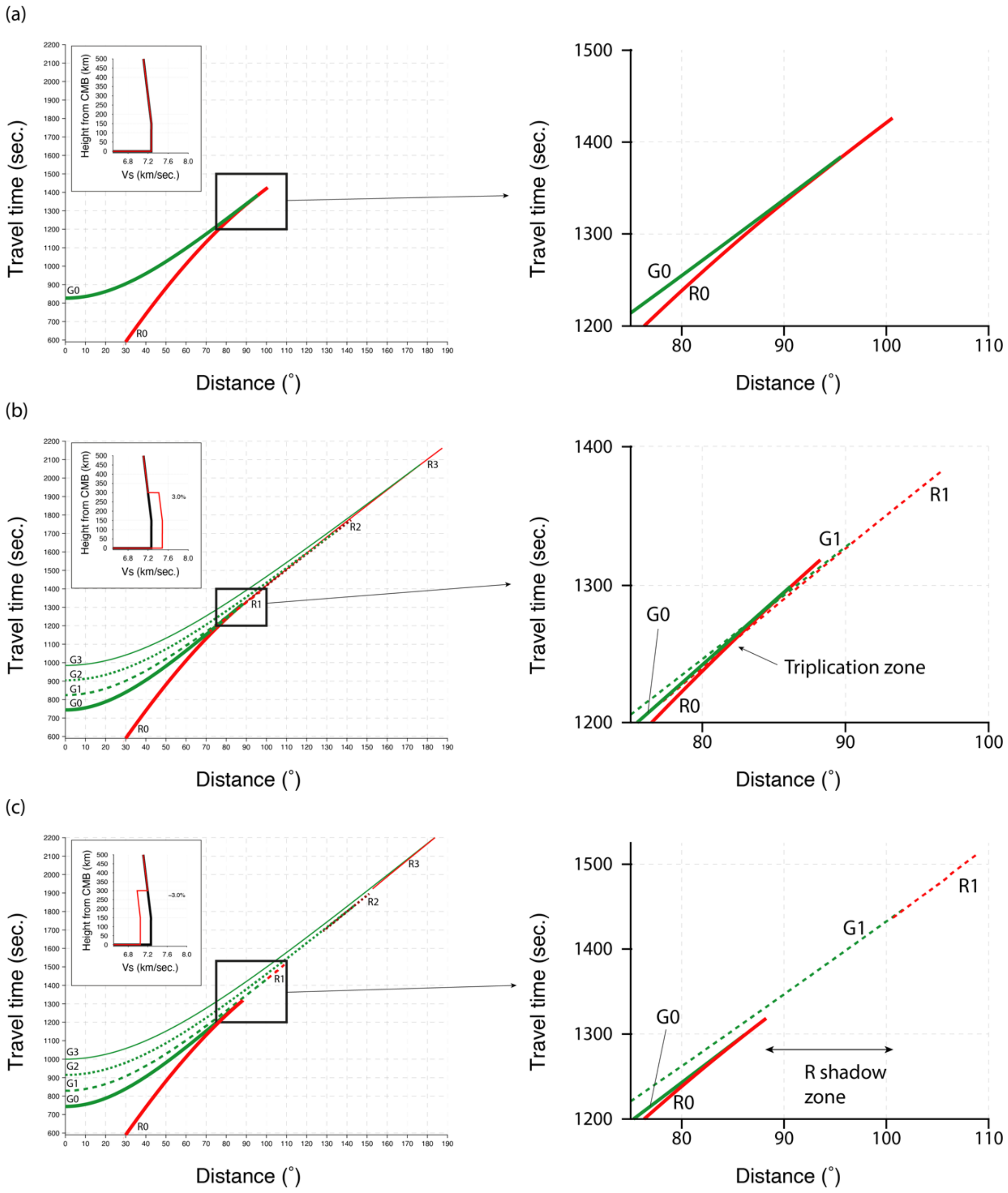

Figure 4.3 S wave multipathing travel time curves. The color scheme is consistent with Figure 4.2: red color is reserved for the R arrivals and green color is reserved for the G arrivals. Notice the transition between R and G waves at large distance, and their travel time curves meet each other. Figures on the right column is zoom-in views within the black squares on the left. In the zoom-in views, R2, R3, G2 and G3 are removed because they have much lower amplitudes. (a) Simple travel time curves for PREM for reference. (b) Travel time curves for R0-R3 and G0-G3 arrivals for a high velocity basal model (300 km, +3% dVs, see inset). The triplication zone is between 80˚ and 88˚, which is marked in its zoom-in view. (c) Travel time curves for a low velocity basal model (300 km, -3% dVs, see inset). The shadow zone for turning waves is between 89˚ to 101˚.

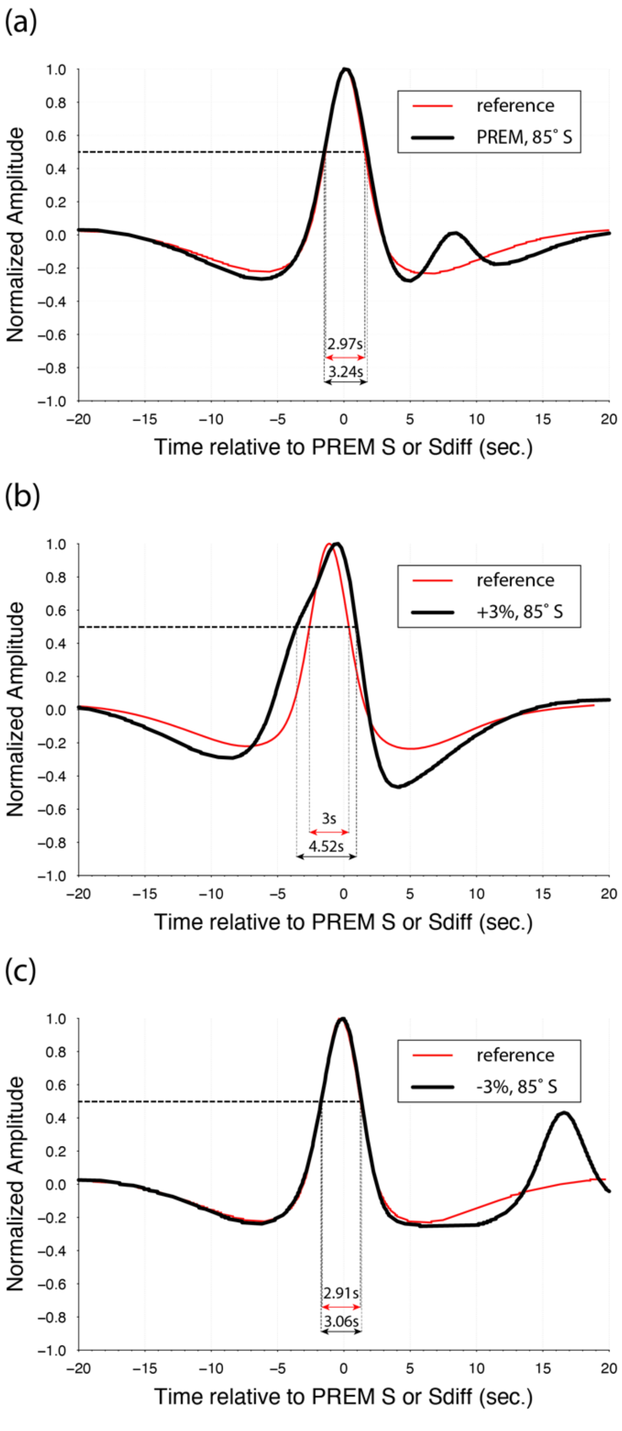

Figure 4.4 Half-height width difference and arrival measurement. S waveforms from 85˚ is plotted in black, and the reference shape, close distance stack, is plotted in red. (a) for PREM, the relative arrival is 0 second, the half-height width difference is about 9%. (b) for a high velocity (+3%) basal layer, the relative arrival is around -2 second, and the half-height width difference is about 50%. (c) for a low velocity (-3%) basal layer, the relative arrival is around 0 second, and the half-height width difference is about 5%.

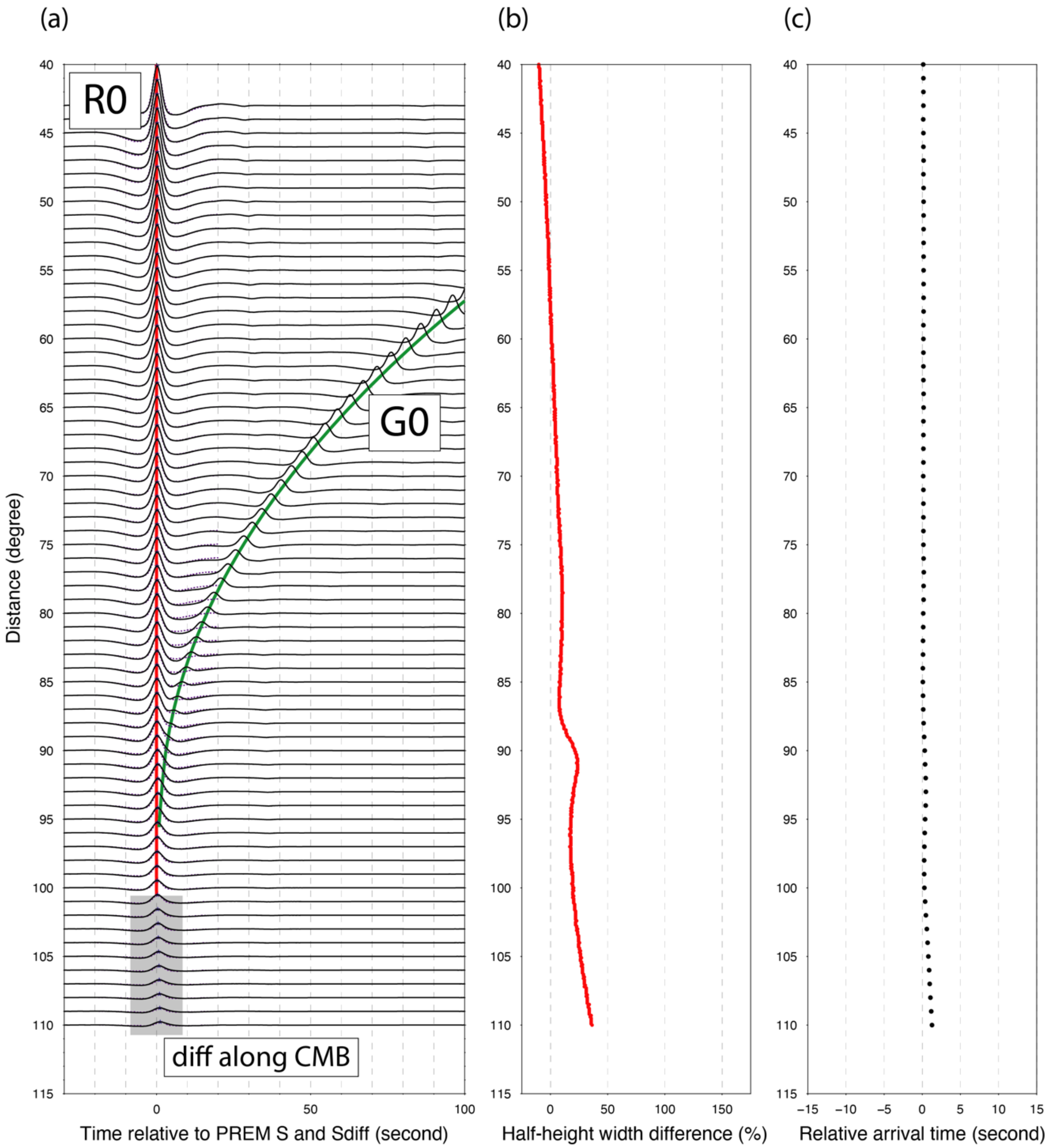

Figure 4.5 (a) Synthetics profile for PREM with travel time curves (red and green, same color scheme as Figure 4.3). Reference wave shapes are plotted in purple dash lines. Blue stars denote the peak where half-height width difference is measured from. (b) PREM half-height width difference measurements versus distance. (c) PREM relative arrival time measurements versus distance. Notice the slight delay beyond 100˚.

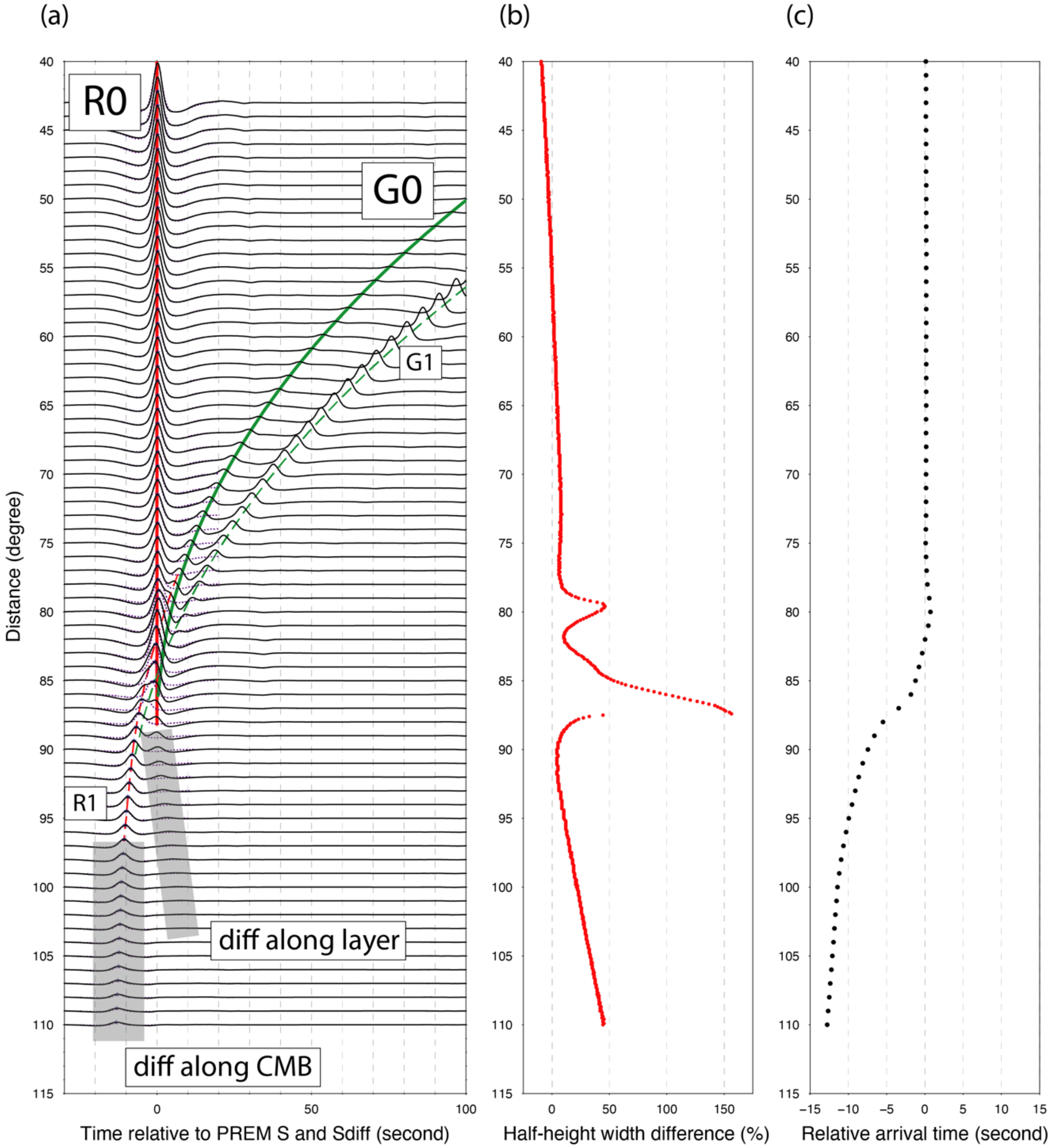

Figure 4.6 (a) Synthetics profile for a high velocity basal layer (300 km, +3% dVs). Travel time curves and reference wave shapes are overlapped plotted. (b) Half-height width difference measurements for this model. (c) relative arrival time measurements for this model.

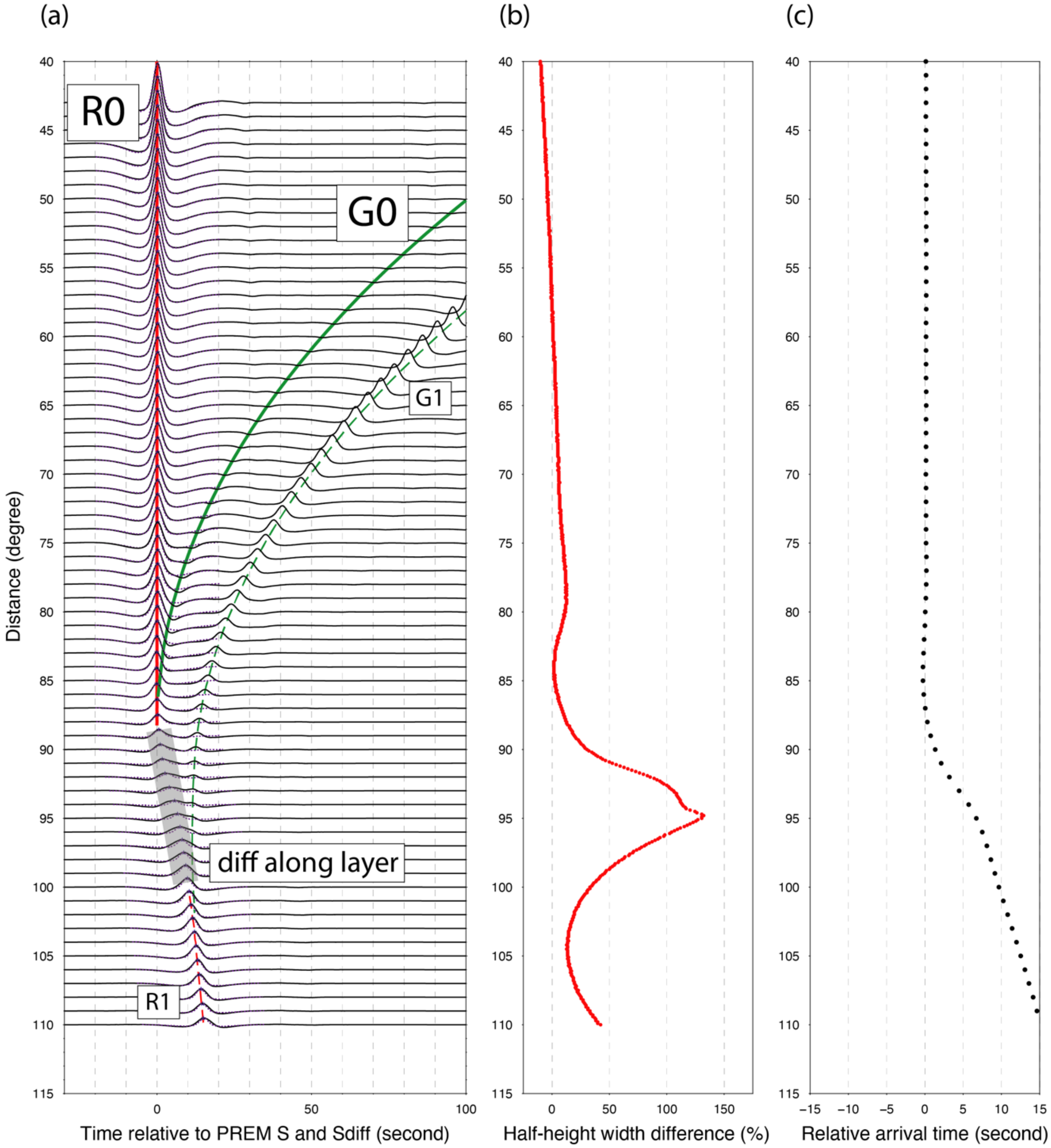

Figure 4.7 (a) Synthetics profile for a low velocity basal layer (300 km, −3% dVs). Travel time curves and reference wave shapes are overlapped plotted. (b) Half-height width difference measurements for this model. (c) relative arrival time measurements for this model.

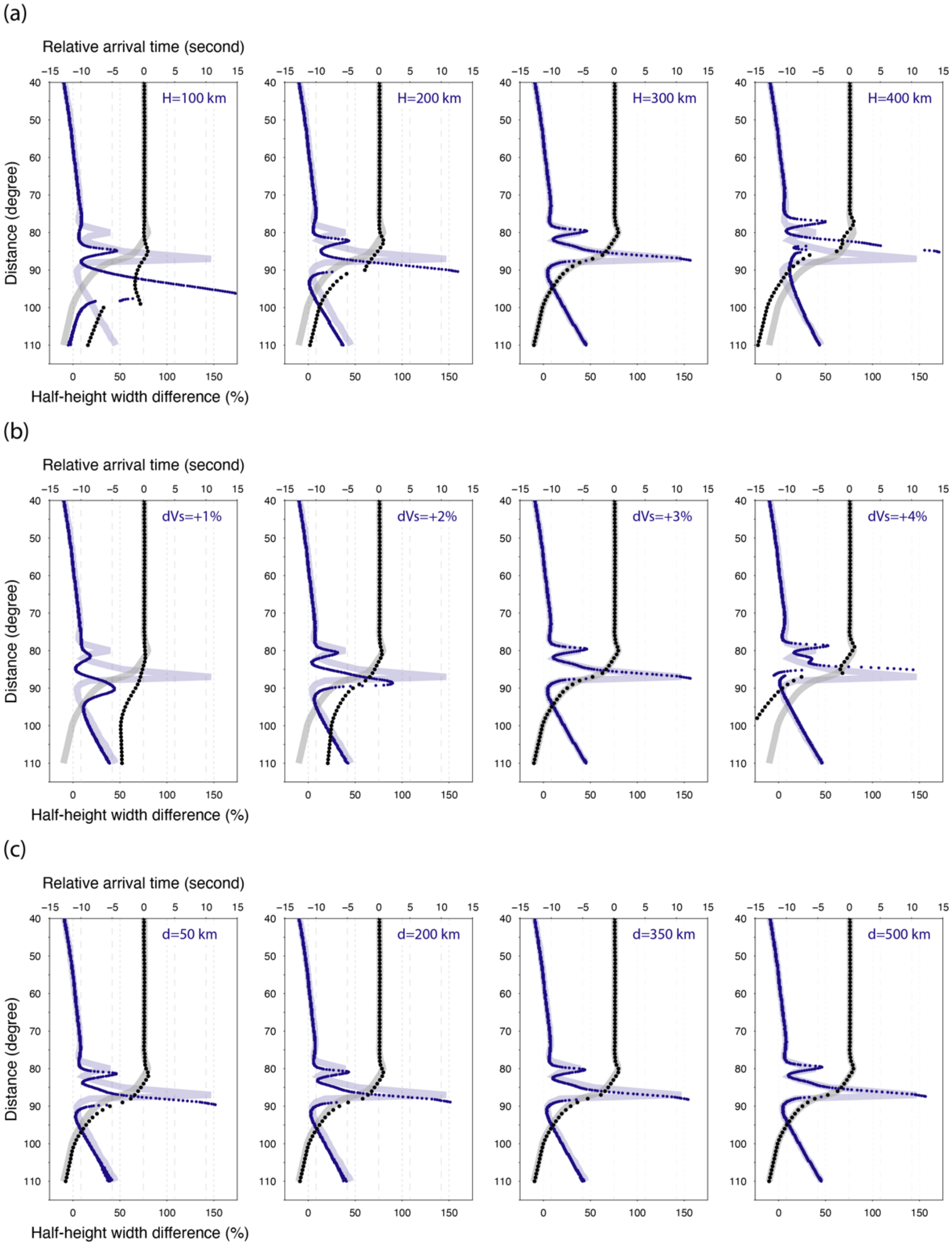

Figure 4.8 Broadening (half-height width difference) and arrival time measurements of S for several high velocity basal layer models. The reference model is 300 km thick, +3% dVs with source at 500 km deep. The measurements from the reference model is plotted in shades, for comparison. (a) varying the layer thickness, (b) varying the layer velocity increase and (c) varying the source depth.

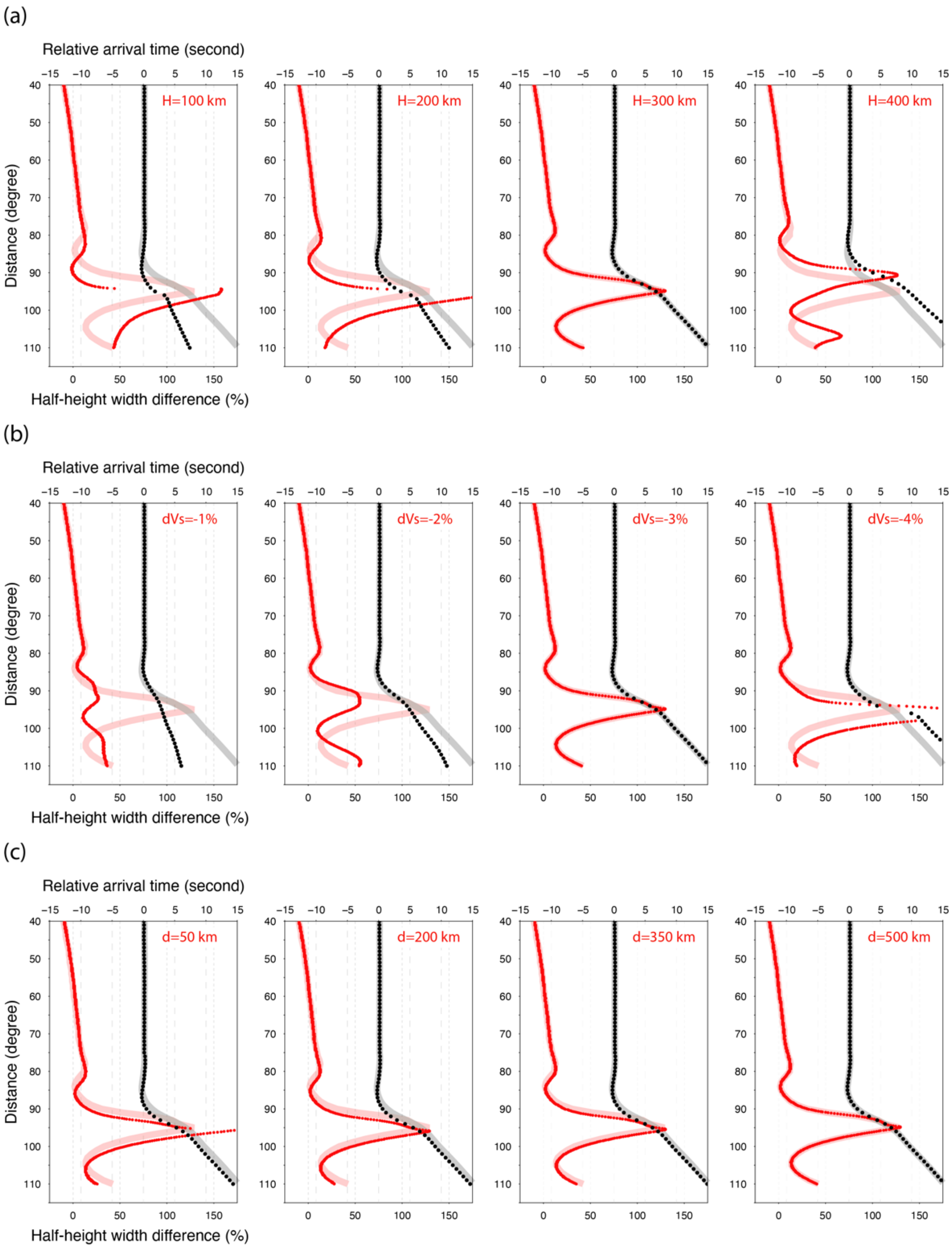

Figure 4.9 Broadening measurements (half-height width difference) and arrival time of S for several low velocity basal layer models. The reference model is 300 km thick, −3% dVs with source at 500 km deep. The measurements from the reference model is plotted in shades, for comparison. (a) varying the layer thickness, (b) varying the layer velocity increase and (c) varying the source depth.

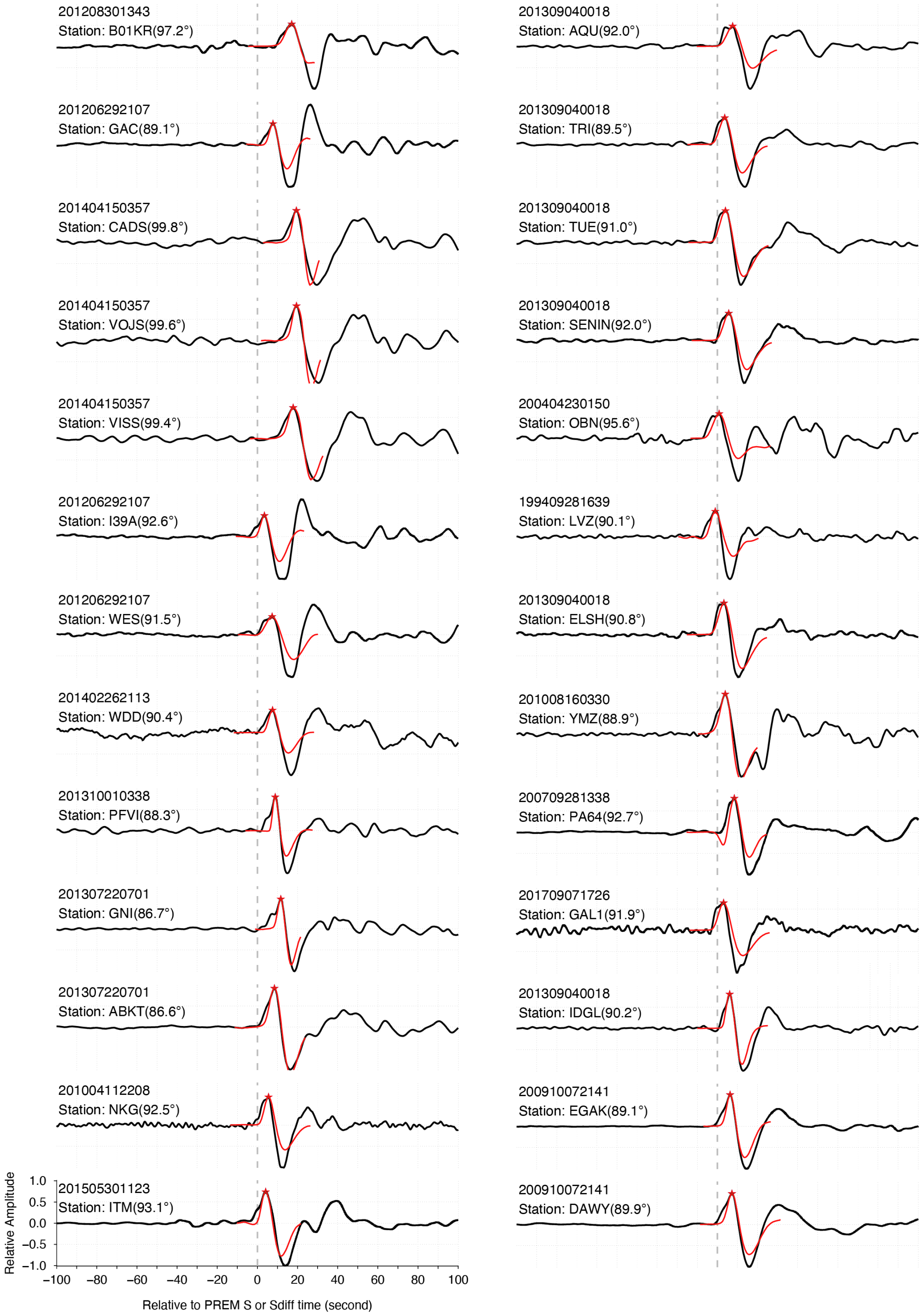

Figure 4.10 Data examples from the hand-picked dataset manifesting R1 birth from R0. Red line is the average shape (source time function) from each individual event. PREM prediction of S or Sdiff are at zero second, which is indicated in a gray vertical dash line. Event name and station name with its great circle distance is marked in text.

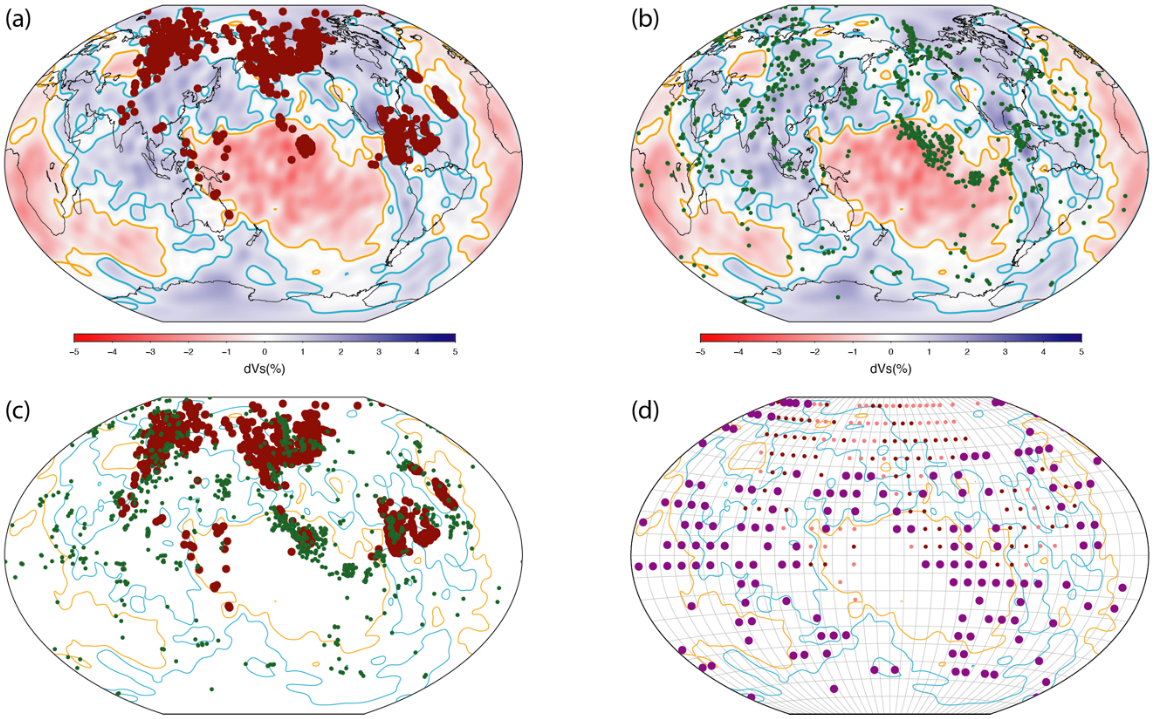

Figure 4.11 (a) previous S-wave D″ discontinuity locations from studies listed in Table 4.1. Tomography model and contours are the same as Figure 4.1 (b) Locations of S wave turning point for the observed birth of R1 (1205 selected records) are plotted in green points. (c) Overlapped plot (b) with previous detected D″ discontinuity locations. (d) 10˚ by 10˚ grid indicate previous and new samplings. Grids with only new samplings (this study) are indicated by slightly larger purple points. Grids with only previous studies are indicated by small pink points. Grids with both old and new samplings are indicated by small red points.

REFERENCES

Ammann, M. W., J. P. Brodholt, J. Wookey, and D. P. Dobson (2010), First-principles constraints on diffusion in lower-mantle minerals and a weak D″ layer, Nature, 465(7297), 462–465, doi:10.1038/nature09052.

Andrault, D., G. Pesce, M. A. Bouhifd, N. Bolfan-Casanova, J. M. Henot, and M. Mezouar (2014), Melting of subducted basalt at the core-mantle boundary, Science, 344(6186), 892–895, doi:10.1126/science.1250466.

Andrault, D., M. Muñoz, N. Bolfan-Casanova, N. Guignot, J.-P. Perrillat, G. Aquilanti, and S. Pascarelli (2010), Experimental evidence for perovskite and post-perovskite coexistence throughout the whole D″ region, Earth and Planetary Science Letters, 293(1-2), 90–96, doi:10.1016/j.epsl.2010.02.026.

Andrault, D., N. Bolfan-Casanova, G. Lo Nigro, M. A. Bouhifd, G. Garbarino, and M. Mezouar (2011), Solidus and liquidus profiles of chondritic mantle: Implication for melting of the Earth across its history, Earth and Planetary Science Letters, 304(1-2), 251–259, doi:10.1016/j.epsl.2011.02.006.

Anzellini, S., A. Dewaele, M. Mezouar, P. Loubeyre, and G. Morard (2013), Melting of Iron at Earth's Inner Core Boundary Based on Fast X-ray Diffraction, Science, 340(6131), 464–466, doi:10.1126/science.1233514.

Avants, M., T. Lay, S. A. Russell, and E. J. Garnero (2006), Shear velocity variation within the D″ region beneath the central Pacific, Journal of Geophysical Research, 111(B5), doi:10.1029/2004JB003270.

Avants, M., T. Lay, and E. J. Garnero (2006), A new probe of ULVZ S-wave velocity structure: Array stacking of ScS waveforms, Geophysical Research Letters, 33(7), 297, doi:10.1029/2005GL024989.

Berryman, J. G. (2000), Seismic velocity decrement ratios for regions of partial melt in the lower mantle, Geophysical Research Letters, 27(3), 421–424, doi:10.1029/1999GL008402.

Brown, S. P., M. S. Thorne, L. Miyagi, and S. Rost (2015), A compositional origin to ultralow-velocity zones, Geophysical Research Letters, 42(4), 1039–1045, doi:10.1002/2014GL062097.

Bréger, L., and B. Romanowicz (1998), Three-dimensional structure at the base of the mantle beneath the central Pacific, Science, 282(5389), 718–720, doi:10.1126/science.282.5389.718.

Buffett, B. A., E. J. Garnero, and R. Jeanloz (2000), Sediments at the Top of Earth's Core, Science, 290(5495), 1338–1342, doi:10.1126/science.290.5495.1338.

Bullen, K. E. (1940), The problem of the earth's density variation, Bulletin of the Seismological Society of America, 30(3), 235–250.

Bullen, K. E. (1949), Compressibility-pressure hypothesis and the Earth's interior, Geophys J Int, 5, 335–368, doi:10.1111/j.1365-246X.1949.tb02952.x.

Castle, J. C., and R. D. Van Der Hilst (2000), The core–mantle boundary under the Gulf of Alaska: no ULVZ for shear waves, Earth and Planetary Science Letters, 176(3-4), 311–321, doi:10.1016/S0012-821X(00)00027-3.

Catalli, K., S.-H. Shim, and V. Prakapenka (2009), Thickness and Clapeyron slope of the post-perovskite boundary, Nature, 462(7274), 782–785, doi:10.1038/nature08598.

Chaloner, J. W., C. Thomas, and A. Rietbrock (2009), P- and S-wave reflectors in D″ beneath southeast Asia, Geophys J Int, 179(2), 1080–1092, doi:10.1111/j.1365-246X.2009.04328.x.

Chambers, K., and J. H. Woodhouse (2006a), Transient D″ discontinuity revealed by seismic migration, Geophysical Research Letters, 33(17), L17312, doi:10.1029/2006GL027043.

Chambers, K., and J. H. Woodhouse (2006b), Investigating the lowermost mantle using migrations of long-period S - ScS data, Geophys J Int, 166(2), 667–678, doi:10.1111/j.1365-246X.2006.03002.x.

Christensen, U. R. (1996), The influence of trench migration on slab penetration into the lower mantle, Earth and Planetary Science Letters, 140(1-4), 27–39, doi:10.1016/0012-821X(96)00023-4.

Christensen, U. R., and A. W. Hofmann (1994), Segregation of subducted oceanic crust in the convecting mantle, Journal of Geophysical Research: Solid Earth (1978–2012), 99(B10), 19867–19884, doi: 10.1029/93JB03403.

Clayton, R. W., and R. A. Wiggins (1976), Source shape estimation and deconvolution of teleseismic body waves, Geophysical Journal of the Royal Astronomical Society, 47(1), 151–177, doi:10.1111/j.1365-246X.1976.tb01267.x.

Cobden, L., C. Thomas, and J. Trampert (2015), Seismic detection of post-perovskite inside the earth, in The Earth's Heterogeneous Mantle: A Geophysical, Geodynamical, and Geochemical Perspective, pp. 391–440, doi: 10.1007/978-3-319-15627-9_13.

Cobden, L., and C. Thomas (2013), The origin of D″ reflections: a systematic study of seismic array data sets, Geophys J Int, 194(2), 1091–1118, doi:10.1093/gji/ggt152.

Cottaar, S., and B. Romanowicz (2012), An unusually large ULVZ at the base of the mantle near Hawaii, Earth and Planetary Science Letters, 355-356, 213–222, doi:10.1016/j.epsl.2012.09.005.

Cottaar, S., T. Heister, I. Rose, and C. Unterborn (2014), BurnMan: A lower mantle mineral physics toolkit, Geochem. Geophys. Geosyst., 15(4), 1164–1179, doi:10.1002/2013gc005122.

Courtier, A. M., B. Bagley, and J. Revenaugh (2007), Whole mantle discontinuity structure beneath Hawaii, Geophysical Research Letters, 34(17), 51, doi:10.1029/2007GL031006.

Courtillot, V., A. Davaille, J. Besse, and J. Stock (2003), Three distinct types of hotspots in the Earth's mantle, Earth and Planetary Science Letters, 205(3), 295–308, doi:10.1016/S0012-821X(02)01048-8.

Davaille, A., E. Stutzmann, G. Silveira, J. Besse, and V. Courtillot (2005), Convective patterns under the Indo-Atlantic « box », Earth and Planetary Science Letters, 239(3-4), 233–252, doi:10.1016/j.epsl.2005.07.024.

Davies, D. R., S. Goes, J. H. Davies, B. S. A. Schuberth, H. P. Bunge, and J. Ritsema (2012), Reconciling dynamic and seismic models of Earth's lower mantle: The dominant role of thermal heterogeneity, Earth and Planetary Science Letters, 353-354, 253–269, doi:10.1016/j.epsl.2012.08.016.

Davis, J. P., and M. Weber (1990), Lower Mantle Velocity Inhomogeneity Observed at GRF Array, Geophysical Research Letters, 17(2), 187–190, doi:10.1029/GL017i002p00187.

Deschamps, F., L. Cobden, and P. J. Tackley (2012), The primitive nature of large low shear-wave velocity provinces, Earth and Planetary Science Letters, 349-350(C), 198–208, doi:10.1016/j.epsl.2012.07.012.

Ding, X., and D. V. Helmberger (1997), Modelling D″ structure beneath Central America with broadband seismic data, Physics of the earth and planetary interiors, 101(3-4), 245–270, doi:10.1016/S0031-9201(97)00001-0.

Dobson, D. P., and J. P. Brodholt (2005), Subducted banded iron formations as a source of ultralow-velocity zones at the core–mantle boundary, Nature, 434(7031), 371–374, doi:10.1038/nature03430.

Dziewonski, A. M., and D. L. Anderson (1981), Preliminary reference Earth model, Physics of the earth and planetary interiors, 25(4), 297-356, doi:10.1016/0031-9201(81)90046-7.

Dziewoński, A. M., and J. H. Woodhouse (1987), Global Images of the Earth's Interior, Science, 236(4797), 37–48, doi:10.1126/science.236.4797.37.

French, S. W., and B. A. Romanowicz (2014), Whole-mantle radially anisotropic shear velocity structure from spectral-element waveform tomography, Geophys J Int, 199(3), 1303–1327, doi:10.1093/gji/ggu334.

Frost, D. A., and S. Rost (2014), The P-wave boundary of the Large-Low Shear Velocity Province beneath the Pacific, Earth and Planetary Science Letters, 403, 380–392, doi:10.1016/j.epsl.2014.06.046.

Fuchs, K., and G. Muller (1971), Computation of Synthetic Seismograms with the Reflectivity Method and Comparison with Observations, Geophysical Journal of the Royal Astronomical Society, 23(4), 417–433, doi:10.1111/j.1365-246X.1971.tb01834.x.

Fuchs, K. (1980), Calculation of Synthetic seismograms by the reflectivity method, *Bureau of Mineral Resources, Geology and Geophysics*, Record 1980/64, c.3.

Fukao, Y., M. Obayashi, T. Nakakuki, the Deep Slab Project Group (2009), Stagnant Slab: A Review, Annu. Rev. Earth Planet. Sci., 37(1), 19–46, doi:10.1146/annurev.earth.36.031207.124224.

Fukao, Y., and M. Obayashi (2013), Subducted slabs stagnant above, penetrating through, and trapped below the 660 km discontinuity, J. Geophys. Res. Solid Earth, 118(11), 5920–5938, doi:10.1002/2013JB010466.

Gaherty, J. B., and T. Lay (1992), Investigation of laterally heterogeneous shear velocity structure in D″ beneath Eurasia, Journal of Geophysical Research, 97(B1), 417–435, doi:10.1029/91JB02347.

Garnero, E. J., A. K. McNamara, and S.-H. Shim (2016), Continent-sized anomalous zones with low seismic velocity at the base of Earth's mantle, Nature Geoscience, 9(7), 481–489, doi:10.1038/ngeo2733.

Garnero, E. J., D. V. Helmberger, and S. Grand (1993), Preliminary evidence for a lower mantle shear wave velocity discontinuity beneath the central Pacific, Physics of the earth and planetary interiors, 79(3-4), 335–347, doi:10.1016/0031-9201(93)90113-N.

Garnero, E. J., and D. V. Helmberger (1998), Further structural constraints and uncertainties of a thin laterally varying ultralow-velocity layer at the base of the mantle, J. Geophys. Res. Solid Earth, 103(6), 12495–12509, doi:10.1029/98JB00700.

Garnero, E. J., and J. E. Vidale (1999), ScP; A probe of ultralow velocity zones at the base of the mantle, Geophysical Research Letters, 26(3), 377–380, doi:10.1029/1998GL900319.

Garnero, E. J., and T. Lay (2003), D″ shear velocity heterogeneity, anisotropy and discontinuity structure beneath the Caribbean and Central America, Physics of the earth and planetary interiors, 140(1-3), 219–242, doi:10.1016/j.pepi.2003.07.014.

Gassner, A., C. Thomas, F. Krüger, and M. Weber (2015), Probing the core-mantle boundary beneath Europe and Western Eurasia: A detailed study using PcP, Physics of the earth and planetary interiors, 246, 9–24, doi:10.1016/j.pepi.2015.06.007.

Goarant, F., F. Guyot, J. Peyronneau, and J. P. Poirier (1992), High-pressure and high-temperature reactions between silicates and liquid iron alloys in the diamond anvil cell, studied by analytical electron microscopy, Journal of Geophysical Research, 97(B4), 4477–4487, doi:10.1029/92JB00018.

Graham, D. W. (2002), Noble Gas Isotope Geochemistry of Mid-Ocean Ridge and Ocean Island Basalts: Characterization of Mantle Source Reservoirs, Reviews in Mineralogy and Geochemistry, 47(1), 247–317, doi:10.2138/rmg.2002.47.8.

Grand, S. P. (2002), Mantle shear-wave tomography and the fate of subducted slabs, edited by J. H. Davies, J. P. Brodholt, and B. J. Wood, Philosophical Transactions of the Royal Society of London Series a-Mathematical Physical and Engineering Sciences, 360(1800), 2475–2491, doi:10.1098/rsta.2002.1077.

Grand, S. P., R. D. Van Der Hilst, and S. Widiyantoro (1997), Global seismic tomography: A snapshot of convection in the earth, GSA Today, 7(4).

Grocholski, B., K. Catalli, S.-H. Shim, and V. Prakapenka (2012), Mineralogical effects on the detectability of the postperovskite boundary, Proceedings of the National Academy of Sciences, 109(7), 2275–2279, doi:10.1073/pnas.1109204109/-/DCSupplemental/pnas.1109204109_SI.pdf.

Gurnis, M., and B. H. Hager (1988), Controls of the structure of subducted slabs, Nature, 335(6188), 317–321, doi:10.1038/335317a0.

Havens, E., and J. Revenaugh (2001), A broadband seismic study of the lowermost mantle beneath Mexico: Constraints on ultralow velocity zone elasticity and density, Journal of Geophysical Research: Solid Earth (1978–2012), 106(B12), 30809–30820, doi:10.1029/2000JB000072.

He, Y., and L. Wen (2009), Structural features and shear-velocity structure of the “Pacific Anomaly,” Journal of Geophysical Research, 114(B2), L07314, doi:10.1029/2008JB005814.

Helffrich, G., M. D. Ballmer, and K. Hirose (2018), Core-Exsolved SiO 2Dispersal in the Earth's Mantle, J. Geophys. Res. Solid Earth, 123(1), 176–188, doi:10.1002/2017JB014865.

Helmberger, D. V., L. Wen, and X. Ding (1998), Seismic evidence that the source of the Iceland hotspot lies at the core-mantle boundary, Nature, 396(6708), 251–255, doi:10.1038/24357.

Helmberger, D., S. Ni, L. Wen, and J. Ritsema (2000), Seismic evidence for ultralow-velocity zones beneath Africa and eastern Atlantic, Journal of Geophysical Research, 105(B10), 23865–23878, doi:10.1029/2000JB900143.

Helmberger, D., and R. A. Wiggins (1971), Upper mantle structure of midwestern United States, Journal of Geophysical Research: Solid Earth (1978–2012), 76(14), 3229–3245, doi:10.1029/JB076i014p03229.

Hernlund, J. W., C. Thomas, and P. J. Tackley (2005), A doubling of the post-perovskite phase boundary and structure of the Earth's lowermost mantle, Nature, 434(7035), 882–886, doi: 10.1038/nature03472.

Hernlund, J. W., and A. K. McNamara (2015), The Core-Mantle Boundary Region, in Treatise on Geophysics, pp. 461–519, Elsevier.

Hernlund, J. W., and P. J. Tackley (2007), Some dynamical consequences of partial melting in Earth’s deep mantle, Physics of the earth and planetary interiors, 162(1-2), 149–163, doi:10.1016/j.pepi.2007.04.005.

Hirose, K., N. Takafuji, N. Sata, and Y. Ohishi (2005), Phase transition and density of subducted MORB crust in the lower mantle, Earth and Planetary Science Letters, 237(1-2), 239–251, doi:10.1016/j.epsl.2005.06.035.

Hofmann, A. W. (1997), Mantle geochemistry: the message from oceanic volcanism, Nature, 385(6613), 219–229, doi: 10.1038/385219a0.

Hofmann, A. W., and S. R. Hart (1978), An assessment of local and regional isotopic equilibrium in the mantle, Earth and Planetary Science Letters, 38(1), 44–62, doi:10.1016/0012-821X(78)90125-5.

Holzapfel, C., D. C. Rubie, D. J. Frost, and F. L. Science (2005), Fe-Mg interdiffusion in (Mg, Fe) SiO3 perovskite and lower mantle re-equilibration, Science, 309(5741), 1707–1710, doi:10.1126/science.1111895.

Houar, S., and H. C. Nataf (1993), Laterally Varying Reflector at the Top of D″ Beneath Northern Siberia, Geophys J Int, 115(1), 168–182, doi:10.1111/j.1365-246X.1993.tb05597.x.

Houser, C., G. Masters, P. Shearer, and G. Laske (2008), Shear and compressional velocity models of the mantle from cluster analysis of long-period waveforms, Geophys J Int, 174(1), 195–212, doi:10.1111/j.1365-246X.2008.03763.x.

Hu, Q., D. Y. Kim, W. Yang, L. Yang, Y. Meng, L. Zhang, and H.-K. Mao (2016), FeO2 and FeOOH under deep lower-mantle conditions and Earth’s oxygen-hydrogen cycles, Nature, 534(7606), 241–244, doi:10.1038/nature18018.

Hutko, A. R., T. Lay, E. J. Garnero, and J. Revenaugh (2006), Seismic detection of folded, subducted lithosphere at the core–mantle boundary, Nature, 441(7091), 333–336, doi:10.1038/nature04757.

Hutko, A. R., T. Lay, J. Revenaugh, and E. J. Garnero (2008), Anticorrelated seismic velocity anomalies from post-perovskite in the lowermost mantle, Science, 320(5879), 1070–1074, doi:10.1126/science.1155822.

Hutko, A. R., T. Lay, and J. Revenaugh (2009), Localized double-array stacking analysis of PcP: D″ and ULVZ structure beneath the Cocos plate, Mexico, central Pacific, and north Pacific, Physics of the earth and planetary interiors, 173(1-2), 60–74, doi:10.1016/j.pepi.2008.11.003.

Hyung, E., S. Huang, M. I. Petaev, and S. B. Jacobsen (2016), Is the mantle chemically stratified? Insights from sound velocity modeling and isotope evolution of an early magma ocean, Earth and Planetary Science Letters, 440(C), 158–168, doi:10.1016/j.epsl.2016.02.001.

Idehara, K. (2011), Structural heterogeneity of an ultra-low-velocity zone beneath the Philippine Islands: Implications for core–mantle chemical interactions induced by massive partial melting at the bottom of the mantle, Physics of the earth and planetary interiors, 184(1), 80–90, doi:10.1016/j.pepi.2010.10.014.

Idehara, K., A. Yamada, and D. Zhao (2007), Seismological constraints on the ultralow velocity zones in the lowermost mantle from core-reflected waves, Physics of the earth and planetary interiors, 165(1-2), 25–46, doi:10.1016/j.pepi.2007.07.005.

Iitaka, T., K. Hirose, K. Kawamura, and M. Murakami (2004), The elasticity of the MgSiO 3 post-perovskite phase in the Earth's lowermost mantle, Nature, 430(6998), 442–445, doi:10.1038/nature02702.

Irifune, T. (1987), An experimental investigation of the pyroxene-garnet transformation in a pyrolite composition and its bearing on the constitution of the mantle, Physics of the earth and planetary interiors, 45(4), 324–336, doi:10.1016/0031-9201(87)90040-9.

Irifune, T. and Ringwood, A. E. (1987). Phase transformations in primitive MORB and pyrolite compositions to 25 GPa and some geophysical implications. In High-pressure research in mineral physics: a volume in honor of Syun-iti Akimoto, pp 231-242. doi:10.1029/GM039p0231.

Ishii, M., and J. Tromp (2004), Constraining large-scale mantle heterogeneity using mantle and inner-core sensitive normal modes, Physics of the earth and planetary interiors, 146(1-2), 113–124, doi:10.1016/j.pepi.2003.06.012.

Jahnke, G., M. S. Thorne, A. Cochard, and H. Igel (2008), Global SH-wave propagation using a parallel axisymmetric spherical finite-difference scheme: application to whole mantle scattering, Geophys J Int, 173(3), 815–826, doi:10.1111/j.1365-246X.2008.03744.x.

Jellinek, A. M., and M. Manga (2004), Links between long-lived hot spots, mantle plumes, D″, and plate tectonics, Rev. Geophys., 42(3), doi:10.1029/2003RG000144.

Jensen, K. J., M. S. Thorne, and S. Rost (2013), SPdKS analysis of ultralow-velocity zones beneath the western Pacific, Geophysical Research Letters, 40(17), 4574–4578, doi:10.1002/grl.50877.

Jones, T. D., D. R. Davies, and P. A. Sossi (2019), Tungsten isotopes in mantle plumes: Heads it's positive, tails it's negative, Earth and Planetary Science Letters, 506, 255–267, doi:10.1016/j.epsl.2018.11.008.

Kaneshima, S. (2016), Seismic scatterers in the mid-lower mantle, Physics of the earth and planetary interiors, 257, 105–114, doi:10.1016/j.pepi.2016.05.004.

Kendall, J. M., and C. Nangini (1996), Lateral variations in D″ below the Caribbean, Geophysical Research Letters, 23(4), 399–402, doi:10.1029/95GL02659.

Kendall, J. M., and P. M. Shearer (1994), Lateral variations in D″ thickness from long-period shear wave data, Journal of Geophysical Research, 99(B6), 11575–11590, doi:10.1029/94JB00236.

Kennett, B. L. N., E. R. Engdahl, and R. Buland (1995), Constraints on seismic velocities in the Earth from traveltimes, Geophys J Int, 122(1), 108–124, doi:10.1111/j.1365-246X.1995.tb03540.x.

Kennett, B., and E. R. Engdahl (1991), Traveltimes for global earthquake location and phase identification, Geophysical Journal International, 105(2), 429–465, doi:10.1111/j.1365-246X.1991.tb06724.x.

Kito, T., S. Rost, C. Thomas, and E. J. Garnero (2007), New insights into the P- and S-wave velocity structure of the D″ discontinuity beneath the Cocos plate, Geophys J Int, 169(2), 631–645, doi:10.1111/j.1365-246X.2007.03350.x.

Knittle, E., and R. Jeanloz (1989), Simulating the core-mantle boundary: An experimental study of high-pressure reactions between silicates and liquid iron, Geophysical Research Letters, 16(7), 609–612, doi:10.1029/GL016i007p00609.

Kobayashi, Y., T. Kondo, E. Ohtani, N. Hirao, N. Miyajima, T. Yagi, T. Nagase, and T. Kikegawa (2005), Fe-Mg partitioning between (Mg, Fe)SiO 3post-perovskite, perovskite, and magnesiowüstite in the Earth's lower mantle, Geophysical Research Letters, 32(19), n/a–n/a, doi:10.1029/2005GL023257.

Koelemeijer, P., A. Deuss, and J. Ritsema (2017), Density structure of Earth’s lowermost mantle from Stoneley mode splitting observations, Nature Communications, 8(1), 15241, doi:10.1038/ncomms15241.

Koelemeijer, P., J. Ritsema, A. Deuss, and H. J. Van Heijst (2015), SP12RTS: a degree-12 model of shear- and compressional-wave velocity for Earth's mantle, Geophys J Int, 204(2), 1024–1039, doi:10.1093/gji/ggv481.

Kohler, M. D., J. E. Vidale, and P. M. Davis (1997), Complex scattering within D″ observed on the very dense Los Angeles Region Seismic Experiment Passive Array, Geophysical Research Letters, 24(15), 1855–1858, doi:10.1029/97GL01823.

Koper, K. D., and M. L. Pyle (2004), Observations of PKiKP/PcP amplitude ratios and implications for Earth structure at the boundaries of the liquid core, Journal of Geophysical Research: Solid Earth (1978–2012), 109(B3), 1227, doi:10.1029/2003JB002750.

Kustowski, B., G. Ekström, and A. M. Dziewoński (2008), Anisotropic shear-wave velocity structure of the Earth's mantle: A global model, Journal of Geophysical Research, 113(B6), B06306, doi:10.1029/2007JB005169.

Labrosse, S., J. W. Hernlund, and N. Coltice (2007), A crystallizing dense magma ocean at the base of the Earth’s mantle, Nature, 450(7171), 866–869, doi:10.1038/nature06355.

Lai, H., E. J. Garnero, S. P. Grand, R. W. Porritt, and T. W. Becker (2019), Global travel time data set from adaptive empirical wavelet construction, Geochem. Geophys. Geosyst., 22(2), 231–24, doi:10.1029/2018GC007905.

Lay, T., E. J. Garnero, and S. A. Russell (2004), Lateral variation of the D″ discontinuity beneath the Cocos Plate, Geophysical Research Letters, 31(15), L15612, doi:10.1029/2004GL020300.

Lay, T., J. Hernlund, E. J. Garnero, and M. S. Thorne (2006), A Post-Perovskite Lens and D″ Heat Flux Beneath the Central Pacific, Science, 314(5), 1272–1276, doi:10.1126/science.1133280.

Lay, T., and C. J. Young (1991), Analysis of seismic SV waves in the core's penumbra, Geophysical Research Letters, 18(8), 1373–1376, doi:10.1029/91GL01691.

Lay, T., and D. V. Helmberger (1983), A lower mantle S-wave triplication and the shear velocity structure of D″, Geophysical Journal of the Royal Astronomical Society, 75(3), 799–837, doi:10.1111/j.1365-246X.1983.tb05010.x.

Lay, T., and E. J. Garnero (2011), Deep Mantle Seismic Modeling and Imaging, Annual Review of Earth and Planetary Sciences, 39(1), 91–123, doi:10.1146/annurev-earth-040610-133354.

Lee, C.-T. A., P. Luffi, T. Höink, J. Li, R. Dasgupta, and J. Hernlund (2011), Upside-down differentiation and generation of a "primordial" lower mantle, Nature, 463(7283), 930–933, doi:10.1038/nature08824.

Lekic, V., S. Cottaar, A. Dziewoński, and B. Romanowicz (2012), Cluster analysis of global lower mantle tomography: A new class of structure and implications for chemical heterogeneity, Earth and Planetary Science Letters, 357-358(C), 68–77, doi:10.1016/j.epsl.2012.09.014.

Li, C., R. D. van der Hilst, E. R. Engdahl, and S. Burdick (2008), A new global model for P-wave speed variations in Earth's mantle, Geochem. Geophys. Geosyst., 9(5), n/a–n/a, doi:10.1029/2007GC001806.

Li, M., A. K. McNamara, E. J. Garnero, and S. Yu (2017), Compositionally-distinct ultra-low velocity zones on Earth's core-mantle boundary, Nature Communications, 8(1), 977, doi:10.1038/s41467-017-00219-x.

Li, M., A. K. McNamara, E. J. Garnero (2014), Chemical complexity of hotspots caused by cycling oceanic crust through mantle reservoirs, Nature Geoscience, 7(5), 366–370, doi:10.1038/ngeo2120.

Li, M., and A. K. McNamara (2013), The difficulty for subducted oceanic crust to accumulate at the Earth's core-mantle boundary, J. Geophys. Res. Solid Earth, 118(4), 1807–1816, doi:10.1002/jgrb.50156.

Li, Y., M. S. Miller, and D. Sun (2019), Seismic imaging the D″ region beneath the Central Atlantic, Physics of the earth and planetary interiors, 292, 76–86, doi:10.1016/j.pepi.2019.05.005.

Liu, J., J. Li, R. Hrubiak, and J. S. Smith (2016), Origins of ultralow velocity zones through slab-derived metallic melt, Proc. Natl. Acad. Sci. U.S.A., 113(20), 5547–5551, doi:10.1073/pnas.1519540113.

Loubet, M., R. Sassi, and G. Di Donato (1988), Mantle heterogeneities: a combined isotope and trace element approach and evidence for recycled continental crust materials in some OIB sources, Earth and Planetary Science Letters, 89(3-4), 299–315, doi:10.1016/0012-821X(88)90118-5.

Luo, S. N., S. Ni, and D. V. Helmberger (2001), Evidence for a sharp lateral variation of velocity at the core–mantle boundary from multipathed PKPab, Earth and Planetary Science Letters, 189(3-4), 155–164, doi:10.1016/S0012-821X(01)00364-8.

Mao, H. K., Y. Wu, L. C. Chen, J. F. Shu, and A. P. Jephcoat (1990), Static compression of iron to 300 GPa and Fe0.8Ni0.2 alloy to 260 GPa: implications for composition of the core, Journal of Geophysical Research, 95(B13), doi: 10.1029/JB095iB13p21737.

Mao, W. L. (2006), Iron-Rich Post-Perovskite and the Origin of Ultralow-Velocity Zones, Science, 312(5773), 564–565, doi:10.1126/science.1123442.

McDonough, W. F., and S. S. Sun (1995), The Composition of the Earth, Chemical Geology, 120(3-4), 223–253, doi:10.1016/0009-2541(94)00140-4.

McNamara, A. K. (2019), A review of large low shear velocity provinces and ultra-low velocity zones, Tectonophysics, 760, 199–220, doi:10.1016/j.tecto.2018.04.015.

McNamara, A. K., E. J. Garnero, and S. Rost (2010), Tracking deep mantle reservoirs with ultra-low velocity zones, Earth and Planetary Science Letters, 299(1-2), 1–9, doi:10.1016/j.epsl.2010.07.042.

McNamara, A. K., and S. Zhong (2005), Thermochemical structures beneath Africa and the Pacific Ocean, Nature, 437(7062), 1136–1139, doi:10.1038/nature04066.

Morgan, W. J. (1971), Convection Plumes in the Lower Mantle, Nature, 230(5288), 42–43, doi:10.1038/230042a0.

Morgan, W. J., and J. P. Morgan (2007), Plate velocities in the hotspot reference frame, Geological Society of America Special Papers, 430, 65–78, doi:10.1130/2007.2430(04).

Mori, J., and D. V. Helmberger (1995), Localized boundary layer below the mid-Pacific velocity anomaly identified from a PcP precursor, Journal of Geophysical Research: Solid Earth (1978–2012), 100(B10), 20359–20365, doi:10.1029/95JB02243.

Mulyukova, E., B. Steinberger, M. Dabrowski, and S. V. Sobolev (2015), Survival of LLSVPs for billions of years in a vigorously convecting mantle: Replenishment and destruction of chemical anomaly, J. Geophys. Res. Solid Earth, 120(5), 3824–3847, doi:10.1002/2014JB011688.

Mundl, A., M. Touboul, M. G. Jackson, J. M. D. Day, M. D. Kurz, V. Lekic, R. T. Helz, and R. J. Walker (2017), Tungsten-182 heterogeneity in modern ocean island basalts, Science, 356(6333), 66–69, doi:10.1126/science.aal4179.

Murakami, M., K. Hirose, K. Kawamura, N. Sata, and Y. Ohishi (2004), Post-Perovskite Phase Transition in MgSiO3, Science, 304(5672), 855-858, doi:10.1126/science.1095932.

Murakami, M., S. V. Sinogeikin, J. D. Bass, N. Sata, Y. Ohishi, and K. Hirose (2007), Sound velocity of MgSiO3 post-perovskite phase: A constraint on the D″ discontinuity, Earth and Planetary Science Letters, 259(1-2), 18–23, doi:10.1016/j.epsl.2007.04.015.

Murakami, M., Y. Ohishi, N. Hirao, and K. Hirose (2012), A perovskitic lower mantle inferred from high-pressure, high-temperature sound velocity data, Nature, 485(7396), 90–94, doi:10.1038/nature11004.

Muller, G. (1985), The reflectivity method: a tutorial, Journal of Geophysics, 58(1-3), 153–174.

Neuberg, J., and J. Wahr (1991), Detailed Investigation of a Spot on the Core Mantle Boundary Using Digital Pcp Data, Physics of the earth and planetary interiors, 68(1-2), 132–143, doi:10.1016/0031-9201(91)90013-8.

Ni, S., and D. V. Helmberger (2001a), Horizontal transition from fast to slow structures at the core–mantle boundary; South Atlantic, Earth and Planetary Science Letters, 187(3-4), 301–310, doi:10.1016/S0012-821X(01)00273-4.

Ni, S., and D. V. Helmberger (2001b), Probing an ultra-low velocity zone at the core mantle boundary with P and S waves, Geophysical Research Letters, 28(12), 2345–2348, doi:10.1029/2000GL012766.

Ni, S., and D. V. Helmberger (2003a), Further constraints on the African superplume structure, Physics of the earth and planetary interiors, 140(1-3), 243–251, doi:10.1016/j.pepi.2003.07.011.

Ni, S., and D. V. Helmberger (2003b), Ridge-like lower mantle structure beneath South Africa, Journal of Geophysical Research, 108(B2), 3433–14, doi:10.1029/2001JB001545.

Ni, S., and D. V. Helmberger (2003c), Seismological constraints on the South African superplume: Could be the oldest distinct structure on earth, Earth and Planetary Science Letters, 206(1-2), 119–131, doi:10.1016/S0012-821X(02)01072-5.

Niu, F., and L. Wen (2001), Strong seismic scatterers near the core-mantle boundary west of Mexico, Geophysical Research Letters, 28(18), 3557–3560, doi:10.1029/2001GL013270.

Nomura, R., H. Ozawa, S. Tateno, K. Hirose, J. Hernlund, S. Muto, H. Ishii, and N. Hiraoka (2011), Spin crossover and iron-rich silicate melt in the Earth's deep mantle, Nature, 473(7346), 199–202, doi:10.1038/nature09940.

Nomura, R., K. Hirose, K. Uesugi, Y. Ohishi, A. Tsuchiyama, A. Miyake, and Y. Ueno (2014), Low Core-Mantle Boundary Temperature Inferred from the Solidus of Pyrolite, Science, 343(6170), 522–525, doi:10.1126/science.1248186.

O'Neill, H. S. C. (1991), The origin of the moon and the early history of the earth-A chemical model. Part 2: The earth, Geochimica et Cosmochimica Acta, 55(4), 1159–1172, doi:10.1016/0016-7037(91)90169-6.

Oganov, A. R., and S. Ono (2004), Theoretical and experimental evidence for a post-perovskite phase of MgSiO3 in Earth's D″ layer, Nature, 430(6998), 445–448, doi:10.1038/nature02701.

Ohta, K., K. Hirose, T. Lay, N. Sata, and Y. Ohishi (2008), Phase transitions in pyrolite and MORB at lowermost mantle conditions: Implications for a MORB-rich pile above the core–mantle boundary, Earth and Planetary Science Letters, 267(1-2), 107–117, doi:10.1016/j.epsl.2007.11.037.

Owens, T. J., H. P. Crotwell, C. Groves, and P. Oliver-Paul (2004), SOD: STANDING ORDER FOR DATA, Seismological Research Letters, 75(4), 515–520, doi:10.1785/gssrl.75.4.515-a.

Pachhai, S., J. Dettmer, and H. Tkalčić (2015), Ultra-low velocity zones beneath the Philippine and Tasman Seas revealed by a trans-dimensional Bayesian waveform inversion, Geophys J Int, 203(2), 1302–1318, doi:10.1093/gji/ggv368.

Pearson, D. G. et al. (2015), Hydrous mantle transition zone indicated by ringwoodite included within diamond, Nature, 507(7491), 221–224, doi:10.1038/nature13080.

Persh, S. E., J. E. Vidale, and P. S. Earle (2001), Absence of Short-Period ULVZ Precursors to PcP and ScP from two Regions of the CMB, Geophysical Research Letters, 28(2), 387–390, doi:10.1029/2000GL011607.

Pradhan, G. K., G. Fiquet, J. Siebert, A.-L. Auzende, G. Morard, D. Antonangeli, and G. Garbarino (2015), Earth and Planetary Science Letters, Earth and Planetary Science Letters, 431(C), 247–255, doi:10.1016/j.epsl.2015.09.034.

Rawlinson, N., and B. L. N. Kennett (2004), Rapid estimation of relative and absolute delay times across a network by adaptive stacking, Geophys J Int, 157(1), 332–340, doi:10.1111/j.1365-246X.2004.02188.x.

Reasoner, C., and J. Revenaugh (1999), Short-period P wave constraints on D″ reflectivity, J. Geophys. Res. Solid Earth, 104(B), 955–961, doi:10.1029/1998JB900053.

Reasoner, C., and J. Revenaugh (2000), ScP constraints on ultralow-velocity zone density and gradient thickness beneath the Pacific, Journal of Geophysical Research: Solid Earth (1978–2012), 105(B12), 28173–28182, doi:10.1029/2000JB900331.

Revenaugh, J., and R. Meyer (1997), Seismic Evidence of Partial Melt Within a Possibly Ubiquitous Low-Velocity Layer at the Base of the Mantle, Science, 277(5326), 670–673, doi:10.1126/science.277.5326.670.

Ricolleau, A. et al. (2009), Density profile of pyrolite under the lower mantle conditions, Geophysical Research Letters, 36(6), 789–5, doi:10.1029/2008GL036759.

Ringwood, A. E. (1962), A model for the upper mantle, Journal of Geophysical Research: Solid Earth (1978–2012), 67(2), 857–867, doi.org/10.1029/JZ067i002p00857

Ringwood, A. E. (1991), Phase transformations and their bearing on the constitution and dynamics of the mantle, Geochimica et Cosmochimica Acta, 55(8), 2083–2110, doi:10.1016/0016-7037(91)90090-R.

Ringwood, A. E., and T. Irifune (1988), Nature of the 650-km seismic discontinuity: Implications for mantle dynamics and differentiation, Nature, 331(6152), 131–136, doi:10.1038/331131a0.

Ritsema, J., A. Deuss, H. J. Van Heijst, and J. H. Woodhouse (2011), S40RTS: a degree-40 shear-velocity model for the mantle from new Rayleigh wave dispersion, teleseismic traveltime and normal-mode splitting function measurements, Geophys J Int, 184(3), 1223–1236, doi: 10.1111/j.1365-246X.2010.04884.x.

Rizo, H., R. J. Walker, R. W. Carlson, M. F. Horan, S. Mukhopadhyay, V. Manthos, D. Francis, and M. G. Jackson (2016), Preservation of Earth-forming events in the tungsten isotopic composition of modern flood basalts, Science, 352(6287), 809-812, doi: 10.1126/science.aad8563.

Rokosky, J. M., T. Lay, and E. J. Garnero (2006), Small-scale lateral variations in azimuthally anisotropic D″ structure beneath the Cocos Plate, Earth and Planetary Science Letters, 248(1-2), 411–425, doi:10.1016/j.epsl.2006.06.005.

Rondenay, S., and K. M. Fischer (2003), Constraints on localized core-mantle boundary structure from multichannel, broadband SKS coda analysis, Journal of Geophysical Research, 108(B), 2537, doi:10.1029/2003JB002518.

Ross, A. R., H. Thybo, and L. N. Solidilov (2004), Reflection seismic profiles of the core-mantle boundary, Journal of Geophysical Research, 109(B8), 1335, doi:10.1029/2003JB002515.

Rost, S., E. J. Garnero, M. S. Thorne, and A. R. Hutko (2010b), On the absence of an ultralow-velocity zone in the North Pacific, Journal of Geophysical Research, 115(B4), L14612, doi:10.1029/2009JB006420.

Rost, S., E. J. Garnero, Q. Williams, and M. Manga (2005), Seismological constraints on a possible plume root at the core–mantle boundary, Nature, 435(7042), 666–669, doi:10.1038/nature03620.

Rost, S., E. J. Garnero, and Q. Williams (2006), Fine-scale ultralow-velocity zone structure from high-frequency seismic array data, Journal of Geophysical Research, 111(B9), 1169, doi:10.1029/2005JB004088.

Rost, S., E. J. Garnero, and W. Stefan (2010a), Thin and intermittent ultralow-velocity zones, Journal of Geophysical Research: Solid Earth (1978–2012), 115(B6), 443, doi:10.1029/2009JB006981.

Rost, S., and C. Thomas (2010), High resolution CMB imaging from migration of short-period core reflected phases, Physics of the earth and planetary interiors, 183(1), 143–150, doi:10.1016/j.pepi.2010.04.005.

Rost, S., and E. J. Garnero (2006), Detection of an ultralow velocity zone at the core-mantle boundary using diffracted PKKPab waves, Journal of Geophysical Research: Solid Earth (1978–2012), 111(B7), 151, doi:10.1029/2005JB003850.

Rost, S., and J. Revenaugh (2001), Seismic detection of rigid zones at the top of the core, Science, 294(5548), 1911–1914, doi:10.1126/science.1065617.

Rost, S., and J. Revenaugh (2003), Small-scale ultralow-velocity zone structure imaged by ScP, Journal of Geophysical Research: Solid Earth (1978–2012), 108(B1), 421, doi:10.1029/2001JB001627.

Roy, S. K., N. Takeuchi, D. Srinagesh, M. Ravi Kumar, and H. Kawakatsu (2019), Topography of the western Pacific LLSVP constrained by S-wave multipathing, Geophys J Int, 218(1), 190–199, doi:10.1093/gji/ggz149.

Rubie, D. C. (1984), The olivine → spinel transformation and the rheology of subducting lithosphere, Nature, 308(5959), 505–508, doi:10.1038/308505a0.

Ruff, L., and D. L. Anderson (1980), Core formation, evolution, and convection: a geophysical model, Physics of the earth and planetary interiors, 21(2-3), 181–201, doi:10.1016/0031-9201(80)90069-2.

Russell, S. A., C. Reasoner, T. Lay, and J. Revenaugh (2001), Coexisting shear- and compressional-wave seismic velocity discontinuities beneath the central Pacific, Geophysical Research Letters, 28(11), 2281–2284, doi:10.1029/2000GL012553.

Schilling, J. G., M. Zajac, R. Evans, T. Johnston, W. White, J. D. Devine, and R. Kingsley (1983), Petrologic and geochemical variations along the Mid-Atlantic Ridge from 29 degrees N to 73 degrees N, Am J Sci, 283(6), 510–586, doi:10.2475/ajs.283.6.510.

Schubert, G., G. Masters, P. Olson, and P. Tackley (2004), Superplumes or plume clusters? Physics of the earth and planetary interiors, 146(1-2), 147–162, doi:10.1016/j.pepi.2003.09.025.

Shim, S. H., T. S. Duffy, R. Jeanloz, and G. Shen (2004), Stability and crystal structure of MgSiO3 perovskite to the core-mantle boundary, Geophysical Research Letters, 31(10), doi:10.1029/2004GL019639.

Shim, S.-H. (2008), The Postperovskite Transition, Annual Review of Earth and Planetary Sciences, 36(1), 569-599, doi:10.1146/annurev.earth.36.031207.124309.

Sigloch, K., N. McQuarrie, and G. Nolet (2008), Two-stage subduction history under North America inferred from multiple-frequency tomography, Nature Geoscience, 1(7), 458–462, doi:10.1038/ngeo231.

Silver, P. G., and C. Bina (1993), An anomaly in the amplitude ratio of SKKS/SKS in the range 100–108° from portable teleseismic data, Geophysical Research Letters, 20(12), 1135–1138, doi:10.1029/92GL02464.

Simmons, N. A., A. M. Forte, L. Boschi, and S. P. Grand (2010), GyPSuM: A joint tomographic model of mantle density and seismic wave speeds, Journal of Geophysical Research, 115(B12), B12310, doi:10.1029/2010JB007631.

Simmons, N. A., and S. P. Grand (2002), Partial melting in the deepest mantle, Geophysical Research Letters, 29(11), 161, doi:10.1029/2001GL013716.

Stixrude, L., and C. Lithgow-Bertelloni (2011), Thermodynamics of mantle minerals - II. Phase equilibria, Geophys J Int, 184(3), 1180–1213, doi:10.1111/j.1365-246X.2010.04890.x.

Stixrude, L., and C. Lithgow-Bertelloni (2012), Geophysics of Chemical Heterogeneity in the Mantle, Annu. Rev. Earth Planet. Sci., 40(1), 569–595, doi:10.1146/annurev.earth.36.031207.124244.

Sun, D., D. Helmberger, S. Ni, and D. Bower (2009), Direct measures of lateral velocity variation in the deep Earth, Journal of Geophysical Research, 114(B5), 97, doi:10.1029/2008JB005873.

Sun, D., D. Helmberger, V. H. Lai, M. Gurnis, J. M. Jackson, and H. Y. Yang (2019), Slab Control on the Northeastern Edge of the Mid-Pacific LLSVP Near Hawaii, Geophysical Research Letters, 46(6), 3142–3152, doi:10.1029/2018GL081130.

Tackley, P. J. (2007), Mantle Geochemical Geodynamics, in Treatise on Geophysics, vol. 7, pp. 437–505, Elsevier, doi:10.1016/B978-044452748-6.00124-3.

Tackley, P. J. (2011), Living dead slabs in 3-D: The dynamics of compositionally-stratified slabs entering a “slab graveyard” above the core-mantle boundary, Physics of the earth and planetary interiors, 188(3-4), 150–162, doi:10.1016/j.pepi.2011.04.013.

Tackley, P.J., 1998. Three-dimensional simulations of mantle convection with a thermochemical basal boundary layer: D″? In: Gurnis, M., Wysession, M.E., Knittle, E., Buffett, B.A. (Eds.), The Core-Mantle Boundary Region. American Geophysical Union (p. 334).

Takafuji, N. (2005), Solubilities of O and Si in liquid iron in equilibrium with (Mg,Fe)SiO 3perovskite and the light elements in the core, Geophysical Research Letters, 32(6), 49–4, doi:10.1029/2005GL022773.

Tan, E., and M. Gurnis (2005), Metastable superplumes and mantle compressibility, Geophysical Research Letters, 32(20), 1–4, doi:10.1029/2005GL024190.

Tan, E., and M. Gurnis (2007), Compressible thermochemical convection and application to lower mantle structures, J. Geophys. Res. Solid Earth, 112(6), doi:10.1029/2006JB004505.

Tateno, S., K. Hirose, N. Sata, and Y. Ohishi (2007), Solubility of FeO in (Mg,Fe)SiO3 perovskite and the post-perovskite phase transition, Physics of the earth and planetary interiors, 160(3-4), 319–325, doi:10.1016/j.pepi.2006.11.010.

Taylor, S. R. (1964), Chondritic earth model, Nature, 202(4929), 281–282, doi:10.1038/202281a0.

Thomas, C., E. J. Garnero, and T. Lay (2004a), High-resolution imaging of lowermost mantle structure under the Cocos plate, Journal of Geophysical Research, 109(B8), 2016–11, doi:10.1029/2004JB003013.

Thomas, C., J. M. Kendall, and M. Weber (2002), The lowermost mantle beneath northern Asia - I. Multi-azimuth studies of a D″ heterogeneity, Geophys J Int, 151(1), 279–295, doi:10.1046/j.1365-246X.2002.01759.x.

Thomas, C., J. Wookey, J. Brodholt, and T. Fieseler (2011), Anisotropy as cause for polarity reversals of D″ reflections, Earth and Planetary Science Letters, 307(3-4), 369–376, doi:10.1016/j.epsl.2011.05.011.

Thomas, C., J.-M. Kendall, and G. Helffrich (2009), Probing two low-velocity regions with PKPb-caustic amplitudes and scattering, Geophys J Int, 178(1), 503–512, doi:10.1111/j.1365-246X.2009.04189.x.

Thomas, C., J.-M. Kendall, and J. Lowman (2004b), Lower-mantle seismic discontinuities and the thermal morphology of subducted slabs, Earth and Planetary Science Letters, 225(1-2), 105–113, doi:10.1016/j.epsl.2004.05.038.

Thomas, C., M. Weber, C. W. Wicks, and F. Scherbaum (1999), Small scatterers in the lower mantle observed at German broadband arrays, Journal of Geophysical Research: Solid Earth (1978–2012), 104(B7), 15073–15088, doi:10.1029/1999JB900128.

Thomas, C., and J. M. Kendall (2002), The lowermost mantle beneath northern Asia - II. Evidence for lower-mantle anisotropy, Geophys J Int, 151(1), 296–308, doi:10.1046/j.1365-246X.2002.01760.x.

Thompson, P. F., and P. J. Tackley (1998), Generation of mega-plumes from the core-mantle boundary in a compressible mantle with temperature-dependent viscosity, Geophysical Research Letters, 25(11), 1999–2002, doi:10.1029/98GL01228.

Thomson, A. R., W. A. Crichton, J. P. Brodholt, I. G. Wood, N. C. Siersch, J. M. R. Muir, D. P. Dobson, and S. A. Hunt (2019), Seismic velocities of CaSiO3 perovskite can explain LLSVPs in Earth’s lower mantle, Nature, 572(7771), 643–647, doi:10.1038/s41586-019-1483-x.

Thorne, M. S., E. J. Garnero, G. Jahnke, H. Igel, and A. K. McNamara (2013), Mega ultra-low velocity zone and mantle flow, Earth and Planetary Science Letters, 364, 59–67, doi:10.1016/j.epsl.2012.12.034.

Thorne, M. S., E. J. Garnero, and S. P. Grand (2004), Geographic correlation between hot spots and deep mantle lateral shear-wave velocity gradients, Physics of the earth and planetary interiors, 146(1-2), 47–63, doi:10.1016/j.pepi.2003.09.026.

Thorne, M. S., T. Lay, E. J. Garnero, G. Jahnke, and H. Igel (2007), Seismic imaging of the laterally varying D″ region beneath the Cocos Plate, Geophys J Int, 170(2), 635–648, doi:10.1111/j.1365-246X.2006.03279.x.

Thorne, M. S., and E. J. Garnero (2004), Inferences on ultralow-velocity zone structure from a global analysis of SPdKS waves, Journal of Geophysical Research, 109(B8), 421, doi:10.1029/2004JB003010.

To, A., Y. Fukao, and S. Tsuboi (2011), Evidence for a thick and localized ultra-low shear velocity zone at the base of the mantle beneath the central Pacific, Physics of the earth and planetary interiors, 184(3-4), 119–133, doi:10.1016/j.pepi.2010.10.015.

Tolstikhin, I., and A. W. Hofmann (2005), Early crust on top of the Earth's core, Physics of the earth and planetary interiors, 148(2-4), 109–130, doi:10.1016/j.pepi.2004.05.011.

Torsvik, T. H., R. van der Voo, P. V. Doubrovine, K. Burke, B. Steinberger, L. D. Ashwal, R. G. Tronnes, S. J. Webb, and A. L. Bull (2014), Deep mantle structure as a reference frame for movements in and on the Earth, Proceedings of the National Academy of Sciences, 111(24), 8735–8740, doi:10.1073/pnas.1318135111.

Trampert, J. (2004), Probabilistic Tomography Maps Chemical Heterogeneities Throughout the Lower Mantle, Science, 306(5697), 853–856, doi:10.1126/science.1101996.

Tsuchiya, T., J. Tsuchiya, K. Umemoto, and R. M. Wentzcovitch (2004), Phase transition in MgSiO3 perovskite in the earth's lower mantle, Earth and Planetary Science Letters, 224(3-4), 241–248, doi:10.1016/j.epsl.2004.05.017.

Tsuchiya, T., and J. Tsuchiya (2006), Effect of impurity on the elasticity of perovskite and postperovskite: Velocity contrast across the postperovskite transition in (Mg,Fe,Al)(Si,Al)O 3, Geophysical Research Letters, 33(12), 383, doi:10.1029/2006GL025706.

van der Hilst, R. D., M. V. De Hoop, P. Wang, S. H. Shim, P. Ma, and L. Tenorio (2007), Seismostratigraphy and thermal structure of earth's core-mantle boundary region, Science, 315(5820), 1813–1817, doi:10.1126/science.1137867.

Vanacore, E. A., S. Rost, and M. S. Thorne (2016), Ultralow-velocity zone geometries resolved by multidimensional waveform modelling, Geophys J Int, 206(1), 659–674, doi:10.1093/gji/ggw114.

Vidale, J. E., and H. M. Benz (1992), A sharp and flat section of the core-mantle boundary, Nature, 359(6396), 627–629, doi:10.1038/359627a0.

Vidale, J. E., and M. A. H. Hedlin (1998), Evidence for partial melt at the core-mantle boundary north of Tonga from the strong scattering of seismic waves, Nature, 391(6668), 682–685, doi:10.1038/35601.

Wallace, M., and C. Thomas (2005), Investigating D″ structure beneath the North Atlantic, Physics of the earth and planetary interiors, 151(1-2), 115–127, doi:10.1016/j.pepi.2005.02.001.

Weber, M. (1993), P-Wave and S-Wave Reflections from Anomalies in the Lowermost Mantle, Geophys J Int, 115(1), 183–210, doi:10.1111/j.1365-246X.1993.tb05598.x.

Weber, M., and J. P. Davis (1990), Evidence of a laterally variable lower mantle structure from P- and S-waves, Geophys J Int, 102(1), 231–255, doi:10.1111/j.1365-246X.1990.tb00544.x.

Weber, M., and M. Körnig (1992), A search for anomalies in the lowermost mantle using seismic bulletins, Physics of the earth and planetary interiors, 73(1-2), 1–28, doi:10.1016/0031-9201(92)90104-4.

Wen, L. (2000), Intense seismic scattering near the Earth's core-mantle boundary beneath the Comoros hotspot, Geophysical Research Letters, 27(22), 3627–3630, doi:10.1029/2000GL011831.

Wen, L., and D. V. Helmberger (1998a), Ultra-Low Velocity Zones Near the Core-Mantle Boundary from Broadband PKP Precursors, Science, 279(5357), 1701–1703, doi:10.1126/science.279.5357.1701.

Wen, L., and D. V. Helmberger (1998b), A two-dimensional P-SV hybrid method and its application to modeling localized structures near the core-mantle boundary, Journal of Geophysical Research, 103(B8), 17901–17918, doi:10.1029/98JB01276.

Wessel, P., W. H. F. Smith, R. Scharroo, J. Luis, and F. Wobbe (2013), Generic Mapping Tools: Improved Version Released, Eos Trans. AGU, 94(45), 409–410, doi:10.1002/2013EO450001.

Whittaker, S., M. S. Thorne, N. C. Schmerr, and L. Miyagi (2016), Seismic array constraints on the D″ discontinuity beneath Central America, J. Geophys. Res. Solid Earth, 121(1), 152–169, doi:10.1002/2015JB012392.

Wicks, J. K., J. M. Jackson, W. Sturhahn, and D. Zhang (2017), Sound velocity and density of magnesiowüstites: Implications for ultralow-velocity zone topography, Geophysical Research Letters, 44(5), 2148–2158, doi:10.1002/2016GL071225.

Wiggins, R. W. C. A. R. A. (1976), Source shape estimation and deconvolution of teleseismic body waves, Geophysical Journal of the Royal Astronomical Society, 47(1), 151–177, doi:10.1111/j.1365-246X.1976.tb01267.x.

Williams, Q., J. Revenaugh, and E. J. Garnero (1998), A Correlation Between Ultra-Low Basal Velocities in the Mantle and Hot Spots, Science, 281(5376), 546–549, doi:10.1126/science.281.5376.546.

Williams, Q., and E. J. Garnero (1996), Seismic Evidence for Partial Melt at the Base of Earth's Mantle, Science, 273(5), 1528–1530, doi:10.1126/science.273.5281.1528.

Wookey, J., S. Stackhouse, J.-M. Kendall, J. Brodholt, and G. D. Price (2005), Efficacy of the post-perovskite phase as an explanation for lowermost-mantle seismic properties, Nature, 438(7070), 1004–1007, doi:10.1038/nature04345.

Workman, R. K., and S. R. Hart (2005), Major and trace element composition of the depleted MORB mantle (DMM), Earth and Planetary Science Letters, 231(1-2), 53–72, doi:10.1016/j.epsl.2004.12.005.

Wysession, M. E., T. Lay, J. Revenaugh, Q. Williams, E. J. Garnero, R. Jeanloz, and L. H. Kellogg (1998), The D″ discontinuity and its implications, The core-mantle boundary region, 28, 273–297, doi: 10.1029/GD028p0273.

Xu, W., C. Lithgow-Bertelloni, L. Stixrude, and J. Ritsema (2008), The effect of bulk composition and temperature on mantle seismic structure, Earth and Planetary Science Letters, 275(1-2), 70–79, doi:10.1016/j.epsl.2008.08.012.

Xu, Y., and K. D. Koper (2009), Detection of a ULVZ at the base of the mantle beneath the northwest Pacific, Geophysical Research Letters, 36(17), L14612, doi:10.1029/2009GL039387.

Yao, J., and L. Wen (2014), Seismic structure and ultra-low velocity zones at the base of the Earth's mantle beneath Southeast Asia, Physics of the earth and planetary interiors, 233, 103–111, doi:10.1016/j.pepi.2014.05.009.

Ye, K., B. Cong, and D. Ye (2000), The possible subduction of continental material to depths greater than 200 km, Nature, 407(6805), 734–736, doi:10.1038/35037566.

Young, C. J., and T. Lay (1990), Multiple phase analysis of the shear velocity structure in the D″ region beneath Alaska, J. Geophys. Res. Solid Earth, 95(B), 17–, doi:10.1029/JB095iB11p17385.

Yu, S., and E. J. Garnero (2017), ULVZ Distribution Database from 54 studies [Data set]. Zenodo. http://doi.org/10.5281/zenodo.1000998

Yuan, K., and B. Romanowicz (2017), Seismic evidence for partial melting at the root of major hot spot plumes, Science, 357(6349), 393–397, doi:10.1126/science.aan0760.

Zhang, J., and T. Lay (1984), Investigation of a lower mantle shear wave triplication using a broadband array, Geophysical Research Letters, 11(6), 620–623, doi:10.1029/GL011i006p00620.

Zhang, S., S. Cottaar, T. Liu, S. Stackhouse, and B. Militzer (2016), High-pressure, temperature elasticity of Fe- and Al-bearing MgSiO3: Implications for the Earth's lower mantle, Earth and Planetary Science Letters, 434, 264–273, doi:10.1016/j.epsl.2015.11.030.

Zhang, Y., J. Ritsema, and M. S. Thorne (2009), Modeling the ratios of SKKS and SKS amplitudes with ultra-low velocity zones at the core-mantle boundary, 36(19), B05305–5, doi:10.1029/2009GL040030.

Zhao, C., E. J. Garnero, A. K. McNamara, N. Schmerr, and R. W. Carlson (2015), Seismic evidence for a chemically distinct thermochemical reservoir in Earth's deep mantle beneath Hawaii, Earth and Planetary Science Letters, 426, 143–153, doi:10.1016/j.epsl.2015.06.012.

Zhao, C., E. J. Garnero, M. Li, A. McNamara, and S. Yu (2017), Intermittent and lateral varying ULVZ structure at the northeastern margin of the Pacific LLSVP, J. Geophys. Res. Solid Earth, 122(2), 1198–1220, doi:10.1002/2016JB013449.

Zou, Z., F. Leyton, and K. D. Koper (2007), Partial melt in the lowermost mantle near the base of a plume, Geophys J Int, 168(2), 809–817, doi:10.1111/j.1365-246X.2006.03266.x.

APPENDIX A

REFLECTIVITY - 1D SYNTHETICS

This appendix contains computation details of the 1D synthetic waveforms of S and ScS, using the reflectivity method [Fuchs and Muller, 1971; Fuchs, 1980; Muller, 1985]. The calculation parameters, reference model and model spaces are detailed. It is intended to be a manual to recreate the synthetics we used for waveform modeling in Chapter 3 and Chapter 4.

A.1 Code Availability

The Fortran reflectivity code is maintained by Dr. Nicholas Schmerr. I obtained the code from my advisor Dr. Edward Garnero. I modified some calculation limitations as well as wrote my own codes on model-making and post-processing. My version of the code, together with the original code, can be found in this Github repository: https://github.com/shuleyu/reflectivity.

A.2 1D Reference Model

We used a spline fitted PREM as the 1D reference model (no CMB structure). This modified PREM model, named as PREMX, was originally designed to smooth out shallow structure contamination in 2.5D synthetics calculations (see section B.2 for details). Here in 1D, PREMX is also used as reference model for consistency. Figure A.1 shows S and ScS waveform comparison between PREM and PREMX. The waveforms are similar comparing to each other. The small arrival time shifts play neglectable effects on waveform distortion study as in chapter 3 and 4. PREMX has a more consistent S waveform at close distances (Figure A.1, around 40˚), comparing to PREM. Therefore, we believe it was both safe and proper to use PREMX as 1D reference model.

A.3 Calculation Parameters

Source is put at 500 km. Receivers are put on a profile line with a 0.1° distance increment from 40° to 85°. The profile line has azimuth equals 0°. For this event-receiver geometry, a good source mechanism with strong ScS is chosen. Its strike equals 0°, dip equals 90° and rake equals -130° (Figure A.2a). A strong ScS minimizes S sidelobe effects at large distances, when S and ScS become close to each other.

The calculation run time depends on the following four factors: phase velocity window, seismogram duration, model layer increment and frequency content window. To make frequency content comparable to the data, frequency window is set as 0.01Hz ~ 1.0Hz and layer increment is set to 10 km for ULVZ/UHVZ models and 1 km for D″ discontinuity models. At the bottom of the mantle, layer increment is decreased to 1 km when a ULVZ or a UHVZ layer is added.

Seismogram duration depends on sampling rate and the number of points in seismogram (which must be a power of 2 for this version of reflectivity code). Sampling rate decides the Nyquist frequency ($F_{nq} = \frac{1}{2dt}$), which is the highest frequency the seismogram represent. A sampling rate of 0.05 second is well-sufficient. The number of points is chosen to be 32768, which gives seismogram duration as 1638.4 seconds to cover both S and ScS arrivals at any receiver distance.

The trickiest parameter to choose is the phase velocity window. Figure A.2b-d shows synthetic waveforms when lower end phase velocity is 5.7 km/sec, 6.4 km/sec and 7.0 km/sec (without phase window taper). The corresponding theoretical travel time curves are given in Figure A.2e. For a 500 km source, the lower end can’t go below 5.7 km/s. Because at 500 km, S wave speed is 5.66 km/s, after the earth-flattening. Also, as observed in Figure A.2b, a 5.7 km/sec leads to artifacts at large distances. This experiment shows synthetic waveforms will have spurious signals traveling at the lower end cut-off phase velocity.

The cosine tapering at each end of the phase velocity window are needed to diminish these spurious signals. It requires a lot of trials and errors to decide which taper suits the need. It's hard to argue which phase velocity window is optimal. Eventually, a 6.4 ~ 8 km/sec to 23 ~ 83 km/sec phase velocity window is chosen for our projects because the S arrival looks most stable, and the spurious energies are almost invisible. The number of rays with this phase velocity window is decided by trial and error. Its value is 1500 for ULVZ/UHVZ models and 2000 for D″ discontinuity models.

As an additional note, the reflectivity zones start depth should above the source depth, otherwise there will be artifacts trailing S arrivals.

A.4 Model Space

There are 3 parameters to characterize a 1D layer anomaly layer: the layer's thickness, its S-wave speed change and its density change (Figure A.3). For the central America project in chapter 3, layer thickness varies through 1 to 30 km with intervals of 1 km, S-wave speed change goes from -30% to +20% with intervals of 1% and density change spans from 0% up to 10% with intervals of 2.5%. In total, 7650 models are included in waveform modeling. In addition, gradient models are calculated to explore ScS waveform distortion. But they are not included in waveform modeling. For the global D″ discontinuity project in chapter 4, layer thickness varies through 100 to 350 km with intervals of 50 km, S-wave speed change goes from -5% to +5% with intervals of

1% and density change spans from 0% up to 5% with intervals of 1%. In total, 396 models are included in waveform modeling.

References

Fuchs, K., and G. Muller (1971), Computation of Synthetic Seismograms with the Reflectivity Method and Comparison with Observations, Geophysical Journal of the Royal Astronomical Society, 23(4), 417–433, doi:10.1111/j.1365-246X.1971.tb01834.x.

Fuchs, K. (1980), Calculation of Synthetic seismograms by the reflectivity method, *Bureau of Mineral Resources, Geology and Geophysics*, Record 1980/64, c.3.

Muller, G. (1985), The reflectivity method: a tutorial, Journal of Geophysics, 58(1-3), 153–174.

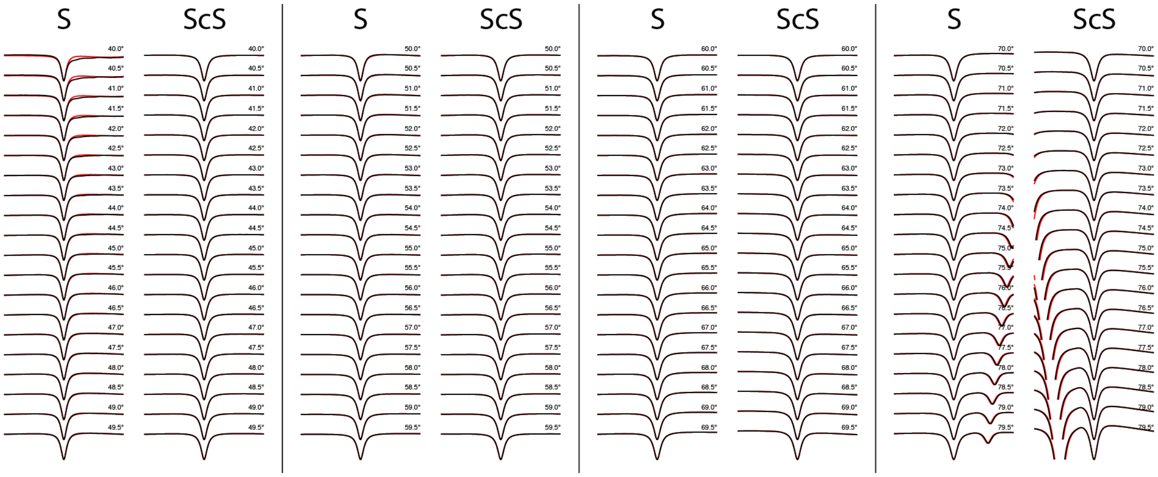

Figure A.1 Waveform comparison between PREM and PREMX. Black lines represent PREM waveforms, red lines represent PREMX waveforms. Distances are marked at the right-hand side of each waveform. These waveforms are normalized and centered at the peak of the S or ScS, marked at the top. Waveforms are cut between the -30 to 30 seconds window.

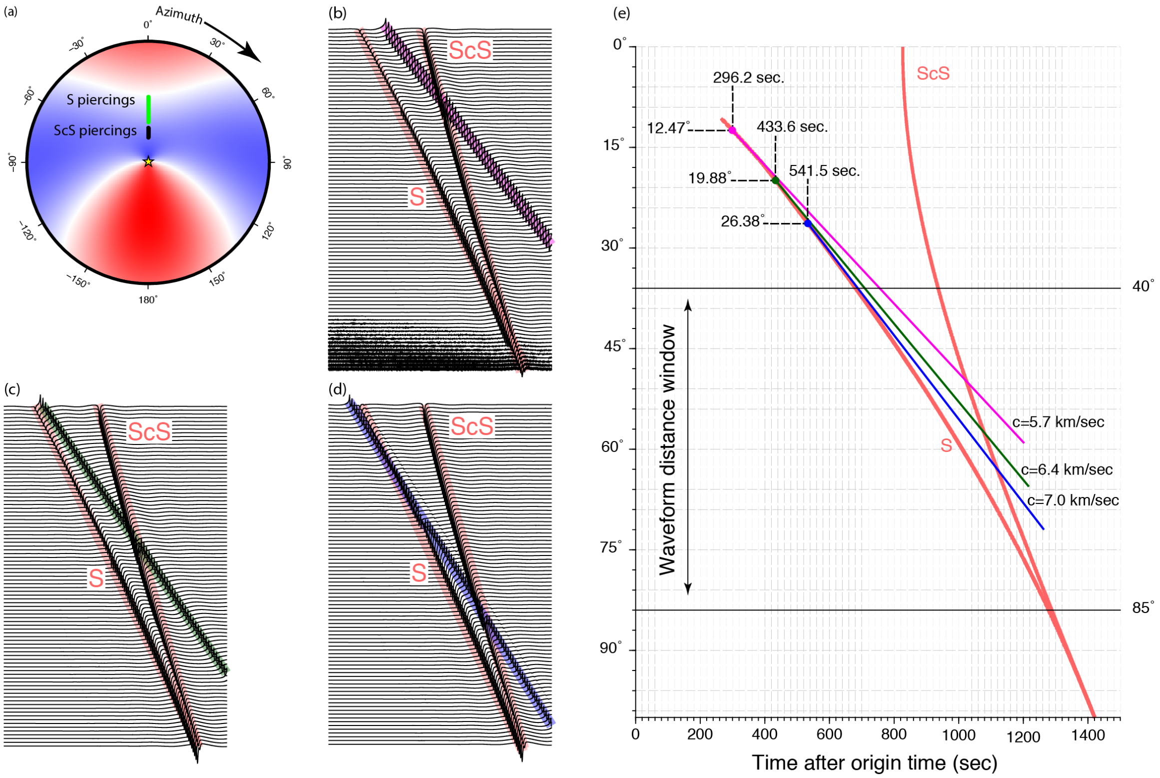

Figure A.2 (a) Lower hemisphere view of source radiation pattern for the chosen focal mechanism. S piercing points on the lower hemisphere are marked in green dots. ScS piercing points are marked in black dots. This CMT solution is chosen for its strong ScS energy. (b-d) Examples of spurious signals traveling at lower end phase velocities. 5.7 km/sec is marked out in magenta, 6.4 km/sec in green and 7.0 km/sec in blue. The waveforms shown are between 40˚ to 85˚. (e) Travel time curves for this experiment. S and ScS are drawn in red curves. Straight lines marks arrival times for the given lower end phase velocities. They are color-coded in the same way as in (b-d).

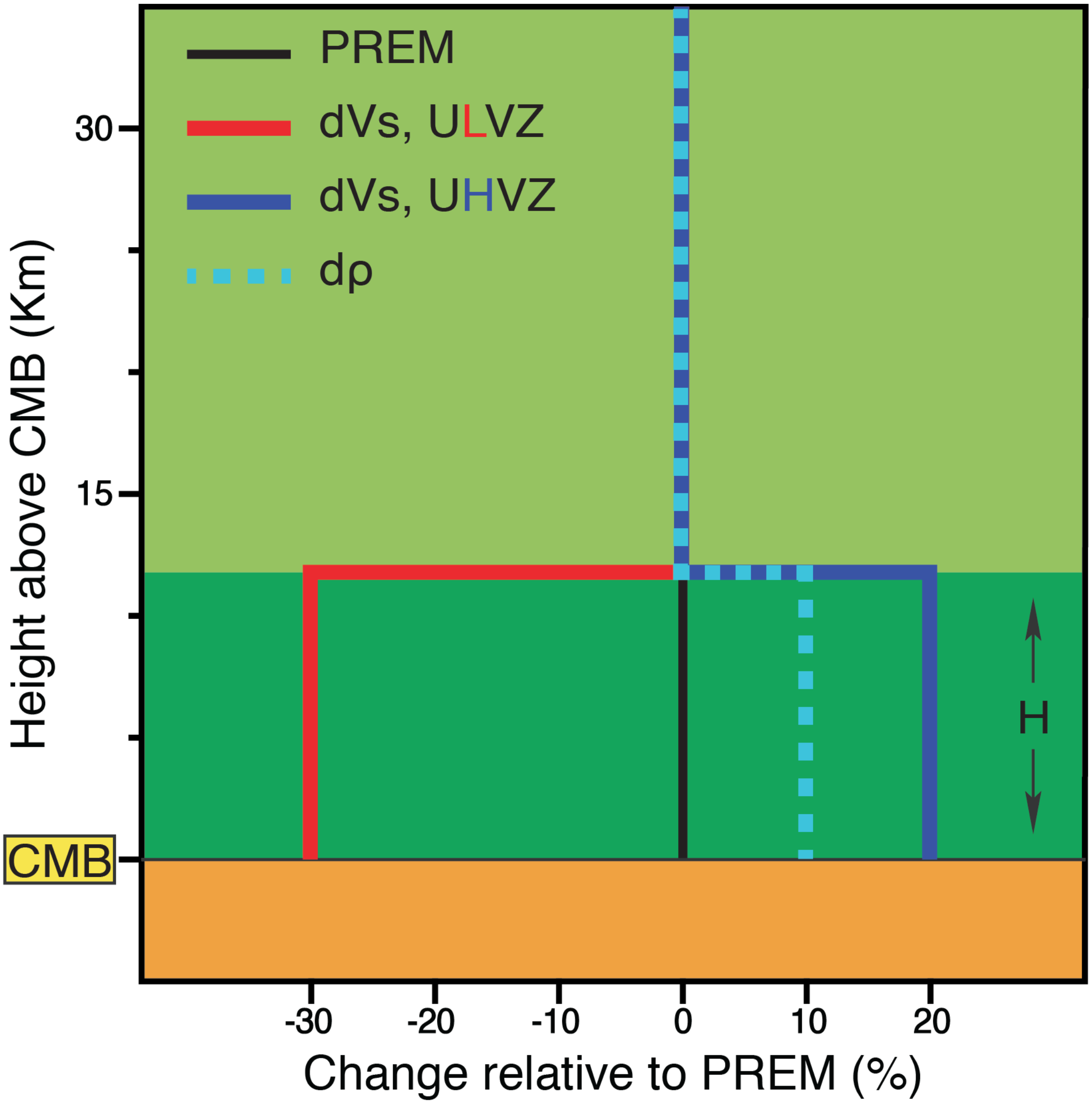

Figure A.3 Model space for central America project in chapter 3. We explored the basal layer S-wave velocities relative to PREM from -30% to +20% with an increment of 1%. The height of the layer ranges from 1 km to 30 km with an increment of 1 km. The density relative to PREM from 0% to 10% with an increment of 2.5%. Total number of models is 7650.

APPENDIX B

SHAXI - 2.5D SYSNTHETICS

This appendix contains computation details of the 2.5D synthetic waveforms using program SHAXI [Jahnke et al., 2008]. The need and derivation of a modified PREM model (named as PREMX), calculation parameters and explored models are detailed. It is intended to be a manual to recreate the synthetics we used in our 2.5D modeling discussion in chapter 3.

B.1 Code Availability

The SHAXI code is downloaded from project SPICE (Seismic wave Propagation and Imaging in Complex media: a European network) homepage. I wrote some codes for model-generating and for post-processing. My own code, together with the original SHAXI code, can be found in this Github repository: https://github.com/shuleyu/shaxi.git.

B.2 PREMX – the 1D Reference Model

The Preliminary reference Earth model (PREM, [Dziewonski and Anderson., 1981]) has 5 first-order discontinuities at depth equals 15 km, 24.4 km, 220 km, 400 km, 670 km and 4 second-order discontinuities at depth equals 80 km, 600 km, 771 km, 2741 km (Figure B.1). S waves undergo multiple reflections and refractions when propagate through upper mantle discontinuities (Figure B.2, marked out in dark green). When the interested Earth's structure is the lowermost mantle, these multiple reflections and refractions from upper mantle discontinuities act as noises, especially at distance when they come across to ScS arrivals (ScS arrivals are marked out in texts in Figure B.2). To remove effects of upper mantle structures in the PREM, we smooth out the second-order discontinuities using spline interpolation. The boundary conditions and polynomial degrees of the interpolation set as:

A. At surface (depth equals 0 km), velocity/density values are fixed to the values after the 24.4 km discontinuity.

B. At surface (depth equals 0 km), velocity/density first-order derivations (slopes) are fixed to 0.

C. At depth equals 400 km, velocity/density values are fixed to the values after the 400 km discontinuity; slopes are fixed to their slopes in PREM between 400 km ~ 600 km.

D. Depth from 0 km to 400 km, degree 3 polynomials are used for all values.

E. At depth equals 600 km, velocity/density values are fixed to PREM values; slopes are kept the same before the discontinuity.

F. At depth equals 970.426 km, P velocity is fixed to PREM value.

G. At depth equals 1155.674 km, S velocity is fixed to PREM value.

H. At depth equals 1726.323 km, density is fixed to PREM value.

The depth at F, G and H are found such that when fitted with a degree 2 polynomial between 600 km and that depth, the slope at that depth agree with the original PREM slope. The smooth result is shown in Table B.1 and is plotted against PREM in Figure B.1. PREMX successfully removes the upper mantle multiple reflections and refractions, and as a result, a more accurate ScS distortion due to lowermost structures. The earlier ScS arrival time from PREMX (Figure B.2) plays neglectable role in ScS waveform distortion study.

B.3 Calculation Parameters

The calculation region is a cross-section of the mantle, spanning from 0˚ to 110˚ and from depth equals 0 km to 2891 km (core is excluded). This 2D region is gridded up into 3800 cells in the radius direction and 20000 cells in the theta direction. These values are chosen to satisfy the frequency requirement. Receivers are on the surface from 40˚ to 85˚ with increment 0.1˚, the same as in 1D reflectivity calculation. Source depth may vary according to the need (see chapter 3 for details.). Seismogram length is 1800 seconds and sampling rate is around 0.025 second. Number of ranks should be able to divide 20000 (cell number in the theta direction).

References

Dziewonski, A. M., and D. L. Anderson (1981), Preliminary reference Earth model, Physics of the earth and planetary interiors, 25(4), 297-356, doi:10.1016/0031-9201(81)90046-7.

Jahnke, G., M. S. Thorne, A. Cochard, and H. Igel (2008), Global SH-wave propagation using a parallel axisymmetric spherical finite-difference scheme: application to whole mantle scattering, Geophys J Int, 173(3), 815–826, doi:10.1111/j.1365-246X.2008.03744.x.

Table B.1 PREM spline interpolation result (PREMX parameters).

Depth(km)	V_P (km/s)	V_S (km/s)	Density (g/cm^3)
$0 \sim 400$	$-4.9209x^3$ $+ 274.0497x^2$ $- 533.3367x$ $+ 272.31852$	$-1147.2266x^3$ $+ 3481.6487x^2$ $- 3521.6177x$ $+ 1191.6866$	$734.7800x^3$ $- 2071.1936x^2$ $+ 1938.0471x$ $- 598.2528$
$400 \sim 600$	PREM values		
$600 \sim$ 970.426 (for V_P) 1155.674 (for V_S) 1726.323 (for Density)	$-189.1929x^2$ $+ 310.1340x$ $- 115.5330$	$-84.4655x^2$ $+ 134.4361x$ $- 46.9541$	$-13.2990x^2$ $+ 16.0633x$ $+ 0.3373$
970.426 (for V_P) 1155.674 (for V_S) 1726.323 (for Density) ~ 2891	PREM values		

i. x in the table is a dimensionless value derived from depth: $x = 1 - Depth/6371$.

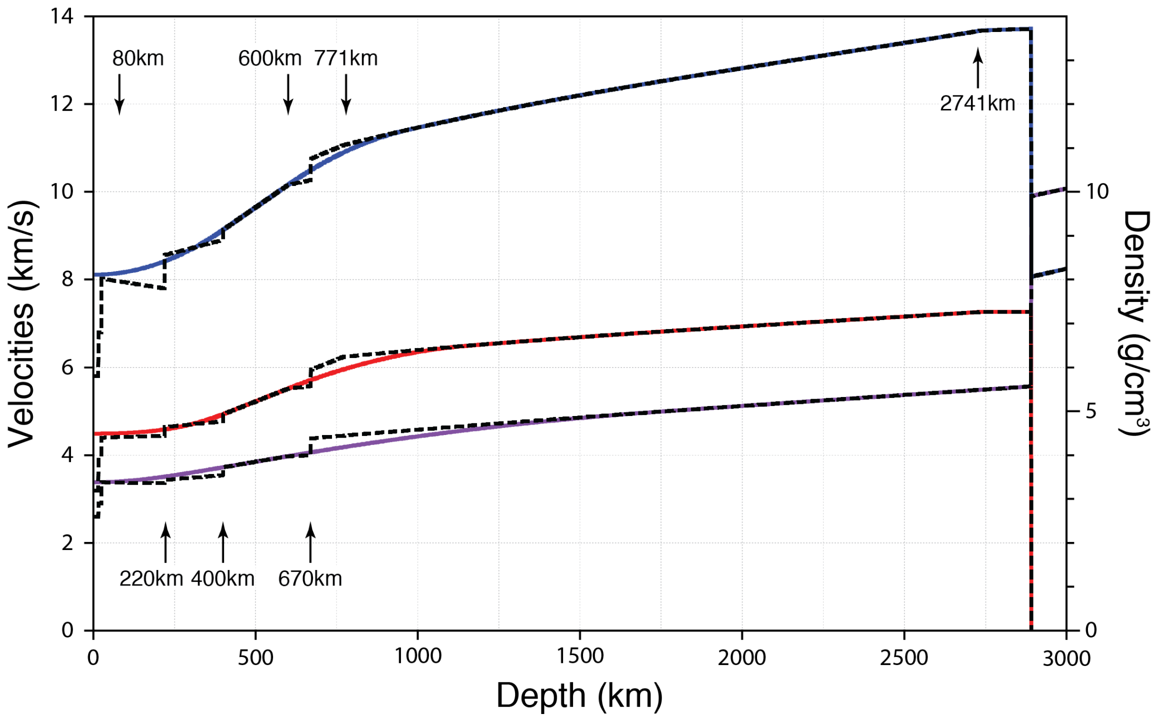

Figure B.1 PREM and modified PREM profile. Dashed lines represent PREM. Blue line represents spline-interpolated P-wave velocity. Red line represented spline-interpolated S-wave velocity. These two properties refer to the left-hand side y-axis. Purple line represented spline-interpolated density. Density refers to the right-hand side y-axis. The discontinuities (except 15 km and 24.4 km) in original PREM model are marked out in texts. The interpolated model is called PREMX, which is used in order to smooth out multiple reflections and refractions caused by upper mantle discontinuities (see text for details).

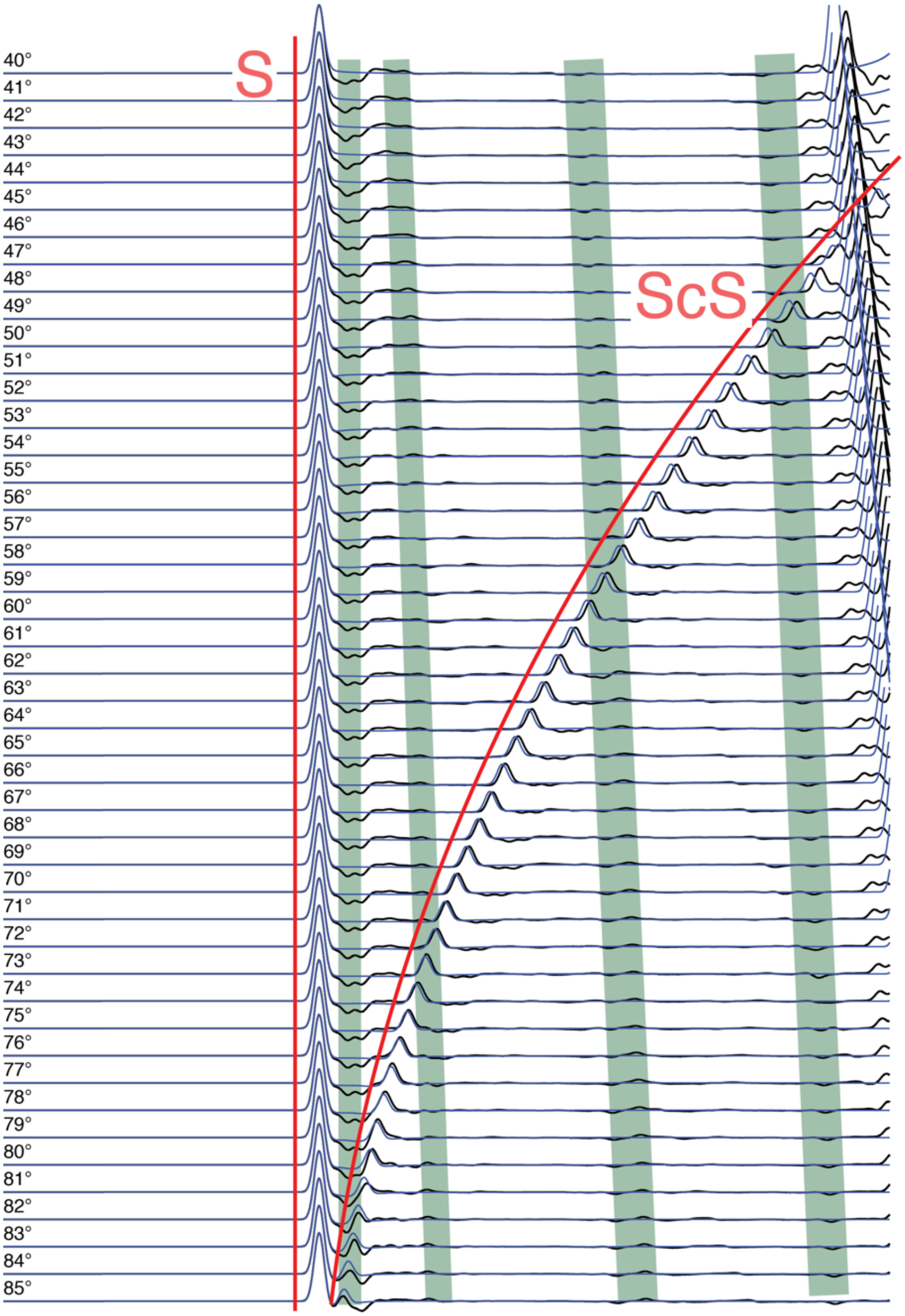

Figure B.2 Waveform comparison between PREM and PREMX, aligned on S arrivals. Synthetic waveforms from original PREM (with all discontinuities) are plotted in black. The modified PREM (PREMX, see in Figure B.1), which smoothed out the discontinuities, produce synthetic waveforms plotted in blue. S and ScS arrivals are marked out in red lines. Dark green shades mark out some of the multiple reflections and refractions caused by PREM discontinuities.